NSEL Report Series
Report No. NSEL-006
December 2007

Model-based Strategies for Real-time Hybrid Testing

Juan E. Carrion
and
Billie F. Spencer, Jr.

NEWMARK STRUCTURAL ENGINEERING LABORATORY

Department of Civil and Environmental Engineering
University of Illinois at Urbana-Champaign

UILU-ENG-2007-1806

ISSN: 1940-9826

The Newmark Structural Engineering Laboratory (NSEL) of the Department of Civil and Environmental Engineering at the University of Illinois at Urbana-Champaign has a long history of excellence in research and education that has contributed greatly to the state-of-the-art in civil engineering. Completed in 1967 and extended in 1971, the structural testing area of the laboratory has a versatile strong-floor/wall and a three-story clear height that can be used to carry out a wide range of tests of building materials, models, and structural systems. The laboratory is named for Dr. Nathan M. Newmark, an internationally known educator and engineer, who was the Head of the Department of Civil Engineering at the University of Illinois [1956-73] and the Chair of the Digital Computing Laboratory [1947-57]. He developed simple, yet powerful and widely used, methods for analyzing complex structures and assemblages subjected to a variety of static, dynamic, blast, and earthquake loadings. Dr. Newmark received numerous honors and awards for his achievements, including the prestigious National Medal of Science awarded in 1968 by President Lyndon B. Johnson. He was also one of the founding members of the National Academy of Engineering.

Contact:
Prof. B.F. Spencer, Jr.
Director, Newmark Structural Engineering Laboratory
2213 NCEL, MC-250
205 North Mathews Ave.
Urbana, IL 61801
Telephone (217) 333-8630
E-mail: bfs@uiuc.edu

This technical report is based on the first author's doctoral dissertation under the same title which was completed in October 2007. The second author served as the dissertation advisor for this work.

Financial support for this research was provided in part by the National Science Foundation under the George E. Brown, Jr. Network for Earthquake Engineering Simulation (NEES) Program (NSF Award No. CMS-0217325). This support is gratefully acknowledged.

The cover photographs are used with permission. The Trans-Alaska Pipeline photograph was provided by Terra Galleria Photography (http://www.terragalleria.com/).

ABSTRACT

Experimental testing is an essential tool for understanding how structures respond to extreme events, thus allowing the design and construction of safer structures. Methods currently used to determine the behavior of structural systems subjected to dynamic loading are quasi-static, shaking-table, and hybrid (or pseudodynamic) testing. In hybrid testing, the dynamic response of the structure is calculated numerically on a computer, and then the restoring forces from the structure are obtained by applying the calculated displacements to a test specimen. The combination of physical testing with numerical simulation provided by hybrid testing facilitates accurate and efficient testing of large and complex structural systems.

Because conventional hybrid testing is executed at slow speeds, the method is not applicable for structures with rate-dependent components (for example, devices associated with vibration control). To allow testing of such structures, researchers have proposed a variation of the method called real-time hybrid testing in which the experiment is executed in real time.

Real-time hybrid testing is challenging because it requires guaranteed execution of each testing cycle within a fixed, small increment of time (typically less than 10 msec). Furthermore, unless appropriate compensation for time delays (from communication and computing time) and actuator dynamics is implemented, stability problems are likely to occur during the experiment. Traditionally, researchers have lumped the effects of time delays and actuator dynamics together and treated them as a constant time delay; techniques were then developed to compensate for this total time delay. However, these techniques only perform well when the delay is small compared to the fundamental period of the structure.

The focus of this report is to develop an approach for real-time hybrid testing that uses model-based methods to compensate for time delays and actuator dynamics and combines fast hardware and software (for high-speed computations and communication) with high performance hydraulic components.

The studies presented in this report extend the capabilities of real-time hybrid testing by facilitating accurate testing of structural systems with larger natural frequencies (e.g., stiff structures or multi-degree-of-freedom systems) and handling larger delays/lags which are typically associated with actuators with high force capacity. Furthermore, these studies demonstrate that real-time hybrid testing is an effective and practical technique to evaluate the response of structures incorporating devices for passive and semiactive structural control.

TABLE OF CONTENTS

CHAPTER 1

INTRODUCTION

1.1 Importance of experimental testing

Natural hazards, such as earthquakes and strong winds, have caused tremendous human suffering and damage to national economies. Understanding how civil engineering structures respond to such dynamic events is extremely important to allow for reduction of the effects of these phenomena. Although design codes have experienced significant improvements over the years and computational methods for dynamic analysis have substantially increased their capabilities, the need for experimental testing still exists today. Indeed, design codes base their methods and requirements largely on the outcome of direct testing. Computational models and constitutive relationships are also developed and evaluated on the basis of the results of experimental testing. When the response characteristics of a structural system are not well understood or difficult to model numerically (e.g., inelasticity, nonlinear effects, and rate dependent behavior), physical testing provides the only accurate way to analyze the dynamic response of the structure. Experimental testing is an essential tool for understanding how structures respond to extreme events, thus allowing the design and construction of safer structures to mitigate natural hazards.

1.2 Experimental testing methods

Several test methods are currently used to determine the behavior of structural systems subjected to dynamic loading. The simplest method is the *quasi-static loading test*, in which the structure or component to be tested is subjected to a predefined displacement or force time history. The predefined inputs (displacements or forces) are applied to the structural component on an extended time scale (i.e., slow rates); therefore, the interaction with the structure to which it is to be attached and the dynamic and rate-dependent behavior of the structure are not considered. Typically, this type of test is used to investigate the hysteretic or cyclic behavior of structural materials or components under earthquake loading. A more realistic approach is the *shaking-table test* method, where the entire structure is subjected to a ground acceleration history applied by the shaking-table. Because the test is conducted in real time, dynamic effects and rate-dependent behavior can be completely modeled. Although there are a few shaking-tables in the world capable of full-scale testing of building structures (e.g., the E-Defense table in Japan), tests generally must be conducted on a reduced scale model due to limitations on the size and payload capacity of the shaking-table, as well as for economical reasons. The results of a reduced-scale model do not necessarily represent the response of the full-scale prototype. Certain types of behavior, especially local effects (e.g., bond and shear in reinforced concrete members, crack propagation, welding effects, and local buckling in steel structures), are well known to have size effects and not to scale, which limits the

applicability and accuracy of the shaking-table test method. The shaking-table test method is also restricted to structures subjected to dynamic base motion; therefore, different loading conditions (e.g., wind) cannot be considered. Inclusion of soil-structure interaction effects in shaking-table testing is also challenging.

Hybrid (or *pseudodynamic*) testing provides an attractive alternative for dynamic testing of structural systems, combining physical testing with numerical simulation (Hakuno et al., 1969; Takanashi et al., 1975; Mahin & Shing, 1985; Takanashi & Nakashima, 1987; Mahin et al., 1989; Shing et al., 1996). The basis of the method is that the structure to be tested is divided into a physical component and a numerical model. The physical component is composed of a test specimen with the stiffness characteristics of the test structure. The numerical model includes the mass of the structure (lumped at discrete locations), and the structural damping. During the test, the dynamic response of the structure due to a particular loading (e.g., earthquake) is calculated numerically on a computer using time step-integration of the equation of motion. The calculated displacements are then applied to the test specimen using actuators at the discrete locations where the lumped masses are assumed. The forces required to produce these displacements are measured and fed back to the computer to calculate the displacements corresponding to the next time step (see Figure 1.1).

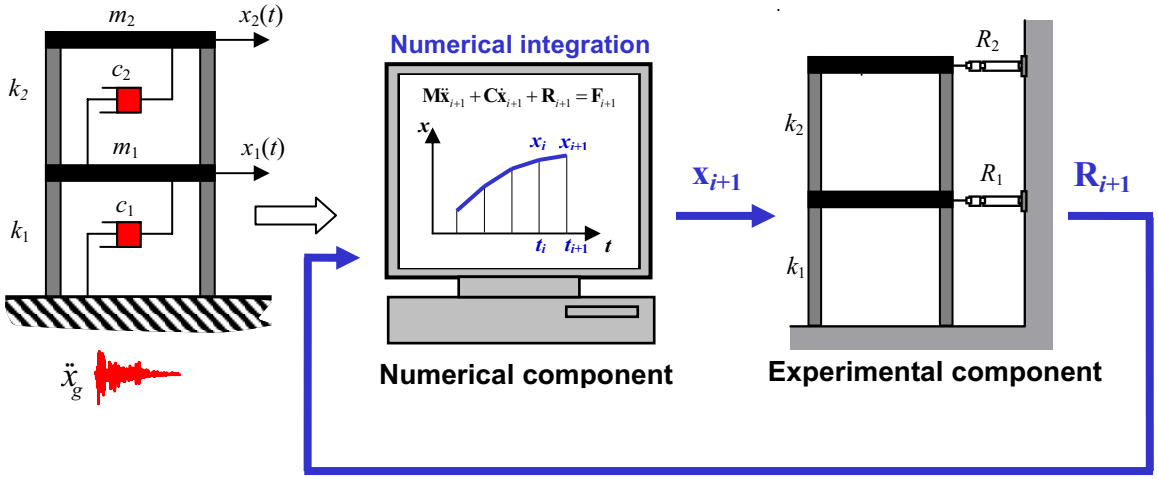

Figure 1.1: Schematic diagram of hybrid test method.

Because damage is intrinsically a local phenomenon, testing of the entire structural system is frequently not required. The *substructure technique* allows physical testing of only the parts of the structure of interest (e.g., where damage is expected and the associated numerical modeling is difficult), while the rest of the structure is modeled numerically. Through the interaction of the physical and numerical substructures during the test, the dynamic response of the entire system is obtained.

In hybrid testing, the displacements are imposed on an extended time-scale which typically ranges from 100 to 1000 times the actual earthquake duration. This time modification allows for the use of larger actuators without high hydraulic flow

requirements, careful observation of the response of the structure during the test, and the ability to pause and resume the experiment. Because the actuators can generate larger forces, structures can be tested readily at large- or full-scale. The mass of the structure (which can be calculated with good accuracy) and the structural damping are modeled numerically and, therefore, need not be accommodated by the physical specimen, in contrast to shaking-table tests. The pseudodynamic test method also has some disadvantages. Because the number of actuators that can be attached to a structure is limited, the method is practical only for structures in which the physical substructure have concentrated masses or can be modeled with a few lumped masses (usually, the number of required actuators is equal to the number of degrees-of-freedom associated with lumped masses). Additionally, the use of an extended time scale renders the method inapplicable when the restoring forces also depend on the velocity (i.e., rate-dependent).

To expand the field of application of the pseudodynamic test method, several variations have been proposed. The *continuous pseudodynamic* method imposes continuous loading to avoid force relaxation effects. The continuous movement of the actuators is commonly achieved by using a response prediction-correction method to generate continuous command signals between each time step.

Distributed pseudodynamic testing uses the internet to link geographically distributed facilities, expanding considerably the type and size of structural systems that can be tested. Because the time required for network communication is relatively large, response prediction-correction methods are required to generate the actuator command signals at continuous or fast-rate tests.

Real-time hybrid testing is a variation of the pseudodynamic test method in which the imposed displacements and response analysis are executed in real time, thus allowing testing of systems with rate-dependent components. Real-time hybrid testing makes possible the testing of a large class of structural components associated with vibration control, including passive, semiactive, and active control devices (e.g., base isolation and dampers), which are typically nonlinear and rate-dependent.

Real-time hybrid testing is challenging because it is necessary to perform all of the calculations, apply the displacements, and measure and feedback the forces within a single time step (typically less than 10 msec). Because the test is conducted in real time, the dynamics of the testing system and specimen become important. For example, when hydraulic actuators are used to apply forces to the test specimen, a time lag exists between when the displacement is commanded and when the actuator actually reaches the commanded position. There are also some inevitable time delays associated with the numerical calculations and the communication between the computer and data acquisition systems. The computing time can become large, especially for complex models (numerous degrees-of-freedom) or numerical substructures with nonlinear response. Because of these time delays and lags, the force measured and fed back from the experiment does not correspond to the desired position (it is measured before the actuator has reached its target position). The effect of this error is to introduce additional energy into the system, which unless properly compensated, will typically cause the experiment to become unstable (Horiuchi et al., 1996).

Traditionally, researchers have not differentiated between time delays and actuator lag; rather, they have been lumped together and treated as a constant time delay. Methods have then been developed to compensate for this total time delay. However, actuator dynamics, and the resulting time lag are, in general, frequency dependent; therefore, their approximation as a pure time delay is valid only in a limited frequency range (e.g., low frequency). Several time delay compensation techniques have been proposed, of which the response prediction method using polynomial extrapolation (Horiuchi et al., 1996) has been the most widely used. However, these techniques perform well only when the prediction time is small compared to the fundamental period of the structure; therefore, for tests in which long extrapolation is required or the structure has large natural frequencies, it is difficult to ensure that the test remains stable. To solve this problem, some researchers have increased the structural damping in the model (Darby et al., 1999; Blakeborough et al., 2001). Although solving the numerical stability problem, the additional damping reduces the accuracy of the test results. More rational methods for evaluating and compensating delay and lag effects are needed to extend the capabilities of the real-time hybrid test method.

1.3 Objectives of the study

The objective of this study is to develop a method for real-time hybrid testing that incorporates model-based compensation techniques for time delays and actuator dynamics, and combines fast hardware and software (for high-speed computations and communication) with high performance hydraulic equipment. Efforts are directed toward algorithm development and experimental verification. There are five major components of this study: (a) advanced hardware and software system for fast hybrid testing, (b) delay compensation using model-based response prediction, (c) effects of actuator dynamics and compensation techniques, (d) model-based filtering in hybrid testing, and (e) verification experiments.

The types of structural systems considered in this study are structures with rate-dependent behavior that cannot be tested using the conventional pseudodynamic testing technique. These systems are generally associated with structures employing supplemental energy dissipation devices. To achieve real-time testing rates, the structural behavior of these systems is represented using a reduced number of degrees-of-freedom and numerical substructures with relatively simple hysteretic behavior (e.g., linear, bilinear, and Bouc-Wen hysteresis). As the speed and capacity of digital processors increase, testing structures with a large number of degrees-of-freedom and with numerical substructures with complex behavior should be possible. Nevertheless, the methods developed in this study are independent of the number of degrees-of-freedom or the models used for the numerical substructures.

Because the focus of this study is to develop algorithms for real-time hybrid testing (as opposed to evaluating a particular structural system), the specimens and actuator used are of small scale and load capacity. Scaled models allow significant reductions in the time and cost of the experiments as well as the ability to investigate and understand the capabilities and limitations of the techniques in a safer and more

controlled manner than when using their full-scale counterparts. However, the techniques developed in this study are readily applicable to larger actuators and test specimens.

The studies presented in this report extend the capabilities of the real-time hybrid testing technique by allowing accurate testing of systems with larger natural frequencies (e.g., stiff structures or multi-degree-of-freedom systems) and handling larger delays/lags, typically associated with actuators with high force capacity. Testing of an MR damper specimen demonstrates the effectiveness of the compensation algorithms presented in this report to test specimens with complex nonlinear hysteretic response that are often encountered in building structures. These studies also demonstrate that real-time hybrid testing is an effective technique to evaluate the response of structural systems incorporating structural control devices. Furthermore, the methods and techniques presented in this report also contribute to the development and advance of the pseudodynamic test methodology by incorporating model-based response prediction techniques, which can also be applied to both continuous and distributed hybrid testing; and model-based filtering, to reduce the effect of experimental errors. These studies, therefore, not only contribute to the advance of the real-time hybrid testing technique but also to the overall hybrid test method.

1.4 Organization of the report

Chapter 2 presents a detailed review of previous studies on the pseudodynamic test method and its extensions for continuous, distributed, and real-time hybrid testing. Focus is placed on developments in fast hybrid testing methods.

Chapter 3 provides the technical background for this study. The pseudodynamic test method and algorithms used for numerical integration in hybrid testing are presented. Current methods for real-time hybrid testing and continuous pseudodynamic testing are reviewed and shortcomings of these approaches are identified. In the subsequent chapters, model-based approaches are developed to address these deficiencies.

In Chapter 4, the experimental setup for real-time hybrid testing is presented. This testing system combines fast hardware and software for high speed calculations and communication with high-performance hydraulic components for dynamic loading of the test specimens. Experiments conducted to characterize the testing system are presented. This testing system is extensively used in subsequent chapters to conduct real-time hybrid experiments and evaluate proposed methods and algorithms.

Chapter 5 presents an approach for real-time hybrid testing in which time delay/lag compensation is implemented using model-based response prediction. The efficacy of the proposed strategy is experimentally verified using both linear-elastic and rate-dependent test specimens. Experimental and analytical results are shown to be in good agreement, indicating the effectiveness of the method and testing system. Results also demonstrate that the proposed method allows accurate testing of structures with larger frequencies than when using conventional time delay compensation methods.

The effects of actuator dynamics and actuator-specimen interaction in real-time hybrid testing are addressed in Chapter 6. First, models of the individual components of the testing system are reviewed and used to develop a model for the entire system. Next, using the experimental data, the parameters for the testing system used in this study are identified. This model is then used to investigate the effect of the testing system and specimen dynamics on the accuracy and stability of real-time hybrid experiments. Both detailed and simplified methods are developed and illustrated using numerical examples.

The models and insight obtained in Chapter 6, regarding the dynamics of the testing system, are used in Chapter 7 to develop model-based compensation techniques for actuator dynamics. The methods are first tested using numerical simulation and then implemented in the laboratory.

In Chapter 8, the compensation techniques developed in Chapter 7 as well as the testing system presented in Chapter 4 are used to conduct real-time hybrid testing of a semiactively controlled structure under earthquake loading. The structure is equipped with an MR damper, which is tested experimentally, and whose properties are varied during the experiment according to structural control algorithms. Experimental results demonstrate the effectiveness of the method and highlight the advantages of using real-time hybrid testing to efficiently and accurately evaluate the response, not only of the energy dissipation device, but also the performance of the structural control strategy and overall structural system.

Chapter 9 presents a technique for reducing the effect of experimental errors on the measurements during hybrid experiments. The technique is based on the concept of model-based filtering using the Kalman filter. Numerical simulations as well as pseudodynamic experiments (using the Mini-Most-2 system) are used to verify the method. Areas that need further investigation are also identified.

Chapter 10 summarizes the studies presented in this report and provides recommendations and possible directions for future research on real-time hybrid testing.

CHAPTER 2

LITERATURE REVIEW

This chapter presents a review of the pseudodynamic test procedures and algorithms, focusing on the extensions of the method for continuous, distributed, and real-time hybrid testing.

2.1 Pseudodynamic test method

The idea of experimentally obtaining the seismic response of a system without using the shaking table was initially proposed by Hakuno et al. (1969), who tested a single-degree-of-freedom system using an analog computer to solve the equation of motion and to control an electromagnetic actuator. The authors suggested the use of a digital computer to improve the accuracy of the simulation. This idea was successfully implemented by Takanashi et al. (1974, 1975, 1978) by discretizing the equation of motion in time and solving it using a digital computer. Because of these modifications, the loading process by the actuators was performed on an extended time scale in a ramp and hold method (i.e., as a repeated process of slow loading and pausing). Names typically used to designate this technique of combining experimental testing with vibration calculations using a computer are: pseudodynamic test method, hybrid testing, and computer-actuator on-line testing (Takanashi & Nakashima, 1987). The pseudodynamic test method has been the subject of significant research contributing to the development and improvement of the method (Mahin & Shing 1985; Takanashi & Nakashima 1987; Mahin et al., 1989; Shing et al., 1996). Figure 2.1 shows a schematic diagram with the different extensions of the method.

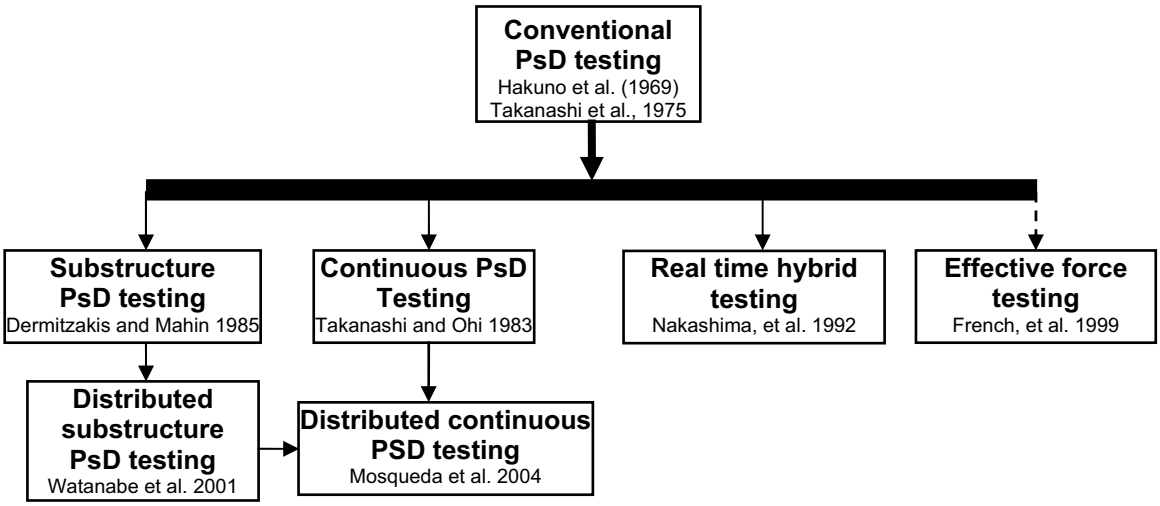

Figure 2.1: Schematic diagram of various types of hybrid testing.

The substructuring technique, which allows testing experimentally only the components or parts of the structure where damage is expected, was first implemented for pseudodynamic testing by Dermitzakis and Mahin (1985), and subsequently has been widely used.

Since its origin, the pseudodynamic test method has been successfully applied in numerous tests to determine the seismic response of structures.

2.2 Continuous pseudodynamic

As opposed to conventional pseudodynamic testing methods, in which the load is applied to the specimen using a ramp-hold procedure, continuous pseudodynamic testing applies the load smoothly, without starts and stops. By eliminating the effects of force relaxation that can occur during the hold phase of each step, the overall quality of the test can be improved. Continuous pseudodynamic testing also enables achievement of a smooth loading for the test structure and a reduction of the test duration (Magonette, 2001).

Takanashi and Ohi (1983) introduced the concept of continuous loading and fast (rapid) hybrid testing. The main differences with conventional pseudodynamic testing were the use of a dynamic actuator and the improvement of the servo-control so that the actuator velocity could be continuously adjusted. The algorithm produced a continuous movement of the actuator in the same direction as in the previous step until receiving the new, updated signal. During load reversals, the method caused the actuator to trace an incorrect path, resulting in an overshoot error. Tests were conducted on a single-degree-of-freedom (SDOF) structure composed of a steel beam connected to two pin-supported rigid columns. The loading rate was the main parameter of the study. Two verification tests were conducted: a quasistatic test with a time-scale factor of 24, and a fast hybrid test with a time-scale factor of 4.4, which was the fastest test that could be performed due to limitations on the processing speed of the computer system. The results showed that the algorithm functioned properly and that no significant differences between the two tests were observed (peak forces about 4% higher for the fast test).

Magonette (2001) presented a method for continuous pseudodynamic testing that was based on subdividing each conventional pseudodynamic step into a number of substeps (matching the sampling rate of the controller, typically 1 or 2 msec), and then conducting the pseudodynamic cycle at each substep. The achievable testing speed depended on the test conditions. For simple tests, the time expansion scale factor was near one, while for large-scale, multi-degree-of-freedom (MDOF) tests, the time-scale factor was as large as 500. The adaptive Minimal Control Synthesis (MCS) algorithm (Stoten & Benchoubane, 1990) was adopted for control of both displacement and velocity. To minimize tracking phase lag during fast substructure tests, a supplementary feedforward circuit was inserted upstream of the MCS algorithm. The feedforward transfer function was the inverse of the MCS reference model combined with a low pass filter. To allow testing of structures with strain-rate dependent elements using the continuous pseudodynamic method at low speeds (i.e., time expansion scale factor much

greater than one), a simple compensation technique was developed. The devices were first characterized by imposing sinusoidal displacements at different speeds (loading frequencies), and then a constant correction factor for the restoring force was determined based on the relation between the forces obtained at real time-speed as compared to the speed at which the pseudodynamic test was to be conducted. During the pseudodynamic experiment, the measured restoring force (applied at slow speed) was multiplied by the constant factor to account for rate effects. To validate the method, tests were conducted on two structures with rate-dependent devices. The first test was applied on a scale model of a three-dimensional, four-story steel frame using high-damping rubber bearing seismic isolators. The test was conducted using a time-scale factor of 500 and with a correction factor for rate effects determined by trial and error to optimize the response in comparison with dynamic tests. The results from the pseudodynamic test were compared to results from a shaking-table test. The results were similar, although some discrepancies existed. The second validation test was performed on a two-thirds-scale model of a two-story reinforced concrete building protected by rate-sensitive rubber energy dissipators (viscoelastic dampers) using a time scale expansion factor of 200. The effectiveness of the strain-rate compensation was evaluated by comparing the results of pseudodynamic experiments, with and without the compensation, with results from a dynamic test, showing that the compensation approach produced good results. Although this correction method provides some compensation for the strain-rate effects (not accounted for when conducting slow speed testing), this approach is, in general, neither practical nor accurate.

Mosqueda et al. (2004) presented a system for continuous hybrid simulation with distributed experimental sites connected through the internet. Because the time required for network communication is random, a solution using an event-driven controller was proposed. The resulting system was an event-driven version of the system proposed by Nakashima and Masaoka (1999), in which the tasks of integration of the equation of motion and signal generation (using polynomial extrapolation/interpolation) run as two different processes. The event-driven algorithm included the following states: extrapolate, interpolate, slow, hold, and free-vibration. The method developed by Horiuchi et al. (1999) was used to compensate for the time lag in the actuators. The method was validated by computing the earthquake response of a two-story shear building model. Response analysis was conducted on a computer 5 miles away from the location of the two remote physical substructures (connected using an Ethernet network). The first and second natural frequencies of the two-degree-of-freedom model were 1.6 and 4.2 Hz, respectively; a stiffness proportional damping with 5% on the first mode was used. The Newmark explicit method was used for numerical integration with a time step of 0.01 sec. A time scale factor of 120 was selected so that 95% of the steps could be executed without slowing down the actuators. The resulting method reduced, and in some cases eliminated, the hold phase at each integration step. Test results for both linear-elastic and inelastic tests correlated well with numerical simulation, showing a maximum drift error of 10%. In the steps in which the hold state was not activated, a smooth force-displacement response was obtained. For steps in which there was a hold of about 5 sec, force relaxation was observed, and because the measured force value is taken while the specimen is recovering from the relaxation, an error is introduced in the simulation (about 1.5% error in the restoring force for a 5-sec.-hold period). For tests involving more distant sites, longer network delays are expected. Therefore, development of predictor-

corrector methods that can accurately predict responses beyond one integration time step is necessary.

2.3 Real-time hybrid experiments

The idea of conducting a real-time hybrid experiment was introduced by Hakuno et al. (1969). The response of a single-degree-of-freedom structure was investigated using an analog computer to solve the equation of motion, while simultaneously controlling an electromagnetic actuator in real time. Because of the limitations of the hardware available at that time, the test was not ideal in terms of control and accuracy. The authors also recognized that, because they used an analog computer, there was phase lag that affected the accuracy of the simulation.

Nakashima et al. (1992) developed an innovative system to test structures with velocity-dependent characteristics. The system was composed of a single dynamic actuator and incorporated a digital servo-mechanism placed between the computer performing the numerical integration of the equation of motion and the actuator's analog servo-controller. The digital servo-mechanism performed digital feedback control at a fast rate (δt = 2 msec) by generating the signal using linear interpolation (between the displacement at the previous step and the new target displacement) and then correcting the signals by using the difference between target and measured displacements at each substep. Analog feedback control for the displacements at each δt step was performed by the servo-controller (with the displacement signal converted from digital-to-analog). The algorithm used for numerical integration was a modified version of the Central Difference Method (CDM) called *staggered* CDM, which performed two integrations running independently, one for the even steps and another for the odd steps. A buffer was provided in the digital servo-mechanism to temporarily store the target displacement for the next time step while the actuator was still moving to the current target displacement, allowing continuous actuator motion. The structure tested was a building sitting on two rubber isolation bearings; a viscous damper was installed in parallel with the isolation bearings. The physical substructure was the viscous damper; the rest of the structure was modeled numerically as a linear-elastic SDOF. The viscous damper used consisted of a steel plate immersed in a high viscosity polymeric material inside a steel box. A time step Δt of 0.02 sec. was used, which implied a time step of 0.04 sec. on each of the two independent integrators. This time step was based on the speed limitations of the system. The test was performed successfully, achieving a time-scale factor of 1.0 (i.e., real-time performance); however, because of the time step constraint, the system was capable of tracing responses at most about 1 Hz; for stiff or MDOF structures, the relatively large time steps used in this research will cause numerical stability and accuracy problems.

The effect of the dynamic response of hydraulic actuators on real-time hybrid experiments was initially considered by Horiuchi et al. (1996) who identified this effect as a "response delay" (i.e., pure time delay). Using a linear-elastic SDOF system Horiuchi et al. (1996) demonstrated that this delay causes an increase in the total energy, which is equivalent to introducing negative damping into the real-time hybrid experiment. When this negative damping is larger than the structural damping, the

response becomes unstable and the experiment is impossible. Previous tests performed without considering such compensation had been applied only to structures with long natural periods or large damping. To make the test applicable to a wider range of systems, Horiuchi et al. (1996) introduced a method to compensate for this actuator delay. The compensation method basically predicted the displacement of the actuator after the delay, T_d, which was then used as the control signal to the actuator. The method used for the prediction was an n-th order polynomial extrapolation based on the previous and current displacements. The limitations of the method were investigated. The prediction was found to cause the damping to become negative and the simulation to diverge when the nondimensional parameter, ωT_d (where ω is the fundamental frequency of the system), is larger than a critical value that is dependent on the order of the polynomial used for the extrapolation. This limitation imposed by the critical value becomes very important when the natural frequency of the structure or the actuator delay is large, as is the case for actuators with large-load capacity. Horiuchi et al. (1996) used the method to experimentally determine the seismic response of several systems, including an electrical power system supported by metal frames with fiber-reinforced-plastic (FRP) columns, an energy absorber for piping systems, and a 4-story steel building with an oil-hydraulic damper. To perform large calculations with a small time step and communicate with other devices, a *Super Real-Time Controller* (Umekita et al., 1995) had to be used as the main computer.

The method developed by Horiuchi et al. (1996) was further explored by Horiuchi et al. (1999). A digital signal processor (DSP-1) performed response analysis and actuator delay compensation at a time step Δt = 0.5 msec (2 KHz). The actuator was simulated using an electronic delay element (with a time delay of 8 msec), while the test specimen was simulated using a second digital signal processor (DSP-2), which output a reaction force based on the input displacement. The test structure was a SDOF system with 5 Hz natural frequency and 5% damping. The mass and damping were considered in the numerical substructure, while the spring element (linear and bilinear) was considered in the experimental substructure. Test results were close to the analytical (exact) solution, with small errors assumed to be a result of the prediction error (from the delay compensation). The method was then used to evaluate the seismic performance of a piping system with an energy absorber. The energy absorber was the physical substructure while the piping system was modeled numerically. Additional tests of the whole system were also performed using a shaking-table. Test results from the hybrid experiment and shaking-table were close but contained discrepancies assumed to be due to differences in the actual earthquake records imposed and the specimens used for the energy absorber.

Nakashima and Masaoka (1999) pointed out some difficulties on the system developed by Horiuchi et al. (1996). To achieve a complete cycle of computation and control within 0.5 msec, a “super real-time controller” was used. The parallel computing techniques and special programming language required made the scheme difficult to adapt to different structural systems. For most structures, an integration time step of 10 msec is sufficient and preferable, because it allows testing of larger systems and use of commercially available processors. Nakashima and Masaoka (1999) proposed a system that separated the tasks of *signal generation* and *response analysis* running as two

independent procedures on a single digital signal processor. The *response analysis* task was to calculate the target displacements at a time interval Δt of 10 msec by solving the equation of motion. The *signal generation* task was to generate commands for the actuator's servo-controller at a faster rate of δt = 1 msec using polynomial extrapolation and interpolation based on information from the previous displacements. Before the target displacement is available, the command signals are generated using extrapolation (see Figure 2.2). Once the *response analysis* task is completed, extrapolation stops and signals are generated using interpolation. The central difference method was used for systems with a few degrees-of-freedom, while the operator-splitting method (Nakashima et al., 1990) was used for larger systems. To compensate for the actuator lag, the method introduced by Horiuchi et al. (1996) was adopted using a third-order polynomial.

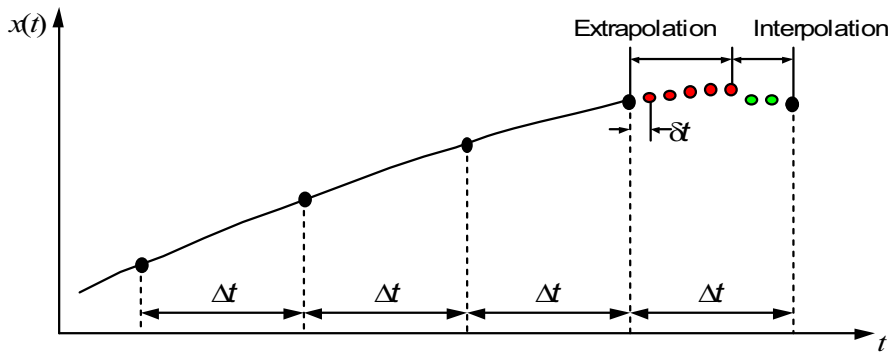

Figure 2.2: Extrapolation and interpolation procedure.

Nakashima and Masaoka (1999) used this procedure and system to test the seismic response of base-isolated buildings with high-damping rubber bearings. Because the response of the bearings is highly dependent on the frequency, amplitude, and loading cycle, real-time testing was required. The physical substructure was a base isolation system consisting of four rubber bearings with a reduced scale of one-third to one-quarter of typical bearings. The superstructure was modeled numerically using a lumped mass approach. Validation tests were conducted using an elastic SDOF system (in which a rigid mass was assumed on the top of the base-isolation system) with 2% critical damping. The mass of the system (in the numerical model) was modified to obtain SDOF systems with natural frequencies ranging from 0.5 to 3.0 Hz. In the tests without compensation, a time delay of about 30 msec was observed throughout the response. The tests with delay compensation produced good results with almost no delay in the response. The effectiveness of the extrapolation/interpolation procedure was also investigated. The number of extrapolation steps was varied to determine the maximum number that can be tolerated. For the system with a natural frequency of 1 Hz, the results between tests with one and nine extrapolations were nearly identical. However, when the natural frequency of the system was 3 Hz, the response was accurate for six extrapolations, but for seven extrapolations the response diverged quickly, and the test had to be stopped. Tests of multistory, base-isolated buildings were also conducted. Damping was stiffness proportional with 2% specified on the first mode. The method

produced reasonable results for a 9-story building (10 DOFs) with response frequencies not greater than 3 Hz (three extrapolations required) and for an 11-story building (12 DOFs) with response frequencies not greater than 2 Hz (four extrapolations required), for the cases with a linear superstructure. A 5-story building (five DOFs) was also tested using an inelastic superstructure where about four to five extrapolations were required to simulate the response accurately. The errors in the simulation were controlled by the number of extrapolations employed, the response frequency, and the number of degrees-of-freedom of the structure. While accurate results were obtained, response frequencies beyond 3 Hz were not stable, primarily because of limitations in the extrapolation and interpolation procedures.

Darby et al. (1999) conducted several tests using the real-time substructure technique. The first set of tests consisted of a simple single-degree-of-freedom system (spring-mass-damper) modeled computationally under the action of an external force with an additional physical test specimen which could be either a spring, inertial (mass), or damper element. The natural frequency of the system was 2 Hz. Real-time processing was performed using a dedicated board in a PC. A single hydraulic actuator with a conventional PID controller was used. For the first test, the physical substructure was an additional mass element. Reported experimental and theoretical results compare well for the cases with 0 and 20% critical damping, although some differences in amplitude and period were observed. For the second test, the physical substructure was a spring element represented by a steel cantilever column. The measured and theoretical responses to a step input were close; however, some differences, especially a period error, existed for the case of zero damping. For the third test, a damper (from a car suspension) was used. Cases of 1% and 25% damping were tested. The experimental and theoretical results compared poorly, yielding a large period error. This poor comparison was attributed to the highly nonlinear behavior of the damper, which made it difficult to characterize. In all of the experiments, the central difference method was used for numerical integration, with a time step chosen so that the response of the system, with zero damping, was stable. Choice of the time step was critical for the case with the mass specimen.

The second set of tests considered a multi-degree-of-freedom-system representing a simple portal frame. The physical substructure was a column with the actuator placed at the pin-jointed, beam-column interface. The rest of the frame (second column and cross beam) were modeled numerically. For this case, actuator lag compensation was performed using the method proposed by Horiuchi et al. (1996) with a fourth-order polynomial. The fundamental natural frequency of the system was 5 Hz. A large value of damping (10%) had to be used (typical damping for steel structures is much smaller), because the negative damping introduced by the actuator delay was not fully cancelled by the delay compensation. The response of the system to an earthquake record and to sinusoidal excitations of 2.5 and 5 Hz was calculated, with the physical specimen remaining linear-elastic throughout the response. The experimental results had significant differences when compared to numerical simulation, particularly with respect to the amplitude of the response. These differences were attributed to nonlinearities in the experimental system, actuator lag compensation, inertial forces in the measured force, and central difference approximations.

To improve the results obtained by Darby et al. (1999) using the central difference method with a large time step (required to allow computation in real time), Darby et al. (2001) presented a new method applicable to structures with linear numerical substructures. The equations of motion were expressed in modal coordinates, and the response was obtained using mode superposition. The numerical substructure was discretized using a first-order-hold approximation, producing an equation of motion whose solution requires matrix exponentials for the solution of the MDOF system. To create an explicit form of the method, the output at the next time step was calculated using a first-order (linear) extrapolation based on the output at the previous steps. To consider significant variations in the input due to large time steps, an integral form of the equation of motion was used (Chang, 1998), which required integration of the measured force over the time-step interval. Because a displacement-held, piecewise constant over each time step would generate erroneous integrals, a quadratic interpolation was used to generate intersample displacements to be sent as command signals to the actuator (generating a smooth response). The measured force for these short time intervals within the time step was then integrated using the trapezoidal rule. Actuator lag compensation was performed using the method proposed by Horiuchi et al. (1996) with a fourth-order polynomial. The actuator lag was estimated to be 15 msec. The method was used to calculate the response of the simple portal frame used by Darby et al. (1999). The fundamental frequency of the system was 5.13 Hz, and a damping ratio of 5% was assumed. The time step was 20 msec (about 1/4 the period of the highest mode considered). The results showed an improved accuracy of the proposed method over the central difference method used by Darby et al. (1999). The systems presented by Darby et al. (1999, 2001) both use relatively large time steps.

Blakeborough et al. (2001) used the method developed by Darby et al. (2001) to test the same simple portal frame but modified it to have two rigid beam-column connections. The physical substructure was again the left column, but with two-degrees-of-freedom (lateral displacement and rotation at the top of the column) imposed using two actuators. Both the physical and numerical substructures were linear elastic. The results for a 2.5 Hz sinusoidal excitation were satisfactory, with the rotation response containing larger errors. The results for an actual earthquake record were less satisfactory, especially in the 6 to 7 Hz range. A high value of damping (5% critical damping) had to be used because the tests were highly prone to instabilities due to the physical coupling between the two actuators, which made it difficult to achieve accurate control. The method was also used to test a 10-story building incorporating a type of knee-bracing element that dissipates energy through inelastic deformation. The physical substructure (knee element which yielded first) was represented by a beam with a single-degree-of-freedom (midspan displacement). The rest of the building was modeled numerically and restricted to linear behavior. The simulation was stable, but the results had errors, which were assumed to be due to large deformations of the test rig. To extend the method for nonlinear problems, a new approximate nonlinear algorithm was developed using a reduced basis of eigenvectors and other orthogonalized deformation shapes. The new reduced set of basis vectors was obtained by adding to the elastic modes a set of vectors corresponding to successive yield events obtained from a pushover analysis of the structure. Because the resulting eigenvectors are not all orthogonal, another eigenvalue problem needed to be solved to obtain a new set of vectors that are

orthogonal, each with its corresponding frequency. This nonlinear algorithm was used to test the portal frame (with the one-degree-of-freedom column as the physical substructure) under an earthquake record scaled to produce nonlinear behavior in both the test specimen and the numerical substructure. A time step of 25 msec was used to allow for computation in real time. Test results were stable, but no comparison with theoretically expected values was presented. The authors recognize that although the results are encouraging, more work was needed to improve the technique.

Continuing the work by Darby et al. (1999, 2001) and Blakeborough et al. (2001) on real-time hybrid testing, Williams et al. (2001) considered a detailed model of the components of a dynamic testing system. The model was implemented using Simulink and included nonlinear effects such as servovalve spool dynamics, flow through the valve orifices, and changes in the actuator oil volumes. The majority of the parameters for the model were obtained from the manufacturer's specifications, while other parameters were determined experimentally by tuning the model against simple (prescribed displacement) tests. The model showed good agreement against these tests; however, results were observed to be quite sensitive to the value of the oil bulk modulus. The model was also compared with results from substructure real-time hybrid experiments. The test structure was the simple portal frame used by Darby et al. (1999, 2001), where a single-degree-of-freedom cantilever column was the physical specimen. Both linear and nonlinear responses were considered. The predictions by the model for these tests, however, did not compare as well as in the tests used to calibrate the model.

Shing et al. (2004) developed a system for fast hybrid testing with rates of loading approaching real time. The system was based on the unconditionally stable α-method (Hilber et al., 1977). To make this implicit algorithm suitable for pseudodynamic applications, Shing et al. (1991) proposed a modified Newton method that uses the initial stiffness of the structure, instead of the tangent stiffness, during the iterative corrections. Because the number of iterations to reach equilibrium at each time step is unknown, and the incremental correction decreases as convergence is approached, the method was not appropriate for high-speed tests. Shing et al. (2004) proposed a new method with a fixed number of iterations and time intervals within each time step. Using quadratic interpolation, the displacements are updated at each iteration, and the displacements at the previous two time steps are used to generate displacement commands at a faster rate (matching the sampling frequency of the controller), allowing the actuators to move in a continuous and smooth way. A time step, Δt, of 10 msec was used, and the interpolated displacements were generated every 1 msec; therefore, 10 interpolations were required per time step. To account for the inherent delay due to digital control (a few milli-seconds), the PID control was supplemented with a feed-forward control implemented in the digital servo-controller (by MTS). Discrete feedback compensation was also incorporated to account for differences between the calculated and measured displacements. The calculated displacement (to be used for the interpolation) was adjusted with the difference between the calculated and measured displacements at the end of the previous time step, times a gain smaller than 1. This compensation also embeds an *ad hoc* correction for the time lag in the actuator response caused by the dynamics of the servo-hydraulic actuator (described to be as large as 10 msec) by overshooting the displacement commands in the next correction if there is a time lag in

the previous correction (Shing et al., 2002). The method and numerical simulation were implemented using Simulink, for tests without substructuring, and using OpenSees for test with substructuring. In both cases, the processes ran on a PC with a real-time kernel. Validation tests were conducted using the system to determine the linear response of two structures to seismic excitation. A two-degree-of-freedom model, representative of a scaled, two-story steel frame, was tested using a cantilever column with two actuators (one at each story level). The natural frequencies of the structure were 2.1 and 11.8 Hz, with critical damping in the two modes of 4% for the test, and 6% for the theoretical solution (the reasons for using different damping ratios in the experiment and the theoretical response are not explained by the authors.). The results between the test, theoretical solution, and a virtual test simulation, were close with some amplitude errors in the response. The second test consisted of a two-story, two-bay steel frame. The physical substructure was a cantilever column with one actuator, and the rest of the frame was modeled using OpenSees. The fundamental natural frequency of the structure was 2.3 Hz, and Rayleigh damping was used with 2% in the first two modes. Experimental and theoretical results were very close.

A conceptually different real-time dynamic testing method is *Effective Force Testing* (EFT), which was proposed by Mahin and coworkers (Mahin et al., 1985, 1989) and experimentally evaluated and implemented by Dimig et al. (1999) and Shield et al. (2001). The basis of the method is to apply the equivalent inertial forces induced by the earthquake ground motion at each degree-of-freedom using hydraulic actuators under force control. The attractive feature of the method is that the command to the actuators (i.e., equivalent inertial forces) can be calculated prior to the experiment, based on the ground acceleration and mass of the structure. Although the effective forces imposed are independent of the structural stiffness and damping, a natural velocity feedback path (intrinsic to servo-hydraulic systems, Dyke et al., 1995) combined with the force control algorithm required by EFT, results in the inability of the actuators to apply the effective forces near the natural frequencies of the structure. Therefore, dynamic force control is effective only when very accurate natural velocity feedback compensation is incorporated, which includes the dynamics of the servovalve and its controller. Servo-system nonlinearities have a significant effect on the performance of the EFT method (Zhao et al., 2003); accurate compensation is very challenging, even after conducting extensive system identification of all the testing components. To date, the EFT method has been successfully used only to test single-degree-of-freedom systems (Shield et al., 2001; Zhao et al., 2005). From a conceptual point of view, the EFT method has some severe limitations for testing large systems when compared to the hybrid test method. The mass and damping must be physically included in the experimental specimen, instead of being modeled numerically as is done in hybrid or pseudodynamic testing. Furthermore, because the basis of the method is that the forces to be applied to the specimen are known before starting the test, the substructuring technique cannot be used.

Real-time hybrid testing is particularly suitable for testing structures with rate-dependent devices. Recently, special attention has been directed toward the application of this technique to evaluate the response of structures with MR dampers. Real-time hybrid experiments of structures with MR dampers have already been conducted by Emmons

and Christenson (2006; numerical simulations and proposed experiments only), Wu et al. (2006), and Carrion and Spencer (2006; as part of the studies presented in this report).

Emmons and Christenson (2006) proposed the experimental verification of semiactive control through the use of real-time hybrid testing. Proposed experiments will employ hybrid testing (at the NEES Fast Hybrid Test System, University of Colorado at Boulder) to simulate the nonlinear response of a building structure with three semiactive, large-scale MR dampers. Analytical results for semiactive control of the nonlinear building model are presented as well as details of the experiments to be conducted.

Wu et al. (2006) used real-time hybrid testing with substructuring to evaluate the performance of an offshore platform with semiactive MR dampers under earthquake- and ice-induced vibration. For the controller, the LQG algorithm was used with the Kalman filter to estimate the states based on measurements from the isolation layer drift and main deck acceleration. The Hrovat optimal control algorithm was used to track the active control force calculated by the LQG algorithm. The authors were not able to accurately represent the dynamic behavior of the damper using existing models (e.g., Spencer et al., 1997); therefore, they used the real-time hybrid testing technique to evaluate the response of the platform. For the hybrid tests, a full-scale damper was the physical substructure, while the rest of the structure was the numerical substructure. A reduced model of the platform (with 8 DOFs) was used for the hybrid test. Numerical integration was performed using the Central Difference Method (CDM), and to avoid stability problems, the mode superposition technique was used considering only the first three modes, whose natural frequencies were 0.57, 2.75, and 5.91 Hz, respectively. The actuator time lag for the system was estimated as a delay of 80 msec. Using numerical simulation, the authors found that the real-time hybrid experiment was stable without using delay compensation for the first three modes. For the cases considered, the actuator lag had a small effect on the test results. Test results showed that the vibration of the structure is effectively controlled with MR dampers both in cases of passive-off (i.e., without input voltage) and semiactive control. When the natural frequencies of the test structure are small (which was the case for the experiments reported by the authors), and the forces from the physical substructure are small compared to the rest of the forces (e.g., forces from the numerical substructure), the effect of actuator dynamics (and experimental errors in general) on the overall system response was not significant. However, when the forces from the test specimen (e.g., MR damper) are considerable compared to the other forces, and the frequencies from the structure are larger, the effect of actuator dynamics is important, and unless properly compensated, the experiment can potentially become unstable.

2.4 Distributed pseudodynamic

The capabilities of the pseudodynamic test method can be greatly expanded by distributing the different substructures at geographically separated facilities and using the internet to link these facilities with the main simulation computer. Distributed pseudodynamic tests have been conducted in Korea by Yun et al. (2000; considering numerical simulations only), between Japan and Korea (Watanabe et al., 2001), in

Taiwan (Tsai et al., 2003), and between Taiwan and Canada (Chang et al., 2005; Yang et al., 2006). In the United States, a major research project was initiated by the National Science Foundation (NSF) in 1999, the George E. Brown, Jr. Network for Earthquake Engineering Simulation (NEES). NEES provided over $80 million to enhance the testing facilities of 15 universities across the United States and build the necessary cyber infrastructure (NEESgrid) to link the different facilities using leading-edge computing resources and the newest and fastest communications technologies. NEESgrid provides resources that support distributed hybrid simulations (e.g., tele-operation, tele-observation, and data repository). Spencer et al. (2004) conducted a geographically distributed pseudodynamic test of a simple steel frame in which the left and right columns were physically tested at the University of Illinois at Urbana-Champaign and the University of Colorado at Boulder, respectively, and the rest of the frame was numerically modeled on a computer at the National Center for Supercomputer Applications (NCSA) at the University of Illinois at Urbana-Champaign. The test was successful, demonstrating the capabilities of the NEESgrid. The continuous pseudodynamic test performed by Mosqueda et al. (2004) was also distributed, with the computer 5 miles apart from the two remote physical substructures; however, this test was not conducted through NEESgrid.

2.5 Summary

This section reviewed some of the studies about the pseudodynamic test method as well as recent developments in the extensions of the method for continuous, real-time, and distributed hybrid testing. Developed over 30 years ago, the pseudodynamic test method is becoming a mature and reliable technique. However, further development is required to realize the full potential of the method and its extensions.

CHAPTER 3

BACKGROUND ON HYBRID TESTING

To lay the foundation of this study, this chapter presents technical background regarding the pseudodynamic test method, the substructuring technique, and algorithms for numerical integration. The effects of rate-of-loading and force relaxation on hybrid experiments are reviewed. Extensions of the pseudodynamic test method for continuous and fast hybrid testing are described, as well as current techniques for these methods and their shortcomings.

3.1 The Pseudodynamic Test Method

The pseudodynamic test method provides an efficient way of simulating the seismic response of large structural systems by combining numerical simulation with experimental testing. The equation of motion of the structural system to be tested is given by the following second-order differential equation

$$\mathbf{M}\ddot{\mathbf{x}}(t) + \mathbf{C}\dot{\mathbf{x}}(t) + \mathbf{R}(\mathbf{x}, \dot{\mathbf{x}}, t) = \mathbf{F}(t) \tag{3-1}$$

in which **M** is the mass matrix, **C** the damping matrix (for linear damping), **R** the resisting force vector, **F** the vector of externally applied forces, and **x** the displacement vector. The dots denote differentiation with respect to time. If the system is linear elastic, $\mathbf{R} = \mathbf{K}\,\mathbf{x}(t)$, where **K** is the elastic stiffness matrix of the structure. In conventional pseudodynamic testing, it is assumed that the restoring force does not depend significantly on the velocity and, therefore, rate-dependent effects can be neglected. When the structure is subjected to a ground acceleration, $\ddot{\mathbf{x}}_g$, the external force vector is $\mathbf{F} = -\mathbf{M}\,\boldsymbol{\Gamma}\,\ddot{\mathbf{x}}_g$, where $\boldsymbol{\Gamma}$ is a mass influence vector. The equation of motion is discretized by dividing the time interval at a uniform interval of Δt, giving the following equation

$$\mathbf{M}\ddot{\mathbf{x}}_{i+1} + \mathbf{C}\dot{\mathbf{x}}_{i+1} + \mathbf{R}_{i+1} = \mathbf{F}_{i+1} \tag{3-2}$$

which is then solved using a step-by-step time integration algorithm. During each time step, the response of the system is obtained by first solving the discrete equation of motion on a computer and then applying the displacements to the test structure using hydraulic actuators. The reaction forces on the actuators are measured and fed back to the computer to calculate the response at the next time step. The procedure is then repeated until the complete response is calculated.

Substructuring

The damage produced to a structure by seismic loads is usually localized within only a few critical regions; therefore, in many cases it is unnecessary to experimentally test the entire structural system. The *substructuring technique* (also employed in finite element analyses) divides the structure in major components called *substructures* that are analyzed in a coordinated way to obtain the response of the entire system. In a pseudodynamic test, the structure is divided into physical and numerical substructures, as shown on Figure 3.1. The *physical substructure*, composed of the parts of the structure of special interest (e.g., where damage is expected, or difficult to model numerically) is tested physically in the laboratory, while the rest of the structure, the *numerical substructure*, is analyzed numerically typically using a finite element model. Because the substructures interact during the test, the dynamic response of the entire system is simulated, allowing accurate testing of large and complex structural systems.

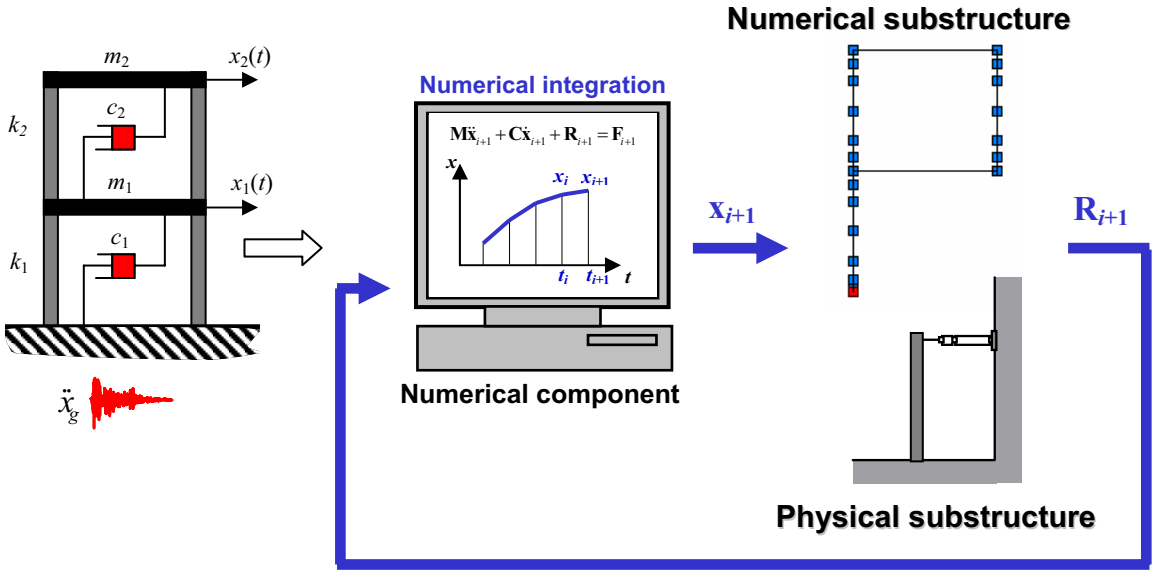

Figure 3.1: Substructuring technique for pseudodynamic testing.

In pseudodynamic testing with substructuring, the restoring force vector, **R,** includes the contributions from the physical and numerical substructures, $\mathbf{R}_{i+1}^{exp}$ and $\mathbf{R}_{i+1}^{num}$, respectively. The equation of motion for the complete system is then given by (Mahin et al., 1989),

$$\mathbf{M}\ddot{\mathbf{x}}_{i+1} + \mathbf{C}\dot{\mathbf{x}}_{i+1} + \mathbf{R}_{i+1}^{exp} + \mathbf{R}_{i+1}^{num} = \mathbf{F}_{i+1} \qquad (3\text{-}3)$$

Because the number of degrees-of-freedom of the entire system is typically large for pseudodynamic tests with substructuring, special attention must be taken in the selection of the numerical integration algorithm to ensure numerical stability and avoid spurious higher mode responses.

3.2 Numerical integration in pseudodynamic testing

The numerical integration algorithm used to solve the equation of motion is a key component in the pseudodynamic test method. Most of the numerical integration algorithms are based on the *Newmark method* (Newmark, 1959). The acceleration is assumed to vary in a predefined way over the time step (e.g., constant, linear, etc.), and then the velocity and displacements are obtained through integration of the acceleration. The following equations are obtained for the velocity and displacement

$$\begin{aligned} \mathbf{x}_{i+1} &= \mathbf{x}_i + \Delta t \dot{\mathbf{x}}_i + \Delta t^2 \left[\left(\frac{1}{2} - \beta \right) \ddot{\mathbf{x}}_i + \beta \, \ddot{\mathbf{x}}_{i+1} \right] \\ \dot{\mathbf{x}}_{i+1} &= \dot{\mathbf{x}}_i + \Delta t \left[\left(1 - \gamma \right) \ddot{\mathbf{x}}_i + \gamma \, \ddot{\mathbf{x}}_{i+1} \right] \end{aligned} \tag{3-4}$$

in which β and γ are the Newmark integration parameters that determine the stability and accuracy of the method and produce the different methods of the family. For $\beta = 0$ and $\gamma = ½$, the *Central Difference Method* (CDM) is obtained. The expression to calculate displacements using the CDM is given by

$$\mathbf{x}_{i+1} = \left[\frac{1}{\Delta t^2} \mathbf{M} + \frac{1}{2\Delta t} \mathbf{C} \right]^{-1} \left[\frac{2}{\Delta t^2} \mathbf{M} \mathbf{x}_i - \left(\frac{1}{\Delta t^2} \mathbf{M} - \frac{1}{2\Delta t} \mathbf{C} \right) \mathbf{x}_{i-1} - \mathbf{R}_i + \mathbf{F}_i \right] \tag{3-5}$$

The advantage of CDM is that it is an explicit method; therefore, it requires only information from the current and previous steps to compute the response at the next time step, making its application to hybrid testing straightforward. For this reason, the CDM has been widely used on pseudodynamic testing. However, the method is only conditionally stable (with stability criterion given by $\omega \Delta t \leq 2$, where ω is the highest natural frequency of the system).

For $\beta = 1/4$ and $\gamma = 1/2$, the *Constant Average Acceleration Method* is obtained, which is unconditionally stable. This method is implicit and of all the Newmark family of algorithms, it is probably the most commonly used. When simulating structures with nonlinear behavior, implicit methods require iteration to accurately capture the path-dependent nature of the response. This required iteration makes implicit methods undesirable for pseudodynamic testing. The additional computing time required by implicit methods also makes them difficult to employ for real-time hybrid tests.

An important property of the Newmark family of methods is that numerical damping can be introduced to the system through the parameter γ (for $\gamma = ½$, no numerical damping is introduced, for $\gamma < ½$, negative numerical damping is introduced, and for $\gamma > ½$, positive numerical damping is introduced). Typically, finite element models represent the lower mode response much more accurately than response in the higher modes. Therefore, it is sometimes advantageous to introduce positive numerical damping to damp out spurious higher-mode responses. In pseudodynamic testing, damping out high-frequency responses is particularly important because the higher modes

of a system are more sensitive to experimental errors than the lower ones (Mahin and Shing, 1985). However, when introducing numerical damping in the Newmark family of methods (i.e., $\gamma \neq 1/2$), the method drops from second-order to first order-accurate, reducing significantly the accuracy of the method.

Hilber et al. (1977) proposed a modification for the Newmark method, classically known as the *HHT-α* method (for Hilber, Hughes, and Taylor), which retains the desirable characteristics of the Newmark family of methods, while allowing the introduction of numerical algorithmic damping without degrading the order of accuracy. This result was achieved by introducing a new parameter, α, to control the amount of numerical damping. The discrete equation of motion was expressed as

$$\mathbf{M}\ddot{\mathbf{x}}_{i+1} + (1+\alpha)\mathbf{C}\dot{\mathbf{x}}_{i+1} - \alpha\mathbf{C}\dot{\mathbf{x}}_i + (1+\alpha)\mathbf{R}_{i+1} - \alpha\mathbf{R}_i = (1+\alpha)\mathbf{F}_{i+1} - \alpha\mathbf{F}_i \qquad (3\text{-}6)$$

with the displacement $\mathbf{x}_{i+1}$ and velocity $\dot{\mathbf{x}}_{i+1}$ given by Equation (3-4) and the β, γ, and α parameters given by

$$\beta = \frac{1}{4}\left(1-\alpha^2\right) \qquad \gamma = \frac{1}{2}\left(1-2\alpha\right) \qquad -1/3 \le \alpha \le 0 \qquad (3\text{-}7)$$

The resulting algorithm is unconditionally stable, second-order accurate, and posses numerical damping controlled by the α parameter with adequate dissipation in the higher modes without affecting the lower modes too strongly. For α = 0, the method reduces to the Constant Average Acceleration method of the Newmark family, which introduces no numerical damping.

Hughes et al. (1979) proposed a method for nonlinear transient analysis using implicit-explicit, finite-element mesh partitions. The method was motivated by the advantages that can be obtained when solving problems with interacting media (e.g., fluid-structure interaction), by treating different parts of the overall system with implicit and explicit algorithms. For the implicit region of the mesh, an implicit algorithm was used implemented in a predictor/corrector way. For the explicit region, the same integration algorithm was expressed as an explicit "predictor-corrector" method, in which the calculations are rendered explicit by evaluating the internal forces based on the predictors (i.e., exclusively in terms of the data available from the previous step). The implicit and explicit methods are then combined producing the following equation

$$\mathbf{M}\ddot{\mathbf{x}}_{i+1} + \mathbf{N}^I\left(\mathbf{x}_{i+1}, \dot{\mathbf{x}}_{i+1}\right) + \mathbf{N}^E\left(\tilde{\mathbf{x}}_{i+1}, \dot{\tilde{\mathbf{x}}}_{i+1}\right) = \mathbf{F}_{i+1} \qquad (3\text{-}8)$$

where $\mathbf{N}$ is a nonlinear algebraic function divided into the implicit and explicit terms, $\boldsymbol{N}^I$ and $\mathbf{N}^E$ respectively. In structural dynamics problems, this function represents the restoring force. The quantities $\tilde{\mathbf{x}}_{i+1}$ and $\dot{\tilde{\mathbf{x}}}_{i+1}$ are referred as the predictors and $\mathbf{x}_{i+1}$ and $\dot{\mathbf{x}}_{i+1}$ as the correctors and are given by

$$\tilde{\mathbf{x}}_{i+1} = \mathbf{x}_i + \Delta t \dot{\mathbf{x}}_i + \frac{\Delta t^2}{2}(1-2\beta)\ddot{\mathbf{x}}_i$$
$$\dot{\tilde{\mathbf{x}}}_{i+1} = \dot{\mathbf{x}}_i + \Delta t(1-\gamma)\ddot{\mathbf{x}}_i \tag{3-9}$$

$$\mathbf{x}_{i+1} = \tilde{\mathbf{x}}_{i+1} + \Delta t^2 \beta \ \ddot{\mathbf{x}}_{i+1}$$
$$\dot{\mathbf{x}}_{i+1} = \dot{\tilde{\mathbf{x}}}_{i+1} + \Delta t \gamma \ \ddot{\mathbf{x}}_{i+1} \tag{3-10}$$

Following the idea of combining implicit and explicit finite element mesh partitions, Plesha and Belytshko (1985) proposed a constitutive operator-splitting method for the solution of problems with nonlinear material behavior. The nonlinear constitutive relation is split into a constant, history-independent relation (linear part), which is integrated using an implicit method, and a variable history dependent relation (nonlinear part), which is integrated using an explicit method. Analysis of the stability indicated that the method is unconditionally stable for materials with softening type nonlinearities.

Based on the ideas from Hughes et al. and Plesha and Belytschko, Nakashima et al. (1990) proposed an operator-splitting algorithm for pseudodynamic testing (designated as the *OS-method*). The algorithm applies an explicit method for the elastic part of the response and an implicit method for the nonlinear part of the response. The key idea of the method is to use the following approximation for the restoring force

$$\mathbf{R}_{i+1} \approx \tilde{\mathbf{R}}_{i+1} + \mathbf{K}_o\left(\mathbf{x}_{i+1} - \tilde{\mathbf{x}}_{i+1}\right) \tag{3-11}$$

where $\mathbf{K}_o$ is a stiffness matrix as close as possible to the elastic stiffness. This approximation allows obtaining the restoring force at the end of the time step, based on the measured restoring force from the experiment at the predictor step (Figure 3.2).

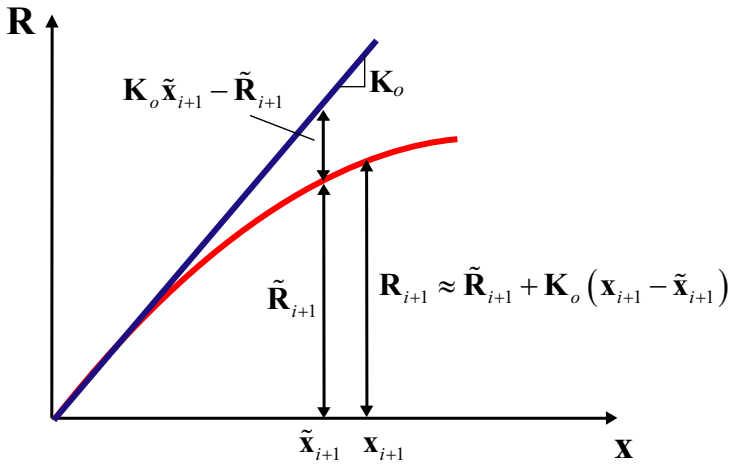

Figure 3.2: OS-method for pseudodynamic testing.

The stability of the method was investigated for both single and multi-degree-of-freedom systems; the algorithm was found to be unconditionally stable if the tangent

stiffness is not greater than the initial elastic stiffness (i.e., the stiffness of the system is of the softening type), which is the case in most structural engineering applications.

Combescure and Pegon (1997) suggested the use of the so-called *α–OS-method* (a combination of the OS-method with the *HHT-α* method) to damp out numerical, undesired, spurious oscillations associated with high frequencies. The method was found to be accurate when the structure does not lose too much of its initial stiffness during the test. However, when the structure undergoes severe stiffness degradation, the method still behaves accurately for the low-frequency modes of the structure. The equations as well as a flow chart for the implementation of the method in pseudodynamic testing are illustrated in Figure 3.3.

Ghaboussi et al. (2006) presented a new predictor–corrector (P–C) method for multisite substructure pseudodynamic testing. The method is an extension of the classical implicit-explicit technique (Hughes & Liu, 1978). The computational components are solved using an implicit time integration method (e.g., Newmark's constant-average-acceleration method), while the restoring forces from the experimental components are obtained based on an explicit prediction of the displacement. The P–C method has the advantage that it does not require the determination of the initial stiffness of the experimental components, making it suitable for analyzing systems where the initial stiffness is difficult to obtain (e.g., earth structures for considering the soil–foundation–structure interaction effect). However, the method is conditionally stable, which poses a potential disadvantage over the α-OS method for real-time hybrid testing.

Among all of the numerical algorithms proposed for hybrid testing, the central difference method (CDM) and the alpha operator-splitting method (α-OS) are the most widely used and are the ones considered in this study. Because of its simplicity and low computational cost, the central difference method is used whenever possible. For structures in which the stability criterion of the CDM becomes difficult to satisfy, the α-OS method (which is unconditionally stable for systems of softening type) is used.

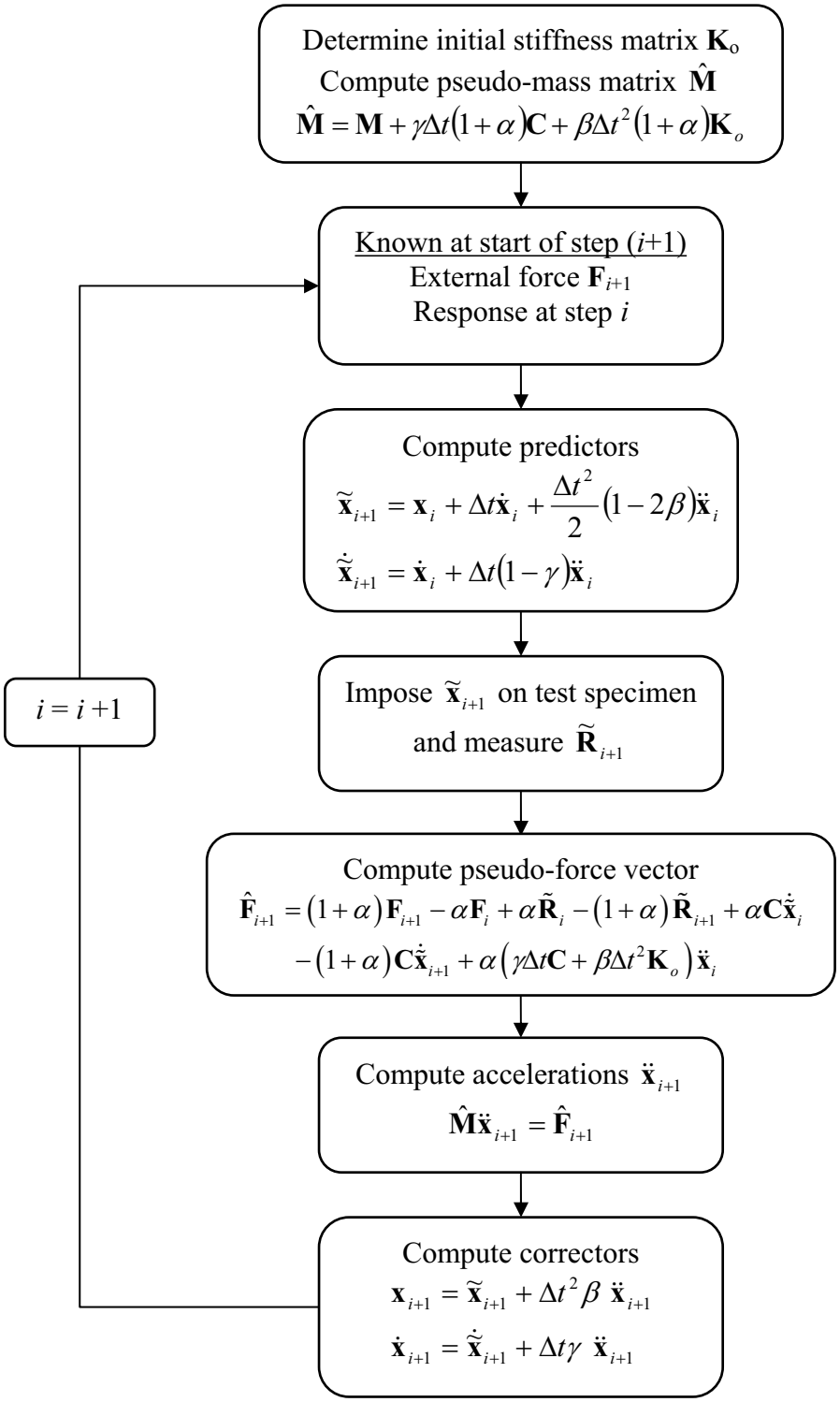

Figure 3.3: Implementation of the α-OS method for pseudodynamic testing.

3.3 Rate-of-loading and force relaxation effects

3.3.1 Strain-rate effects

The load resistance of most structural materials is sensitive to the rate of loading; therefore, the seismic response of a structure evaluated on the basis of its quasi-static behavior could be different from the actual response during an earthquake (Shing & Mahin, 1988). Structures subjected to severe earthquakes can experience strain rates as high as 0.1 sec^{-1} at critical sections, depending on the fundamental frequency of the structure and amplitude of vibration (Chang & Lee, 1987; Shing & Mahin, 1988).

Increases in strain rate produce increases in both yield and ultimate strengths of steel, with the yield strength being more sensitive than the ultimate. However, the elastic properties (e.g., Young's modulus) do not demonstrate rate-sensitivity (Shing & Mahin, 1988). Chang and Lee (1987) conducted a series of tests to determine the effects of strain rate and strain rate history on structural steel A36 at room temperature under monotonic and cyclic loading. Strain rates between 10^{-6} to 10^{-1} sec^{-1} were used, covering the typical range that might be experienced by steel frames during earthquakes. Considerable strain rate effects were observed, resulting in higher yield stress and longer plastic plateau for the higher strain rates. Tests results showed relatively more significant strain rate sensitivity for monotonic loading than cyclic loading. Changes in strain rates from 10^{-2} to 10^{-5} sec^{-1} resulted in differences as high as 27% for monotonic tests with loading and unloading, and about 10% for cyclic tests. The strain rate history effect, however, was not significant. Tests conducted by Udagawa et al. (1984) showed an increase on the moment capacity of wide-flange steel and composite beams of 16-20% for monotonic tests and 5-11% for cyclic tests corresponding to a change of 200 times in the loading rate.

Shing and Mahin (1988) studied the rate-of-loading effects on pseudodynamic tests using a single-degree-of-freedom model with the rate-dependant characteristics of mild steel. Numerical results indicate that the higher the rate of loading is, the larger is the load resistance and the smaller is the displacement induced by plastic deformation. It was also found that neglecting rate effects (i.e., using the static strength) can lead to a significant overestimation of the inelastic response for structures that have a fundamental period less than 0.6 sec (Shing & Mahin, 1988). For the model used, the dynamic strength was about 30% higher than the static strength and 13% higher than that developed under a typical pseudodynamic rate of loading (using a 200 time scale factor). These numerical analyses indicated higher rate-of-loading-effects in pseudodynamic testing than previous comparisons between results from pseudodynamic and shaking-table tests (Thewalt et al., 1986). Some of the explanations given are the limited amount of experimental data used to calibrate the model, strain hardening, and the fact that inelastic deformation in multi-degree-of-freedom structures may not occur simultaneously at various critical locations.

Results from tests conducted at slower rates (e.g., pseudodynamic) tend to be conservative (Shing & Mahin, 1988). However, rate-of-loading effects can be significant for structures that have relatively high fundamental frequencies and structures subjected primarily to impulsive type loading. By assuming a minimum fundamental response period of 0.1 sec, the strain-rate effects can be neglected for most steel structures under seismic excitation (Mahin & Shing, 1985).

When conducting real-time and fast hybrid testing, rate effects are directly taken into account on the measured restoring force from the specimen (i.e., physical substructure). However, typical models used for the numerical substructure do not include rate effects because it is assumed that the critical components, or those that suffer most of the damage, are tested experimentally. However, for numerical substructures in which significant rate sensitivity is expected, models that include these effects should be considered.

A relatively simple relation for uniaxial, rate-dependent behavior is given by an elastic/viscoplastic model (Perzyna, 1966). The basis for the model is that the total strain rate, $\dot{\varepsilon}$, can be separated into two components: an elastic strain rate, $\dot{\varepsilon}^e$ obtainable from an elastic stress-strain relation (e.g., $\dot{\varepsilon}^e = \dot{\sigma} / E$, where E is the Young's modulus), and the viscoplastic flow, $\dot{\varepsilon}^p$, which occurs only when the stress exceeds a critical value, therefore,

$$\dot{\varepsilon} = \dot{\varepsilon}^e + \dot{\varepsilon}^p \tag{3-12}$$

Malvern (1951) proposed a model for the viscoplastic flow based on the fact that the plastic strain rate is a function of the excess of the instantaneous stress over the stress at the same strain in a static test. An overstress relation used for problems regarding the dynamic plastic deformation of structures is:

$$\dot{\varepsilon}^p = \gamma \left\langle \frac{|\sigma|}{\sigma_y} - 1 \right\rangle^{\delta} \tag{3-13}$$

where γ and δ are material constants that can be obtained from experimental tests, σ is the dynamic flow stress, and σ_y is the quasi-static (reference) yield stress. Using this model, the total strain rate can be expressed as:

$$\dot{\varepsilon} = \frac{\dot{\sigma}}{E} + \gamma \left\langle \frac{|\sigma|}{\sigma_y} - 1 \right\rangle^{\delta} sign(\sigma) \tag{3-14}$$

Bending behavior can be considered by using the above constitutive model with a fiber formulation. Based on experimental data for mild steel, Shing and Mahin (1988) estimated the material parameters as γ = 14, and δ = 3 for cyclic loading (however, these values tend to overestimate strain-rate effects). Figure 3.4 shows the normalized stress (σ/σ_y) vs. the normalized strain ($\varepsilon/\varepsilon_y$) obtained using the model for a triangular strain time

history producing strain rates of 10^{-5}, 10^{-3}, 10^{-2}, and 10^{-1} sec^{-1} corresponding to loading frequencies of approximately $4x10^{-4}$, 0.04, 0.4, and 4 Hz. Increases on the stress as high as 20% are observed for the faster rate.

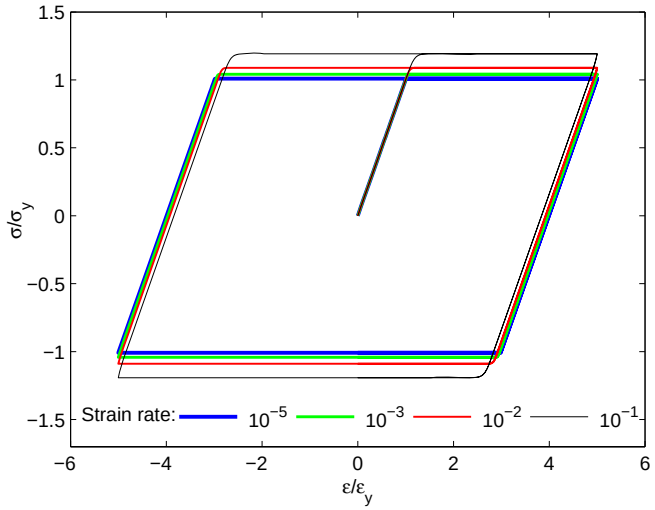

Figure 3.4: Stress-strain behavior of elastic/viscoplastic model.

The numerical solution of models that include rate-dependent behavior is definitely more time consuming than conventional models excluding these effects. Therefore, the applicability of rate-dependent models for high-speed and real-time hybrid testing is highly dependent on the computing speed of the system. To date, hybrid tests have not included rate-dependent models.

For reinforced concrete structures, the effects of the rate-of-loading should be carefully considered because cracking and other failure mechanisms occur in real time (Mahin & Shing, 1985). Experiments by Mahin and Bertero (1972) indicated an increase of 20% on the yield resistance of a reinforced concrete beam, for a change in the loading rate of 100 times.

In general, there is a significant scatter on the results presented regarding the strain-rate effect for conventional structural materials. However, reported experimental results indicate that the effect is significantly smaller for cyclic tests than for monotonic test. Therefore, for experiments conducted to determine the earthquake response of structures, strain-rate effects may not be very significant (except for structures with large natural frequencies). Fast- and real-time hybrid testing methods can be used to efficiently evaluate the relevance of strain-rate effects on conventional structural materials under realistic earthquake loading histories.

3.3.2 Stress relaxation

During the hold period in conventional pseudodynamic testing, reductions in the restoring force can occur due to force relaxation. Force relaxation is caused by stress

relaxation, which is the decay in stress over time while the strain is held constant. Stress relaxation results from the redistribution of elastic and inelastic strain (Stouffer & Dame, 1996). In general, stress relaxation follows a logarithmic behavior with most of the effects occurring during the initial seconds. Stress relaxation effects in structural steel have been observed by Chang and Lee (1987), about 8% during a 10-min hold for a strain rate of 10^{-4} sec^{-1}, Mosqueda et al. (2004), about 1.5% on a 5-sec hold period, and Mahin et al. (1989), reductions of as high as 10% within a 0.5-sec hold interval.

A very important characteristic of stress relaxation is that once straining is resumed at the end of the relaxation period, the original stress-strain characteristics are reached quickly (transition strains as low as 0.01% can be observed), and the material follows the same stress-strain curve as without relaxation periods (Krempl, 2001). This result indicates that after a relaxation event, the stress-strain curve is reached quickly, and the relaxation periods are forgotten, as illustrated in Figure 3.5.

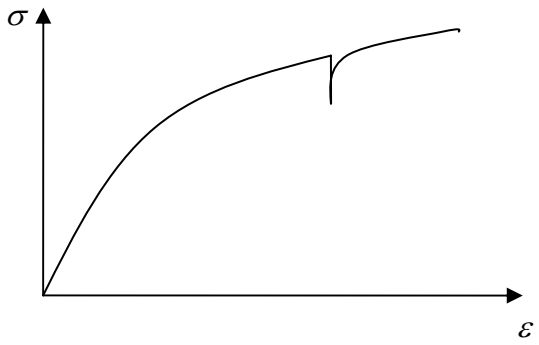

Figure 3.5: Stress-strain curve with stress relaxation.

During pseudodynamic testing, if force relaxation occurs during a given step, the force-deformation characteristics of the specimen and, therefore, future force values will not be directly affected. However, if the restoring forces are measured after force relaxation has occurred, their values are incorrect, and errors are introduced into the experiment. Force-relaxations errors in pseudodynamic testing can, therefore, be mitigated by measuring the restoring force immediately after the actuator has reached the commanded target displacement and by reducing or eliminating the hold period.

3.4 Fast hybrid testing

Fast hybrid testing is a variation of the pseudodynamic test method in which the speed of the test is significantly increased. In the limit, when the imposed displacements and response analysis are executed in a common time scale (i.e., real time), the method is called *real-time hybrid testing.* Real-time hybrid testing allows testing systems with rate-dependent components. In principle, real-time hybrid testing can be conducted to experimentally test the entire structure, or only the critical components (using the substructuring technique), as in pseudodynamic testing. However, only tests using the substructuring technique have been conducted to date.

Real-time hybrid testing requires high performance of both the physical testing system and the computers and software used to perform the numerical calculations and data acquisition. Furthermore, because the test is conducted in real time, the dynamics of the testing system and specimen become important.

3.4.1 Types of delays

In hybrid testing, there are some inevitable time lags and delays that can be grouped into three main categories: communication delays, computing time delays, and actuator dynamics.

Communication delays

Because hybrid testing is a closed-loop experiment, there is a continuous exchange of information between all of the components required to conduct the test (i.e., computer, servo-controller, and data acquisition systems) producing communication delays. The main communication delays are associated with: (a) the time required to pass the target displacements from the computer solving the equation of motion to the actuator's controller, and (b) the time required to send back the measured force and displacement from the data acquisition system to the computer performing numerical integration. These delays become especially important when conducting distributed simulations through the internet, where network delays are random and can be significant.

Computing time

The computer solving the equation of motion requires some time to perform the calculations associated with the numerical integration. This time required to calculate the target displacements for the next time step becomes important especially for large models (several degrees-of-freedom), and for numerical substructures with nonlinear response.

Actuator dynamics

Displacements in hybrid testing are generally imposed on the structure using hydraulic actuators. When displacements are applied at fast rates, the dynamics of the actuator and attached specimen become important. Dyke et al. (1995) analyzed the effects of control-structure-interaction (CSI) and showed that the dynamics of the actuator and structure are intrinsically coupled through a natural velocity feedback link. This work demonstrated that neglecting phase differences between the command input and the resulting force (i.e., neglecting the CSI) resulted in an apparent time delay associated in the literature with generation of the control forces. In structural testing, this effect is not significant when the tests are conducted at slow speeds. However, when performing fast- and real-time hybrid tests, this dynamic coupling and the finite response time of the hydraulic actuators become particularly important, resulting in a *time lag* between the commanded displacement and the realization of this command by the actuator. Although

the time lag is caused by both actuator dynamics and the attached test specimen, the contribution from the former is dominant (Zhao et al., 2003). Typically, the natural frequency of the test specimen is large compared to the bandwidth of interest and in the pseudostatic region (low-frequency region), the phase of the actuator transfer function can be approximated as linear and modeled as a pure time delay. Actuator time lags can be several times larger than the typical time-step used for seismic testing. Typical values reported in the literature range from 8 to 30 msec (Horiuchi et al., 1999; Nakashima & Masaoka, 1999; Darby et al., 2001; Shing et al., 2004).

The time lag due to actuator dynamics and actuator-specimen interaction depends on the response frequency; therefore, the characterization by a constant time delay is accurate only over a limited range (e.g., low frequency).

3.4.2 Effects of time delays and time lag

In real-time hybrid testing, the effect of time delays (denoted here as T_d) is that the output or imposed displacement lags the commanded displacement by an amount of time equal to the delay, as shown in Figure 3.6 (a). Because of this delay, the force measured and fed back from the experiment does not correspond to the commanded displacement (it is measured before the actuator has reached its target position), however, the algorithm assumes that the measured force corresponds to the commanded displacement. For a linear-elastic system, the resulting response, as seen by the algorithm, is a counter-clockwise hysteretic loop, instead of the straight line corresponding to the linear behavior, as shown schematically in Figure 3.6 (b). The effect of this counter-clockwise loop is to introduce additional energy into the simulation. Horiuchi et al. (1996) demonstrated that for a linear-elastic SDOF system, the increase in the total system energy caused by the delay/lag is equivalent to introducing negative damping into the system (given by $c_{eq} = -kT_d$, where k is the stiffness of the system). This artificial negative damping becomes large when either the stiffness of the system or the time delay/lag is large. When this negative damping is larger than the structural damping, the response will diverge (become unstable), and the experiment must be halted. Instability almost invariably occurs in practice due to the low levels of damping associated with structural frames and the large time delays/lags associated with large hydraulic actuators (Darby et al., 2001). Therefore, introduction of compensation for time delays/lags is essential when conducting fast-hybrid experiments.

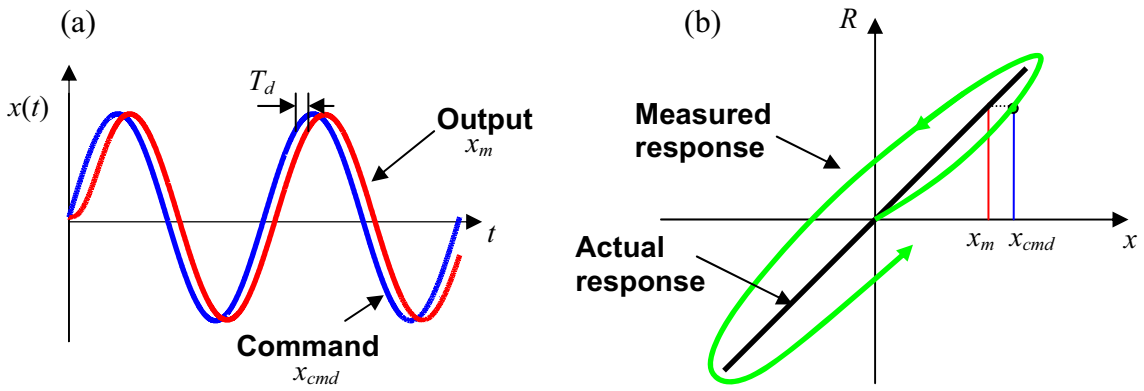

Figure 3.6: Effects of time delays/lags: (a) displacement history, (b) load-deformation curve.

The effects of the delays and actuator time lag have been traditionally treated together by determining a total delay that includes all of these effects. However, because the actuator time lag varies with frequency, this approximation is valid only over the frequency range used for the approximation. If the conditions change significantly during the test (e.g., natural frequency of the test structure due to changes in specimen stiffness), this method is not very satisfactory because the system can become unstable (Blakeborough et al., 2001). Additionally, when the response of the test structure includes significant contributions at different frequencies (e.g., multi-degree-of-freedom-systems), approximating the actuator time lag with a single time delay may not yield satisfactory results. In this study, methods that allow evaluating and compensating time delays and actuator dynamics independently are developed.

3.5 Continuous pseudodynamic test method

In conventional pseudodynamic testing, the displacements are imposed by the actuators as a repeated process of slow loading and pausing. The servo-controller receives the target displacement and generates the command signals for the actuator typically using a ramp function, which is then applied to the specimen (loading phase). Once the target displacement is reached, the actuator pauses and holds in that position until a new target displacement is received (hold phase). This process of ramp loading and holding is generally denoted as ramp-hold procedure and is schematically shown on Figure 3.7.

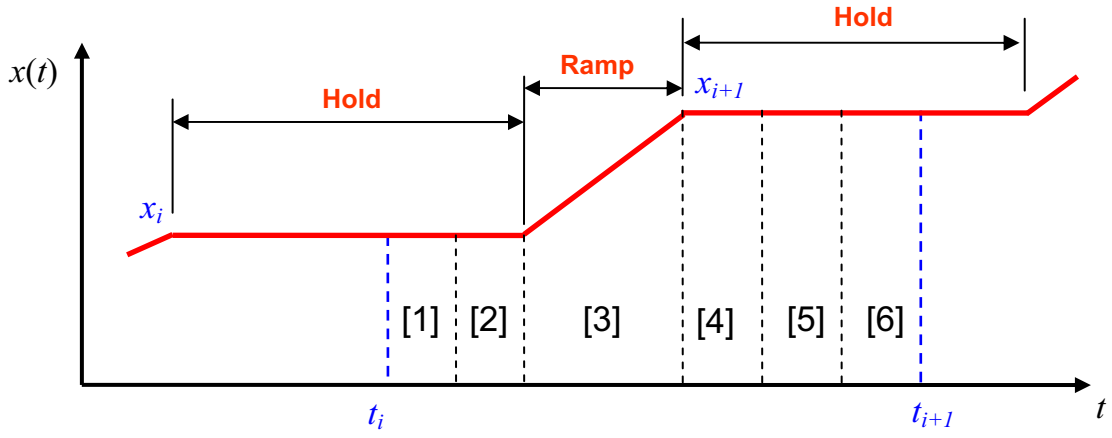

Figure 3.7: Ramp-Hold procedure used in conventional pseudodynamic testing.

The tasks involved in each time step are: [1] compute target displacement, [2] send target displacement, [3] impose target displacement using the actuators, [4] measure the restoring force and displacement, [5] send force and displacement, and [6] update response.

The ramp-hold procedure used in conventional pseudodynamic testing has some disadvantages. During the hold period, while the displacement is held constant, force relaxation may occur in the test specimen, causing the measured restoring force, which is fed back to the algorithm, to be erroneous. Because most of the force relaxation occurs during the initial portion of the hold period, only a few seconds of hold may be needed to produce force relaxation effects (Mosqueda et al., 2004).

An alternative to the ramp-hold loading procedure used in conventional hybrid tests is to use a continuous loading procedure. In this method, called *continuous pseudodynamic*, the displacements are applied continuously to the test specimen, and the restoring forces are measured when the specimen reaches the target displacement without stopping the actuators. By achieving a continuous motion of the actuators and eliminating the hold phase, force relaxation effects are eliminated and the speed of the test is increased. The smooth motion of the actuators also contributes to keep control errors small (Magonette, 2001).

The challenge in continuous pseudodynamic testing is that after the target displacement has been reached, there is a period of time in which the actuators have to continue moving even though the next target displacement is yet unknown. Therefore, to keep the actuators moving continuously, prediction of the response is necessary within the time step (prediction phase). Once the next target displacement has been calculated and is available, the actuators should correct their path and move towards the target displacement (correction phase). This allows for continuous movement of the actuators and smooth actuator displacement time history, as shown in Figure 3.8.

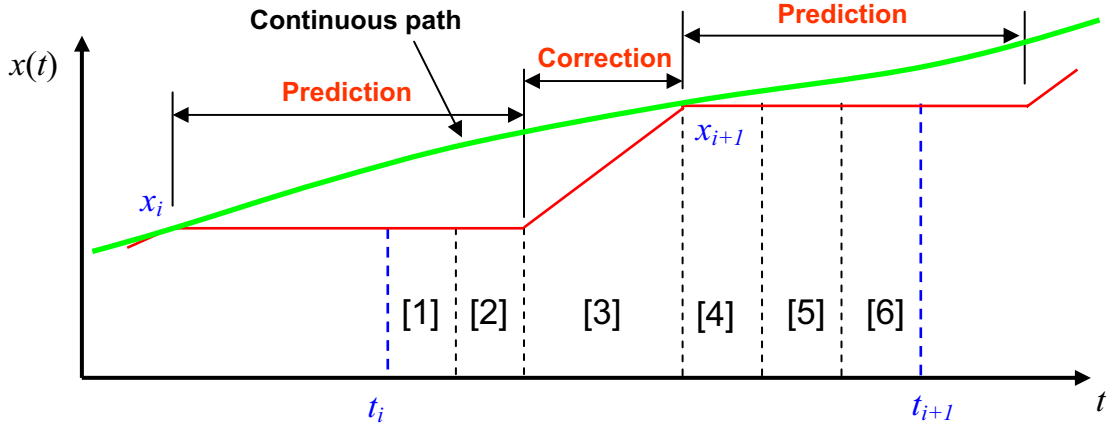

Figure 3.8: Response prediction for continuous pseudodynamic.

Response prediction is difficult because the main motivation to conduct a hybrid experiment is to determine the unknown response of a structural system. The predictor/corrector method should be as accurate as possible so that the actuator path is very close to actual one, while at the same time, simple enough so that the calculations can be executed rapidly, providing command signals in a fast and continuous manner. The method used for the prediction and correction of the response is the key component in a continuous hybrid simulation.

Different methods have been proposed for continuous hybrid testing (Takanashi & Ohi, 1983; Nakashima & Masaoka, 1999; Magonette, 2001; Mosqueda et al., 2004), however, only the method proposed by Nakashima and Masaoka (1999) has been successfully applied for real-time hybrid tests. The method proposed by Nakashima and Masaoka (1999) performed response prediction-correction using simple polynomial extrapolation-interpolation. Command signals are generated at a fast rate, δt, while response analysis is performed at a slower rate Δt. Lagrangean polynomials based on the information from the previous displacements are used for the extrapolation and interpolation. By assuming that the structure's response is sinusoidal, the differences between the extrapolated and true displacements were characterized by an amplitude change and a phase lag. The extrapolated displacement was found to be less accurate for a larger number of extrapolation steps, for a larger value of $\omega\Delta t$, and for lower-order polynomials. Using a similar procedure, the interpolation was shown to be more accurate than the extrapolation (smaller amplitude change and phase lag) for the same $\omega\Delta t$ and number of predictions. The transition from extrapolation to interpolation is also important and was characterized by the velocity in the switching interval (given by the difference between the signals corresponding to the last extrapolation and the first interpolation divided by the time interval). By determining the amplitude change and phase lag, the third- and fourth-order polynomials were found to be significantly more accurate than the first- and second-order ones. The phase was shown to be advanced for the first- and second-order polynomials, while it is delayed for the third and fourth order, which was considered more acceptable. Nakashima and Masaoka (1999) suggested the use of a

third-order polynomial for extrapolation and interpolation, because it has good accuracy in both extrapolation and velocity in the switching interval. For the third-order polynomial, the *j*-th command signal (at a time, $j\delta t$, from the start of the current time step) is given by

$$\hat{x}_j = \sum_{k=0}^{n} a_{kj} x_k \tag{3-15}$$

where the coefficients for the case of extrapolation are given by

$$\begin{aligned} a_{0j} &= \frac{1}{6}\left(\frac{j\delta t}{\Delta t}+1\right)\left(\frac{j\delta t}{\Delta t}+2\right)\left(\frac{j\delta t}{\Delta t}+3\right), & a_{1j} &= -\frac{1}{2}\frac{j\delta t}{\Delta t}\left(\frac{j\delta t}{\Delta t}+2\right)\left(\frac{j\delta t}{\Delta t}+3\right) \\ a_{2j} &= \frac{1}{2}\frac{j\delta t}{\Delta t}\left(\frac{j\delta t}{\Delta t}+1\right)\left(\frac{j\delta t}{\Delta t}+3\right), & a_{3j} &= -\frac{1}{6}\frac{j\delta t}{\Delta t}\left(\frac{j\delta t}{\Delta t}+1\right)\left(\frac{j\delta t}{\Delta t}+2\right) \end{aligned} \tag{3-16}$$

and for the case of interpolation by

$$\begin{aligned} a_{0j} &= \frac{1}{6}\frac{j\delta t}{\Delta t}\left(\frac{j\delta t}{\Delta t}+1\right)\left(\frac{j\delta t}{\Delta t}+2\right), & a_{1j} &= -\frac{1}{2}\left(\frac{j\delta t}{\Delta t}-1\right)\left(\frac{j\delta t}{\Delta t}+1\right)\left(\frac{j\delta t}{\Delta t}+2\right) \\ a_{2j} &= \frac{1}{2}\left(\frac{j\delta t}{\Delta t}-1\right)\frac{j\delta t}{\Delta t}\left(\frac{j\delta t}{\Delta t}+2\right), & a_{3j} &= -\frac{1}{6}\left(\frac{j\delta t}{\Delta t}-1\right)\frac{j\delta t}{\Delta t}\left(\frac{j\delta t}{\Delta t}13\right) \end{aligned} \tag{3-17}$$

The number of extrapolation steps required depends on the size (number of degrees-of-freedom) and characteristics of the structural system (linear or nonlinear). Tests performed by Nakashima and Masaoka (1999) indicated that the limitations of the system based on stability and accuracy were controlled by the number of extrapolations required, the response frequency, and by the number of degrees-of-freedom of the structure. Response frequencies beyond 3 Hz were not guaranteed to be stable, primarily because of limitations of the extrapolation and interpolation procedures. Techniques for better prediction of the response are needed to allow testing of structures with larger natural frequencies, as is typically the case for multi-degree-of-freedom systems.

3.6 Summary

This section provided background information regarding the pseudodynamic test method and its implementation. Solution of the equation of motion is a key component in hybrid testing. Numerical integrations algorithms used for transient analysis were reviewed, with especial attention to stability and its applicability to hybrid testing. The effects of rate-of-loading and force relaxation on hybrid testing were reviewed. Extensions of the pseudodynamic test method (continuous and fast-hybrid testing) developed to account for these effects were presented. The sources and effects of time delays and lags on fast-hybrid testing were reviewed, and the need for more rational methods to account for these parameters was identified.

CHAPTER 4

SYSTEM FOR REAL-TIME HYBRID TESTING

A testing system that combines fast hardware, for high-speed computations and communication, with high-performance hydraulic components has been designed to allow execution of real-time hybrid testing. The system is used throughout the remaining part of this report to experimentally evaluate proposed algorithms and compensation techniques. This chapter presents a description of the system architecture, components, and tests conducted to characterize its performance.

4.1 System architecture

The architecture of the testing system is shown schematically in Figure 4.1. The system consists of a hydraulic actuator controlled by a digital servo-controller, a displacement transducer that measures the displacements imposed by the actuator and provides position feedback, a load cell to measure the force imposed by the actuator (which corresponds to the restoring force from the specimen), a computer with a board for real-time control (to solve the equation of motion and generate the target displacements), and digital-to-analog and analog-to-digital converters.

4.2 System components

Figure 4.2 shows the main components of the testing system, and Figure 4.3 shows a detailed view of the load frame. This testing equipment is located at the Smart Structures Technology Laboratory (SSTL) at the University of Illinois at Urbana-Champaign (*http://sstl.cee.uiuc.edu*).

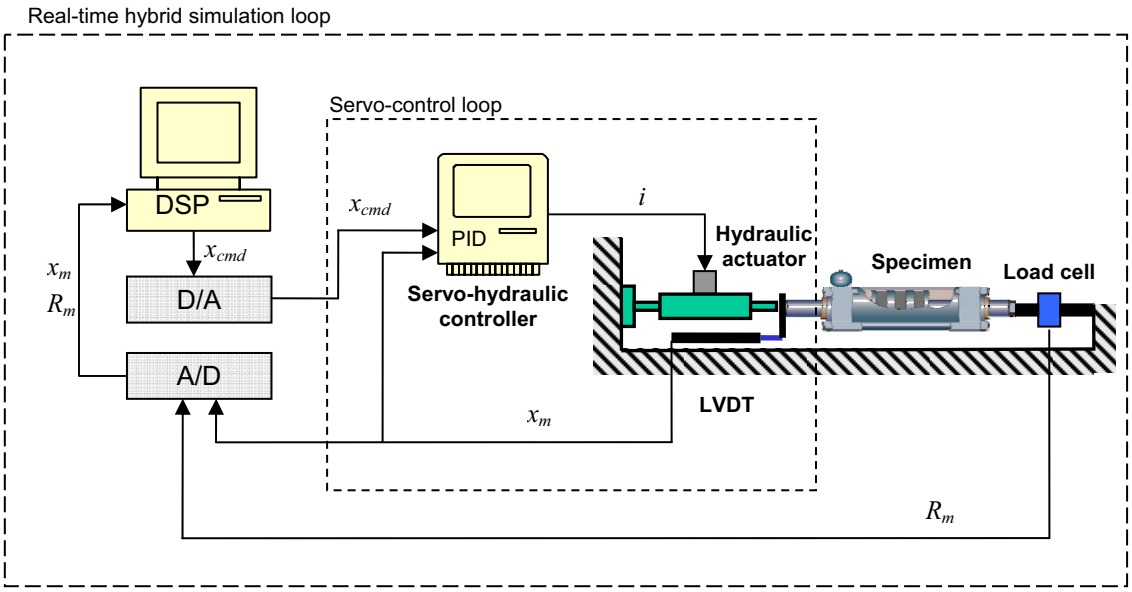

Figure 4.1: Schematic of system for real-time hybrid testing (x_m = measured displacement, R_m = measured force, x_{cmd} = command displacement, and i = command to actuator).

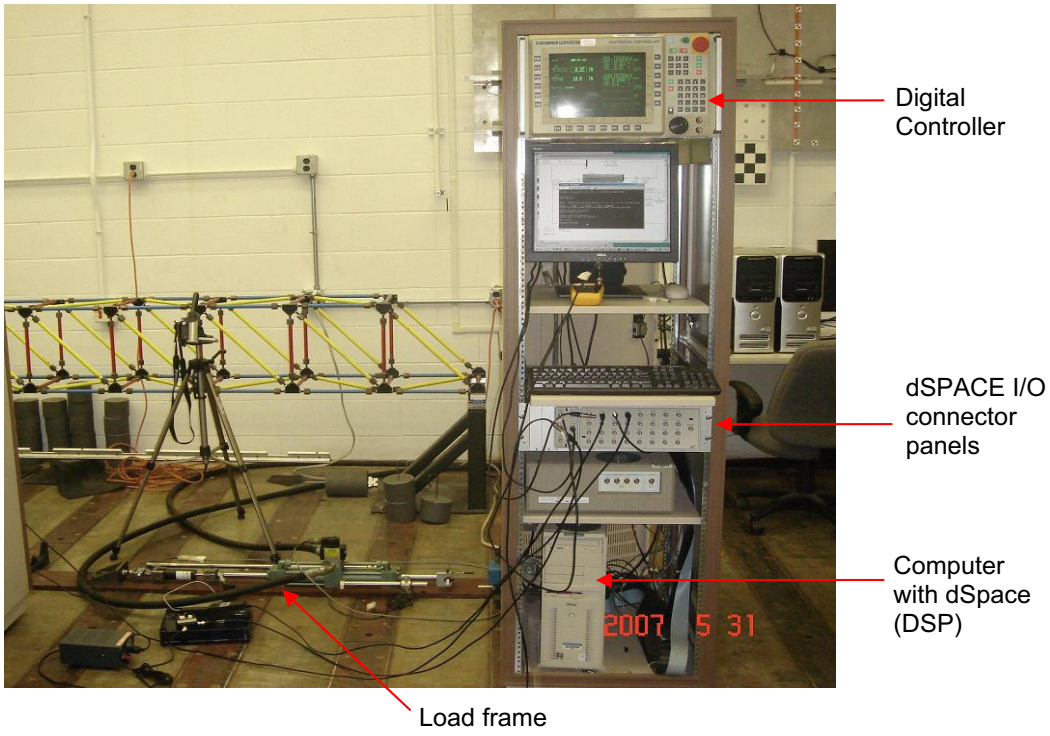

Figure 4.2: Experimental setup (system for real-time hybrid testing).

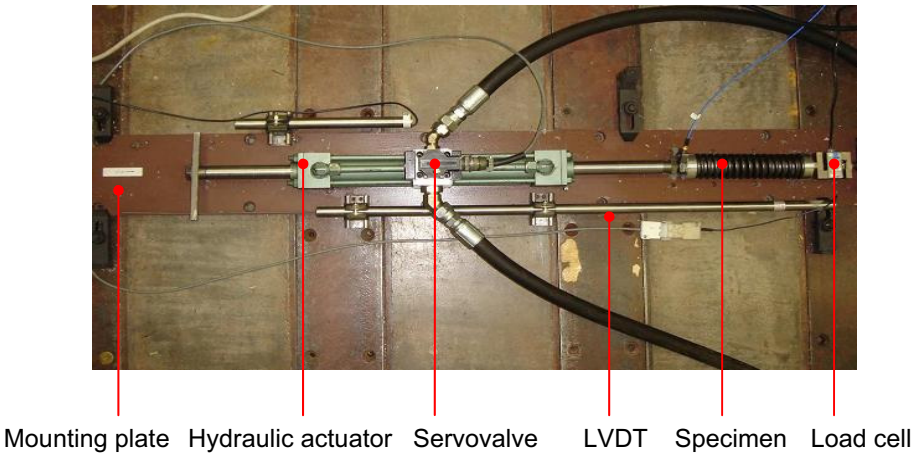

Figure 4.3: Experimental setup (load frame).

Descriptions of the different components of this real-time hybrid testing system are as follows:

Hydraulic actuation system

A double-ended hydraulic actuator manufactured by Nopak is used. The actuator has a ±6 in (±152 mm) stroke and is equipped with low-friction Teflon seals to reduce friction effects. The actuator has a cylinder diameter of 1.5 in (38.1 mm) and a rod diameter of 1.0 in (25.4 mm), which results in an effective piston area of 0.98 in^2 (633 mm^2). A steel plate with a thickness of 0.5 in (12.7 mm) is used as mounting plate, to connect the actuator and test specimen to the test floor. A Schenck-Pegasus 132A two-stage servovalve rated for 10 gpm at 1,000 psi pressure drop is used to control the actuator. A hydraulic service manifold provides conditioning and filtering of the oil supply. The system is connected to the main hydraulic power supply line of the Newmark Structural Engineering Laboratory operating at 3,000 psi pressure.

Controller and sensors

The actuator is controlled by a Schenck-Pegasus 5910 digital servo-hydraulic controller in displacement feedback mode. The displacement of the actuator is measured using a Lucas-Schaevitz 10,000 DC-EC linear variable differential transformer (LVDT) having a range of ±10 in (±254 mm). An Omega load cell with a range of ±1.0 Kip (±4,540 N) is used to measure the applied force.

DSP and hardware

A PC computer with a dSPACE DS1003 (dSPACE Inc., *www.dspaceinc.com*) parallel processing DSP board based on a Texas Instrument TMS320C40 processor is used to solve the equations of motion and provide real-time control. A dSPACE DS2102 High-Resolution, 6-channel D/A Board and a dSPACE DS2002/DS2003 32-channel A/D

Board are employed to convert the signals from digital to analog, and analog to digital, respectively, both having a resolution of 16 bits. Access to the input and output channels is provided by dSPACE connector panels that allow the signals to be connected via BNC ports. During system characterization tests, a 4-input/2-output channel, PC-based SigLab spectrum analyzer manufactured by DSP Technology is used for data acquisition and analysis.

Software

The algorithms (numerical integration and compensation techniques) are implemented in SIMULINK/MATLAB and then downloaded to the dSPACE processor using the Real-time Workshop (*http://www.mathworks.com/products/rtw/*). Because real-time hybrid testing is a closed-loop experiment, the displacements to be imposed to the test specimen are not known in advance (they are determined during the experiment). To prevent damage of the specimens and testing system, limits are set to prevent these values from becoming too large. At each time step, the values of certain key quantities (e.g., command displacement to the actuator) are compared to user-defined maximum allowable values, and if any of these values is exceeded, the experiment is stopped automatically.

During the real-time hybrid experiments, two additional programs are run on the PC and have access to the DSP board: (a) COCKPIT for signal monitoring and control of the experiment, and (b) TRACE for data acquisition. Figure 4.4 shows a schematic diagram of the software configuration and its interaction with the hardware.

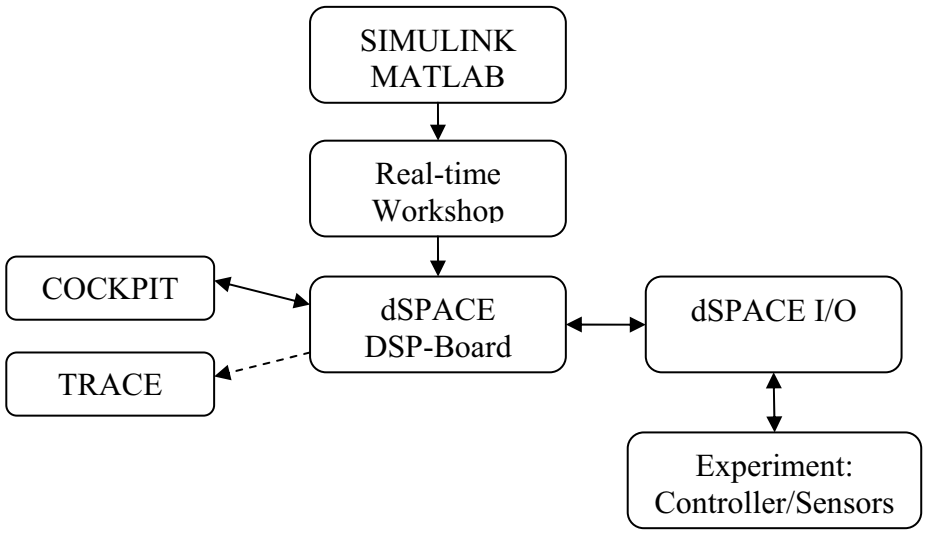

Figure 4.4: Hardware and software configuration.

The software TRACE allows capturing data during the real-time hybrid experiments. This software records and displays graphically time histories of variables and measurements (of processes running on the dSPACE processor board) without interrupting or interfering with the DSP application. Some of the measurements that are

typically captured during a hybrid experiment, include calculated displacements (i.e., structural response), commanded displacement (to servo-controller), measured displacement (from LVDT), and measured force (from load-cell).

COCKPIT allows monitoring and interacting with the DSP application running on the dSPACE processor board. Using this software, a supervisory program was created that runs on the PC during the real-time hybrid experiments and controls the application running on the DSP. Figure 4.5 shows the version of this program used for the real-time hybrid experiments conducted in Chapter 8 (testing of a semiactively controlled structure).

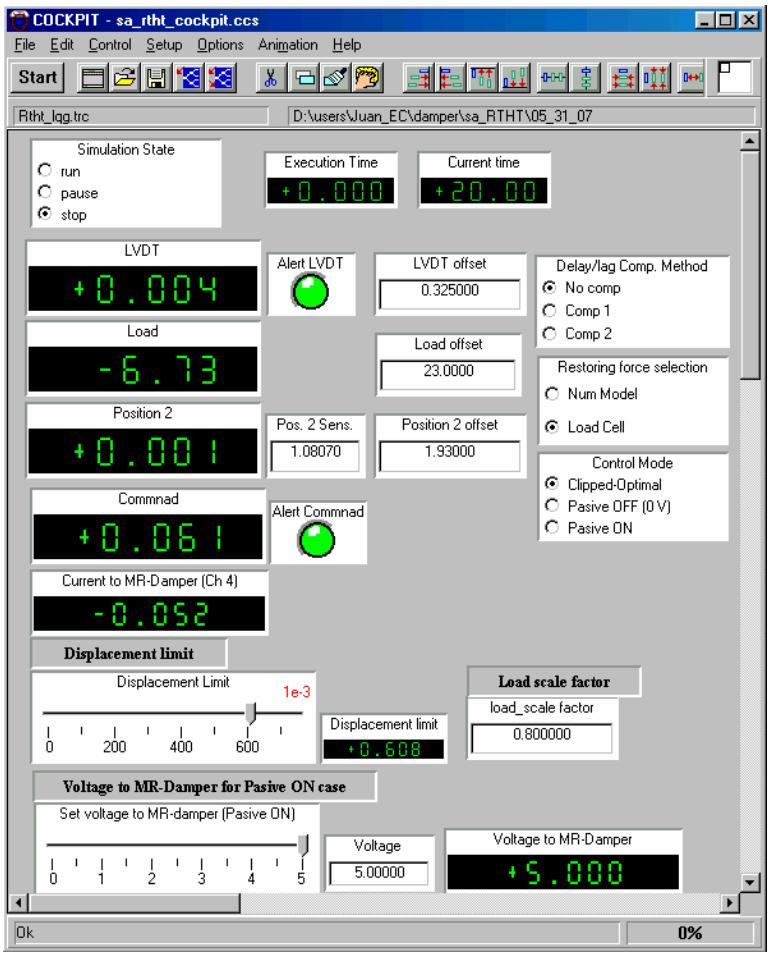

Figure 4.5: COCKPIT supervisory program for real-time hybrid experiments.

The main functions that this supervisory program provides are the following:

- Control of the real-time hybrid experiment by allowing the user to start, pause, or stop the DSP application and, therefore, the experiment.

- Real-time monitoring of certain quantities and measurements during the experiment (e.g., command displacement, LVDT and load cell measurements, and

execution time). Warnings are implemented when some of the values exceed certain limits.

- Ability to interactively modify parameters before or during the experiments (e.g., magnitude of the earthquake record and maximum allowable command displacement).

- Options to select between several compensation strategies for time-delays/lags or a no-compensation option.

- Option to select between *simulation* and *experiment* modes for running the real-time hybrid test. In the *simulation* mode, displacements are still imposed to the specimen and measurements acquired; however, the force corresponding to the physical substructure is determined using a numerical model of the test specimen instead of the measurement from the load cell. This mode is very useful for debugging the system and ensuring that all of the components are working properly (e.g., sensors, actuator, and algorithms). Once the system has been checked, the running mode is set to *experiment*, and the real-time hybrid experiment is conducted using the measurement from the load cell.

4.3 Limits of testing system

Every testing system has a limited range on its ability to apply forces and displacements. These limitations depend on several factors; to properly conduct experiments, understanding and quantifying these limits is critical.

Displacement limits

The displacement transducer used to provide the feedback signal to the controller should have a range equal or larger than the actuator stroke. For the system considered in this study, the actuator and LVDT have ranges of ±6 in (±152.4 mm) and ±10 in (±254 mm), respectively, which are larger than the displacements intended during the experiments, less than 1 in (25.4 mm).

Force-velocity limits

In dynamic applications, the maximum force that can be applied by the actuator is dependent on the velocity at which this force must be achieved. The following analysis determines this force-velocity limitation of the testing system.

Servovalves are typically rated by the load flow, Q_L, called *rated flow,* Q_R obtained with a maximum input current, i_R, and at a given valve pressure drop, ΔP, across the valve (Merritt, 1967). The steady-state flow-load characteristics of a servovalve are defined by the following flow equation:

$$Q_L = Q_R \left(\frac{i_c}{i_R} \right) \sqrt{\frac{P_s - p_L}{\Delta P}} \tag{4-1}$$

The rated conditions of a particular servovalve are typically found in the technical specifications from the manufacturer. The servovalve used in this study has a rated flow Q_R of 10 gpm (38.5 in^3/s) at a 1,000 psi pressure drop ΔP, and a rated current i_R of 50 mA. The supply pressure, P_s, of the system is 3,000 psi. Figure 4.6 shows the resulting flow graph of the servovalve. Notice that the rated flow is obtained when the input current to the valve is equal to the rated current (i.e., i_c/i_R = 1.0) and the pressure drop across the valve (P_s - P_L) is equal to the rated pressure drop, ΔP, which results in a pressure ratio, P_L/P_s of 2/3.

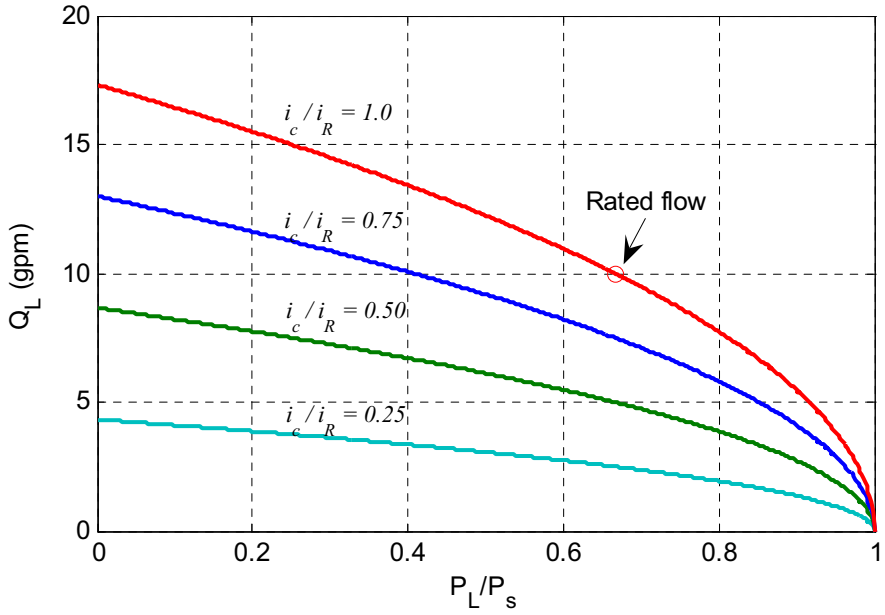

Figure 4.6: Flow Graph of servovalve.

The force generated by the actuator, f_p, is obtained by the product of the effective piston area, A, and the pressure drop across the load, p_L. The piston velocity, v, and the power generated by the hydraulic actuator are given by the following equations:

$$v = \frac{Q_L}{A} \tag{4-2}$$

$$\text{Power} = f_p \; v \tag{4-3}$$

Figure 4.7 shows the relationship between the power and the pressure ratio (P_L/P_s). As observed from the graph, maximum power is generated and transmitted to the load when P_L/P_s = 2/3, i.e., the pressure across the load is two-thirds of the supply pressure (P_L = 2/3

P_s). For this reason, and because a supply pressure of 3,000 psi is the most widely used, a valve drop of 1,000 psi is typically used for rating servovalves.

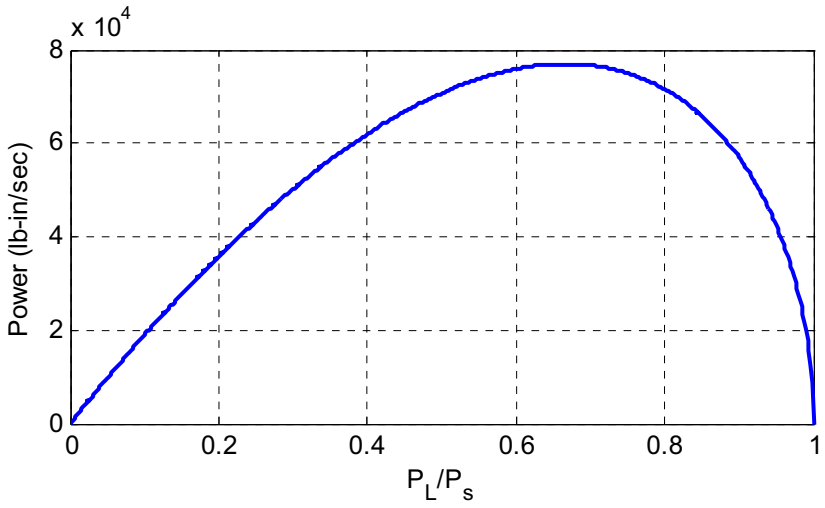

Figure 4.7: Power transmitted to the load (i_c/i_R = 1).

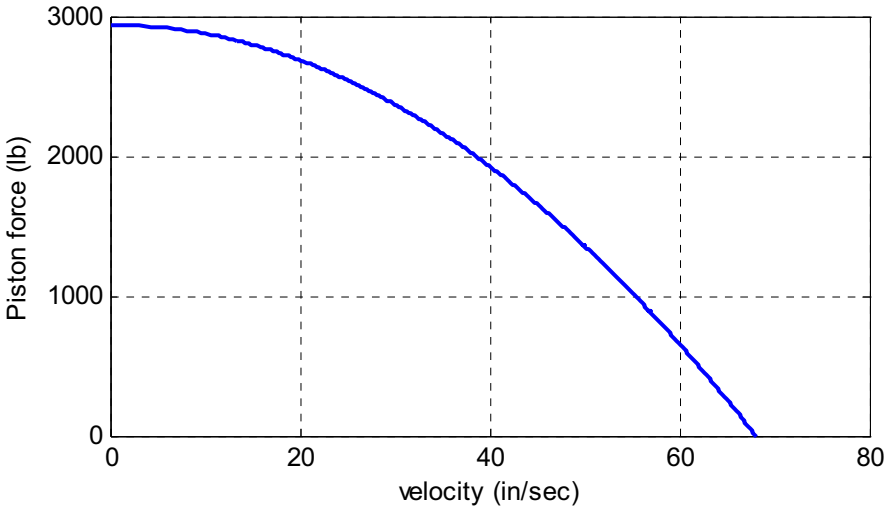

Figure 4.8: Force vs. velocity graph of actuator (i_c/i_R = 1).

Figure 4.8 shows the force-velocity relationship for the servo-hydraulic actuator used in this study. The force generated by the actuator is divided into several components: the force to the load, an inertial force, and a friction force. The friction force is considered small in the system because the actuator employs low-friction Teflon seals. The inertial force depends on the accelerations generated by the piston as well as on the mass of the piston, specimen, and attachments. Based on the maximum forces and velocities expected to be imposed on the specimens (less than 500 lb and 20 in/sec, respectively), this force-velocity envelope is adequate for the applications considered in this study.

4.4 Test specimens

Two different specimens are provided to be used as physical substructures during the real-time hybrid experiments conducted in subsequent chapters: a linear elastic specimen and a specimen with rate-dependent behavior. The specimens are designed to have relatively similar properties (length, displacement, and force capacity) in order to fit in the same test setup, making the two specimens easily interchangeable.

4.4.1 Linear elastic specimen

The linear elastic specimen is composed of a steel compression spring having a length of 8 in (203 mm), an outside diameter of 1.9375 in (49.2 mm), and a wire size of 0.312 in (7.9 mm), see Figure 4.9. The specimen was designed to minimize backlash effects and deformation of the loading frame, while fitting into the experimental setup. The spring is mounted on end supports made of aluminum. The spring has a nominal stiffness of 215 lb/in (37.7 N/mm), and a maximum deflection capacity of 2.77 in (70.4 mm), which corresponds to a maximum load of 0.6 kips (2,669 N). To avoid nonlinear effects on the supports (e.g., backlash), the spring is set to work under compression only. An initial precompression of 0.4 in (10.16 mm) is applied for all the experiments conducted using this specimen, followed by displacements with amplitudes smaller than this initial displacement.

Figure 4.9: Spring specimen.

The spring specimen was subjected to a low-frequency (0.2 Hz) sinusoidal displacement excitation with an amplitude of 0.2 in (5.08 mm). Figure 4.10 shows the force-displacement response of the specimen, which is seen to be very linear behavior, without any backlash or hysteretic effects due to friction. Using a least-squares linear fit, the stiffness of the specimen was found to be 234 lb/in (41.0 N/mm), which was about 9% higher than the manufacturer's specification.

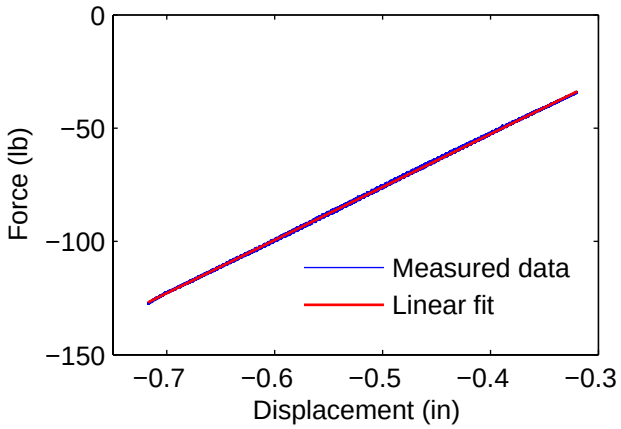

Figure 4.10: Spring specimen force vs. displacement response.

4.4.2 MR Damper specimen

The second specimen used in this study is a small-scale magnetorheological damper (MR damper). The damper considered is a RD-1005 MR fluid damper manufactured by the Lord Corporation (*http://www.lord.com/*), see Figure 4.11 (a).

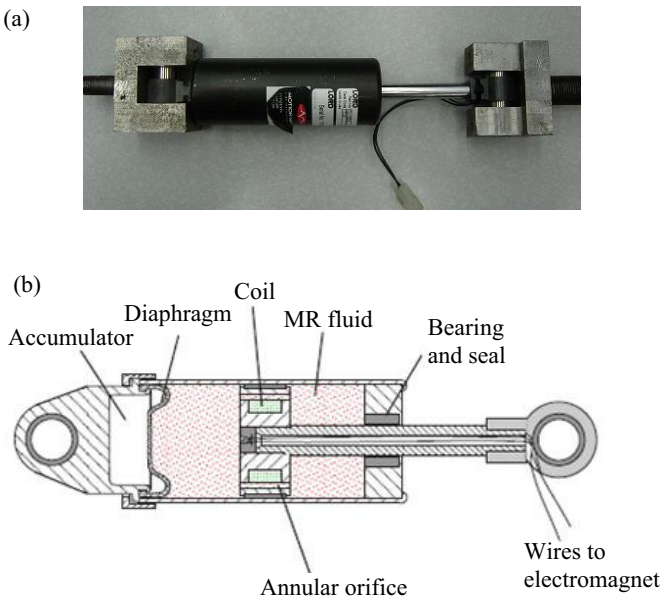

Figure 4.11: Small-scale MR damper.

The damper is 8.5 in (216 mm) long in its extended position, and the main cylinder is 1.5 in (38.1 mm) diameter. The damper has a stroke of ± 1.0 in (25.4 mm) and can generate forces up to about 0.67 kip (3,000 N). The main cylinder of the damper accommodates the piston, the magnetic circuit, an accumulator, and 50 ml of MR fluid,

see Figure 4.11 (b). The magnetic field produced in the device is generated by a small electromagnet in the piston head (Spencer et al., 1997). Input current commands are supplied to the damper using an RD-1002 Wonder Box™ Device Controller from Lord, which uses a PWM amplifier to generate a current that is proportional to the applied voltage. By selecting the input current, the characteristics of the damper may be changed in real-time to vary the forces exerted by the damper. The power required by the MR damper is very small (less than 10 watts), and the system, damper and the current driver, have a response time of typically less than 10 msec (Spencer et al., 1997).

The response of the MR damper to a 0.4 in (10.16 mm) sinusoidal displacement excitation with a frequency of 1.273 Hz is shown in Figure 4.12. Two cases are presented: without input current and with maximum current applied to the damper. As observed the response of the damper is velocity-dependent and nonlinear, and the magnitude of the force generated by the damper increases significantly with the input current (i.e., magnetic field).

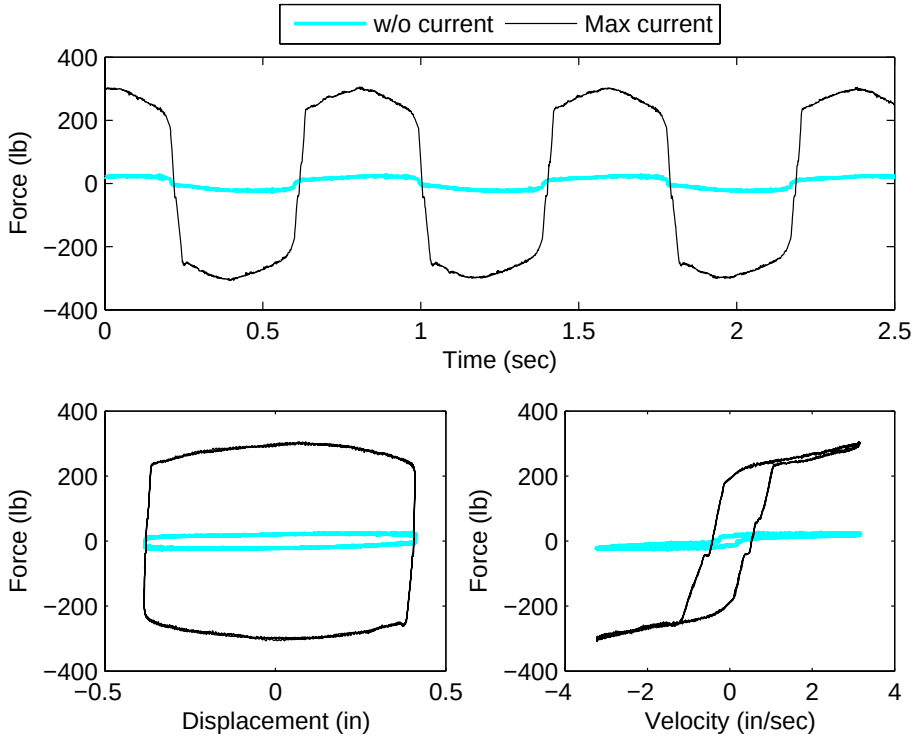

Figure 4.12: Response of MR damper to sinusoidal command displacement.

4.5 System characterization

When conducting real-time hybrid experiments, the dynamic response of the testing system is extremely important. Effects associated with actuator dynamics and time delays must be properly determined before conducting the hybrid experiments. This section presents the experiments conducted to understand and quantify these effects.

4.5.1 Actuator dynamics

The linear-elastic spring specimen was used to determine the characteristics of the testing system. First, the gains of the PID controller were selected. The following values, K_{prop} = 3.0, K_{int} = 0, and K_{der} = 0, were found to give a good step response (2% overshoot and 15 msec rise time). Figure 4.13 shows the response of the system to a 0.4 in amplitude step function.

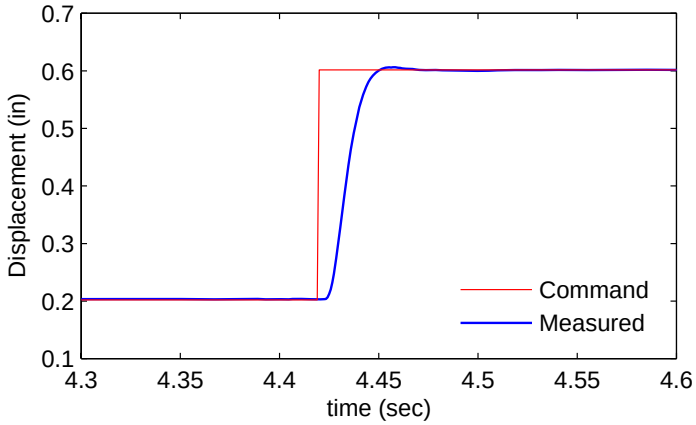

Figure 4.13: Step response of the actuator.

The dynamics of the actuator and the resulting time-lag are critical parameters in real-time hybrid testing. Figure 4.14 shows the response of the system to a 1 Hz displacement sine wave having a 0.25 in amplitude. The difference between the command and measured displacement (i.e., time lag) is estimated to be 12 msec, which is within the typical values reported in the literature.

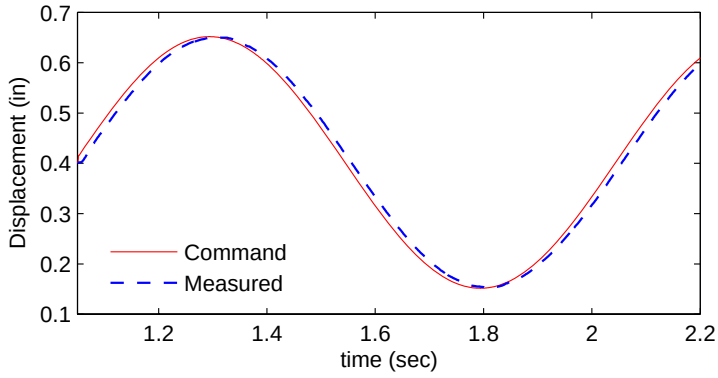

Figure 4.14: Command and measured displacements.

To understand the behavior of the system over a wide range of frequencies, the frequency response function (FRF) from the commanded displacement to the measured displacement was determined using a random excitation as input. The excitation signal was a band-limited white noise with a bandwidth of 50 Hz and an RMS of 0.01 in. A PC-

based SigLab spectrum analyzer manufactured by DSP Technology was employed for data acquisition and analysis. The data were captured using a sampling rate of 128 Hz. The FRF was calculated using 2,048 FFT points, resulting in a frequency resolution of 0.0625 Hz, a Hanning windowing with 50% overlap, and 10 averages. Eight-pole elliptic anti-aliasing (AA) filters were used during the data acquisition. Figure 4.15 shows the frequency response function of the system. Ideally, one would want a system with a magnitude of one (0 dB) and a phase of zero over the entire frequency range, however, this behavior is not possible. After about 15 Hz, the magnitude starts to roll off, and assuming a cutoff frequency of -3dB, the bandwidth of the system is determined to be 28.7 Hz. The phase plot shows that within the bandwidth, the phase of the system is nearly linear, resulting in a relatively constant time lag of about 12.4 msec.

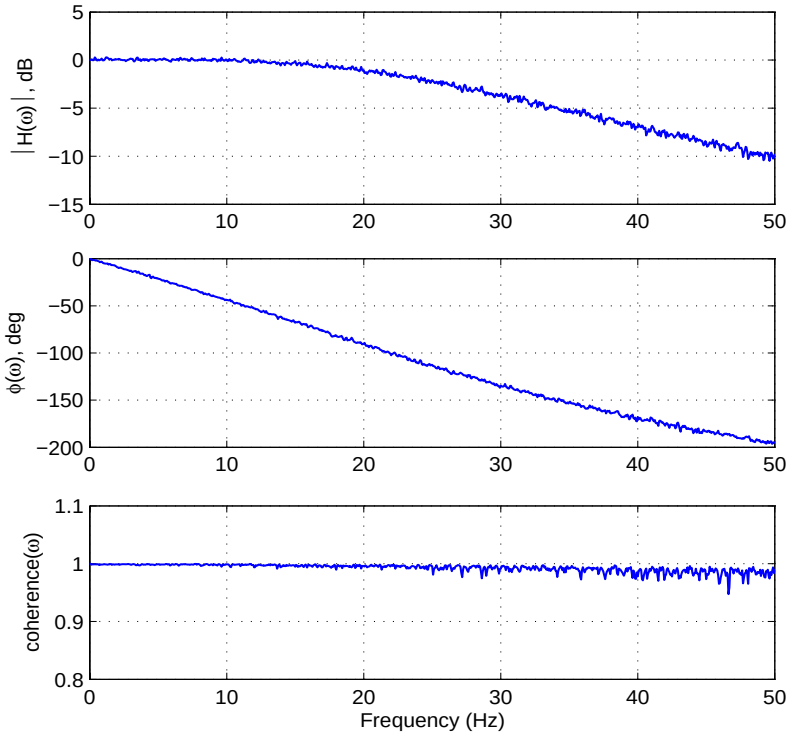

Figure 4.15: Frequency response function from command displacement to measured displacement.

4.5.2 Time delays

In contrast to time lags, which are frequency-dependent, time delays have a constant magnitude and, therefore, do not depend on frequency. In addition to the actuator time lag, some pure time delays exist in a real-time hybrid experiment. Possible sources of these delays are the following:

- Computation time
- D/A converter for command signal

- Communication delays
- Sampling rate of controller
- A/D converter for measured signals

Several tests where performed to quantify these time delays. For the first test, a simple step function was generated on the DSP, sent out the D/A, and subsequently captured by the A/D. The DSP was set to run with a sampling time of 0.1 msec (sampling rate of 10,000 Hz). Figure 4.16 shows the results of this test, where two delayed signals were monitored, *data* 1 and *data* 2. The *data* 1 signal incorporates the total delay associated with the D/A and A/D converters. As can be observed, the associated delay is one time step (i.e., 0.1 msec). The second signal monitored, *data* 2, also includes the time delay associated with the digital servo-controller as well as the communication delays that are found in a real-time hybrid experiment. The resulting time delay is approximately 1.2 msec.

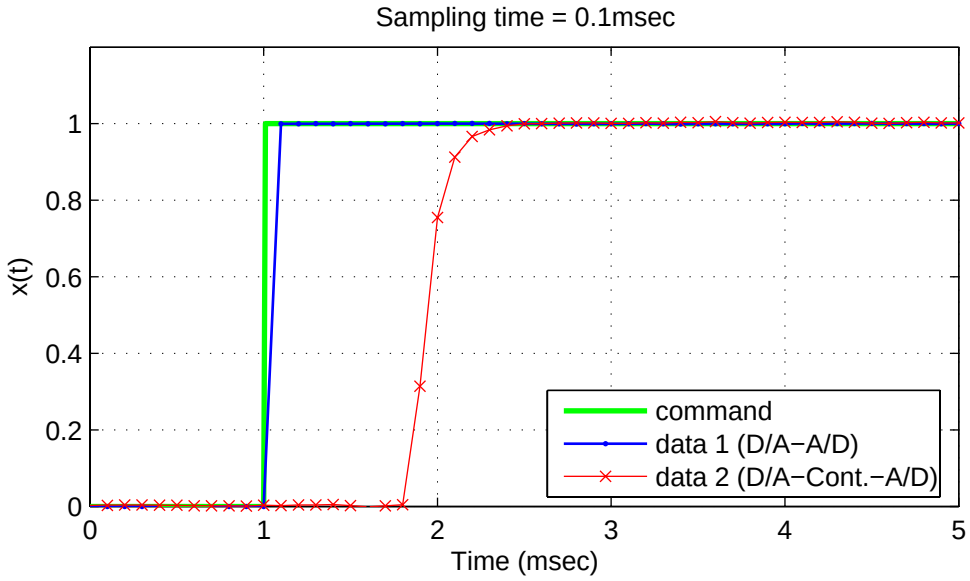

Figure 4.16: Time delays in experimental setup (using simple model for signal generation).

For the second experiment, a larger and more complex model was set to run on the DSP during the delay estimation. The model was the same as the one used for conducting real-time hybrid testing of a semiactively controlled, three-story building employing a MR damper, as described in Chapter 8. Because of the larger size of the model and, therefore, the more calculations required at each time step, the fastest rate at which the DSP could run this application was 2,000 Hz (sampling time of 0.5 msec). Figure 4.17 shows the measured signal that includes the computation time and delays associated with the converters, digital servo-controller, and communication. The total time delay is estimated as 1.5 msec for this larger model. Therefore, the computing time can be estimated as the difference between the delays obtained using the simple model (in which the computation time is assumed negligible) and the larger model. For this application the computing time is estimated as 0.3 msec.

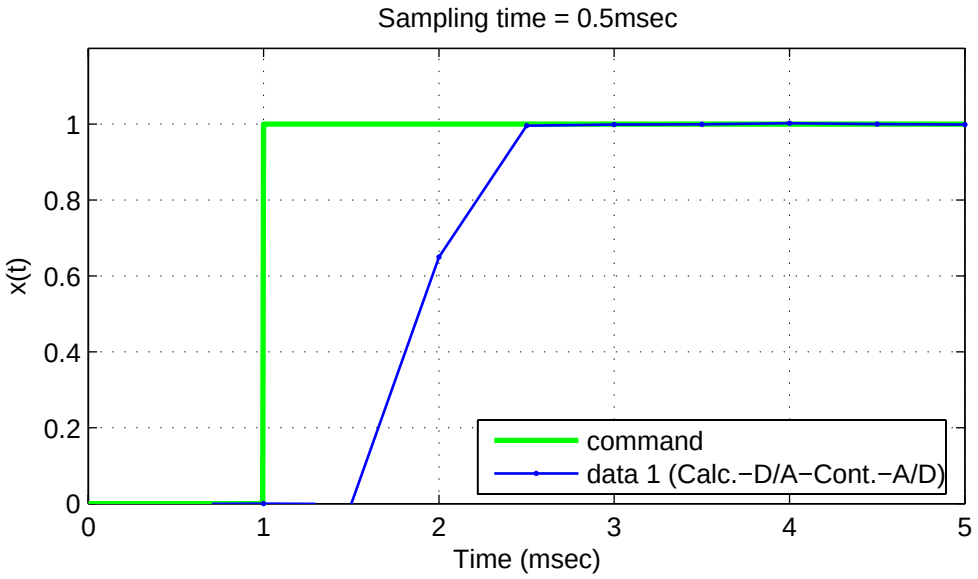

Figure 4.17: Time delays in experimental setup (using complex model for RTHT).

The characterization of the testing system conducted provides valuable insight regarding the performance of the testing system for real-time hybrid experiments. Comparison between the magnitude of the different delays/lags shows that the main source of delay in a real-time hybrid experiment corresponds to the lag associated with the dynamics of the actuator.

4.6 Selection of sampling rate

Several factors must be considered when evaluating the sampling rate that is required for satisfactory execution of a real-time hybrid experiment. These factors include accurate integration of the equation of motion (capturing all of the natural frequencies of interest), stability of the numerical integration strategy, maintaining a sufficiently smooth displacement command signal, and accurately imposing velocities by the actuator.

The numerical model to be integrated in a real-time hybrid experiment includes the components of the test structure (mass, damping, and numerical substructures), as well as additional dynamic components (e.g., delay/lag compensators). To accurately integrate the entire dynamical system, the sampling rate is typically required to be 10-25 times greater than the significant frequencies and damping in the measured responses, depending on the specific application (Dyke, 1996). The stability of the numerical integration depends on the algorithm used. For the Central Difference Method, the stability condition is given by $\Delta t \leq T_n/\pi$, where T_n is the period corresponding to the highest natural frequency of the system.

One of the main motivations to conduct a real-time hybrid experiment is to test systems with rate-dependent components. Therefore, when the restoring force depends also on the velocity, care must be taken to assure that velocities are accurately imposed.

With the state-of-the-practice of servo-hydraulic control, simultaneous realization of velocity and displacement feedback control is difficult (Wu et al., 2005). In principle, if the displacements are accurately imposed and the experiment is conducted in real-time, the correct velocity should be automatically achieved on the specimen during a real-time hybrid experiment. However, if the sampling time of the experiment is relatively large, the actuator will impose the displacement at the beginning of the time step and then hold that displacement for the remaining portion of the time step, i.e., ramp-hold procedure. The resulting velocity will be large at the beginning of the time step and small, or zero, at the end of the time step. The measured restoring force, therefore, will be erroneous, and consequently, the entire experiment inaccurate.

Two approaches have been used to accurately impose the velocities in real-time hybrid testing. The first approach consists of making the time step of the experiment relatively small (Horiuchi et al., 1996, 1999), resulting in smooth displacements and velocities imposed on the specimen. The second approach consists of using two different time steps during the experiment. Response analysis is performed using a relatively large time step (determined to accurately integrate the equation of motion), while a smaller time step is used to generate the command displacements for the actuator's servo-controller. The intermediate displacements are generated using some type of interpolation, e.g., linear interpolation (Nakashima et al., 1992), or polynomial extrapolation/interpolation (Nakashima & Masaoka, 1999).

The spring specimen used in this study is basically rate-independent; therefore, only displacements need to be imposed accurately. However, the MR damper specimen is highly rate-dependent; therefore, both displacement and velocity must be accurately imposed. To determine the required sampling rate for satisfactory response of the MR damper, tests were conducted by imposing a predefined command displacement at different execution rates. The command displacement was a sinusoidal with 0.2 in (5.08 mm) amplitude and 1 Hz frequency, which resembles typical responses of the specimen during the hybrid experiments conducted in subsequent chapters.

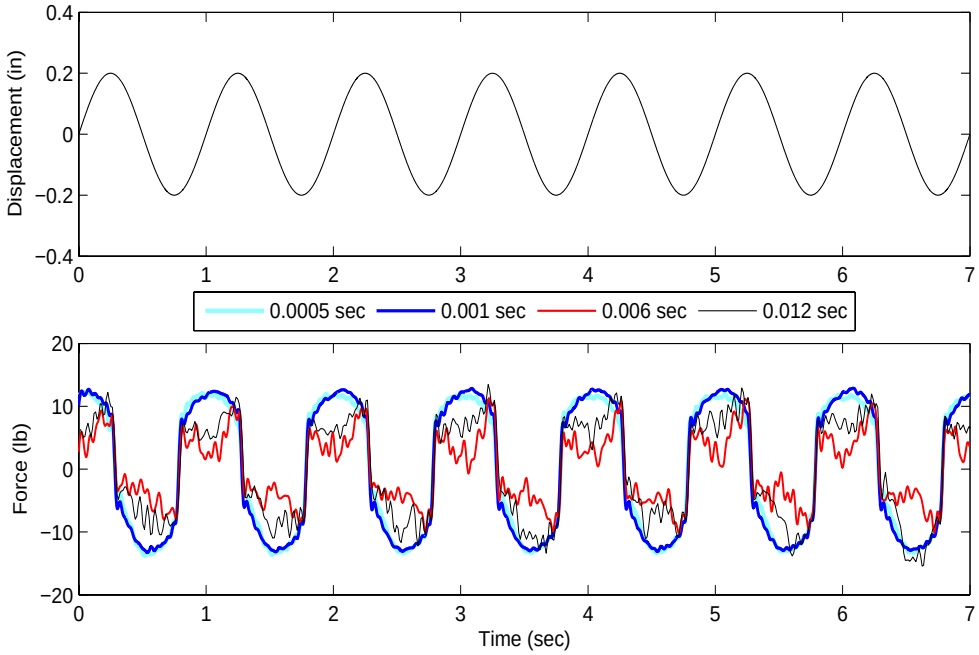

Figure 4.18: Effect of sampling rate on MR damper response.

Figure 4.18 shows the response of the MR damper for different values of the sampling rate used on the dSPACE processor for running the experiment. The sampling times varied from 0.0005 to 0.012 sec (sampling frequencies from 2 kHz to 83.3 Hz, respectively). As observed, although the command displacement is the same in all cases, the measured force from the damper varies. For the larger values of the sampling time (0.006 and 0.012 sec), the response from the damper was considerably different from the tests with faster samplings rates and from the expected response, which indicates that this sampling times are inappropriate. For the faster sampling rates, no significant difference was observed when the sampling time was reduced from 0.001 to 0.0005 sec (sampling rate increased from 1 to 2 kHz). This result indicates that a sampling time of a least 0.001 sec (1-kHz sampling frequency) is required to properly impose both displacement and velocity to the MR damper specimen during the real-time hybrid experiments. The dSPACE digital signal processor used in this study easily accommodates this sampling frequency, even for the largest and most complex models considered in this study. Therefore, there is no need to run the response analysis and signal generation at different rates.

4.7 Summary

A testing system that combines fast hardware and software with high-performance hydraulic components has been assembled for conducting real-time hybrid testing. Characterization tests conducted show that the system is capable of performing high-speed computations and communication as well as delivering the high loading rates

required for fast hybrid testing. Two specimens (spring and MR damper) with rather different behavior are considered for later use in the real-time hybrid experiments.

Time delays/lags are critical parameters in real-time hybrid testing. Tests conducted to quantify these parameters show that the time lag associated with the dynamics of the actuator is the dominant factor, while computing time and delays related to communication, converters, and controller are, in general, relatively small.

CHAPTER 5

MODEL-BASED TIME DELAY COMPENSATION

This chapter presents an approach for real-time hybrid testing that implements model-based time delay/lag compensation. The efficacy of the proposed strategy is verified by conducting substructure real-time hybrid testing of a steel frame under earthquake loads in which the physical substructure is a small-scale specimen representing one of the columns. The performance of the testing system and compensation technique is investigated by considering structures with different fundamental frequencies. The proposed time delay/lag compensation technique is also compared to the traditionally used polynomial extrapolation method. The proposed method is then used to conduct real-time hybrid tests of a structure with a supplementary energy dissipation device, a magnetorheological damper (MR damper), which is tested experimentally.

5.1 Delay compensation

When conducting fast and real-time hybrid experiments, delay compensation is essential to ensure the stability of the experiment. Several techniques have been proposed to compensate for time delays and actuator lags, of which the response prediction method (Horiuchi et al., 1996) has been the most widely used. In this approach, instead of using the calculated displacement as the command signal to the actuator, the displacement of the actuator after the delay, T_d, is predicted and used as the command signal to the actuator. Because of the time delay, the resulting displacement imposed by the actuator approximates the calculated one. This approach is illustrated in Figure 5.1, where $x(t_{i+1})$ is the calculated displacement, $\hat{x}\,(t_{i+1} + T_d)$ is the predicted (compensated) displacement, and $x^m(t_{i+1})$ is the actual displacement achieved by the actuator.

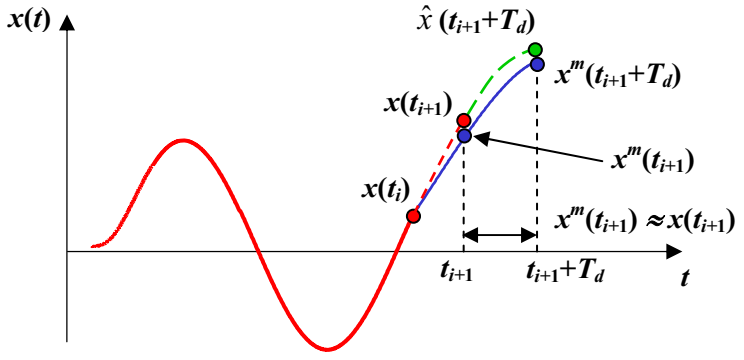

Figure 5.1: Delay compensation using response prediction.

The method used for response prediction by Horiuchi et al. (1996) was based on an *n*-th order polynomial extrapolation of the displacements at the present and previous time steps (Figure 5.2).

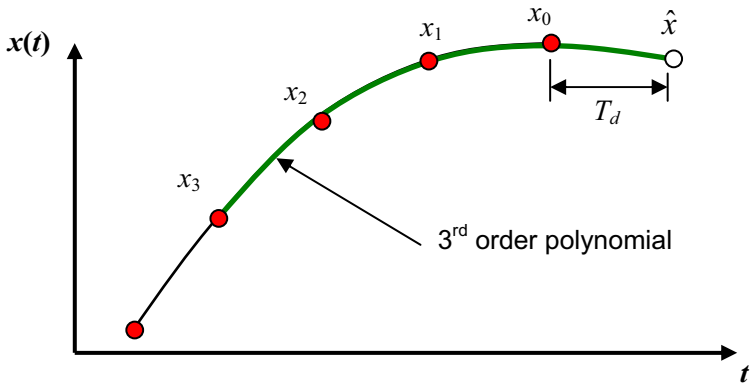

Figure 5.2: Polynomial extrapolation (n = 3).

The predicted command signal (at a time, T_d, from the beginning of the current time step) is given by

$$\hat{x} = \sum_{i=0}^{n} a_i x_i \tag{5-1}$$

where x_i is the displacement corresponding to a time, $i \times T_d$ units ago, and a_i are coefficients that depend on the order of the polynomial. The accuracy and stability of the method were investigated using a linear single-degree-of-freedom system. The prediction method was found to cause variations in both stiffness and damping. Furthermore, damping becomes negative and the simulation diverges when the nondimensional parameter, ωT_d, (where ω is the natural frequency of the system) is larger than a critical value that depends on the order of the polynomial used for the extrapolation. For multi-degree-of-freedom systems, the critical value should be based on the highest natural frequency of the structure (Horiuchi et al., 1999). A third-order polynomial extrapolation was recommended because it requires little calculation time and gives a relatively large critical value, $\omega T_d = 1.571$. For the third-order polynomial extrapolation, the coefficients are: $a_0 = 4$, $a_1 = -6$, $a_2 = 4$, and $a_3 = -1$. The limitation imposed by the critical value for stability becomes more important when the delays/lags are large compared to the smallest period of the structure (e.g., for stiff structures or multi-degree-of-freedom systems that have higher modal frequencies).

5.2 Model-based response prediction

The polynomial extrapolation method for response prediction uses only information from the displacements at a few previous time steps. For small prediction times, the response of a structure (which is nearly harmonic) can be well represented by

polynomials, but when longer prediction times are required, or for systems with larger natural frequencies (i.e., shorter natural periods), more precise prediction methods are necessary. A *model-based response prediction* method estimates the response using known information and physical characteristics of the system. Although complete characteristics of the system are not known in advance, there is some information that is known prior to testing or can be calculated at the beginning of the experiment. This information includes: the mass matrix, **M**, the damping matrix, **C**, the external excitation, **F** (e.g., ground acceleration $\ddot{\mathbf{x}}_g$ for seismic loading), and the initial elastic stiffness of the structure, $\mathbf{K}_e$. By incorporating known information about the system and the excitation, a more accurate prediction of the response can be achieved, allowing larger prediction horizons, stability improvements, and testing of structures with higher natural frequencies or more degrees-of-freedom.

The proposed model-based response predictor uses the information available at the beginning of each time step to predict the displacement response at the end of the prediction horizon (i.e., the time delay/lag). The prediction is performed using a model of the system with the uncompensated target displacement, x_{i+1}, as the initial condition. The response of the predictor model is then computed for the displacements, $\hat{x}_{i+1}^{(k)}$ for k = 1, 2,…, λ, where λ is the ratio between the time delay and the time step (i.e., $\lambda = T_d/\Delta t$), as shown on Figure 5.3. (The time step size, Δt, is set so that the time delay is an integer multiple of Δt for simplicity). The predicted displacement at the end of the prediction horizon, $\hat{x}_{i+1}^{(\lambda)}$, is then sent as a command to the actuator, providing compensation for the time delay.

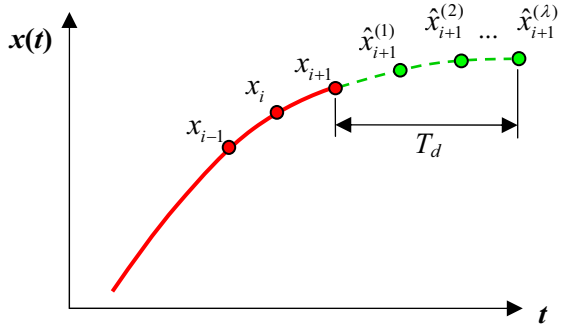

Figure 5.3: Calculation of predicted displacements using model-based response prediction.

To predict the response of structural systems with a small number of degrees-of-freedom, a complete model of the system is used to generate the predictions. By considering the solution of the equation of motion [e.g., Equation (3-5) when using the Central Difference Method], the only unknown parameter is the restoring force vector, **R,** while the mass matrix, damping matrix, and external force vector are known. An approximation of the restoring force vector can be obtained using the previous measured restoring force vector and a certain stiffness matrix, **K,** as given by

$$\mathbf{R}_i \approx \mathbf{R}_{i-1} + \mathbf{K}\left(\mathbf{x}_i - \mathbf{x}_{i-1}\right) \tag{5-2}$$

When the stiffness of the system does not change significantly during the experiment (e.g., linear and moderately nonlinear response), using the initial elastic stiffness of the system for the approximation (i.e., $\mathbf{K} = \mathbf{K_e}$) yields good estimates of the restoring force (a similar approximation is used in the Operator-Splitting method for numerical integration; Nakashima et al., 1990). When the response of the structure is limited to the elastic range, this approximation and the proposed model-based compensation method yields the exact prediction; theoretically the experiment should be stable for any value of the parameter ωT_d.

For cases when the stiffness of the system changes significantly during the experiment, an estimate of the tangent stiffness based on the last increment of the measured restoring force is used. A simple estimate of the tangent stiffness can be obtained using the Broyden formula (Broyden, 1965), which corresponds to a generalization of the one-dimensional secant approximation to the tangent stiffness. The tangent stiffness, $\mathbf{K}_i$, is obtained by making the least change to $\mathbf{K}_{i\text{-}1}$ that satisfies the equation, $\mathbf{K}_i \Delta \mathbf{x}_i = \Delta \mathbf{r}_i$, where $\Delta \mathbf{x_i} = \mathbf{x_i} - \mathbf{x_{i\text{-}1}}$ and $\Delta \mathbf{r_i} = \mathbf{R_i} - \mathbf{R_{i\text{-}1}}$ are the displacement and force increments, respectively. The equation for the stiffness using the Broyden formula is

$$\mathbf{K}_i = \mathbf{K}_{i-1} + \frac{\left(\Delta \mathbf{r}_i - \mathbf{K}_{i-1} \Delta \mathbf{x}_i\right) \Delta \mathbf{x}_i^T}{\Delta \mathbf{x}_i^T \Delta \mathbf{x}_i} \tag{5-3}$$

For systems with a large number of degrees-of-freedom, using a complete model of the system to conduct the response prediction is not efficient. Considering that the earthquake response of typical structures is dominated by a few lower modes, the mode superposition technique (based on the elastic mode shapes) is used to predict the response of larger systems.

The above formulation provides a simple and efficient method for model-based response prediction, which gives good predictions of the response even for systems with inelastic response. The next section describes the experiments conducted to validate the proposed approach.

5.3 Verification experiments

5.3.1 Structure with linear-elastic physical substructure

Real-time hybrid testing of a simple structural system under earthquake loads was conducted to verify the efficacy of the testing system and compensation strategy. The test structure consisted of a single-story, one-bay steel frame assumed to have a rigid floor beam (i.e., shear frame), as shown schematically in Figure 5.4.

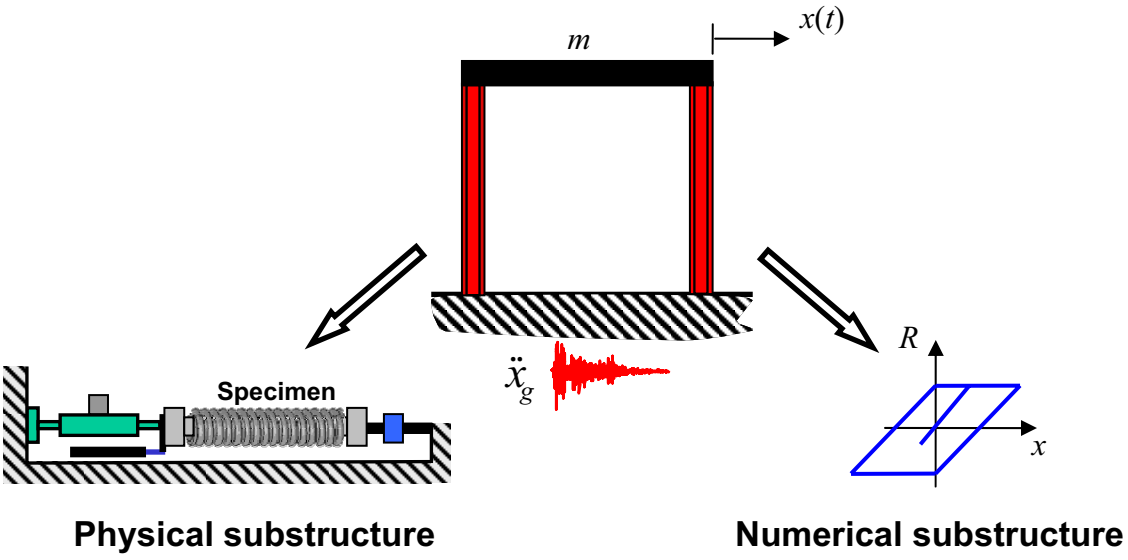

Figure 5.4: Structural model and substructures for hybrid experiment.

The structure was divided into two substructures: The left column is tested experimentally (physical substructure), while the right column is modeled numerically (numerical substructure). The columns have stiffnesses of 20.6 Kip/in (3.61 KN/mm) and 38.0 Kip/in (6.65 KN/mm) for the physical and numerical substructures, respectively. The force-displacement relationship corresponding to the numerical substructure is modeled using a bilinear hysteretic model with a yield displacement of 0.04 in (1 mm) and a ratio of post- to pre-yield stiffness of 0.02. Because the purpose of this experiment is to verify the testing system and methodology, instead of using an actual steel cantilever column as the physical substructure, an alternative small-scale specimen was used. The specimen used was the steel compression spring described previously (Section 4.4.1 and Figure 4.9). The spring has a stiffness of 234 lb/in (41.0 N/mm); therefore, a force scaling factor of 88.0 is used (to match the stiffness of the full-scale column). The linear elastic behavior of the spring specimen allows repeatable test results that can be compared against the theoretical expected response, providing an assessment of the effectiveness of the proposed approach.

The dynamics of the actuator and the resulting time-lag of the actuator are critical parameters in real-time hybrid testing. The actuator frequency response function (with the spring specimen attached) from the commanded displacement to the measured displacement was experimentally determined and presented in the previous chapter. The bandwidth of the system (assuming a cutoff frequency of -3dB) was determined to be 28.7 Hz. Within this bandwidth, the phase of the system is nearly linear. From this slope, the time lag of the actuator is approximated as a time delay of 12.4 msec. The approximation of the transfer function as a pure time delay is shown in Figure 5.5. As can be observed, the approximation is accurate in the low-frequency range (up to approximately 10 to 13 Hz for the magnitude, and 28 Hz for the phase).

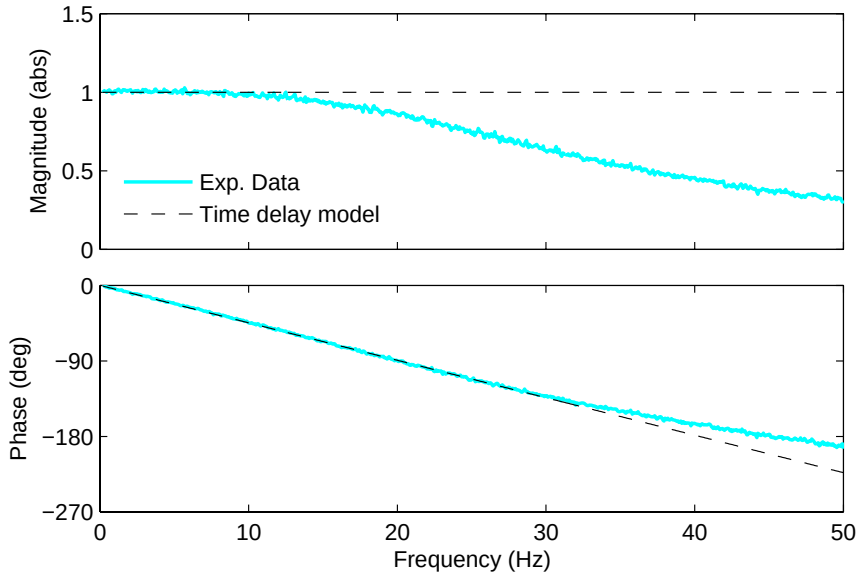

Figure 5.5: Transfer function from command displacement to measured displacement.

Several real-time hybrid tests were conducted by changing the fundamental frequency of the test structure. During each experiment, the mass of the structure was adjusted accordingly to obtain the desired natural frequency. Modal damping was assumed to be 2% of critical damping. The structure was subjected to the artificial earthquake record shown in Figure 5.6 (which was used for the MOST experiment; Spencer et al., 2004). The Central Difference Method (CDM) was used for integration of the equation of motion with a time step, $\Delta t = 0.0062$ sec, which corresponds to half of the time delay, (i.e., $T_d = 2\Delta t$). This time step was adequate to accurately integrate the equation of motion for all of the natural frequencies considered in the experiments (0.5 to 15 Hz). The stability criterion for the CDM was easily satisfied with this time step.

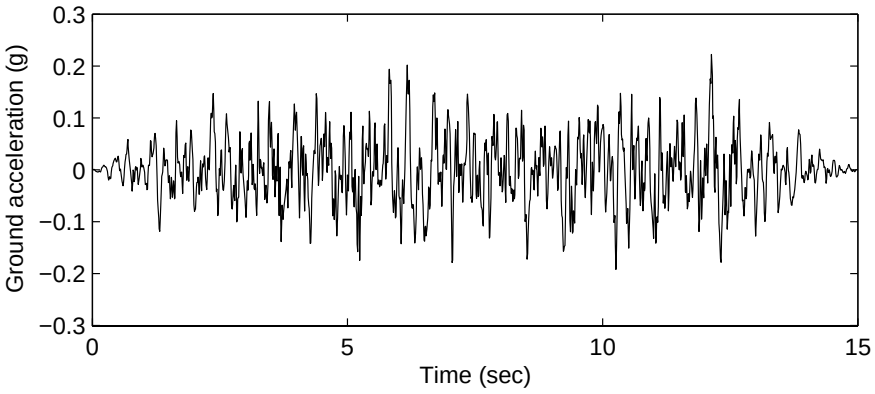

Figure 5.6: Input ground acceleration.

For the initial set of experiments, the structure was assumed to be linear–elastic; therefore the ratio of post- to pre-yield stiffness in the numerical substructure was set to

1.0. Tests corresponding to natural frequencies of the test structure of 0.5, 1, 5, 6, 7, 8, 10, 13, and 15 Hz were conducted. The amplitude of the ground acceleration was scaled so that the maximum displacement (calculated using an analytical model) was about 0.2 in (5.08 mm). For each natural frequency, tests were conducted using (a) no delay compensation, (b) proposed model-based compensation, and (c) third-order polynomial extrapolation. To evaluate the accuracy of the tests results, the analytical response was calculated using a numerical model of the test structure with the experimentally measured stiffness of the test specimen. Figure 5.7 shows the experimental results for the structure with a 1.0 Hz natural frequency. The duration of the earthquake record used is 15 sec; therefore, the additional 5 sec shown in the figure correspond to zeros padded at the end of the input record to observe the effect of the compensation methods on the free vibration response of the system. As can be seen, excellent agreement is obtained between the test results and the analytical solution for both compensation methods (polynomial extrapolation and model-based). The test without delay compensation results in a larger response than the exact analytical solution due to the effect of the negative damping introduced by the uncompensated phase lag from the actuator.

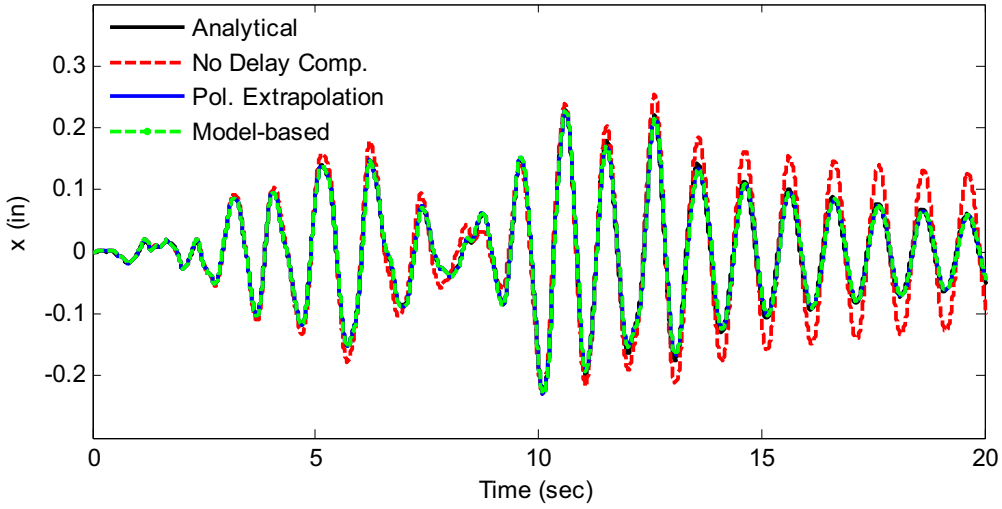

Figure 5.7: Test results for 1 Hz natural frequency.

The effect of the time delays on the real-time hybrid experiment and the performance of the delay compensation approach can be further analyzed using *x*-*y* plots of the response. The parameters considered are the *desired* displacement (calculated by solving the equation of motion), the *commanded* displacement sent to the controller (which includes the delay/lag compensation), the *measured* displacement (displacement actually applied by the actuator), and measured restoring force. Figure 5.8 (a) shows the measured force vs. desired displacement (i.e., response of the specimen, as seen by the numerical integration algorithm) for the case when no delay compensation is used. As observed, a counter-clockwise loop is obtained because of the uncompensated time delay/lag (which adds energy into the experiment), instead of the straight line corresponding to the linear response of the spring specimen. The results for the case when model-based delay compensation is used are presented in Figure 5.9. Figure 5.9 (a)

shows the measured force vs. the desired displacement; as observed, because of the time delay compensation, the response is linear and accurate. Figure 5.9 (b) shows the effect of the time delay (a counter-clockwise loop in the force vs. commanded displacement response), which is cancelled by the delay compensation. Figure 5.9 (c) shows the performance of the delay compensation method by comparing the desired displacement with the measured displacement. The resulting response is effectively a straight line with a slope of one, which demonstrates the accuracy and efficiency of the delay compensation approach.

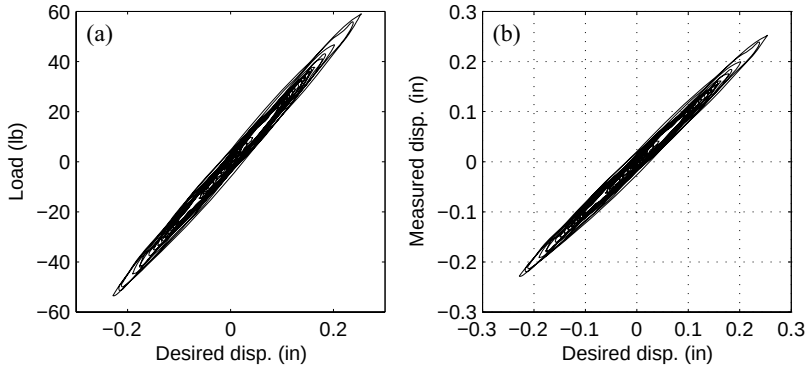

Figure 5.8: Test results for 1 Hz natural frequency (no delay compensation): (a) Force vs. desired displacement, (b) Measured displacement vs. desired displacement.

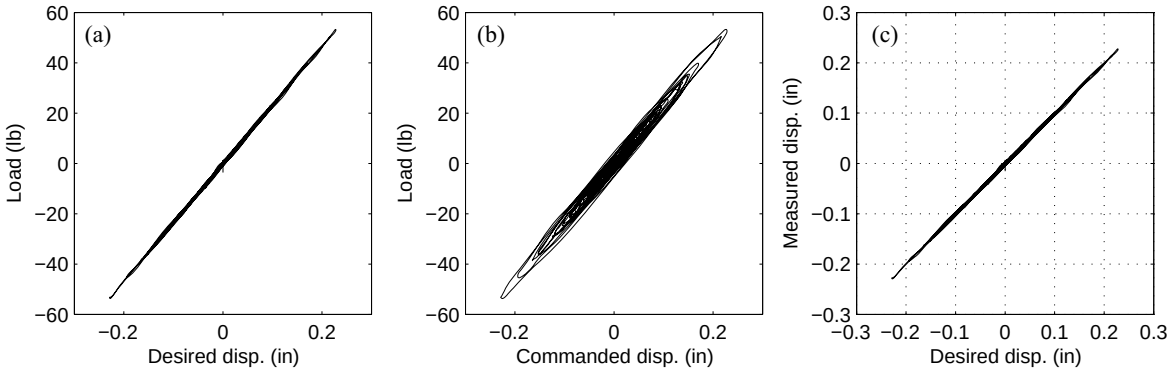

Figure 5.9: Test results for 1 Hz natural frequency (with model-based delay compensation): (a) Force vs. desired displacement, (b) Force vs. command displacement, (c) Measured displacement vs. desired displacement

To measure the error between the analytical and experimental results and allow comparison between the different compensation strategies, the RMS of the error normalized by the RMS of the analytical solution is used. Figure 5.10 shows the results for the tests conducted considering different natural frequencies of the test structure and using the different compensation strategies. For each delay compensation method, the highest natural frequency plotted corresponds to the highest natural frequency of the test structure that was tested prior to the experiment becoming unstable.

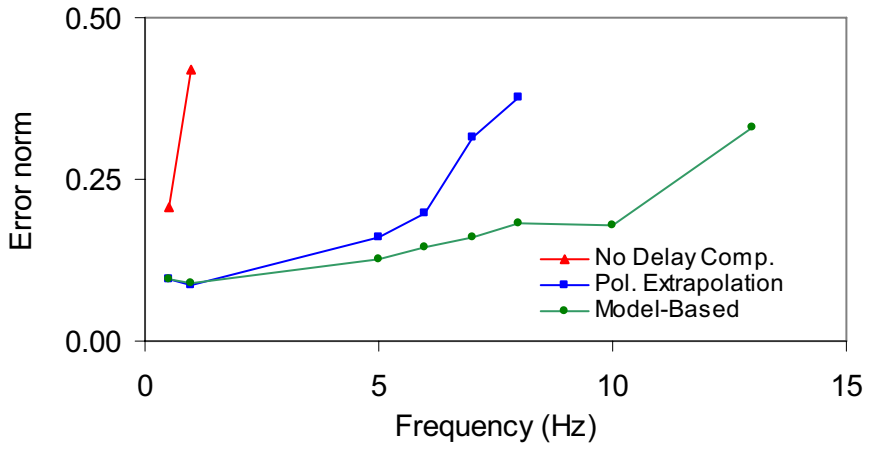

Figure 5.10: Test results using different delay compensation methods, linear case.

As observed, when no delay/lag compensation is used, the experiment becomes unstable even for relatively low frequencies of the structure. The theoretical stability limit corresponds to the frequency where the negative damping introduced by the actuator lag becomes equal to the inherent structural damping (1.46 Hz for the test structure considered). Using the proposed model-based compensation method, experiments with natural frequencies as high as 13 Hz were successfully conducted. The maximum frequency that was effectively tested using the polynomial extrapolation was 8 Hz. Figure 5.10 (a) shows that the error is small and, therefore, the tests are accurate for frequencies of about 5-6 Hz for the polynomial extrapolation and up to 10 Hz for the model-based delay compensation method. Figure 5.11 shows the results for the test corresponding to a natural frequency of 10 Hz using model-based delay compensation; results are seen to match well with the analytical solution.

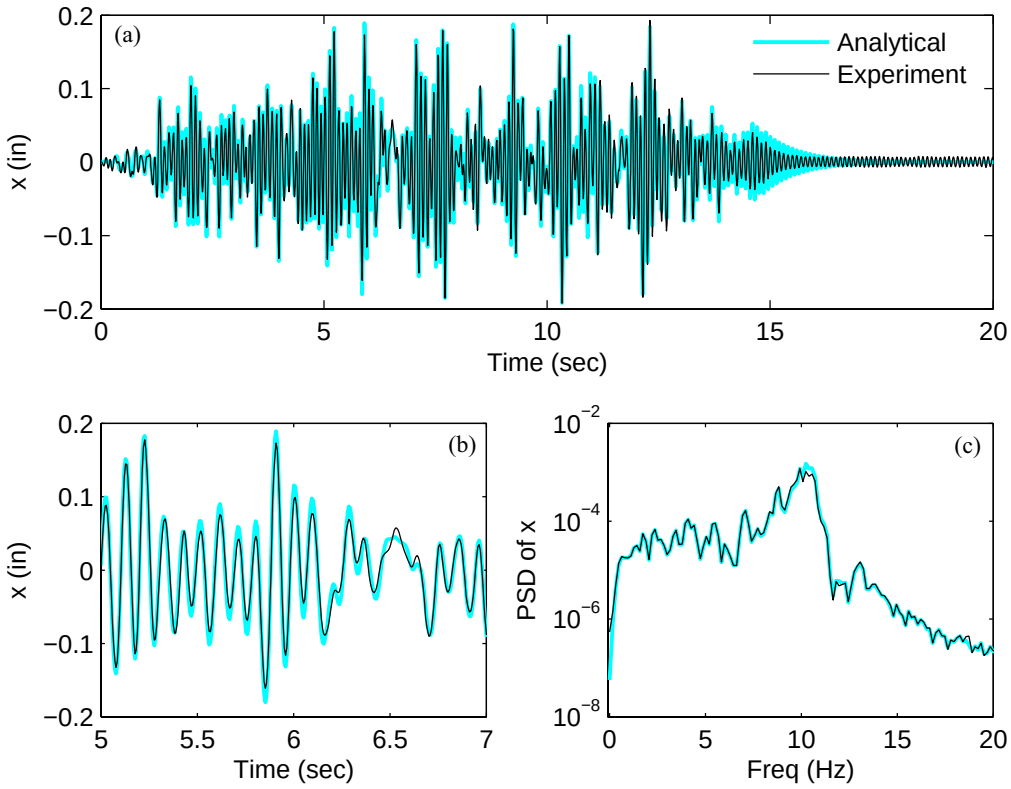

Figure 5.11: Test results for 10 Hz natural frequency using model-based compensation: (a) Displacement response, (b) Displacement response (close up view), (c) Power spectrum of displacement.

The maximum natural frequencies for which the experiment was stable using both delay compensation methods are smaller than theoretically predicted. Possible causes are: the effect of experimental errors present in the hybrid experiment, which are more severe at higher frequencies; differences in the estimated actuator time delay and the actual phase lag; the fact that the time lag is close, but not exactly, a constant time delay; and the effect of the roll-off in the magnitude of the actuator transfer function (e.g., at a frequency of 15 Hz, the magnitude is 0.94, causing an undershoot error, which adds energy to the system and results in a negative damping that can led to system instability, Mahin et al., 1989).

To evaluate the performance of the delay compensation methods for nonlinear structures, tests were conducted considering a structure with inelastic response (numerical substructure with a bilinear force-displacement relationship). Tests corresponding to natural frequencies of the structure of 0.5, 5, 10, 13, and 15 Hz were performed using both delay compensation methods. For the model-based compensation method, the initial elastic stiffness was used for the approximation of the restoring force in Equation (5-2). The ratio between the maximum and yield displacement (i.e., displacement ductility) was about 4.0. The error norms for the test results are shown on Figure 5.13. As can be seen, the trends are similar to the linear case; however, the

maximum frequencies that were achieved are slightly larger (10 Hz for the polynomial extrapolation and 15 Hz for model-based compensation). This greater stability is due to the damping introduced by the energy dissipated during inelastic deformation.

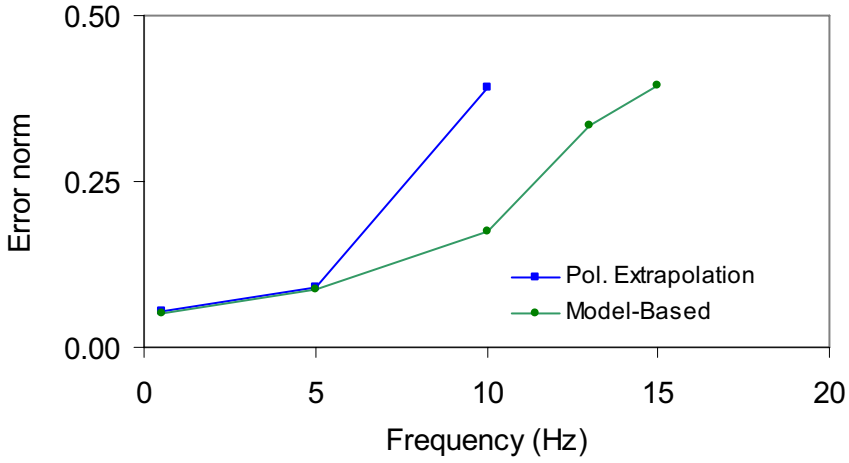

Figure 5.12: Test results using different delay compensation methods, nonlinear case.

5.3.2 Structure with MR damper

The use of magnetorheological (MR) dampers as supplemental damping devices for reducing the response of civil engineering structures under severe earthquakes and winds is becoming increasingly accepted (Spencer & Nagarajaiah, 2003). MR dampers can be used as semiactive control devices, offering the reliability of passive devices, yet maintaining the versatility and adaptability of fully active systems. Some of the attractive features of MR dampers include: very low power requirements (allowing operation under battery power), the ability to provide a readily controllable damping force, large achievable force capacity, and low sensitivity to temperature changes (Spencer et al., 1997). The second application considered in this study consists of a building structure with an MR damper used as a supplementary energy dissipation device. The specimen used is the small-scale RD-1005 MR fluid damper described previously (Section 4.4.2 and Figure 4.11).

Characterization of MR Damper

A model that represents the behavior of the MR damper is necessary to calculate the expected response of the test structure and, therefore, allow comparison with the results from the real-time hybrid experiment. A series of simple tests were conducted to measure the response of the damper and provide the necessary data to characterize/model its behavior. The MR damper (with 0 V input voltage) was subjected to sinusoidal displacement excitations of 0.2 in (5.08 mm) and 0.4 in (10.16 mm) amplitude with frequencies of 0.637, 1.273, and 2 Hz. Figure 5.13 shows the response of the MR damper for the tests corresponding to 0.4 in (10.16 mm) amplitude. As observed the response of the damper is rate-dependent and nonlinear.

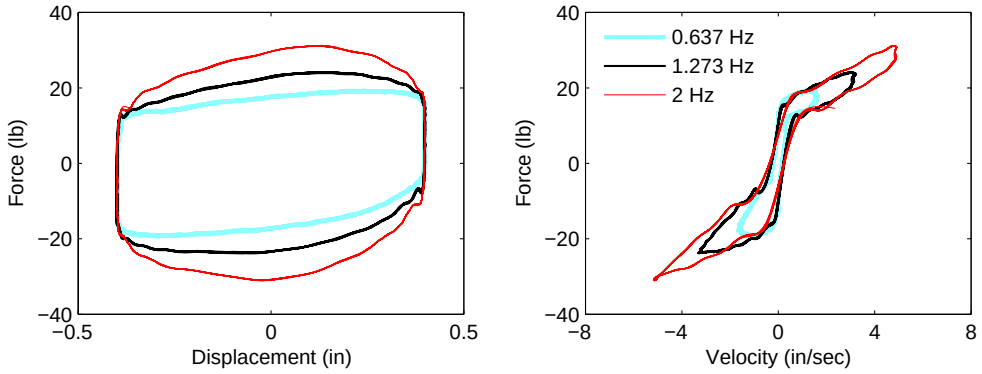

Figure 5.13: Response of MR damper for test with 0.4 in amplitude sinusoidal displacement.

A simple model that can be used to represent the behavior of MR dampers (and ER dampers) is based on the Bingham viscoplastic model. The model can be idealized using mechanical elements, e.g., a viscous damper and a Coulomb friction element placed in parallel (Stanway et al., 1987; Spencer et al., 1997). For the data obtained from the tests conducted in this study, a better fit can be obtained by adding a stiffness term to the model. The model is represented schematically in Figure 5.14; the force produced by the damper, F_D, is given by

$$F_D = f_c \,\mathrm{sgn}(\dot{x}) + c\dot{x} + kx + f_o \tag{5-4}$$

where f_c is the frictional force, c is the damping coefficient, k is the stiffness coefficient, and f_o is the offset in force. The parameters for the model were determined to fit the entire set of data using nonlinear least-squares parameter estimation, which yielded the following results: f_c = 8.94 lb (39.8 N), c = 4.57 lb-s/in (0.801 N-sec/mm), f_o = 0.336 lb (1.49 N), and k = 12.2 lb/in (2.14 N/mm). Figure 5.15 shows a comparison between the response of the damper measured experimentally and that predicted by the model for the test corresponding to a frequency of 1.273 Hz and an amplitude of 0.4 in (10.16 mm) (similar results were obtained for the other tests using these parameters). As observed, except for the response at velocities near zero, the behavior of the damper is reasonably well represented by the model.

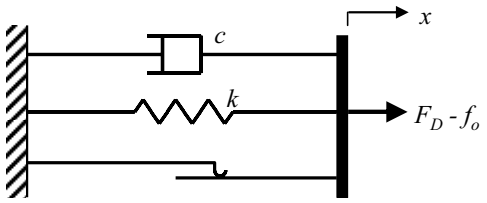

Figure 5.14: Model for MR damper.

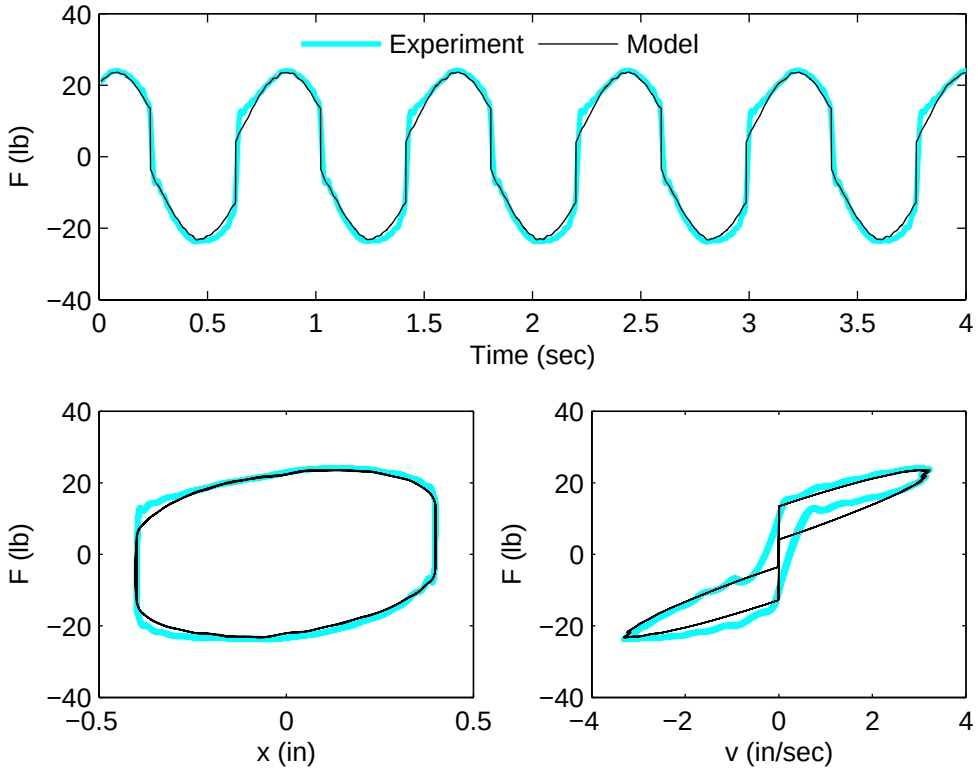

Figure 5.15: Comparison between experimentally measured damper force and predicted by model for 1.273 Hz frequency test with 0.4 in (10.16 mm) amplitude.

Real-time hybrid experiment

Because MR dampers, as most semiactive control devices, are rate-dependent (and highly nonlinear), real-time hybrid testing is required to accurately test structural systems that incorporate such devices. The test structure for this example is a one-story, one-bay, steel shear frame with an installed MR damper, as shown schematically in Figure 5.16. The structure is identical to the one used in the previous example, with the exception of the added MR damper. To conduct the real-time hybrid experiment, the structure was divided into two substructures: the MR damper was tested experimentally (physical substructure), while the rest of the structure was tested numerically (numerical substructure), see Figure 5.16.

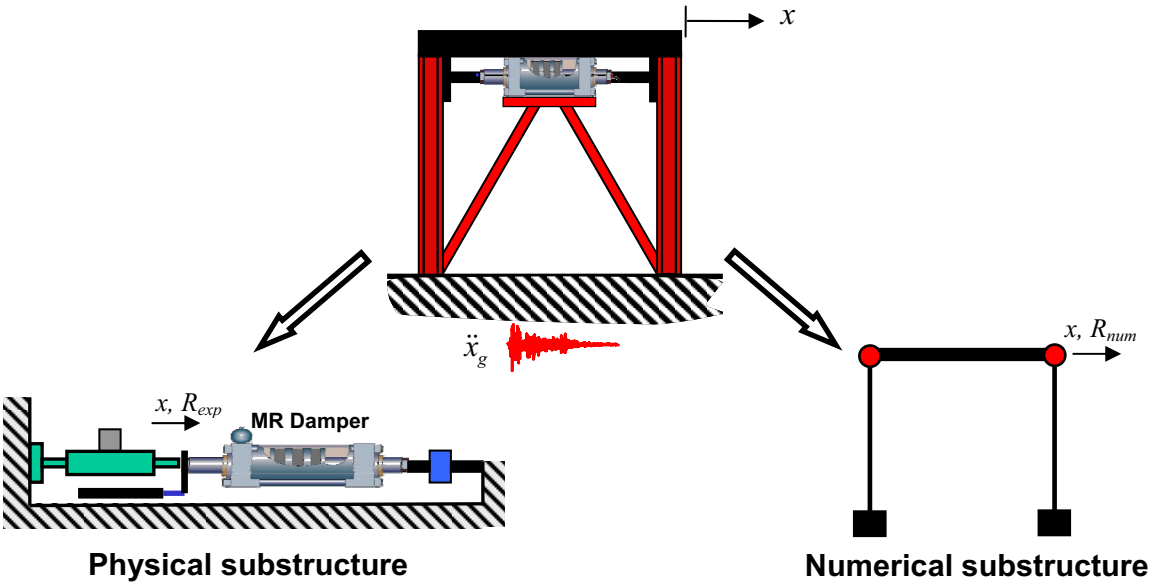

Figure 5.16: Structure with MR damper: structural model and substructures for real-time hybrid test.

The stiffness of the test structure, structural damping, earthquake record, and numerical integration method were the same as in the previous example. Delay compensation was performed using the proposed model-based approach. The amplitude of the ground acceleration was scaled so that the maximum displacement was about 5.08 mm (0.2 in). Because the specimen is small-scale, a force scaling factor of 100 was used to represent the behavior of a full-scale damper (Yang et al., 2002). Input voltage for the damper was set to 0 V throughout the experiment; therefore, the MR damper was used as a passive energy dissipation device.

Because the force generated by the MR damper is rate dependent, it is important to impose accurately not only the displacement but also the velocity. Preliminary experiments conducted on the MR damper using sinusoidal input displacements showed that a sampling time of 0.001 sec allows both the displacement and velocity to be accurately imposed (see Section 4.6). Therefore, a time step of 0.001 sec was selected for numerical integration in this real-time hybrid experiment.

Experiments were conducted for natural frequencies of the test structure of 0.5, 1.0, and 2.0 Hz. The behavior of the numerical substructure (i.e., steel frame) was assumed to remain in the linear range and, therefore, the ratio of the post- to pre-yield stiffness in the numerical substructure was set to 1.0. Figure 5.17 shows a comparison between the results from the real-time hybrid experiments as well as the analytically predicted responses for the three cases considered. As observed, very good agreement is achieved between the experimental results and the analytical solution. Small discrepancies can be attributed to experimental errors and differences between the actual damper response and the model used to characterize its behavior. Figure 5.17 also shows the analytical response of the structure without the damper; as observed here, the damper

significantly reduces the response of the structure (the maximum displacement for the case with the damper is, in general, about half of the corresponding one without the damper).

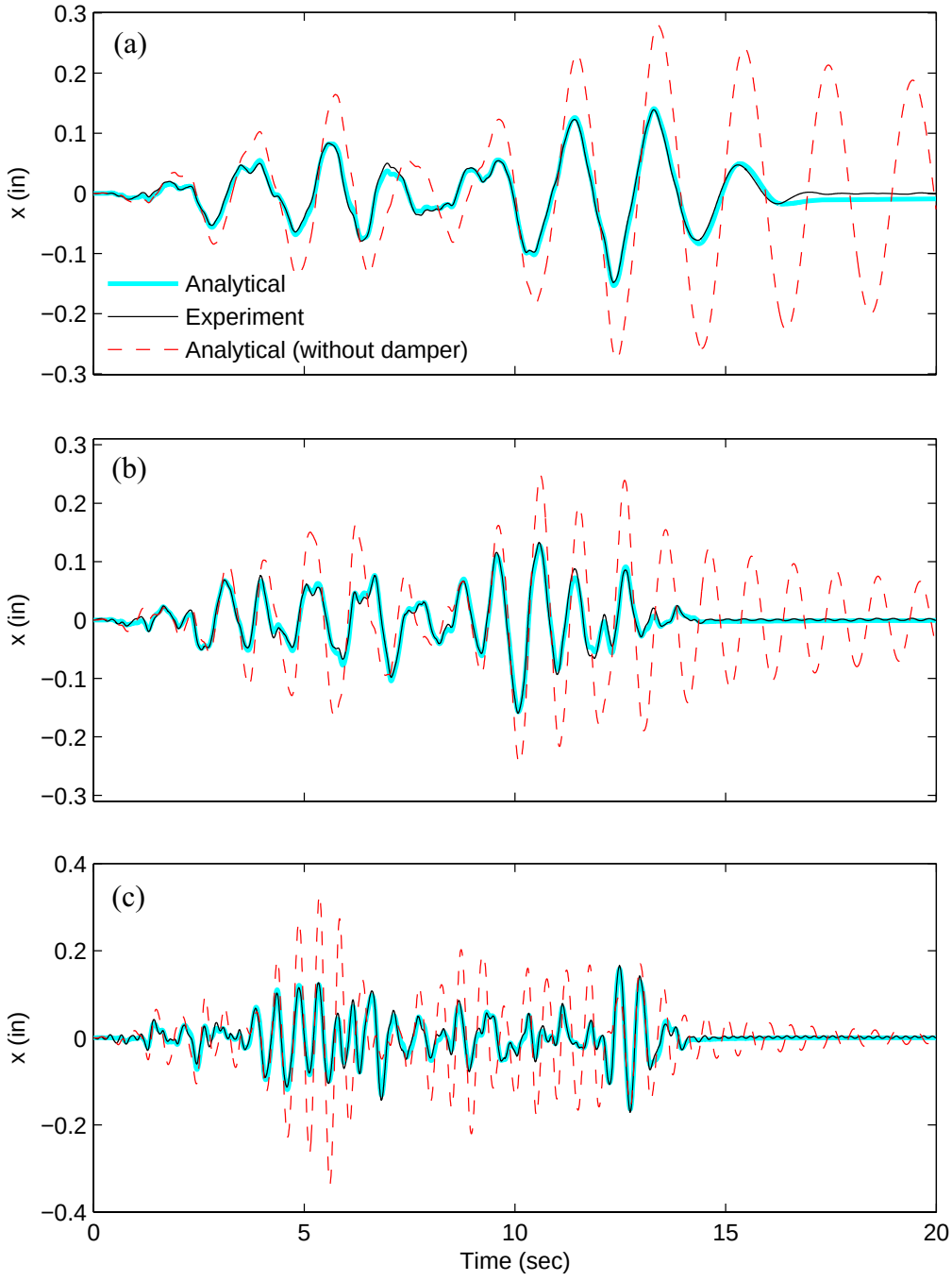

Figure 5.17: Results from real-time hybrid experiment: (a) 0.5 Hz structure, (b) 1.0 Hz structure, (c) 2.0 Hz structure.

5.4 Summary

An approach for real-time hybrid testing has been presented in which time delay/lag compensation is implemented using model-based response prediction. Two sets of verification experiments were conducted. Experimental results from the first example demonstrate that the proposed approach performs well for structures exhibiting both elastic and inelastic response. Model-based compensation allowed testing systems with natural frequencies as high as 13 Hz for linear response and 15 Hz for inelastic response, which corresponds to a relatively large bandwidth for hybrid testing. The model-based compensation method allows accurately testing of systems with natural frequencies about twice as large as the traditionally-used polynomial extrapolation method. However, the computationally cost is somewhat larger for the model-based approach. Experimental results from the second example (structure with the MR damper) verify that the approach and testing system presented are capable of accurately testing rate-dependent devices.

CHAPTER 6

MODELING OF ACTUATOR DYNAMICS

Numerical simulation can be a useful technique to understand the behavior of testing systems and their influence on hybrid experiments. This chapter analyses the effects of the dynamics of the testing system (e.g., actuator dynamics) on experiments conducted using the real-time hybrid testing technique. Initially, a model of the entire dynamic testing system (including servo-hydraulic actuator, controller, and test specimen) is presented. The model of the testing system is then used to develop a complete numerical representation of the real-time hybrid experiment. Figure 6.1 shows a schematic block diagram of the real-time hybrid experiment with the components of the testing system. The resulting model allows "virtual" experiments to be conducted in a similar way as the actual experiment, providing an efficient and safe method to investigate the performance and stability of the system, compensation strategies, and the influence of the different system parameters.

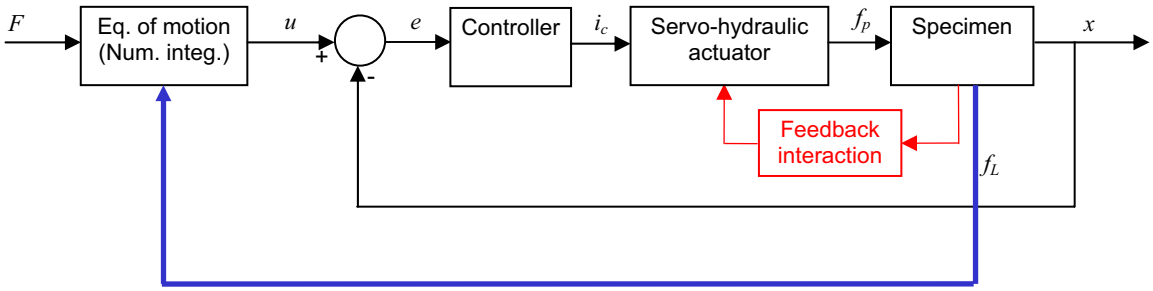

Figure 6.1: Schematic block diagram of the components of a hybrid experiment.

6.1 Model of dynamic testing system

This section presents a model of the entire dynamic testing system. The model includes mathematical representations of the different components of the testing system, including the servo-hydraulic actuator, the controller, and the test specimen. Initially, the equations for modeling of the different components of the system are introduced. Because some of the equations are nonlinear, a linear version of the model is obtained by linearizing the equations with respect to an operating point. The resulting linear model allows use of techniques for linear systems such as Laplace transforms and frequency response methods to understand the system behavior.

6.1.1 Test specimen

Typically, real-time hybrid testing is conducted using the substructuring technique, with the physical specimen corresponding to a critical component of the structural system being analyzed. In this section, the physical specimen is modeled as a linear elastic single-degree-of-freedom system, with mass (m), damping (c), and stiffness (k). The specimen, therefore, has its own dynamic characteristics, which can be described using the following equation of motion:

$$m\ddot{x} + c\dot{x} + kx = f_L \tag{6-1}$$

where f_L is the force applied to the specimen by the actuator. The specimen transfer function, G_{xf}, is obtained by taking the Laplace transform of Equation (6-1), and is given by the following equation:

$$G_{xf}(s) = \frac{1}{ms^2 + cs + k} \tag{6-2}$$

where s is the Laplace variable.

6.1.2 Servo hydraulic actuator

Testing systems intended for the assessment of structural components typically use hydraulic actuators to impose the loads (or displacements) on the test specimens. Hydraulic actuators can generate large forces and apply them within a relatively large frequency bandwidth.

The servo hydraulic actuator is composed of two main components: a servovalve and a hydraulic actuator. The servovalve responds to an electrical input signal and controls the movement of oil to and from the actuator chambers. The oil flow produces a pressure drop between the two chambers which generates a force that causes the actuator piston to move and apply a force to the test specimen. The servo-hydraulic actuator is one of the key components in a hybrid simulation; therefore, to understand its behavior is critical. This section provides a detailed description of the components and operation of the servovalve and hydraulic actuator, as well as the mathematical models that describe their behavior.

Servovalve

The servovalve connects the electronic and mechanical parts of the system. While there are many different types of servovalves, the following description (MOOG 1965, technical publication) corresponds to a two-stage servovalve similar to the one used in the testing system described in this study.

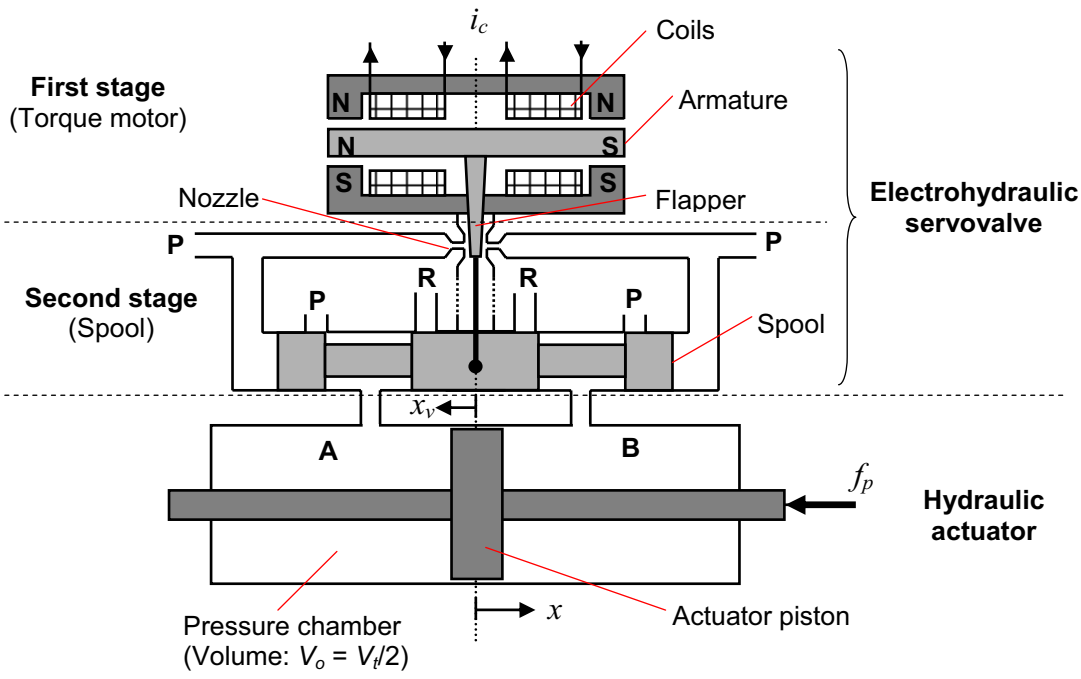

Figure 6.2: Detail of servovalve/actuator system.

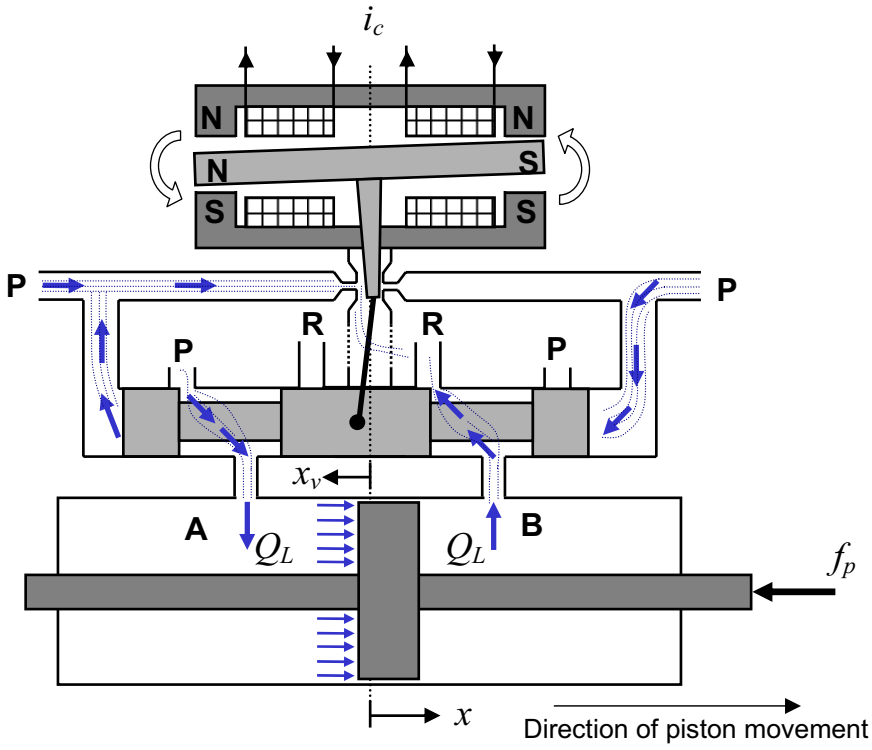

Figure 6.3: System responding to an input.

Figure 6.2 shows the main components of a two-stage electrohydraulic servovalve and hydraulic actuator, while Figure 6.3 shows the system responding to an input signal. The servovalve receives an electrical command signal that is applied to the torque motor coils and creates a torque on the armature, causing a deflection of the armature/flapper assembly. The flapper closes the right nozzle and diverts flow to the other end of spool, producing a displacement of the spool to the right. Movement of the spool opens flow paths between the pressure and return (P and R ports), and the two control ports (A and B), allowing oil to flow to and from the actuator chambers. The spool motion also applies a force to the cantilever spring, creating a restoring torque on the armature/flapper assembly. Once the restoring torque becomes equal to the torque from the magnetic forces, the armature/flapper assembly moves back to the neutral position, and the spool remains in this equilibrium position until a new command signal is received. In addition to this mechanical feedback, external feedback is necessary to control the actuator through the servovalve.

Servovalve dynamics

Servovalves are relatively complex devices that exhibit high-order, nonlinear responses (Poley 2005). Each of the components of the servovalve has some dynamics; for example, torque motor dynamics (from input voltage or current to armature/flapper rotation) and spool valve dynamics (from armature/flapper rotation to spool position). Merritt (1967) presented detailed linear models of the dynamics of each of these components, resulting in a quite complex eighth-order servovalve transfer function. The difficulty with explicit transfer functions for servovalves is that many design factors, as well as operational and environmental variables, produce significant differences in the actual dynamic response under operating conditions (MOOG, 1965). Additionally, not all factors contribute significantly to the servovalve response. Because information about the required parameters is rarely available, simplified models are typically used. In general, the dynamic response of a servovalve is much faster than the other elements of the testing system; therefore, these simplified models of servovalve dynamics are generally satisfactory. An alternative way of modeling the servovalve dynamics is to use an assumed model with certain dynamics. Different models have been used. For example, a pure time delay (Conte & Trombetti, 2000), a second order model (Williams et al., 2001; Zhao et al., 2003; Jung & Shing, 2006), or when the dynamics of the servovalve are much faster than the other elements, a simple lag can generally yield satisfactory results (Merritt, 1967). Typically, a first-order transfer function usually produces good approximations throughout the frequency range, to about 50 Hz (MOOG, 1965). For servovalve responses to frequencies up to the 90^{o} phase lag point, a second-order transfer function is better suited (MOOG, 1965). For low frequencies, the servovalve dynamics have also been approximated by a constant (Merritt, 1967; Dyke et al., 1995; Zhao et al., 2003), as given by:

$$x_v = k_v \, i_c \tag{6-3}$$

or in the Laplace domain as:

$$G_v(s) = \frac{x_v(s)}{i_c(s)} = k_v \tag{6-4}$$

where x_v is the valve (spool) displacement from the neutral position, i_c is the electrical command signal to the servovalve, and k_v is the valve gain. For a first-order model, the servovalve transfer function is given by:

$$G_v(s) = \frac{k_v}{1 + \tau_v s} \tag{6-5}$$

where τ_v is the servovalve time constant.

Figure 6.4 shows the typical frequency response (obtained from the manufacturer specifications) of a Schenck-Pegasus 132A two-stage servovalve, which is the servovalve used in this study. As observed, for frequencies less than approximately 10 Hz, the transfer function is close to a constant; for frequencies up to about 50 Hz, the transfer function can be well represented using a first-order system, and for frequencies larger than approximately 50 Hz, a higher-order model is needed. For the frequency range typically required for hybrid experiments (i.e., less than 50 Hz), the simple models given by the above equations (constant and first-order models) are considered adequate to represent the servovalve dynamics.

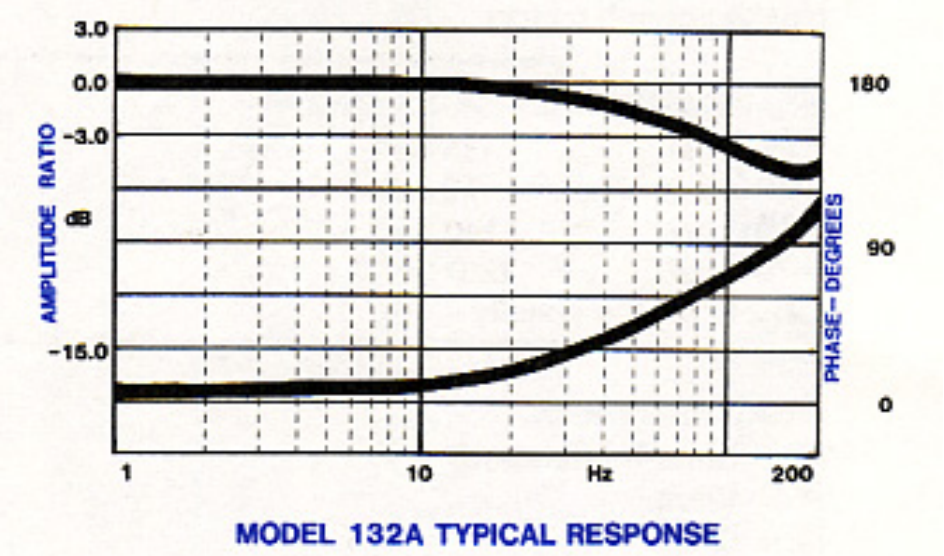

Figure 6.4: Servovalve frequency response (illustration courtesy of Schenck Pegasus).

Flow equation of servovalve

The flow characteristics of the servovalve (i.e., the relationship between spool displacement, controlled flow, and pressure drop across the load) are given by the following general flow equation (Merritt, 1967):

$$Q_L = C_d w x_v \sqrt{\frac{1}{\rho}\left(P_s - \frac{x_v}{|x_v|} p_L \right)} \tag{6-6}$$

where p_L is the pressure drop across the load (i.e., difference in pressure between the two actuator chambers), Q_L is the controlled flow through the load, x_v is the valve (spool) displacement from the neutral position, P_s is the system supply pressure, w is the opening or area gradient of the valve orifices (rate of change of orifice area with spool displacement), C_d is the coefficient of discharge of the valve orifices, and ρ is the fluid density. This equation is a complete description of the steady-state performance of the valve, and its plot is known as the *pressure-flow curves* of the valve (Merritt, 1967). The equation assumes that the return pressure is negligible, as it is typically much smaller than the other pressure values in the equation. The nonlinear flow equation can be linearized with respect to an operating point producing the following linearized flow equation:

$$Q_L = K_q' x_v - K_c' p_L \tag{6-7}$$

where K'_q is the valve flow gain and K'_c is the valve flow-pressure gain. The operating point that is typically used to evaluate these valve coefficients is the origin (i.e., $Q_L = p_L = x_v = 0$), because the system typically operates near this region (Merritt, 1967); however, this point may vary depending on each application.

Hydraulic actuator

A hydraulic actuator converts the hydraulic energy into mechanical force or motion. The actuator used in the testing system described herein, is a double-ended linear actuator. In double-ended actuators, the pressure is applied to both sides of the piston (see Figure 6.2); therefore, these types of actuators are capable of controlling movement in both directions with equal force and speed (Poley, 2005). The actuator consists of a rod and central piston, and incorporates low-friction seals fitted to the piston at each of the cylinder end caps to minimize leakage. Control ports at the ends of the actuator allow hydraulic fluid to flow in and out of the actuator chambers. The position of the piston is determined by the hydraulic fluid pressures in the chambers on either side of the piston and may be adjusted by forcing fluid into one control port (e.g., port A), while allowing it to escape from the other (e.g., port B). This movement of fluid causes an increase in fluid pressure in one chamber (e.g., A) and a decrease in pressure in the other chamber (e.g., B). The net pressure difference exerts a force on the active area of the piston, causing the piston to move (e.g., movement to the right, as shown in Figure 6.3). The position of the piston is, therefore, adjusted by controlling the differential oil flow between the two actuator control ports (Poley, 2005).

The fundamental equations that govern the behavior of a hydraulic actuator are the continuity equation and the equilibrium or force balance. The continuity equation is given by the following relationship (Merritt, 1967):

$$Q_L = A\,\dot{x} + C_l p_L + \frac{V_t}{4\beta_e}\dot{p}_L \tag{6-8}$$

which can be expressed in the Laplace domain as:

$$\frac{p_L(s)}{Q_L(s) - Asx(s)} = \frac{1}{C_l + \frac{V_t}{4\beta_e}s} \tag{6-9}$$

where Q_L is the controlled flow through the load, p_L is the pressure drop across the load, x is the displacement of the piston, A is the area of the piston, C_l is the total leakage coefficient of the piston, V_t is the total volume of fluid under compression in both actuator chambers, and β_e is the effective bulk modulus of the system (including oil, entrapped air, and mechanical compliance of the champers). The load flow, Q_L, has three components: the flow to displace the actuator (proportional to the piston position derivative), flow consumed by leakage (proportional to the pressure), and flow stored due to compressibility (proportional to the pressure derivative), also known as *compressibility flow* (Merritt, 1967). The force generated by the actuator piston, f_p, is given by the following equation:

$$f_p = A\,p_L\,. \tag{6-10}$$

The equilibrium of forces on the piston or force balance equation is obtained using Newton's second law,

$$f_p = m_t\ddot{x} + c_t\dot{x} + kx + F_s\,, \tag{6-11}$$

where m_t is the total mass of piston and load referred to piston (e.g., mass of specimen and attachments used to connect specimen to piston), c_t is the viscous damping coefficient for the piston and load, k is the stiffness of the load, and F_s is the force on the piston due to seal friction.

The actuator used in this study is equipped with low-friction Teflon seals; therefore, the friction force is assumed negligible. The transfer function of the specimen can be modified to include the additional mass and damping, resulting in the following expression that corresponds to the transfer function of the experimental component:

$$G'_{xf}(s) = \frac{x(s)}{f_p(s)} = \frac{1}{m_t s^2 + c_t s + k}\,. \tag{6-12}$$

The trapped volume of oil in both actuator chambers produces a hydraulic spring with stiffness:

$$K_h = \frac{4\beta_e A^2}{V_t}\,. \tag{6-13}$$

The interaction of this oil spring with the mass, m_t produces a hydraulic natural frequency, ω_h, which is given by the following equation:

$$\omega_h = \sqrt{\frac{4\beta_e A^2}{m_t V_t}}. \tag{6-14}$$

This hydraulic natural frequency is an important parameter because it determines the overall speed of response of the actuator (Merritt, 1967).

6.1.3 Servo controller

Hydraulic actuators are inherently unstable, therefore, some type of control (e.g., position, velocity, and/or force feedback) is needed to stabilize the system (Dyke et al., 1995). In pseudodynamic and hybrid testing, actuators are typically controlled using displacement feedback, where the commanded displacement, *u,* is compared against the measured displacement, *x,* obtained using a displacement transducer. The error signal, *e,* is then defined as the difference between the command and measured displacements:

$$e = u - x. \tag{6-15}$$

One of the most common and well-known closed-loop control algorithms is the *Proportional-Integral-Derivative* (*PID*) where the control law is given by the following equation:

$$i_c = K_{prop} e + K_{int} \int e dt + K_{der} \frac{de}{dt} \tag{6-16}$$

or expressed in the Laplace domain as:

$$i_c(s) = \left(K_{prop} + \frac{k_{int}}{s} + k_{der} s \right) e(s) \tag{6-17}$$

where i_c is the electrical command signal to the servovalve, and K_{prop}, K_{int}, and K_{der} are the proportional, integral, and derivative gains, respectively.

Proportional control reduces the error response to reference inputs or disturbances; however, it allows a nonzero, steady-state error to constant inputs. As the gain is increased, the steady-state error becomes smaller, but the overshoot of the system is increased. Furthermore, large values of the proportional gain almost always lead to instability; therefore, a limit is placed on the value of this gain in order to achieve a well-damped stable response (Franklin et al., 2002). *Integral control* improves the steady-state error properties. The integral gain, K_{int}, is used to reduce or eliminate steady-state errors without adding extremely high-proportional gains. However, these improvements are achieved typically at the cost of deterioration in the dynamic response (increased oscillatory behavior and reduced system stability). Integral control is typically used only in slow or quasi-static tests (e.g., conventional pseudodynamic testing). In practice, the

gain is set to zero for dynamic applications (e.g., real-time hybrid testing). *Derivative control* is introduced to improve the system's dynamic response. The derivative term usually increases the damping in the system, resulting in a reduced oscillatory behavior and improved stability (Franklin et al., 2002).

Most applications using position loops can be handled with a straight proportional controller. Therefore, only the proportional part of the controller is considered herein. The resulting control law is given by:

$$i_c = K_{prop}(u - x) \tag{6-18}$$

6.1.4 Combined model of testing system

The model of the servo-hydraulic testing system can be obtained by combining the mathematical models of the controller, servovalve (dynamic and flow characteristics), hydraulic actuator (continuity and force balance equations), and test specimen. Figure 6.5 shows a block diagram of the combined system with the linearized models for each component.

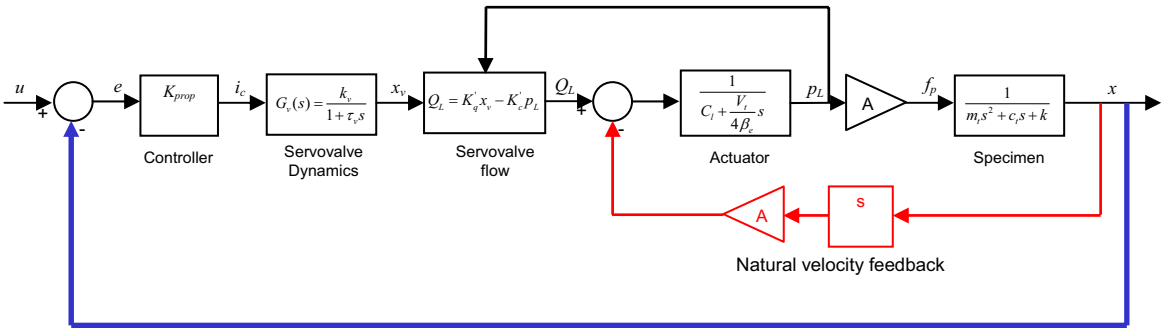

Figure 6.5: Block diagram of servo controlled hydraulic system.

Note the intrinsic interaction between the dynamics of the actuator and the experimental component (or test specimen), which is proportional to the velocity response of the actuator piston. Through this "natural" velocity feedback, the dynamics of the experimental component directly affect the response of the actuator (Dyke et al., 1995).

In real-time hybrid testing, the dynamic response of the testing system can be characterized by the transfer function, G_{xu}, from the command displacement (input) to the measured displacement (output). By combining the linear models of the different components of the testing system and using the expression for constant servovalve dynamics, the following expression is obtained after some algebraic manipulation:

$$G_{xu}(s) = \frac{K_{prop}\dfrac{K_q A}{K_c}}{\left(\dfrac{V_t}{4\beta_e K_c}m_t\right)s^3 + \left(m_t + \dfrac{V_t}{4\beta_e K_c}c_t\right)s^2 + \left(c_t + \dfrac{V_t}{4\beta_e K_c}k + \dfrac{A^2}{K_c}\right)s + \left(k + K_{prop}\dfrac{K_q A}{K_c}\right)} \tag{6-19}$$

where $K_q = K'_q \cdot K_v$ is the servovalve gain, and $K_c = K'_c + C_l$ is the total flow pressure coefficient. The resulting transfer function has three poles and no zeros. When a first-order model for the servovalve dynamics is used, the following expression is obtained

$$G_{xu}(s) = \frac{K_{prop}\dfrac{K_q A}{K_c}}{\left(\dfrac{V_t}{4\beta_e K_c}m_t\tau_v\right)s^4 + \left(\dfrac{V_t}{4\beta_e K_c}m_t + m_t\tau_v + \dfrac{V_t}{4\beta_e K_c}c_t\tau_v\right)s^3 + \left(m_t + \dfrac{V_t}{4\beta_e K_c}c_t + \dfrac{A^2}{K_c}\tau_v + c_t\tau_v + \dfrac{V_t}{4\beta_e K_c}k\tau_v\right)s^2 + \left(c_t + \dfrac{V_t}{4\beta_e K_c}k + \dfrac{A^2}{K_c} + k\tau_v\right)s + \left(k + K_{prop}\dfrac{K_q A}{K_c}\right)} \tag{6-20}$$

which has four poles and no zeros.

In cases where commanded forces are prescribed instead of displacements, for example Effective Force Testing (Dimig et al., 1999; Shield et al., 2001), the dynamics of the transfer function G_{fu} become critically important. This transfer function is given by

$$G_{fu}(s) = \frac{K_{prop}\dfrac{K_q A}{K_c}\left(m_t s^2 + c_t s + k\right)}{\left(\dfrac{V_t}{4\beta_e k_c}m_t\right)s^3 + \left(m_t + \dfrac{V_t}{4\beta_e K_c}c_t\right)s^2 + \left(c_t + \dfrac{V_t}{4\beta_e K_c}k + \dfrac{A^2}{K_c}\right)s + \left(k + K_{prop}\dfrac{K_q A}{k_c}\right)}. \tag{6-21}$$

Notice that the zeros of this transfer function correspond to the poles of the experimental component (or attached structure to the actuator). Therefore, actuators attached to lightly damped structures have a greatly limited ability to apply forces at the natural frequencies of the structure; and if the structure is undamped, the actuator will not be able to apply a force at its natural frequency (Dyke et al., 1995). Therefore, force control in dynamic applications is effective only when very accurate natural velocity feedback compensation is incorporated, which has proven to be challenging due to nonlinearities and uncertainties in the servo-system.

6.2 Experimental parameters

The previous section presented the equations for modeling a servo-hydraulic testing system. In this section, numerical models of the testing system and its parameters are estimated using experimental measurements of the dynamic behavior of the system.

In theory, the values of the parameters required for modeling of the testing system can be determined using data from the manufacturer, and experimental tests conducted to

determine individually the remaining parameters. See, for example, Zhao et al. (2006) and Williams et al. (2001). Although all of the information about the individual parameters may be available, models determined based on this data usually do not correlate well with the experimental response. The response of the system is highly dependent on the actual conditions during testing. For example, the effective oil bulk modulus can exhibit significant variations on its value, and the response of the system is, in general, quite sensitive to this parameter (Williams et al., 2001). Additionally, servo-controlled hydraulic actuators are very complex and nonlinear devices, therefore, the response, as approximated by a linear model, is valid only on a range close to the linearization conditions. Therefore, in order for the response from the models to match the experimental behavior, estimation based on the overall system response is, in general, required for some of the parameters.

In this study, two approaches are used for determining the numerical values of the parameters: (a) a frequency domain identification technique that allows obtaining accurate representations of the measured actuator transfer functions for different test specimens and testing conditions; and (b) a time domain identification that provides individual values of each parameter and, therefore, allows investigating their effect on the overall system response.

6.2.1 Frequency domain identification

Assuming linear behavior of the dynamics of the actuator and testing system, the transfer function, G_{xu}, from the command actuator displacement to the measured displacement can be determined. The approach used in this section to estimate the parameters for the actuator and testing system is as follows: First, the characteristics of the transfer function (i.e., number of zeros and poles) are determined based on the theoretical models developed in previous sections. Second, using an experimentally measured frequency response data, rational polynomial transfer function models of the system dynamics are identified. For this estimation, the software MFDID (Multiple-Input-Multiple-Output Structural System Frequency Domain Identification) is used (Kim et al., 2005).

The mathematical model of the testing system presented previously demonstrated that the dynamics of the testing system are dependent on the test specimen attached to the actuator (i.e., actuator-specimen interaction). The actuator transfer function for the case of the spring specimen was presented in Chapter 4. Using the same procedure (bandlimited white-noise excitation), the actuator transfer function was determined with the MR damper attached to the actuator. Figure 6.6 shows the resulting actuator transfer function for two extreme conditions of the MR damper, as well as for the spring specimen case. The actuator transfer function when the MR damper is OFF (i.e., 0V input voltage) is very similar to the transfer function with the spring specimen. The other extreme case, MR damper ON, corresponds to when a constant maximum input voltage is supplied to the MR damper (i.e., 5V input). For this case, the actuator transfer function is different than for the spring and MR damper OFF cases (and also not as smooth, due to

nonlinearities in the system introduced by the MR damper). Therefore, separate models are required for each case.

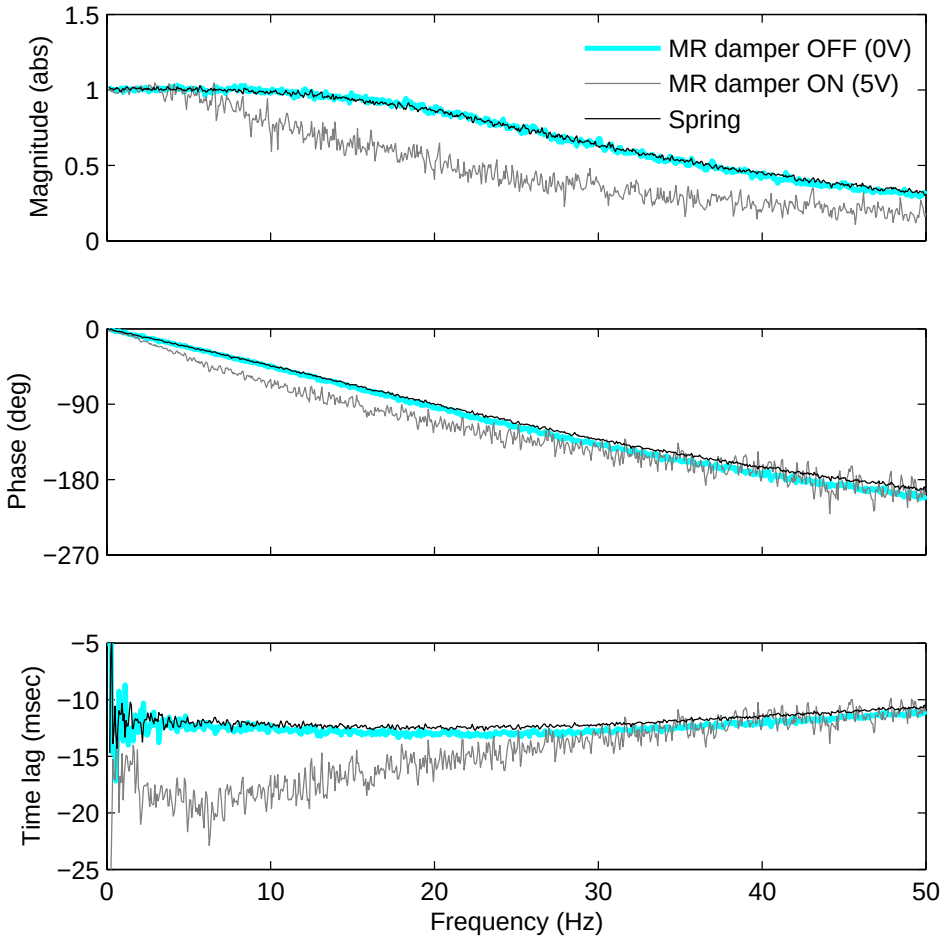

Figure 6.6: Actuator transfer function for spring and MR damper specimens.

For a linear elastic single-degree-of-freedom test specimen, the actuator transfer function has a third-order denominator (i.e., three poles) and a zero-order numerator (i.e., no zeros), when the expression for constant servovalve dynamics is used (see Equation 6-19). When the first-order model of servovalve dynamics is used, the actuator transfer function presents four poles and no zeros (see Equation 6-20). When a second-order model for the servovalve dynamics is used, the resulting actuator transfer function presents five poles and no zeros. Using the measured frequency response function of the actuator with the spring specimen, the software MFDID was used to estimate the poles (and, therefore, the polynomial coefficients) for the third-, fourth-, and fifth-order models. The resulting models are given by the following transfer functions, respectively:

$$G_{xu}(s) = \frac{6.12e6}{s^3 + 384s^2 + 73770s + 6.12e6} \tag{6-22}$$

$$G_{xu}(s) = \frac{4.10e9}{s^4 + 584s^3 + 2.68e5s^2 + 4.70e7s + 4.10e9} \tag{6-23}$$

$$G_{xu}(s) = \frac{3.40e12}{s^5 + 878s^4 + 5.79e5s^3 + 2.26e8s^2 + 4.04e10s + 3.37e12}. \tag{6-24}$$

Figure 6.7 shows the location of the poles of the models in the *s*-plane. Lines of constant damping ratio and natural frequency (i.e., *s*-grid) are also shown in the plot. As observed from the plot, even though an independent fit was used for each model, the dominant complex poles from the three models are located relatively closely.

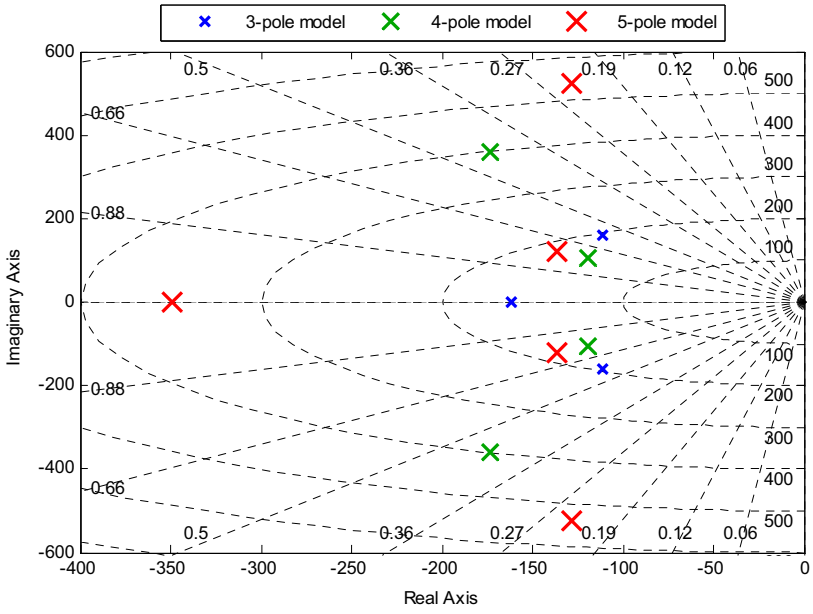

Figure 6.7: Pole location for different models of actuator dynamics.

Figure 6.8, 6.9, and 6.10 compare the frequency response functions of the models with the experimentally measured data. As can be observed, the three-pole model provides a good fit up to about 25 Hz. After this frequency, the magnitude and the time lag start to deviate from the measured data. The model with four poles provides a good fit for magnitude and phase within the 50 Hz frequency range, however, the time lag from the model deviates from the measured data, especially in the low frequency range, from 0 to about 20 Hz. The five-pole model provides an excellent match in terms of magnitude, phase, and time lag throughout the measured frequency range. Furthermore, comparison of this model with measured data in the frequency range 0 to 100 Hz, shows that this model provides a very good fit up to about 70 Hz.

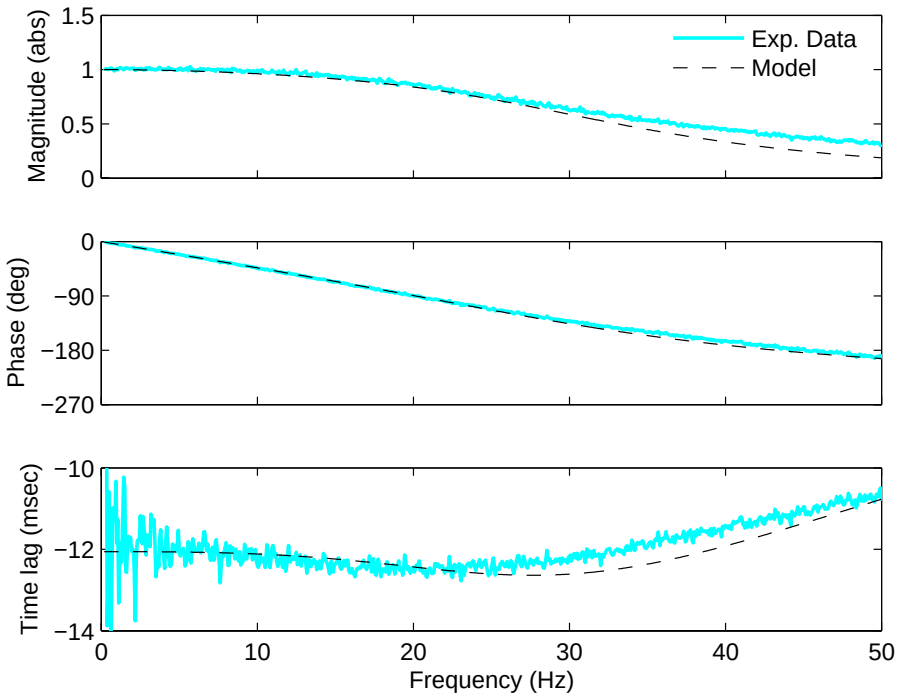

Figure 6.8: Three-pole model.

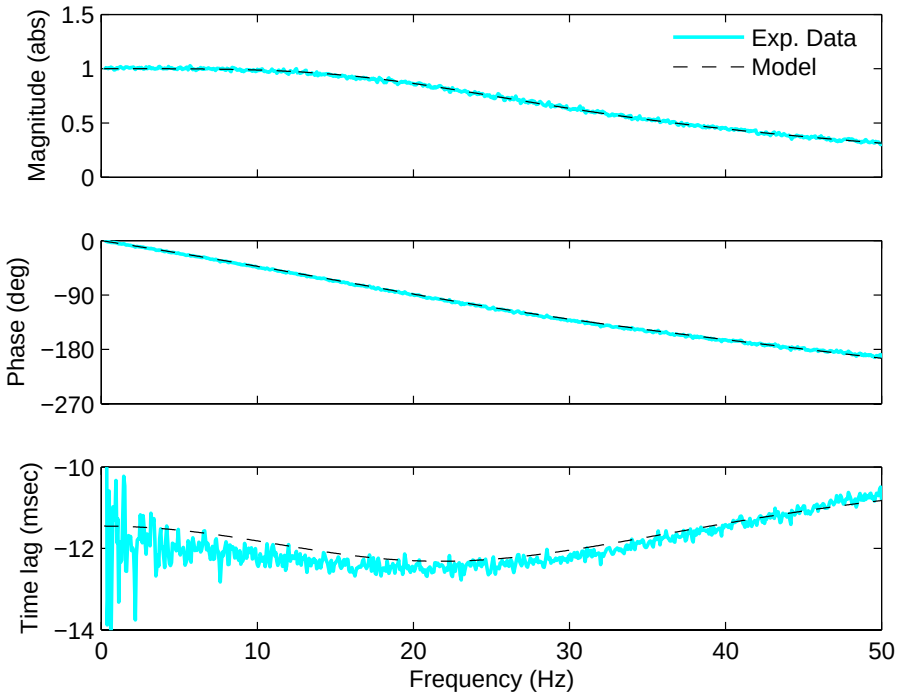

Figure 6.9: Four-pole model.

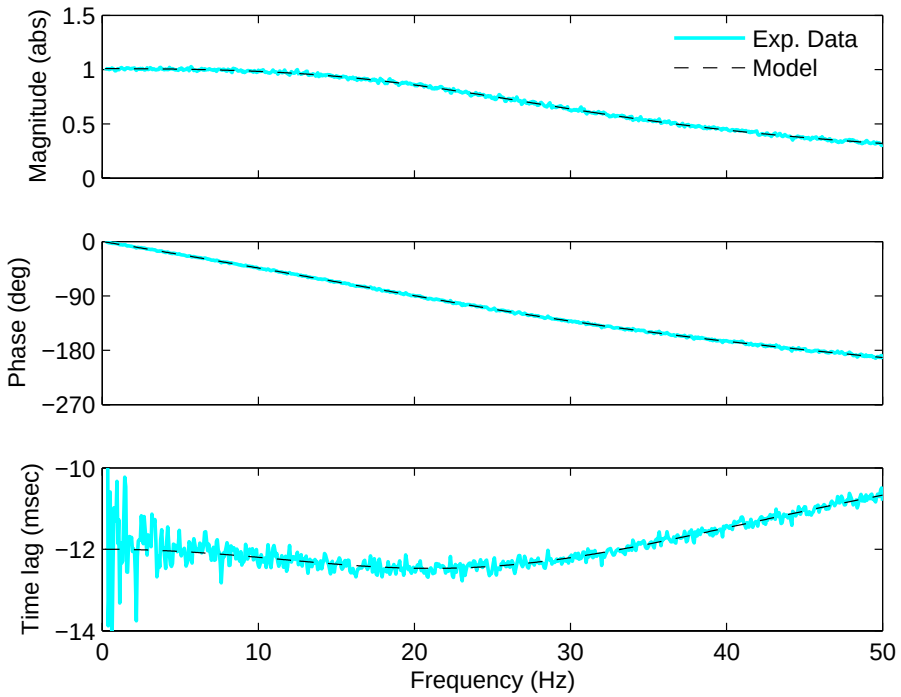

Figure 6.10: Five-pole model.

Actuator transfer function for system with MR damper

The actuator transfer function when the MR damper is OFF (i.e., 0V input voltage) was very similar to the transfer function with the spring specimen; therefore, the models developed for that specimen are also used for the MR damper OFF case. However, for the other extreme case (MR damper ON), the actuator transfer function was different than for the spring and MR damper OFF cases. Using a similar procedure as for the spring specimen, models of different orders were obtained for this damper condition. The fourth-order model was found to give a good representation of the actuator dynamics throughout the measured frequency range. The transfer function of this model is

$$G_{xu}(s) = \frac{1.478e9}{s^4 + 430s^3 + 1.780e5s^2 + 2.846e7s + 1.478e9}. \qquad (6\text{-}25)$$

The two sets of complex poles of the model are located at -108±26.2i (natural frequency 17.7 Hz and damping 0.972) and at -107±328i (natural frequency 54.9 Hz and damping 0.31), respectively. Figure 6.11 shows a comparison of the frequency response of the model with the experimentally measured data. As can be seen, the four-pole model provides a very good fit of the actuator transfer function.

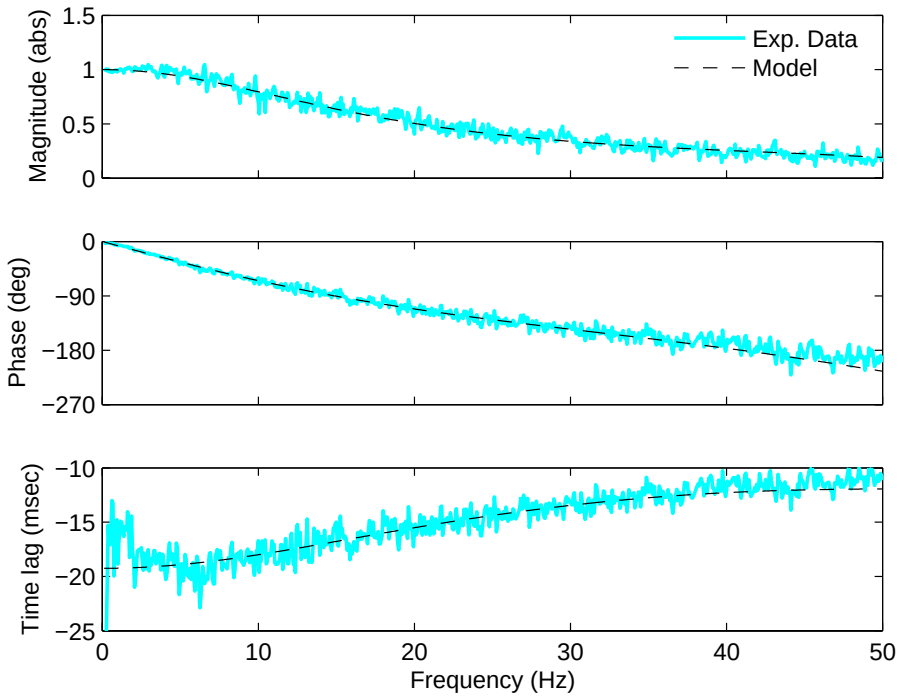

Figure 6.11: Actuator transfer function with MR damper ON.

Using the software MFDID, rational polynomial transfer function models of the actuator transfer function have been identified for the spring and MR damper cases. Comparison with the experimentally measured frequency response data shows that excellent fits throughout the 0 – 50 Hz range are obtained using: a fifth-order model for the spring specimen (and MR damper OFF), and a fourth-order model for the MR damper ON case.

6.2.2 Time domain identification

Although the models of actuator dynamics presented in the previous section provide a very good representation of the dynamic response of the testing system, they do not provide information about the system's individual parameters. In this section, the individual parameters of the system are determined using measured data in the time domain. The resulting model allows analyzing the effect of the different parameters on the dynamic response of the system. Figure 6.12 shows a SIMULINK implementation of the dynamical model of the testing system. The servovalve dynamics in this model have been represented using the first order model (i.e., Equation 6-5).

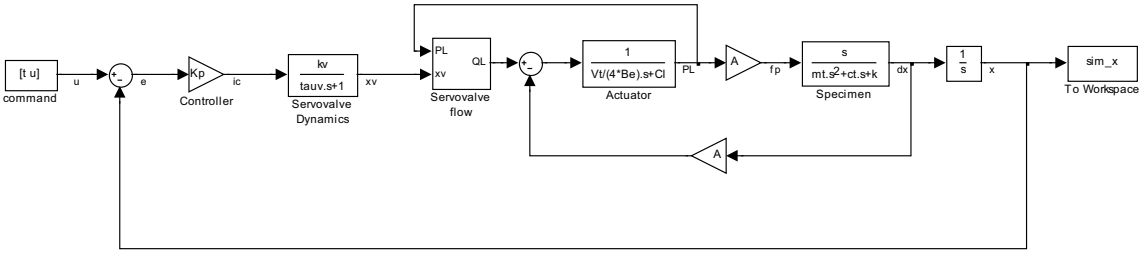

Figure 6.12: SIMULINNK model of the testing system.

The approach for determining the individual parameters was the following: First, an initial estimate of the parameters was obtained using different sources depending on the parameter, e.g., system settings for K_{prop}, physical measurements for A, V_t, k, and m_t, manufacturer's technical data for τ_v, and K_q, and values published in the literature for β_e. Second, a constrained, nonlinear least-squares parameter estimation was conducted using MATLAB/SIMULINK. The allowable range for the different parameters was set, depending on the level of confidence in the initial estimates. Experimental data corresponding to the spring specimen were used for the estimation, which included sinusoidal and random excitation tests, and data generated using the measured system transfer function. The parameters resulting from this estimation are presented on Table 6.1. Figure 6.13 shows a comparison of the experimentally measured response to a sinusoidal input command (having an amplitude of 0.15 in and a frequency of 5 Hz), as well as the simulated response obtained using the model. As can be observed, the response from the model matches well with the measured response.

Table 6.1: System parameters

Component	Parameter	Value	Unit	Description
Controller	K_p	3.0	mA/in	proportional gain
Servovalve	τ_v	0.00332	s	servovalve time constant
	K_q	23.01	$in^3/s/mA$	valve gain
	K'_c	1.36e-05	$in^3/s/psi$	valve flow-pressure gain
Actuator	A	0.751	in^2	area of the piston
	C_l	5.89e-06	$in^3/s/psi$	leakage coefficient of the actuator
	V_t	48.66	in^3	total volume of fluid in actuator chambers
	β_e	95958	psi	effective oil bulk modulus
Experimental component	m_t	0.023	$lb\text{-}s^2/in$	total mass of piston and load referred to piston
	c_t	9.509	lb-s/in	viscous damping coefficient of actuator and load
	k	234.0	Lb/in	stiffness of the load

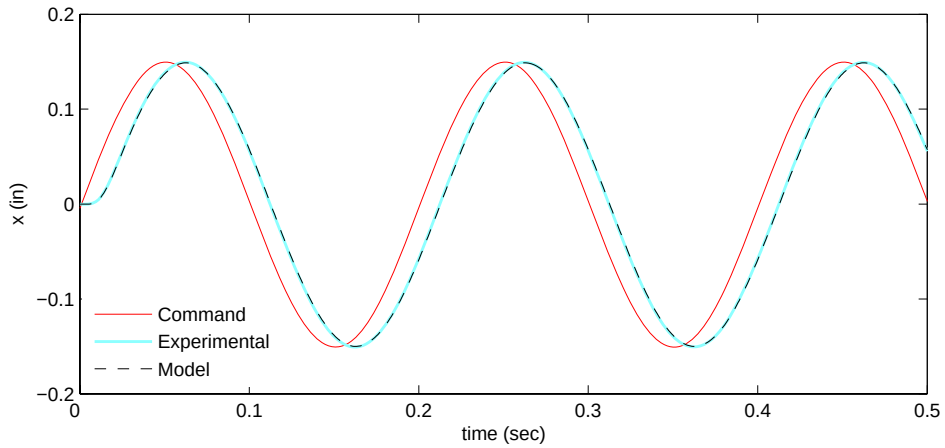

Figure 6.13: Comparison of measured and simulated responses.

The actuator transfer function, $G_{xu}(s)$, can be obtained using Equation (6-20) and the estimated values of the parameters, resulting in the following transfer function:

$$G_{xu}(s) = \frac{5.362\text{e}9}{s^4 + 715s^3 + 3.285\text{e}5\, s^2 + 6.145\text{e}7s + 5.362\text{e}9}. \qquad (6\text{-}26)$$

Figure 6.14 shows a comparison of the frequency response of the model with the experimentally measured data. As can be observed, the model matches reasonably well with the experimental data, and although there are some small discrepancies, the model is considered adequate for the purpose of analyzing the effect of the different parameters.

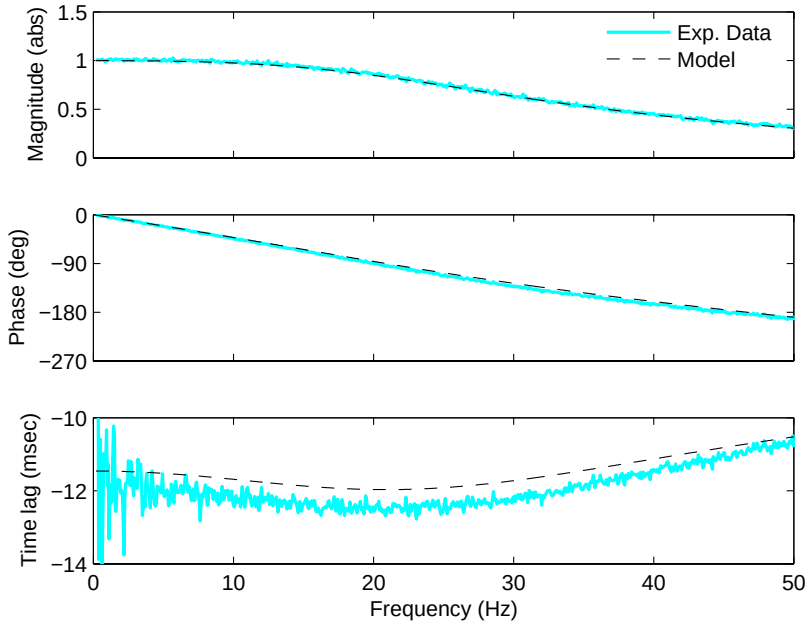

Figure 6.14: Frequency response from model and experimentally measured data.

6.3 Effect of parameters on actuator transfer function

The numerical model of the testing system developed in the previous section is used to investigate the effect of some of its parameters on the response of the actuator and testing system.

Effect of proportional gain

Initially, the effect of the proportional gain is investigated. Figure 6.15 shows the frequency response of the actuator transfer function for different values of the gain. As the proportional gain increases in size, the bandwidth of the system is also increased and the phase (and, therefore, the time lag) is reduced. From this plot, it may seem apparent that one would want the gain as large as possible; however, as mentioned previously, large values of this gain can make the system unstable. Figure 6.16 shows the root-locus of the system, where the locations of the closed-loop poles are given for different values of the proportional gain. From this plot, the maximum value of the gain for stability is determined to be K_{prop} = 11.7. As the proportional gain is increased, the oscillatory response and overshoot are also increased; therefore, to have a good response, the value of this gain must be set significantly smaller than the stability limit (e.g., K_{prop} = 3.0, as in the current configuration).

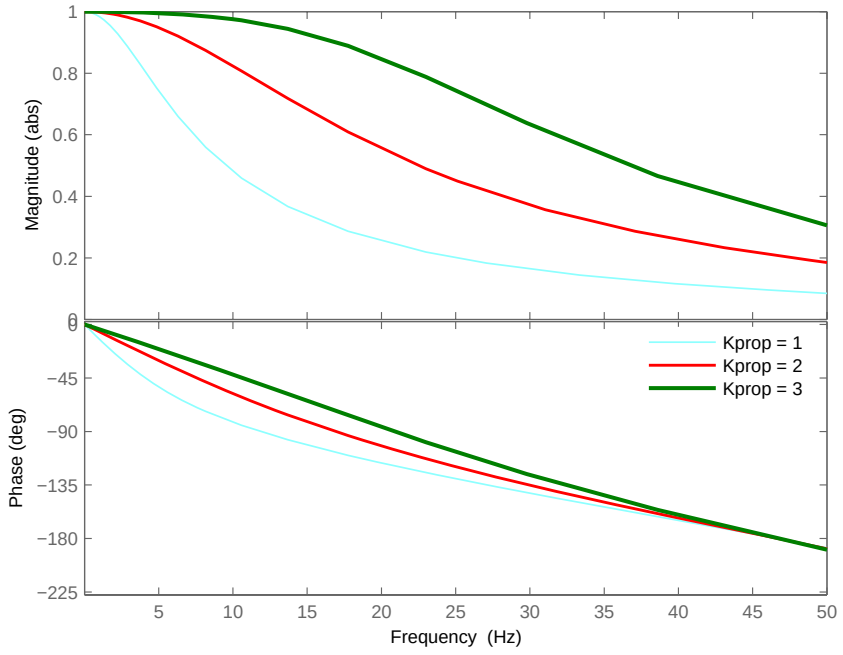

Figure 6.15: Bode plot of actuator transfer function, G_{xu} for different values of the proportional gain, K_{prop}.

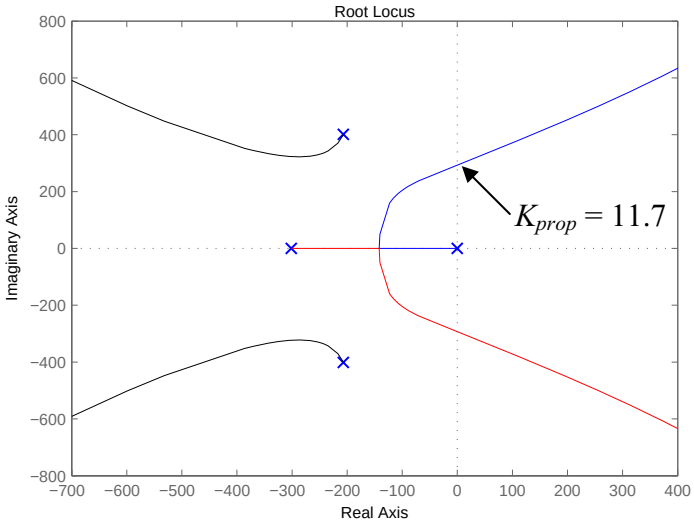

Figure 6.16: Root locus of the system with respect to the proportional gain, K_{prop}.

Effect of mass

The effective mass includes the mass of the actuator's piston, the specimen, and any moving attachments that may be used to connect the actuator to the specimen. Figure 6.17 shows the frequency response of the actuator transfer function for different values of the effective mass, where α_m represents the effective mass normalized with respect to the initially estimated value. For relatively small values of the total mass (e.g., α_m = 0.5 and 1.0), the variations have a small effect both in the magnitude and phase of the transfer function. However, as the effective mass becomes large (e.g., α_m = 3), the transfer function is significantly affected. The large peak observed in the magnitude is associated with the oil-column resonance that gets smaller as the total mass increases (see Equation 6-14), therefore, affecting more severely the low-frequency response.

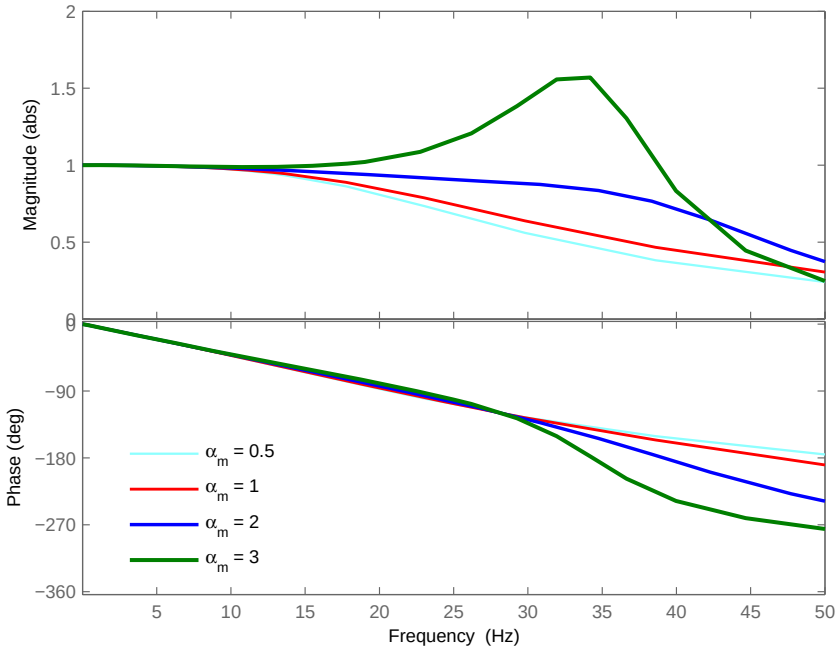

Figure 6.17: Bode plot of actuator transfer function, G_{xu}, for different values of total mass.

Effect of specimen stiffness

The stiffness of the test specimen can, in general, change during the experiment. Figure 6.18 shows the frequency response of the actuator transfer function for different values of the specimen stiffness, where α_k represents the ratio between the varied and initial values of the stiffness. When the stiffness is decreased 10 times (i.e., $\alpha_k = 0.1$), the transfer function does not change significantly, which is believed to be due to the fact that the forces imposed by the actuator during these two cases (i.e., $\alpha_k = 0.1$ and 1.0), are small compared to the capacity of the actuator. Therefore, the actuator behaves as if there was no load attached. However, when the stiffness of the specimen is increased by a factor of 10 (i.e., $\alpha_k = 10$), significant changes are observed, especially in the magnitude of the transfer function. The bandwidth is reduced (and the phase lag is slightly increased), i.e., the actuator gets slower and has more difficulty following the commanded displacement.

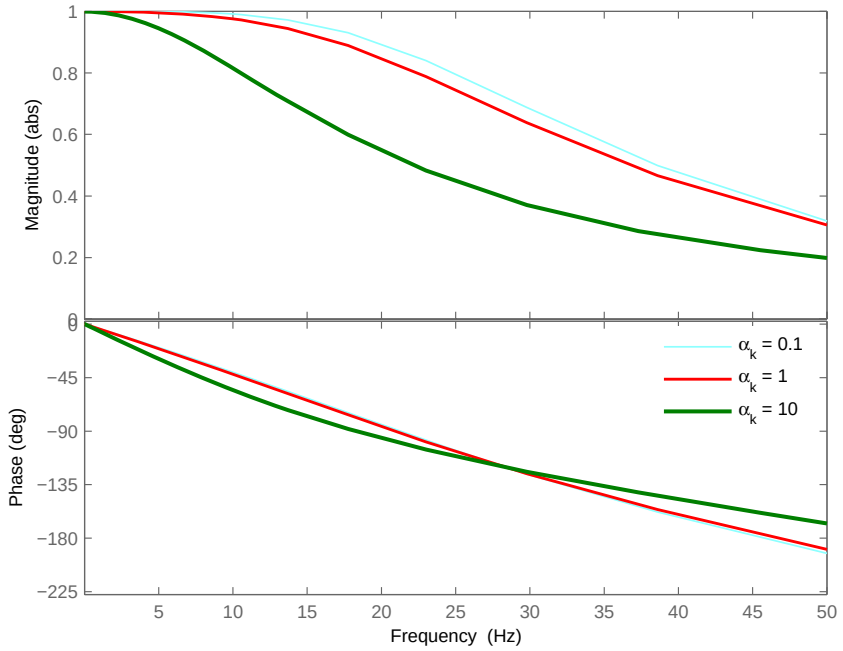

Figure 6.18: Bode plot of actuator transfer function, G_{xu}, for different values of specimen stiffness, k.

Summary

The analysis conducted provides insight into the effect of some important parameters of the testing system on its response. The proportional gain of the controller has a significant effect on both magnitude and phase. However, this gain is typically set prior to the experiments (through tuning of the actuator) and, in general, does not change during the experiment. The effective mass referred to the piston has a direct influence on the location of the hydraulic natural frequency, and if the mass becomes significant, the actuator transfer function is greatly modified. A similar effect is obtained when the hydraulic stiffness is low due to large volumes of oil in the actuator chambers, as in the case of long-stroke or large-capacity actuators. Variations on specimen stiffness were shown to have a small effect on the actuator transfer function when the loads applied by the actuator are small compared to its capacity. However, as the relative magnitude of applied force is increased, changes in the stiffness have a more substantial effect on the magnitude of the transfer function, with a smaller effect on the phase.

The analysis conducted by varying some important parameters on the testing system shows that, in general, the phase lag (and, therefore, the time lag), does not change significantly, except for the case of the proportional gain.

6.4 Simplified actuator transfer function

Under certain conditions, the actuator transfer function can be reasonably well approximated by a lower-order model. When the first-order servovalve model is used, the

complete actuator transfer function has four poles and no zeros (see Equation 6-20). This equation can also be expressed as

$$G_{xu}(s) = \frac{1}{\frac{A}{K_q K_{prop}}(1+\tau_v s)s + 1 + \frac{1}{K_{prop}}\frac{K_c}{K_q A}(1+\tau_v s)\left(1+\frac{V_t}{4\beta_e K_c}s\right)\frac{1}{G'_{xf}(s)}} \tag{6-27}$$

where $G'_{xf}(s)$ was defined in previous sections and represents the transfer function of the experimental component (i.e., the transfer function of the specimen modified to include the additional mass and damping from the actuator and attachments), see Equation (6-12). When the last term of the denominator of $G_{xu}(s)$ is small compared to the first two terms (and, therefore, can be neglected), the following approximation for the actuator transfer function is obtained:

$$G_{xu}(s) \approx \frac{1}{\tau_{xu}\tau_v s^2 + \tau_{xu} s + 1} \tag{6-28}$$

where τ_{xu} is defined as the actuator time constant and is given by

$$\tau_{xu} = \frac{A}{K_q K_{prop}}. \tag{6-29}$$

When the servovalve dynamics are modeled using a constant transfer function (i.e., τ_v = 0), the actuator transfer function can be further simplified as

$$G_{xu}(s) \approx \frac{1}{\tau_{xu} s + 1} \tag{6-30}$$

These simplified transfer functions are close to the actual actuator transfer function and, therefore, are considered accurate when: (a) the term $1/G'_{xf}(s)$ is small, i.e., at frequencies close to the natural frequency of the experimental component (this effect was also observed by Zhao et al., 2003); and (b) when the high-frequency dynamics in the actuator transfer function can be neglected (e.g., dynamics associated with oil-column resonance and actuator specimen interaction).

The parameters of the testing system and actuator estimated in the previous section (see Table 6.1) are used to illustrate the approximations of the actuator transfer function. The effective mass has been increased by a factor of 3 to highlight the effects of the oil-column resonance. Figure 6.19 shows a comparison of the first- and second-order approximations of the actuator transfer function (Equations 6-30 and 6-28, respectively). As observed, both approximations capture relatively well the low-frequency response in terms of both magnitude and phase. However, the accuracy of the approximations decreases as the frequency increases, and effects such as oil-column resonance (represented by the resonant peak on the *exact* transfer function at about 35 Hz), are not captured. Nevertheless, these approximations are practical for representing the low-

frequency response and are used in subsequent sections to derive simplified stability formulas.

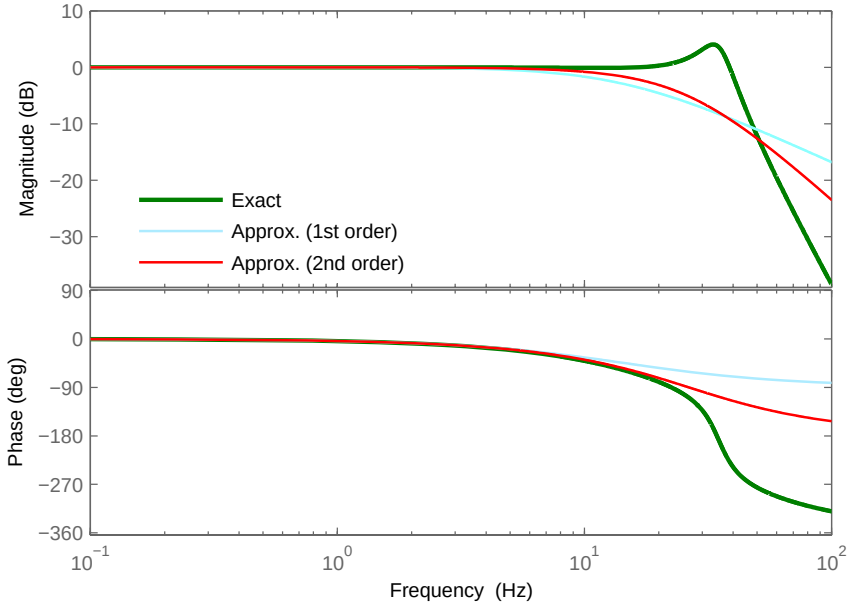

Figure 6.19: Simplified actuator transfer functions.

6.5 Modeling of real-time hybrid experiments

The dynamic model of the testing system presented in Section 6.1 is now used to develop a complete model of the real-time hybrid experiment. This model allows the investigation of the influence of various parameters, the stability characteristics of the experiment, and the development and evaluation of compensation strategies.

6.5.1 Model of the structural system

To understand the effects of the substructure real-time hybrid experiment on the calculated structural response, a linear, elastic, single-degree-of-freedom system is used as the test structure. Figure 6.20 shows a schematic of the entire structural system and substructures, where $d(t)$ is the displacement of the system, M is the mass, C is the damping, K is the stiffness, and $F(t)$ is the external force applied to the system. The subscripts, *num* and *exp*, are used to indicate properties corresponding to the numerical and experimental substructures, respectively. The system has a natural frequency, ω_n, and damping ratio, ξ, given by:

$$\omega_n = \sqrt{\frac{K_{exp} + K_{num}}{M}}, \qquad \xi = \frac{C_{exp} + C_{num}}{2\sqrt{M\left(K_{exp} + K_{num}\right)}} \tag{6-31}$$

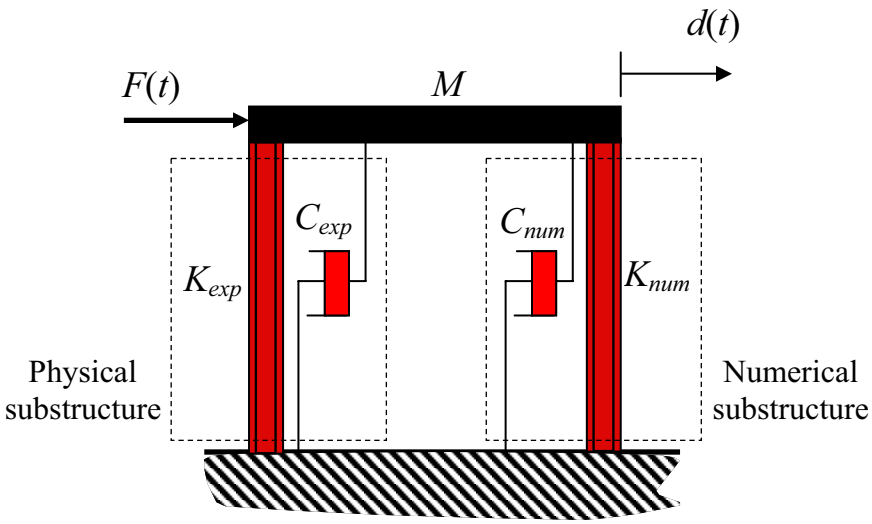

Figure 6.20: SDOF system for substructure real-time hybrid testing.

The stiffness and damping properties of the test specimen are denoted as k_{exp} and c_{exp}, respectively. Except for the case when a scaled version of the physical substructure is used as a test specimen, these properties are the same as the ones from the physical substructure. When using a scaled specimen, factors must be introduced to properly account for scaling effects. The two scaling factors that are needed in a hybrid simulation are the length scale factor, S_L, and the force scale factor, S_F. In both cases, the scaling factor represents the ratio between the variable in the prototype (i.e., full-scale) over the variable in the model (i.e., test specimen).

6.5.2 Exact response

The response of the system determined analytically (i.e., without using a hybrid simulation approach) is referred to herein as the *exact* response, and is determined by solving the equation of motion of the system, which is given by:

$$M\ddot{d} + \left(C_{num} + C_{exp}\right)\dot{d} + \left(K_{num} + K_{exp}\right)d = F\,. \tag{6-32}$$

The characteristics of the system response can be analyzed using the transfer function, $G_{dF}(s)$, from the external force applied to the system, (input) F, to the resulting displacement of the system, (output) d, see Figure 6.21. The *exact* transfer function of the system, determined from the equation of motion, is the following:

$$G_{dF}(s) = \frac{1}{Ms^2 + \left(C_{num} + C_{exp}\right)s + \left(K_{num} + K_{exp}\right)} \tag{6-33}$$

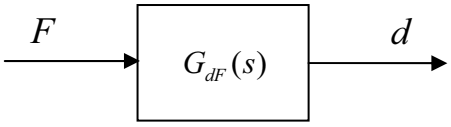

Figure 6.21: Input-output relationship for *exact* response.

6.5.3 Response from real-time hybrid test

To investigate the effect of the real-time hybrid experiment on the response of the test structure, the system transfer function is also calculated considering that the response of the structure is determined using the hybrid testing method. The effects of the hybrid simulation can then be analyzed by comparing this *experimental transfer function* with the exact one. Figure 6.22 shows the block diagram and signal flow of the real-time hybrid experiment. The calculated displacement, *d,* is scaled using the length scale factor, $1/S_L$, which results in the command displacement, *u,* to the controller; *x,* is the displacement imposed by the actuator to the specimen; f_L is the force to the load (i.e., force that the actuator piston applies to the specimen); and *R* is the restoring force which results from scaling the measured actuator force using the force scale factor, S_F.

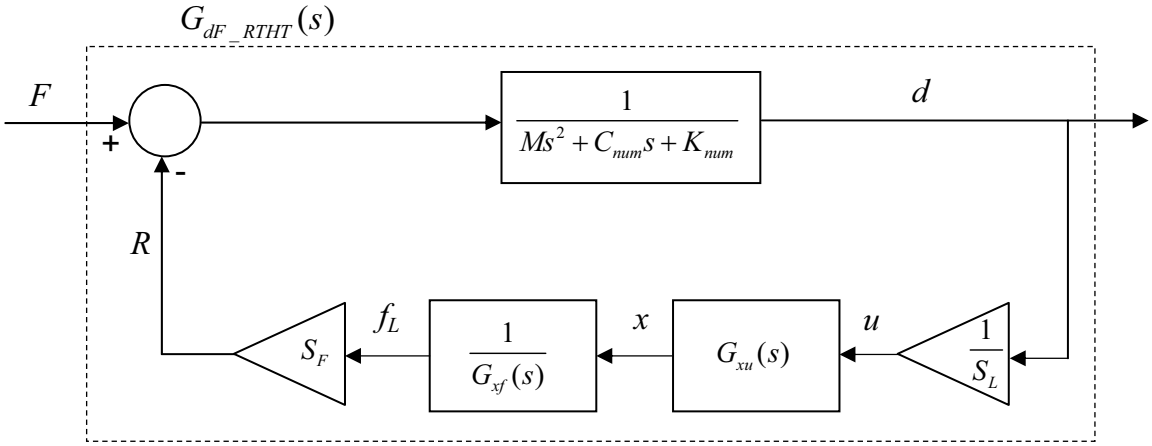

Figure 6.22: Block diagram of real-time hybrid experiment.

In a hybrid simulation, the restoring force, *R*, which, in general, is a function of the displacement and velocity, is obtained directly from the experiment. The equation of motion for the system is then given by:

$$M\ddot{d} + C_{num}\dot{d} + K_{num}d + R\left(d,\dot{d}\right) = F\,. \tag{6-34}$$

Because the physical substructure is assumed linear elastic, the restoring force can be expressed as:

$$R\left(d,\dot{d}\right) = K_{exp}d + C_{exp}\dot{d}\,. \tag{6-35}$$

The response of the system, expressed in the Laplace domain, is:

$$d(s) = \frac{1}{Ms^2 + C_{num}s + K_{num}}\left(F(s) - R(s)\right). \tag{6-36}$$

From the block diagram (Figure 6.22), the restoring force is given by

$$R(s) = \frac{S_F}{S_L}\frac{G_{xu}(s)}{G_{xf}(s)}d(s). \tag{6-37}$$

The *experimental* transfer function of the system (i.e., when the response is determined using the hybrid testing method), $G_{dF\_RTHT}(s)$, is given by:

$$G_{dF\_RTHT}(s) = \frac{1}{Ms^2 + C_{num}s + K_{num} + \frac{S_F}{S_L}\frac{G_{xu}(s)}{G_{xf}(s)}}. \tag{6-38}$$

The actuator transfer function, $G_{xu}(s)$, can be expressed in terms of its numerator and denominator polynomials, $n_{xu}(s)$ and $d_{xu}(s)$, respectively. Considering that the specimen transfer function is given by

$$G_{xf}(s) = \frac{1}{ms^2 + c_{exp}s + k_{exp}}, \tag{6-39}$$

the transfer function for the real-time hybrid experiment is

$$G_{dF\_RTHT}(s) = \frac{d_{xu}(s)}{\left(Ms^2 + C_{num}s + K_{num}\right)d_{xu}(s) + \frac{S_F}{S_L}n_{xu}(s)\left(ms^2 + c_{exp}s + k_{exp}\right)}. \tag{6-40}$$

In contrast to the *exact* transfer function of the system, which had two poles and no zeros (see Equation 6-33), in the closed-loop real-time hybrid simulation, the poles of the actuator transfer function become zeros of the system transfer function, and the number of poles is equal to the number of poles of the actuator transfer function plus two. The additional terms are due to the actuator and specimen dynamics that are present during the hybrid simulation.

Specific cases: no-actuator dynamics and slow speed pseudodynamic testing

In the ideal case that the actuator has no dynamics, i.e., $G_{xu}(s) = 1$, the experimental transfer function becomes

$$G_{uF\_RTHT}(s) = \frac{1}{\left(M + \frac{S_F}{S_L}m\right)s^2 + \left(C + \frac{S_F}{S_L}c\right)s + \left(K_{num} + \frac{S_F}{S_L}k_{exp}\right)}. \quad (6\text{-}41)$$

This equation shows that for this ideal case, a sufficient condition for stability is that the mass, damping, and stiffness of both test structure and specimen are positive. Furthermore, if the displacements are applied slowly, as in conventional pseudodynamic testing, the terms corresponding to the specimen mass and damping can be neglected. The experimental transfer function for pseudodynamic testing, $G_{dF\_PsD}(s)$, is then given by:

$$G_{uF\_PsD}(s) = \frac{1}{M\,s^2 + C_{num}s + \frac{S_F}{S_L}k_{exp}}, \quad (6\text{-}42)$$

which yields the same results as the exact transfer function when the experimental substructure is rate independent (i.e., $C_{exp} = 0$), and assuming no experimental errors.

6.5.4 Stability analysis

One of the most important effects of actuator dynamics on a real-time hybrid experiment is the stability reduction. By approximating actuator dynamics as a pure time delay, Horiuchi et al. (1996) demonstrated that the effect of this delay was to introduce energy into the system, in a manner similar to negative damping. If this negative damping was larger than the structural damping, the experiment became unstable. However, the time-delay approximation is only accurate for relatively low frequencies. The approach considered in this study is to investigate the stability of the real-time hybrid experiment using the mathematical models of the testing system dynamics presented in previous sections, therefore, without restricting the analysis to the time-delay approximation.

The stability of a linear time-invariant system can be determined by analyzing the location of its poles. A system is BIBO *stable* (bounded-input bounded-output stable) if and only if every pole of the system has a negative real part or, equivalently, lies inside the left-half *s*-plane (Chen, 1999). This condition guarantees that the transient response of a stable system will decay exponentially with time. If any pole has a positive real part (i.e., is in the right-half *s*-plane), then the system is *unstable*. Therefore, the $j\omega$ –axis is the stability boundary between stable and unstable response. If the system has nonrepeated $j\omega$ –axis poles, then the system is neutrally stable (Franklin et al., 2002).

The stability of the real-time hybrid experiment can, therefore, be analyzed from the poles of the experiment transfer function, $G_{dF\_RTHT}(s)$. These poles are the roots of the transfer function denominator, which is given by:

$$d_{dF\_RTHT}(s) = \left(Ms^2 + C_{num}s + K_{num}\right)d_{xu}(s) + \frac{S_F}{S_L}n_{xu}(s)\left(ms^2 + c_{exp}s + k_{exp}\right). \quad (6\text{-}43)$$

Finding a closed-form solution for the roots of this equation (i.e., for the poles of the system), is very laborious. Even though symbolic manipulation software can be used (e.g., Matlab's symbolic toolbox), the solutions are extremely long and involve numerous terms. An alternative approach is to determine the roots of the equation, and consequently the stability conditions, numerically as in the example presented in the following section.

6.5.5 Illustrative example

The effect of actuator dynamics on real-time hybrid testing is illustrated considering a simple, linear elastic, single-degree-of-freedom structure, similar to the one shown in Figure 6.20. The properties of the structure and test specimen are listed in Table 6.2. The parameters of the testing system described in Table 6.1 are used to determine the actuator dynamics.

Table 6.2: Properties of structure and test specimen.

Parameter	Value	Unit	Parameter	Value	Unit
Test structure			Test specimen		
f_n	1	Hz	k_{exp}	234	lb/in
ξ	5.0	%	M	0.0023	lb-sec^2/in
K_{exp}	234	lb/in	ξ	1.0	%
C_{exp}	0.0148	lb-sec/in	c_{exp}	0.0148	lb-sec/in
K_{num}	0	lb/in	Scaling factors		
C_{num}	3.71	lb-sec/in	S_L	1	-
M	5.93	lb-sec^2/in	S_F	1	-

Figure 6.23 shows a comparison between the exact transfer function of the test structure and the transfer function calculated assuming that the response of the structure is obtained using the real-time hybrid testing method (RTHT), i.e., including actuator dynamics. The figure shows that the two transfer functions are, in general, similar; both have a resonant peak at the natural frequency of the test structure, (i.e., 1 Hz). However, some differences are evident, especially close to the natural frequency: (a) the magnitude is larger, and (b) the slope of the phase is steeper for the RTHT case. Both of these differences are due to actuator dynamics, and as clearly seen, the effect is similar to a reduction on the damping during the experiment (i.e., by introducing negative damping). This result is equivalent to the one obtained by Horiuchi et al. (1996) in the time domain and using a time delay to represent actuator dynamics.

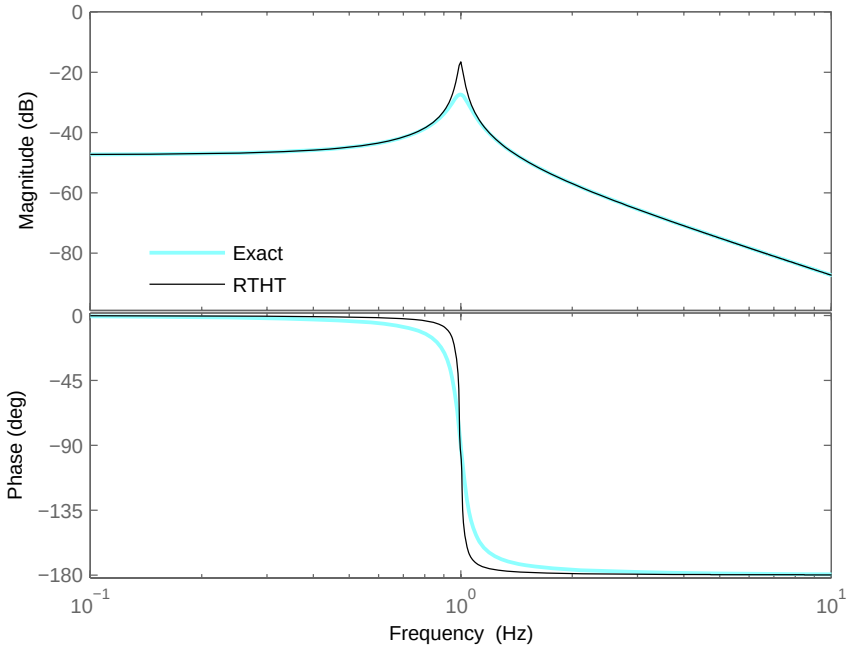

Figure 6.23: Comparison of exact and real-time hybrid experiment transfer functions of test structure.

Figure 6.25 shows a comparison of the impulse response of the structure using both exact and real-time hybrid simulation approaches. The effect of actuator dynamics on the amplitude of the response is pronounced, and although the system is still stable, the response is greatly amplified for the RTHT case.

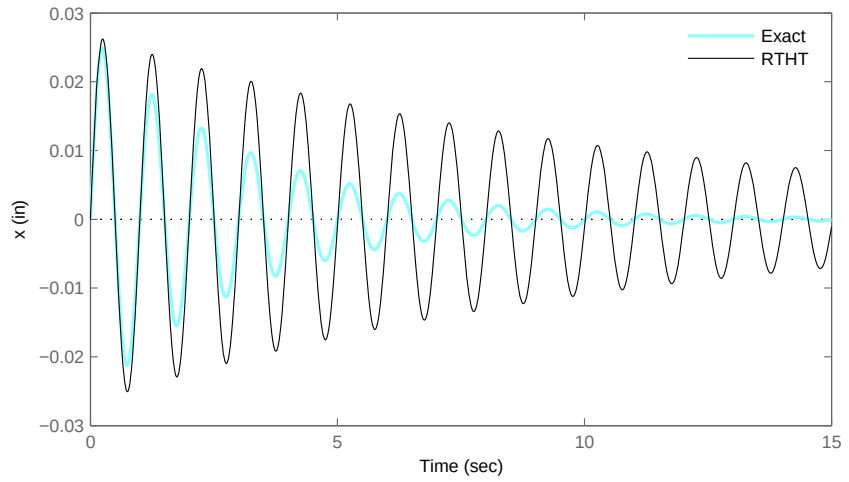

Figure 6.24: Comparison of impulse response of tested structure.

Figure 6.25 shows the location of the poles and zeros of the transfer function of the structure for the cases of exact response and real-time hybrid simulation. For the exact response, two complex poles (located at s = -0.314 ± 6.28i) are found, which correspond to a natural frequency of 1 Hz and a damping ratio of 5 %, as expected. The

real-time hybrid simulation case has six poles and four zeros. The additional poles and zeros are due to the dynamics of the testing system, and as can be observed in the figure, these poles and zeros practically cancel each other. However, a close-up view of the dominant complex poles [see Figure 6.25 (c)] shows that these poles are shifted to the right for the RTHT case, which shows that the stability of the system is reduced (if the poles cross into the right-half plane, the simulation will be unstable). The complex poles for the RTHT case are located at s = -0.0892 ± 6.27i, corresponding to a natural frequency of 0.998 Hz and a damping ratio of 1.42 %, which shows that although the main effect of the uncompensated actuator dynamics is to reduce the damping on the system, it also produces small errors on the natural frequency of the tested structure.

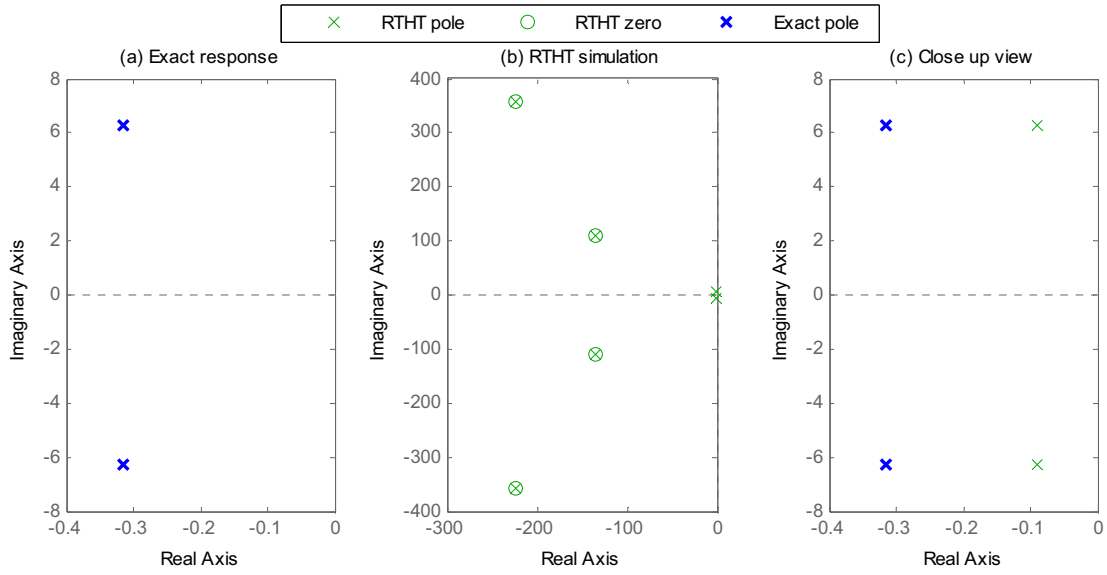

Figure 6.25: Location of poles and zeros of tested structure: (a) Exact transfer function, (b) Real-time hybrid simulation, (c) Close-up view of dominant poles.

The stability of the real-time hybrid simulation can be analyzed using the method described in the previous section, i.e., analyzing the roots of the denominator of the RTHT transfer function $G_{dF\_RTHT}(s)$ using Equation (6-43). The analysis shows that for the 1 Hz structure considered, the minimum damping required for stability (i.e., critical damping) is ξ_{cr} = 3.54 %. Figure 6.26 shows the impulse response for a case where the structural damping of the test structure is 3% (i.e., less than the minimum required for stability). As can be seen, the response of the real-time hybrid simulation is unstable, increasing with time. The pole-zero map shown (Figure 6.27) shows that the dominant complex poles from the real-time hybrid simulation are now on the right-half plane, which confirms the instability of the system.

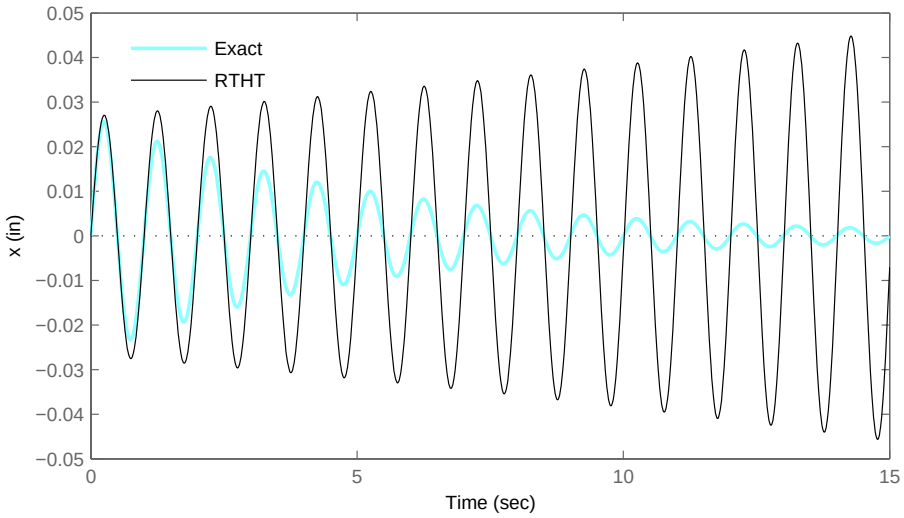

Figure 6.26: Comparison of impulse response of tested structure ($\xi = 3\%$).

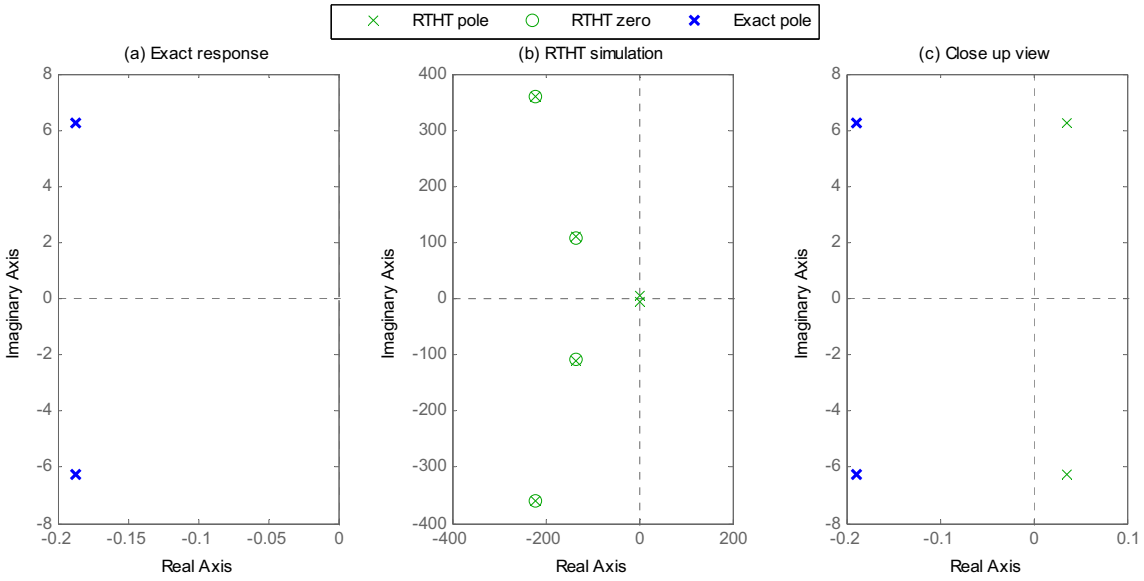

Figure 6.27: Location of poles and zeros for exact and real-time hybrid experiment transfer functions ($\xi = 3\%$).

6.5.6 Stability analysis using simplified actuator transfer function

The previous example illustrated the effects that the dynamics of the testing system have on the stability of the overall experiment. To further analyze the stability conditions of the real-time hybrid experiment, an approximation of the actuator transfer

function is used. This approximation allows finding a closed-form solution for the stability condition.

The simplified, first-order model of the actuator transfer function was shown in Section 6.4 to provide a good approximation of the actuator dynamics (and especially of the phase) at low frequencies. The transfer function of this simplified model is given by

$$G_{xu}(s) = \frac{1}{\tau_{xu} s + 1}. \tag{6-44}$$

Using this first-order model of actuator transfer function, the experimental transfer function $G_{dF\_RTHT}(s)$, is given by

$$G_{dF\_RTHT}(s) = \frac{\tau_{xu} s + 1}{M\tau_{xu} s^3 + \left(C_{num}\tau_{xu} + M + \frac{S_F}{S_L} m \right) s^2 + \left(K_{num}\tau_{xu} + C_{num} + \frac{S_F}{S_L} c_{exp} \right) s + \left(K_{num} + \frac{S_F}{S_L} k_{exp} \right)} \tag{6-45}$$

The stability of the real-time hybrid experiment can be determined by analyzing the denominator of this transfer function. The Routh-Hurwitz stability criterion allows determining the ranges of the polynomial coefficients required for stability without actually solving for the roots. Using the Routh-Hurwitz method, the following conditions are required in order for the poles of the system (or roots of the denominator) to be stable:

1. $M > 0$

2. $K_{num} + \frac{S_F}{S_L} k_{exp} > 0$

3. $\left(C_{num}\tau_{xu} + M + \frac{S_F}{S_L} m \right)\left(K_{num}\tau_{xu} + C_{num} + \frac{S_F}{S_L} c_{exp} \right) - M\tau_{xu}\left(K_{num} + \frac{S_F}{S_L} k_{exp} \right) > 0$

The first two conditions are the general conditions for stability of a linear, single-degree-of-freedom system. However, the third condition introduces additional requirements based on the actuator and specimen dynamics. For simplicity and to find a closed-form solution, assume $K_{num} = 0$, $S_L = S_F = 1$ (i.e., full-scale test specimen), and that the mass and damping of the specimen are small compared to the ones from the test structure, and, therefore, can be neglected (i.e., $m = c = 0$) . The last stability condition then becomes:

$$\tau_{xu} C_{num}^2 + M\, C_{num} - \tau_{xu} k_{exp} M > 0 \tag{6-46}$$

or alternatively

$$\left(2\xi\omega_n\right)^2 \tau_{xu} + 2\xi\omega_n - \omega_n{}^2 \tau_{xu} > 0 \tag{6-47}$$

where ξ and ω_n are the damping ratio and natural frequency of the single-degree-of-freedom test structure. After rearranging terms, the stability condition is:

$$\tau_{xu} < \frac{2\xi}{\omega_n\left(1-4\xi^2\right)} \tag{6-48}$$

which gives the maximum or critical value of the actuator time constant, τ_{xu}, for stability. Figure 6.28 shows the frequency response of the simplified first-order actuator transfer function for different values of τ_{xu}. As can be observed, as τ_{xu} increases, the phase lag also increases and the bandwidth is reduced. Therefore, as the time constant increases, the actuator becomes slower, and the stability of the real-time hybrid experiment is reduced. If the time constant is larger than the critical value, the experiment will be unstable.

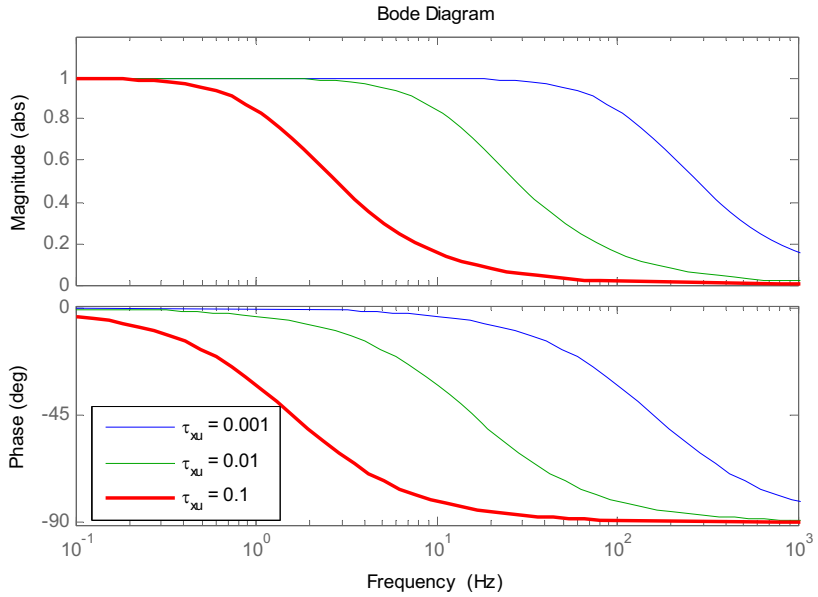

Figure 6.28: Effect of the time constant (τ_{xu}) on the actuator transfer function.

Alternatively, the stability condition can be used to determine the minimum damping of the system required for stability. The stability condition is then expressed as:

$$\xi^2 + \frac{1}{2\omega_n\tau_{xu}}\xi - \frac{1}{4} > 0 \tag{6-49}$$

The solution of the quadratic inequality is

$$\xi > \frac{-1+\sqrt{1+4\omega_n{}^2\tau_{xu}{}^2}}{4\omega_n\tau_{xu}} \tag{6-50}$$

which gives the minimum value of damping (i.e., critical damping) that is required to ensure the stability of the experiment.

When the structural damping of the system is small, the approximation, $1-4\xi^2 \approx 1$, is accurate (see Equation 6-48). Therefore, the stability condition becomes

$$\xi > \frac{\tau_{xu}\omega_n}{2} \tag{6-51}$$

or is expressed in terms of the stiffness and total damping

$$C > K\,\tau_{xu} \tag{6-52}$$

The above equation provides a simple way to check the stability of the real-time hybrid experiment. As can be seen, the required damping for stability increases as the natural frequency (and stiffness) of the system and the time constant of the actuator increase.

Relation between the time constant, τ_{xu}, and the time delay, T_d

To compare the stability condition obtained using the above approach to the stability criterion traditionally used in the literature (i.e., based on the time delay approximation; Horiuchi et al., 1996), the relationship between the actuator time constant and the actuator time delay needs to be determined.

The magnitude and phase of the transfer function can be determined using a semigraphic method. The magnitude (evaluated at $s_o = j\omega$) is the ratio between the product of the distances from the zeros to s_o, and the product of the distances from the poles. The phase is given by the sum of the angles from the zeros to s_o, minus the sum of the angles from the poles (Franklin et al., 2002). Figure 6.29 shows the location of the single pole in the s-plane for the first-order approximation of the actuator transfer function.

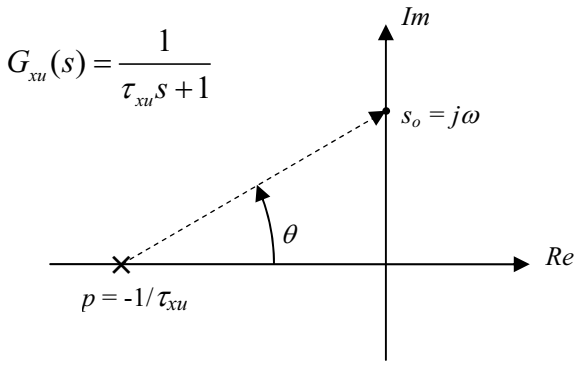

Figure 6.29: *S*-plane with pole location.

Using the semigraphic method, the magnitude and phase of the transfer function are given by

$$\left|G_{xu}(\omega)\right| = \frac{1}{\sqrt{1+\tau_{xu}{}^2\omega^2}}, \qquad \phi_{xu}(\omega) = -\tan^{-1}\left(\tau_{xu}\omega\right). \tag{6-53}$$

The time lag of the transfer function, τ_{lag}, is defined as the negative of the phase divided by the angular frequency. The time lag for the actuator transfer function is, therefore, given by

$$\tau_{lag}(\omega) = \frac{\tan^{-1}\left(\tau_{xu}\omega\right)}{\omega} \tag{6-54}$$

The actuator transfer function has been traditionally approximated as a pure time delay for low frequencies, i.e., $G^{Td}{}_{xu}(s) = e^{-T_d s}$. This approximation assumes that within the frequency range of interests (i.e., low frequency) the magnitude is very close to unity and the phase is linear, which results in a constant time lag. The time delay (T_d) approximation of the actuator transfer function can be obtained considering the limit of the time lag of the system, as the frequency tends to zero:

$$T_d = \lim_{\omega\to 0} \tau_{lag}(\omega)\,. \tag{6-55}$$

Using the expression for the time lag of the actuator transfer function, the time delay is then given by

$$T_d = \lim_{\omega\to 0} \frac{\tan^{-1}\left(\tau_{xu}\omega\right)}{\omega} \tag{6-56}$$

Because both numerator and denominator go to zero, this is an indeterminate form. Using L'Hospital's rule to solve the limit, we obtain

$$T_d = \lim_{\omega\to 0}\left[\frac{\tau_{xu}}{1+(\tau_{xu}\omega)^2}\right] \tag{6-57}$$

which yields

$$\tau_d = \tau_{xu} \tag{6-58}$$

This result shows that at low frequencies (i.e., $\omega \approx 0$), the time delay is equal to the time constant of the actuator transfer function. However for other frequencies, the time lag varies according to the expression obtained previously (Equation 6-54).

With this result, the previously determined stability condition for the real-time hybrid experiment, i.e., $C > K\,\tau_{xu}$, becomes at low frequencies the same as the one presented in the literature when using a pure time delay, i.e., $C > K\,\tau_d$ (Horiuchi et al., 1996). However, the approach considered herein is more general and includes the time delay approximation as a degenerate case.

Example

The simplified stability condition derived using the above procedure is used to analyze the example presented in Section 6.5.5. Figure 6.30 shows the minimum damping required for the stability of the real-time hybrid simulation (i.e., minimum damping) as a function of the natural frequency of the test structure, calculated using both exact and simplified analysis (i.e., Equations 6-43 and 6-52, respectively). As can be observed, the results from the simplified stability condition are very close to the exact one, up to frequencies of about 10 Hz. After this point, the simplified method overestimates the critical damping, therefore providing a conservative estimate of the stability condition. For the 1 Hz structure considered, the minimum damping required for stability is 3.54% and 3.42% for the exact and simplified analyses, respectively.

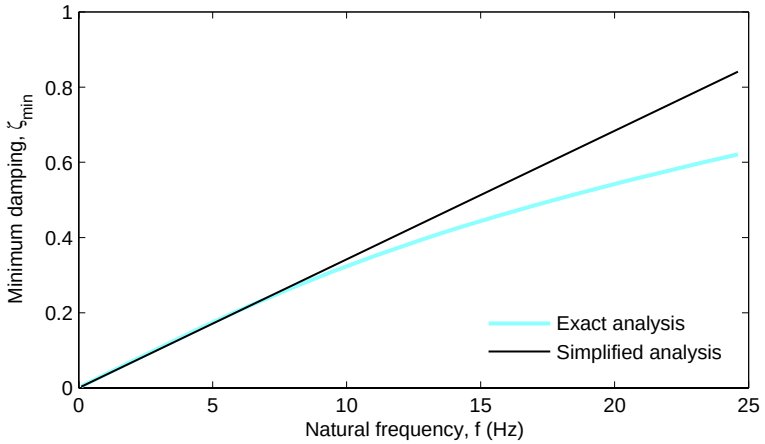

Figure 6.30: Minimum damping for stability as a function of the natural frequency of the test structure.

Figure 6.30 also shows how the required damping for stability becomes very large as the natural frequency of the test structure increases, becoming far greater than the damping associated with typical structural systems. Compensation for actuator dynamics is, therefore, essential, especially for systems with important high frequencies, such as are associated with stiff structures and multi-degree-of-freedom systems.

6.5.7 Effect of specimen mass on the real-time hybrid simulation

The effect of the specimen mass on real-time hybrid experiments is analyzed in this section. The effective mass of the experimental component includes the mass of the test specimen, any attachments that may be used to connect the actuator to the specimen, and the mass of the actuator's piston. Because the first-order approximation for the actuator transfer function does not include actuator-specimen interaction, the complete actuator transfer function (i.e., Equation 6-20) is used for the analysis.

The normalized mass of the experimental component with respect to the mass of the test structure is termed the *effective mass ratio,* α_{mt}, defined as the mass of the

experimental component divided by the mass of the test structure (i.e., $\alpha_{mt} = m_t/M$). For the 1 Hz natural frequency test structure considered throughout this chapter, the effective mass ratio is 0.4% ($\alpha_{mt} = 0.004$).

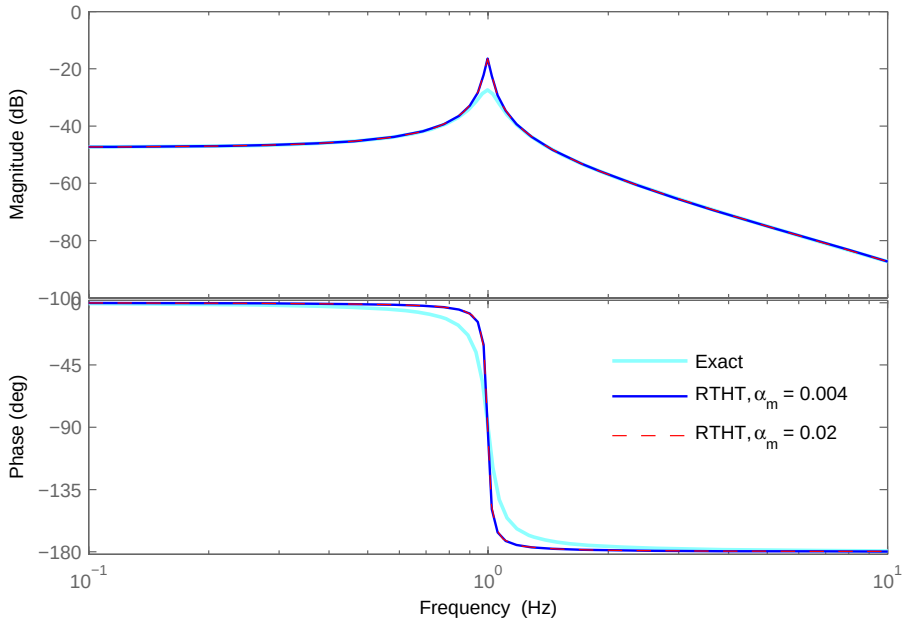

Figure 6.31: Comparison of exact and real-time hybrid experiment transfer functions of test structure for changes in total mass.

Figure 6.31 shows the effect of an increase on the mass of the experimental component by a factor of 5 (which results in $\alpha_{mt} = 0.02$). As can be seen, the responses from the two real-time hybrid simulation cases with different mass ratios are nearly identical. However, an analysis on the location of the poles and zeros from the real-time hybrid testing transfer function indicates some interesting effects associated with the mass of the experimental component. Figure 6.32 shows the pole-zero maps for the real-time hybrid simulation cases. As observed, although the effect from the increased mass of the experimental component is negligible on the low-frequency complex poles, the location of the remaining poles and zeros changes considerably. The increase in the mass ratio from 0.4 to 2% causes a pair of fast, complex poles to move to the right (and also closer to the real-axis), which corresponds to a reduction on the natural frequency and damping of the poles. The position of the poles is now closer to the imaginary axis and right-half plane; therefore, a reduction in the stability of the simulation is found. Figure 6.32 also shows the pole-zero map for a further increase in the total mass ratio to 4% (which results in $\alpha_{mt} = 0.04$). Similar trends to the previous case are observed; however, now the fast complex poles are actually in the right-half plane, and the real-time hybrid simulation is unstable.

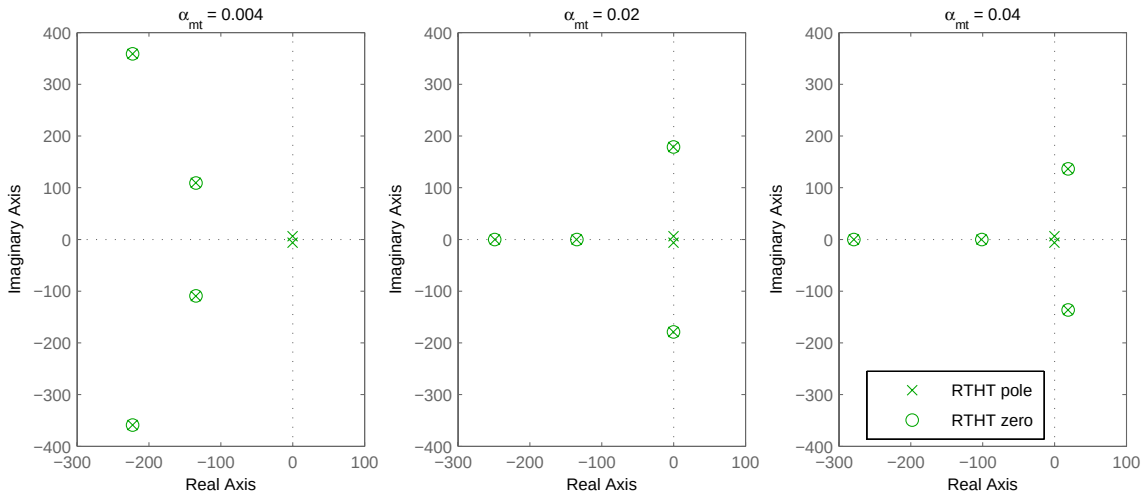

Figure 6.32: Effect of total mass ratio on the location of poles and zeros of real-time hybrid simulations.

The analysis conducted shows that although the total mass of the experimental component has a small effect on the amplitude and phase of the simulated response, the effect on the stability of the simulation is pronounced. If the mass of the experimental component is large and causes the total mass ratio to exceed a critical value, the real-time hybrid experiment will be unstable. For the structure considered in this example, instability of the hybrid simulations occurred when the mass of the experimental component exceeded 2% of the mass of the test structure.

6.6 Summary

Equations for modeling the different components of the testing system (including servo-hydraulic actuator, controller, and test specimen) have been presented. The individual models were then combined to produce a linearized dynamic representation of the entire testing system. Numerical values of the parameters of the testing system were obtained using both time domain and frequency domain identification techniques. The time domain method allowed individual values to be obtained for each parameter; subsequently, analyses were conducted to determine their effect on the overall system response. The frequency domain identification technique allowed accurate representations of the measured actuator transfer function to be obtained for different test specimens and testing conditions.

The linearized dynamic model of the testing system was used to develop a complete model of the real-time hybrid experiment. This "virtual" model allowed the effect of the dynamics of the testing system on the accuracy and stability of the real-time hybrid testing technique to be investigated. Methods for predicting the stability of the hybrid experiment were developed considering detailed and simplified models for the actuator dynamics. The stability analysis confirmed that the minimum damping of the system required for stability increases as the natural frequency of the test structure and

time constant of the actuator increase. Stability of the low-frequency, dominant poles was predicted quite well by the formula derived using the approximation of the actuator transfer function. The stability criteria based on the complete-detailed model allowed investigation of effects that cannot be captured by simple approximations of actuator dynamics. The mass of the experimental component (which includes the mass of the test specimen, any attachments that may be used to connect the actuator to the specimen, and the mass of the actuator's piston) was found to be important on the stability of the hybrid experiment. For the structure considered in this chapter, the real-time hybrid simulation became unstable when the relative value of the mass with respect to the mass of the tested structure became larger than 2%.

The models for actuator dynamics and hybrid testing presented in this chapter have proven to be valuable for investigating the stability of the real-time hybrid testing technique as well as the effect of system parameters. These models are used in subsequent chapters for developing and evaluating compensation strategies for actuator dynamics.

CHAPTER 7

COMPENSATION FOR ACTUATOR DYNAMICS

The effects of actuator dynamics in real-time hybrid testing were analyzed in detail in the previous chapter. Both magnitude and phase lag (and, therefore, time lag) were demonstrated to vary with frequency (i.e., were not constant). Because time lag varies with frequency, compensation techniques based on their approximation as a pure time delay become ineffective for structures that present significant responses at different frequencies, e.g., multi-degree-of-freedom systems. Additionally, the actuator transfer function was found to be dependent on the specimen that is attached to the actuator (i.e., actuator-specimen interaction). Consequently, the dynamics of the actuator may vary during the experiment, because of changes in the properties of the test specimen (e.g., stiffness). Therefore, when the characteristics of the specimen change significantly and frequently (e.g., nonlinear hysteretic systems and semiactively controlled MR dampers), traditional delay-compensation methods may not perform adequately. In this chapter, compensation strategies are developed directly for actuator dynamics, without using the time-delay approximation. The models exhibiting the observed actuator dynamics are used to develop a model-based compensation approach that provides compensation for both phase and magnitude effects. The approach is verified experimentally and then used in the next chapter to conduct hybrid testing of a semiactively controlled structure.

7.1 Framework for actuator dynamics compensation

The dynamics of the actuator and testing system can be accurately approximated by the actuator transfer function, $G_{xu}(s)$. This transfer function includes the effects of the actuator, servovalve, servocontroller, and test specimen. In the experimental setup used in this study, the actuator servocontroller can perform PID (proportional-integral-derivate) control; the associated dynamics and settings are already included in the actuator transfer function, $G_{xu}(s)$. The approach proposed in this chapter is to add an outer controller or outer loop that performs the compensation for actuator dynamics, while the PID control performed by the actuator servocontroller is treated as an internal, or inner, loop. Figure 7.1 shows a schematic block diagram of the configuration for the additional compensation for actuator dynamics, where d is the desired displacement (or reference signal), u is the command to the actuator servocontroller generated by the outer controller, and x is the measured displacement realized by the actuator.

For the outer controller performing the compensation for actuator dynamics, the plant or system to be compensated is the closed-loop system represented by the actuator transfer function, $G_{xu}(s)$. The main objective of the additional control is to cause the measured displacement, x, to more accurately track the desired displacement, d,

minimizing phase lag and amplitude changes. Compensation techniques and their implementation are presented in the following sections.

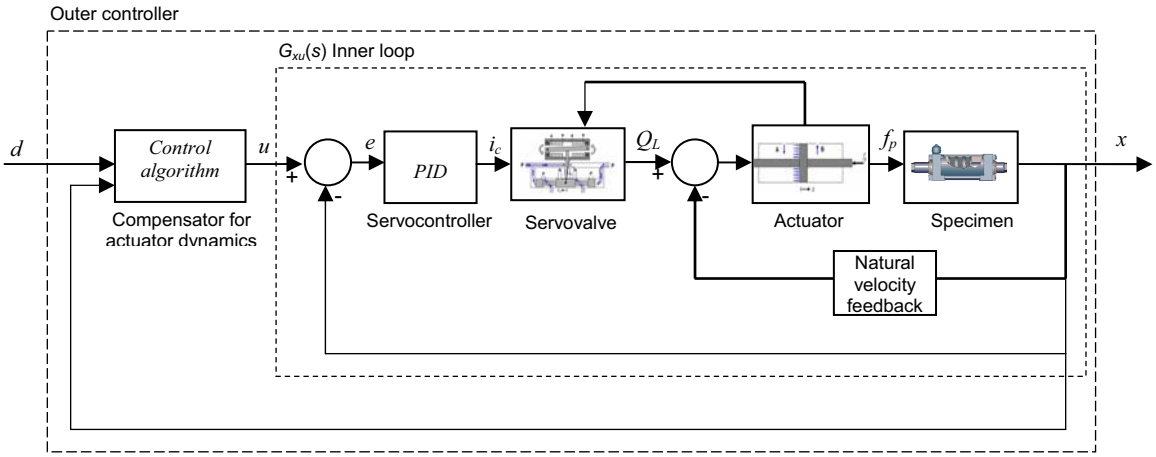

Figure 7.1: Schematic block diagram of compensation for actuator dynamics.

7.2 Open-loop feedforward compensation

When the controller does not use a measurement of the system being controlled in computing the control action, the control system is called open-loop (Franklin et al., 2002). Feedforward is a type of open-loop control that processes the reference signal directly by calculating a best guess or prediction to produce the ideal response of the plant (Ellis, 2000). Feedforward control allows combining knowledge of the command and the plant to improve the system response (Ellis, 2000). Because the output of the system is not used in calculating the control signal (i.e., does not form a closed loop), feedforward control does not have the potential stability problems associated with feedback control, provided that the plant and controller are stable (Ellis, 2000). Feedforward control also avoids the slowness and delays associated with feedback control, therefore, allowing much faster responses.

Figure 7.2 shows a block diagram of the system with the implementation of feedforward control, where the controller transfer function, $G_{FF}(s)$, is placed before the plant, $G_{xu}(s)$. The resulting transfer function of the compensated system, $G_{xd}(s)$, including controller and plant, is given by

$$G_{xd}(s) = G_{FF}(s)G_{xu}(s) \tag{7-1}$$

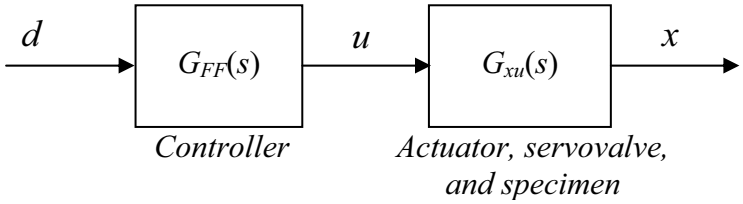

Figure 7.2: Block diagram of feedforward control.

7.2.1 Feedforward controller with pure inverse dynamics

Ideally, the feedforward controller should completely cancel the dynamics of the plant, resulting in a compensated system with a magnitude of one and a phase of zero. The design of a feedforward compensator, therefore, is in essence the calculation of the inverse of a dynamic system (Åström & Wittenmark, 1984). Given the model of the system to be controlled, $G_{xu}(s)$, the feedforward controller can be designed as a pure inverse of the plant dynamics, as given by

$$G_{FF}(s) = G_{xu}^{-1}(s). \tag{7-2}$$

When the model of the system provides a perfect representation of the plant dynamics, the resulting transfer function of the compensated system becomes $G_{xd}(s) = 1$, as desired. However, for a pure inverse controller to be applicable, the inverse of the plant has to be minimum-phase (which means that the system plant and its inverse are causal and stable).

The characteristics of the system considered in this application were analyzed in detail the previous chapter. The transfer function, $G_{xu}(s)$, had three poles and no zeros, for frequencies below 25 Hz, and four poles and no zeros, for frequencies below 50 Hz (see Equations 6-19 and 6-20). The actuator transfer function can therefore be expressed in the general form

$$G_{xu}(s) = \frac{K}{\prod_{i=1}^{n}\left(s - p_{xu,i}\right)} \tag{7-3}$$

where K is the gain, $p_{xu,i}$ are the poles of the system, n is the number of poles, and $\prod\{\cdot\}$ represents the product operator. The transfer function of the controller with a pure inverse of the plant dynamics then becomes

$$G_{FF}(s) = \frac{\prod_{i=1}^{n}\left(s - p_{xu,i}\right)}{K}. \tag{7-4}$$

This controller is not a proper system (i.e., the degree of the numerator exceeds the degree of the denominator) and is not stable. It is a pure derivative action, which has a magnitude that increases unbounded with frequency (see Figure 7.3).

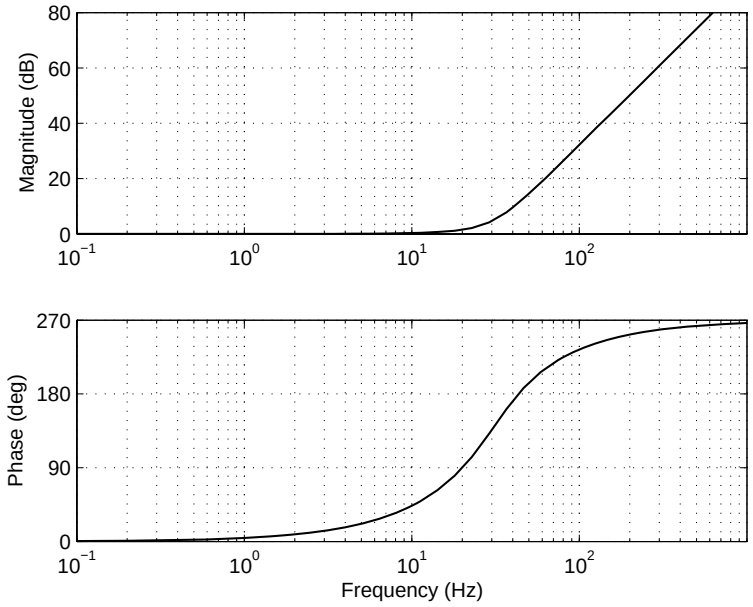

Figure 7.3: Bode plot of pure inverse controller [for third order $G_{xu}(s)$].

Under certain conditions, unstable controllers can result in stable, controlled systems. However, if the plant has uncertainty, use of unstable controllers is impractical. The plant model of the system considered in this study is a linearized version of the system, and consequently has uncertainties. Therefore, a requirement for the controller is to be stable

7.2.2 Feedforward controller with modified inverse dynamics

To obtain a stable, feedforward controller that approximates the controller with inverse dynamics, some modifications were made. The feedforward controller was realized using the inverse of the plant dynamics in series with a unity gain low-pass filter, with appropriate dynamics to make the controller stable. The order of the filter was the minimum to make the controller proper (i.e., n). The poles of the filter were selected as the zeros of the inverse controller times a factor, α, greater than one, to make the poles large enough to not interfere with the low frequency dynamics of the original inverse controller. The resulting transfer function of the feedforward controller is given by

$$G_{FF}(s) = \alpha^n \frac{\prod_{i=1}^{n}\left(s - p_{xu,i}\right)}{\prod_{i=1}^{n}\left(s - \alpha p_{xu,i}\right)} \tag{7-5}$$

For α = 1, the transfer function of the controller becomes one, therefore the controller provides no compensation. On the other hand, when $\alpha = \infty$, the controller becomes the pure inverse controller presented in the previous section. Therefore, the factor α should be large enough so that the dynamics of the pure inverse controller are not much affected in the frequency range of interest (and, therefore, cancel the dynamics of the plant), while at the same time, small enough so that the frequencies associated with the poles can be represented on the digital implementation of the controller with the sampling period used for the experiment. When the reference signal is subject to sudden changes, the value of α should be kept small enough so that the derivative action introduced by the controller is not too high. For the application considered in this study, the reference signal (i.e., target displacements) is the result of a double integration and, therefore, is rather smooth and without sudden changes.

Analysis using first order actuator transfer function

The simplified, first-order model of the actuator transfer function is used to analyze the characteristics of the compensated system. The transfer function of this simplified model is given by

$$G_{xu}(s) = \frac{1}{\tau_{xu} s + 1} \tag{7-6}$$

where the single pole is located at $p_{xu} = -1/\tau_{xu}$. The transfer function of the feedforward controller with modified inverse dynamics can be expressed as

$$G_{FF}(s) = \frac{\tau_{xu} s + 1}{\frac{\tau_{xu}}{\alpha} s + 1} \tag{7-7}$$

which is similar to the expression of a lead compensator (Franklin et al., 2002). Because α is assumed larger than one, the poles are larger than the zeros, and, therefore, the compensator provides a phase lead. The transfer function of the compensated system is given by

$$G_{xd}(s) = \frac{1}{\frac{\tau_{xu}}{\alpha} s + 1} \tag{7-8}$$

which shows that the effect of the compensation is to reduce the actuator time constant by a factor equal to the parameter α, therefore, making the system faster and increasing the bandwidth. The magnitude, phase, and time lag of this transfer function are given by

$$\left|G_{xd}(\omega)\right| = \frac{1}{\sqrt{1 + \frac{{\tau_{xu}}^2 \omega^2}{\alpha^2}}} \tag{7-9}$$

$$\phi_{xd}(\omega) = -\tan^{-1}\left(\frac{\tau_{xu}\omega}{\alpha}\right) \tag{7-10}$$

$$\tau_{lag,xd}(\omega) = \frac{\tan^{-1}\left(\frac{\tau_{xu}\omega}{\alpha}\right)}{\omega}. \tag{7-11}$$

In the limit when ω tends to zero, the time lag of the compensated system becomes

$$\tau_{lag,xd}(0) = \frac{\tau_{xu}}{\alpha}. \tag{7-12}$$

The above equations show that the magnitude and phase lag for the compensated system tends to one and zero, respectively, as α increases. The time lag at low frequencies is reduced by an amount equal to the magnitude of α, which suggests that values of α, such as 10 or 20, can produce significant reductions on the phase and time lag, resulting in values that are adequate for real-time hybrid testing (and typically within the accuracy of the estimated parameters).

Application of feedforward controller to MR damper

The performance of the feedforward compensator with modified inverse dynamics was experimentally verified using the MR damper specimen for the case of zero input voltage. The model of actuator dynamics used to create the feedforward compensator was a third-order model with the following transfer function

$$G_{xu}(s) = \frac{6118670}{(s+161.5)\ (s^2\ +\ 222.2s\ +\ 3.79\text{e}4)} \tag{7-13}$$

where the poles are located at -161.5 and -111.1±159.9i. The low-pass filter for the feedforward controller was designed using a value of α = 15 and three poles. Figure 7.4 shows the frequency response of the low-pass filter which has a cut-off frequency (determined at -3 dB) of 390 Hz.

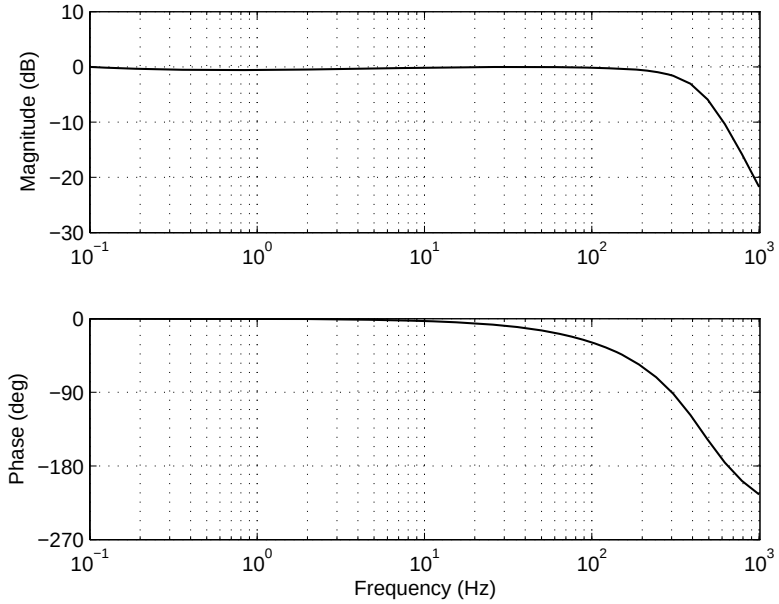

Figure 7.4: Frequency response of low pass filter.

Figure 7.5 shows the frequency response of the resulting feedforward compensator for the system with the MR damper specimen which has the following transfer function

$$G_{FF}(s) = \frac{3375(s+161.5)\ (s^2\ +\ 222.2s\ +\ 3.79e4)}{(s+2422)\ (s^2\ +\ 3333s\ +\ 8.527e6)} \tag{7-14}$$

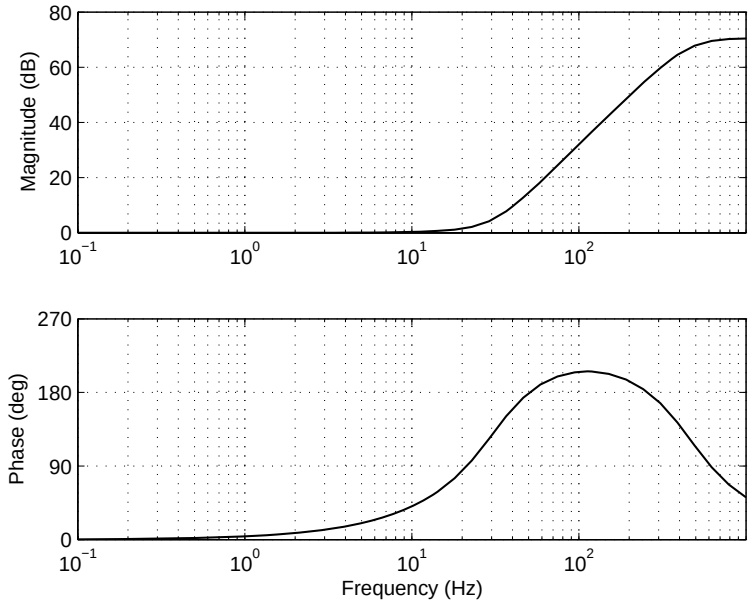

Figure 7.5: Feedforward compensator for MR damper with 0V.

Figure 7.6 shows a comparison of the step response of the compensated and uncompensated systems. As can be observed, the compensation algorithm significantly improves the response, resulting in a much smaller rise time, 0.93 msec as compared to 14 msec for the uncompensated system (rise time specified at 10 and 90%). The overshoot for both compensated and uncompensated cases, is about 3%, which is adequate.

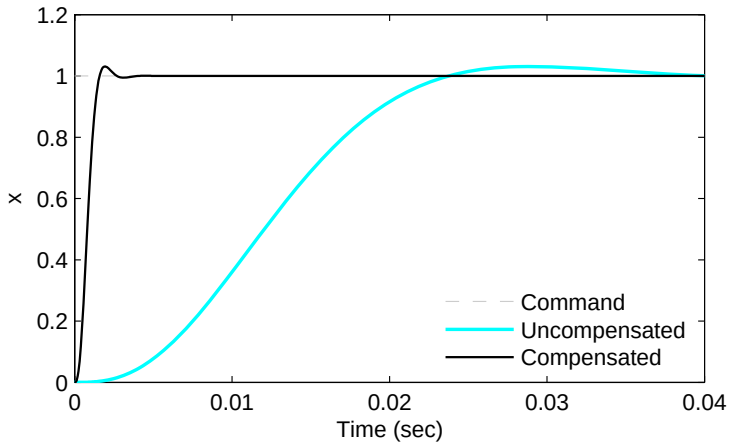

Figure 7.6: Step response of compensated system (Feedforward compensator for MR damper with 0V).

Figure 7.7 shows a comparison of the frequency response of the compensated and uncompensated systems. The dynamics of the compensated system have improved significantly: the magnitude is very close to unity up to about 25 Hz; the phase is nearly zero throughout the 0-50 Hz range; and the time lag has been reduced to less than 1 msec. The increase in the magnitude at frequencies larger than 25 Hz is due to differences between the model used for actuator dynamics (which is only accurate up to about 25 Hz) and the actual plant response. After 25 Hz, the model underestimates the magnitude, which when inverted, results in larger magnitude values. Higher-order models of actuator dynamics could be used, like the fourth- and fifth-order models, which were accurate in the entire 50 Hz frequency range, however, for the applications considered in this study, the 25 Hz range is sufficient.

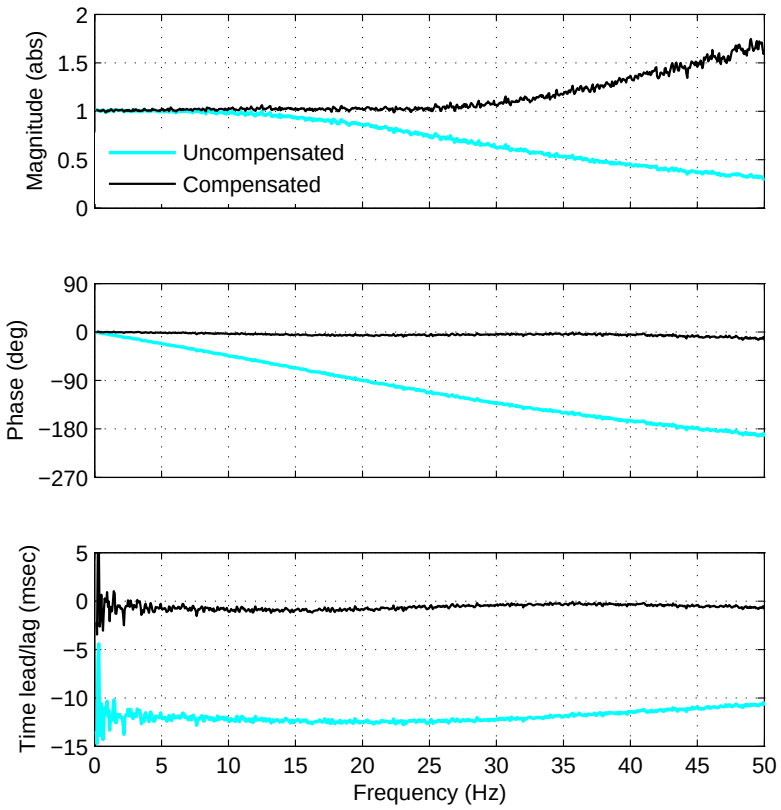

Figure 7.7: Frequency response of compensated and uncompensated systems.

Experimental verification

The performance of the feedforward controller with modified inverse dynamics was verified experimentally. Figure 7.8 shows schematically the implementation of the control algorithm.

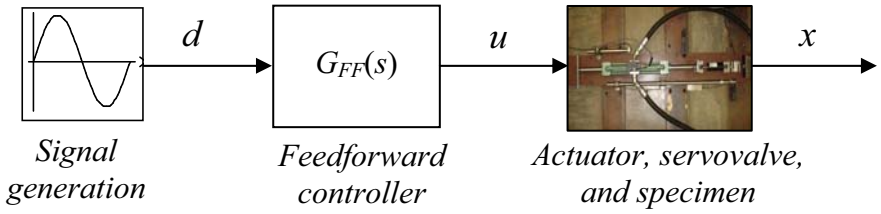

Figure 7.8: Schematic block diagram for experimental verification of feedforward compensator.

Two different reference signals were used to verify the compensation algorithm: (*a*) sinusoidal displacement with an amplitude of 0.2 in (5.08 mm) and 1 Hz frequency, and (*b*) bandlimited white noise random reference signal with a bandwidth of 5 Hz and an RMS of 0.11 in (2.85 mm). These two reference signals were selected because they represent approximately the fundamental and highest natural frequencies, respectively, of

the structure described in the next chapter, which is tested using the real-time hybrid technique. The sampling time used in the experiments was 0.0005 sec, which corresponds to a sampling frequency of 2,000 Hz.

Figure 7.9 shows the results for the test using a sinusoidal reference signal. Similarly to previous cases, the performance of the compensation approach is analyzed by comparing the *desired*, *commanded*, and *measured* displacements. To make the results easier to compare, a low-pass filter (with a 30 Hz cutoff frequency) was used as a postprocess to remove sensor noise in the measured displacement. As can be observed from the time history plots, the measured and desired displacements are almost identical, which shows the good tracking performance of the control algorithm. Figure 7.9 (c-d) shows *x*-*y* plots of the response. The plot of desired versus measured displacement is nearly a straight line with a slope of one, which demonstrates the accuracy and efficiency of the compensation approach for actuator dynamics. The plot of commanded displacement versus measured displacement shows the effect of actuator dynamics, i.e., a counter-clockwise loop that is effectively cancelled by the compensation algorithm. The large command from the feedforward controller at the beginning of the simulation is caused by the sudden change on the reference signal (and its derivatives) when the sinusoidal signal starts. However, the effect of this discontinuity disappears quickly and is not present on the measured displacement. The accuracy of the compensation approach was quantified using the *error norm* defined as the RMS of the control error (desired displacement minus measured displacement) divided by the RMS of the desired displacement, as given by

$$Error\ norm = \sqrt{\frac{\frac{1}{N}\sum_{i=i}^{N}\left[d_i - x_i\right]^2}{\frac{1}{N}\sum_{i=i}^{N}\left[d_i\right]^2}} \tag{7-15}$$

where N is the number of number of time steps. The error norm for the tests with and without compensation was 0.98% and 7.48%, respectively, demonstrating the good performance of the control algorithm.

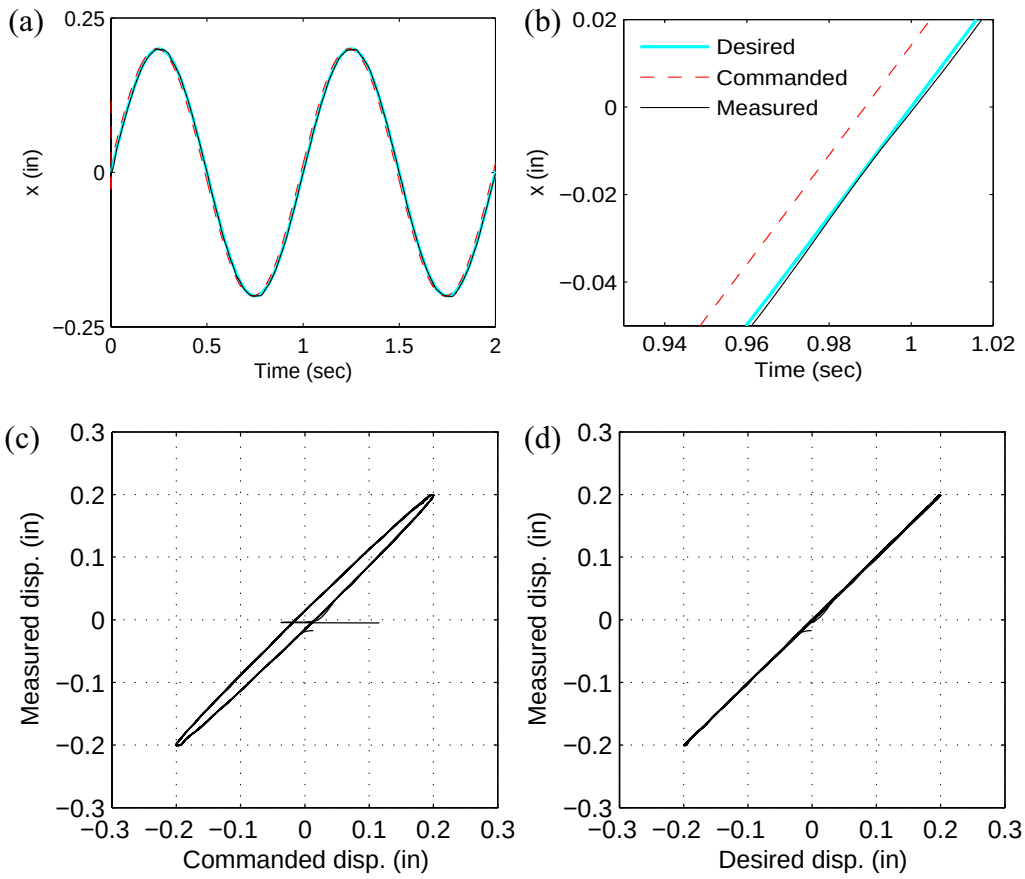

Figure 7.9: Test results for sinusoidal reference signal.

Figure 7.10 shows the experimental results for the bandlimited white noise random reference signal. As in the sinusoidal case, the desired and measured displacements are almost identical and the plot of desired displacement versus measured displacement is practically a straight line with slope of one. The error norm for the case with and without compensation was 2.09% and 22.15%, respectively, demonstrating the good accuracy of the compensation algorithm to track signals with broadband frequency content.

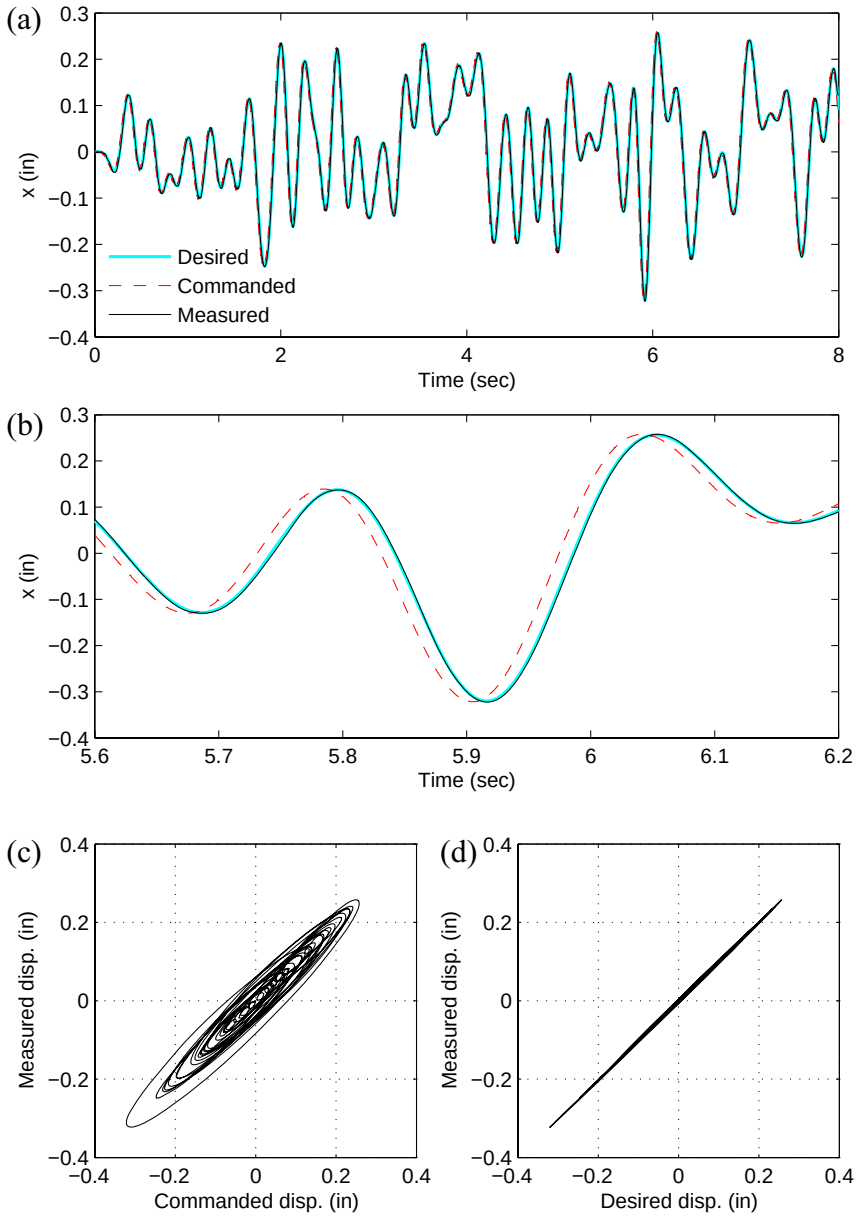

Figure 7.10: Test results for bandlimited white noise reference signal: (a) time histories, (b) close-up view, (c-d) *x*-*y* plots.

7.3 Closed-loop compensation

Because feedforward is an open-loop compensation, it requires a good model of the process to be controlled (Åström & Wittenmark, 1984). Feedforward control is, therefore, more sensitive to errors in the model used to create the compensator and also to variations on the plant dynamics. In contrast, feedback control uses the error between the desired and measured signals to determine the desired control action; inaccuracies in the model usually have a smaller effect on the controller performance. However, feedback control is slower than feedforward control; therefore, an outer control loop based on

feedback only is not effective for reducing or eliminating the actuator time lag, which is the main objective in this application (i.e., real-time hybrid testing).

A compensator using both feedforward and feedback, can combine the advantages of both control approaches. Figure 7.11 shows a schematic block diagram of a combined feedforward and feedback controller, where $G_{FF}(s)$ and $G_{FB}(s)$ are the transfer functions of the feedforward and feedback controllers, respectively. The total control command, u, is obtained by adding the two individual control signals from the feedforward and feedback controllers, u_{ff} and u_{fb}, respectively.

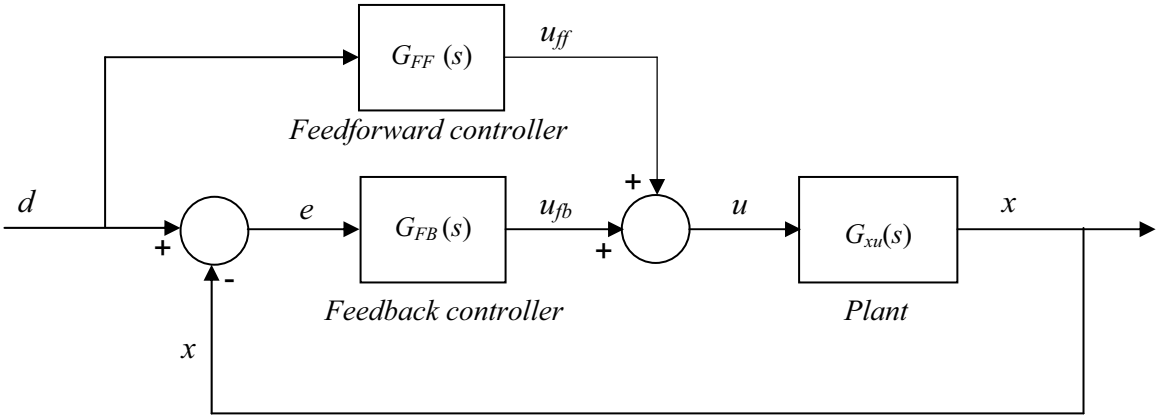

Figure 7.11: Block diagram of combined feedforward-feedback controller.

The characteristics of the controller depend on the feedforward and feedback links. For the feedforward link, the method with modified inverse dynamics is used, while for the feedback term a proportional controller with constant gain, K_{FF}, is adopted. The transfer functions of the two controllers are, therefore, given by

$$G_{FF}(s) = K_{FF} \frac{\prod_{i=1}^{n}\left(s - p_{xu,i}\right)}{\prod_{i=1}^{n}\left(s - \alpha p_{xu,i}\right)}, \qquad G_{FB}(s) = K_{FB} \tag{7-16}$$

When the feedforward controller completely cancels the plant dynamics, the error, e, is zero (and, therefore, also the command from the feedback block, u_{fb}) and the combined controller works as a pure feedforward compensator. However, when the dynamics of the plant are not completely cancelled by the feedforward control, the feedback term works to reduce the error between desired and measured signals.

A nonzero error signal can be caused by several sources: differences between the model used for the feedforward controller and the plant (e.g., nonlinearities in the servo-hydraulic system), dynamics that have to be added to the feedforward control to make it realizable and stable, or due to variations in the plant during the experiment (e.g., due to changes in specimen stiffness).

Stability analysis of combined compensator

Because feedback is used in the combined compensator, the system can potentially become unstable; therefore, understanding the stability of the compensated system, whose transfer function is given by

$$G_{xd}(s) = \frac{G_{xu}(s)\left[G_{FF}(s) + G_{FB}(s)\right]}{1 + G_{xu}(s)G_{FB}(s)} \tag{7-17}$$

is important. The stability conditions of the compensated system can be determined by analyzing the location of the poles of its transfer function. For the case when the feedback term is a proportional gain (i.e., $G_{FB}(s) = K_{FB}$), the transfer function can be expressed as:

$$G_{xd}(s) = \frac{n_{xu}(s)\left[n_{FF}(s) + K_{FB}d_{FF}(s)\right]}{d_{FF}(s)\left[d_{xu}(s) + K_{FB}n_{xu}(s)\right]} \tag{7-18}$$

where the transfer functions of the actuator and feedforward controller have been expressed in terms of their numerator and denominator polynomials, as given by

$$G_{xu}(s) = \frac{n_{xu}(s)}{d_{xu}(s)}, \text{ and } \quad G_{FF}(s) = \frac{n_{FF}(s)}{d_{FF}(s)}. \tag{7-19}$$

The stability of the combined system is governed by the denominator of $G_{xd}(s)$. Because the poles of the feedforward controller [roots of $d_{FF}(s)$] are selected to be stable, the stability condition of the combined system is determined from the roots of

$$\Delta(s) = d_{xu}(s) + K_{FB}n_{xu}(s) \tag{7-20}$$

This equation was used to determine the maximum value of the feedback gain for the case considered previously in this chapter, i.e., actuator with MR damper specimen (with zero input voltage). The dynamics of the plant were represented using the most accurate actuator transfer function, i.e., the fifth-order model given by Equation 6-24. The maximum value of the feedback gain for stability was determined to be $K_{FB} = 2.72$. Figure 7.12 presents a root locus plot showing the stability limit and the effect of the feedback gain on the roots of the characteristic equation. As can be observed, values of the feedback gain larger than 2.72 cause two of the complex poles to move into the right-half plane and, therefore, the system becomes unstable.

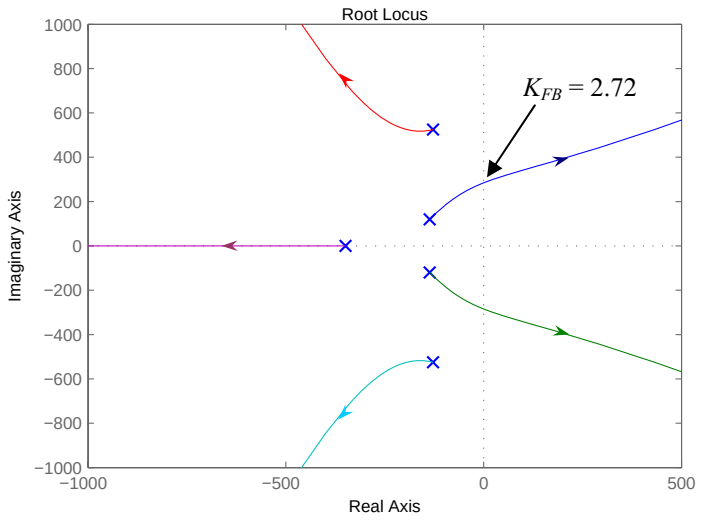

Figure 7.12: Root locus plot for stability of combined controller.

Experimental verification

The feedforward-feedback controller was verified experimentally using the sinusoidal and bandlimited white noise reference signals employed previously. Figure 7.13 shows a schematic block diagram of the implementation of the control algorithm for the experiments.

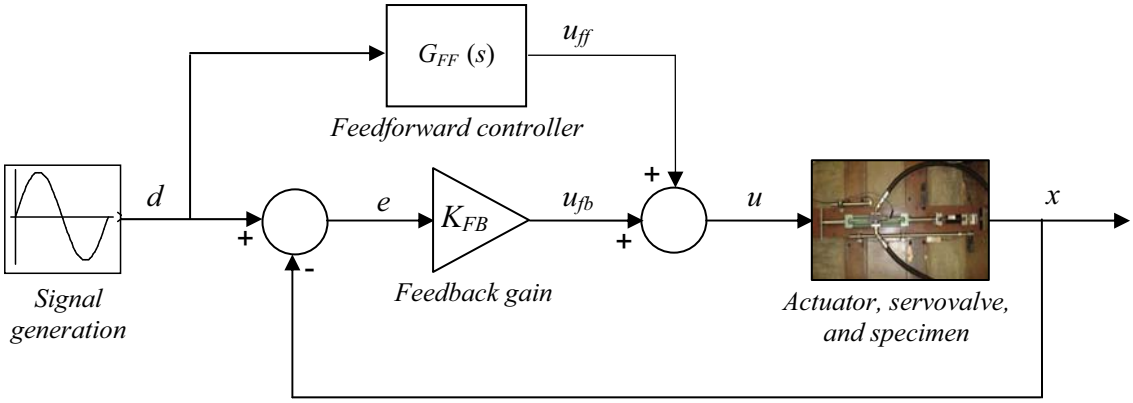

Figure 7.13: Schematic block diagram for experimental verification of feedback-feedforward controller.

Results from the experiments using sinusoidal reference signal demonstrated that the tracking performance of the combined controller surpassed the performance of the feedforward-only controller, producing an error norm of 0.58%, which is about 60% of the one obtained with the feedforward controller alone.

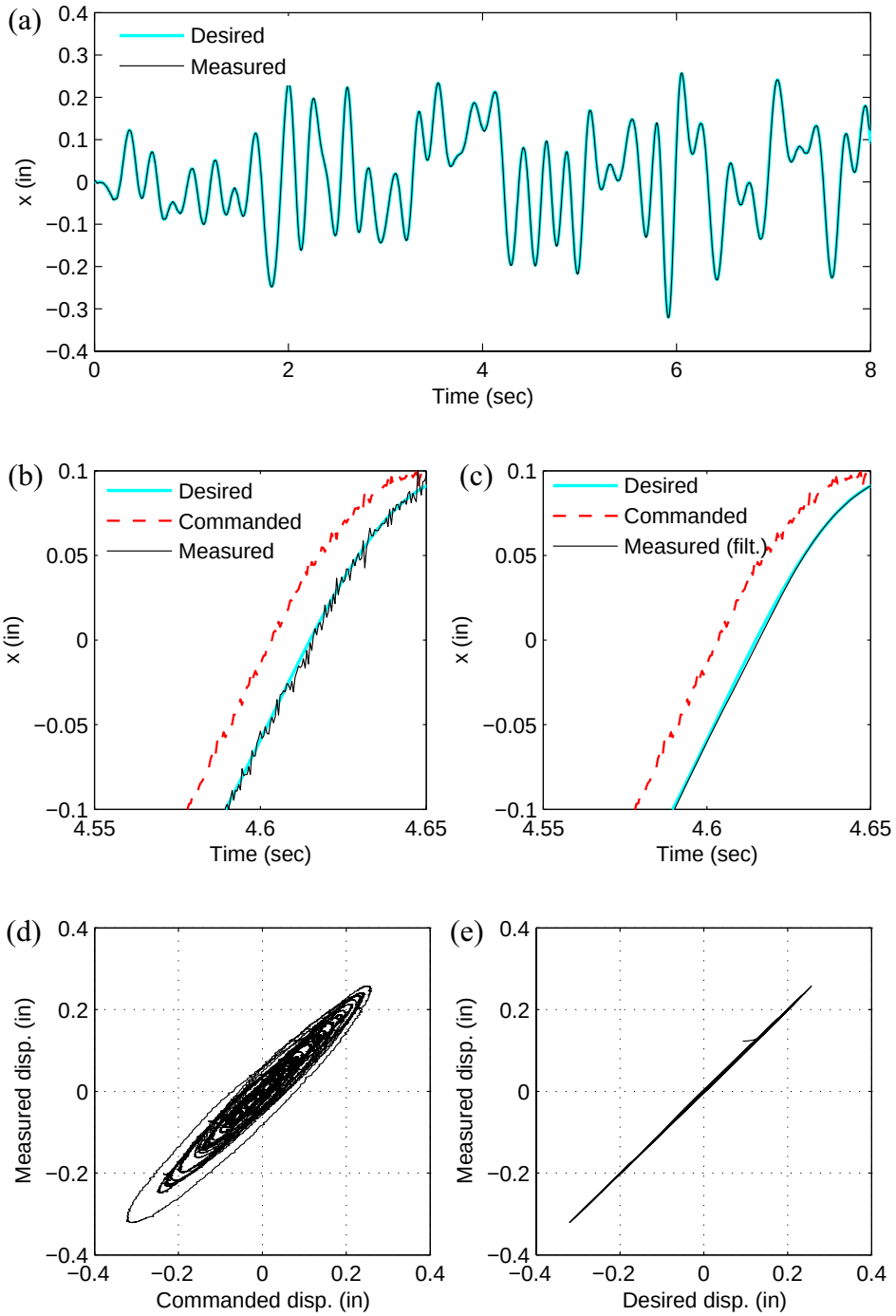

Figure 7.14: Test results for bandlimited white noise reference signal using combined controller with K_{FB} = 0.5: (a) Time histories, (b-c) Close-up views, (d-e) *x*-*y* plots.

Figure 7.14 shows the results for the bandlimited white noise reference signal with the feedback gain set to K_{FB} = 0.5. As can be observed from the time history and *x*-*y* plots, the measured displacement tracks very well the reference signal. The error norm for this test was 1.19%, which is about half of the value obtained with feedforward-only

compensation, demonstrating that the combined feedforward-feedback compensator produces accuracy improvements over the feedforward-only compensator.

Tests were also conducted for different values of the feedback gain, K_{FB}, to observe its effect on the tracking performance and the stability of the controller; values of 0.25, 0.5, 1.0, 1.5, 2.0, and 3.0 were used. As the gain increased, the control error decreased. However, when the gain became large (e.g., 1.5 or larger), oscillatory behavior was observed on the command, u, generated by the controller. This oscillatory behavior had a deleterious effect on the measured force from the MR damper, because this force is greatly dependent on the velocity, and oscillations on the displacement have a large effect on the velocity. When the gain was set to 3.0, the test actually became unstable and was stopped. This result agreed well with the stability limit of the combined controller determined analytical in the previous section (i.e., $K_{FB,max} = 2.72$).

Experiments conducted using the combined feedforward-feedback compensation demonstrate that this technique produces very good results, offering improvements over the feedforward-only compensator. However, because of the closed-loop term, oscillatory behavior and instability can occur when the feedback gain is large. The analytically determined stability limit was shown to correlate well with the experimentally observed limit; therefore, adequate values of the gain can be obtained prior to the experiment.

7.4 Controller for MR damper with variable voltage

The model-based feedforward compensator works very well for cases in which the characteristics of the system to be compensated do not change significantly. When the changes are small, the feedback term helps to accommodate differences between the plant and the model. However, when the changes in the plant are significant, the model-based combined compensator does not provide adequate compensation. When testing semiactive control devices (e.g., MR dampers), the properties of the specimen change substantially in only a few milliseconds, producing variations on the plant dynamics. Compensation of actuator dynamics is, therefore, challenging when testing MR dampers used as semiactive control devices. A compensation method that accommodates changes in the plant dynamics is presented in this section and verified experimentally using the MR damper specimen subjected to changes on the input voltage.

7.4.1 Actuator dynamics for MR damper with variable input voltage

Figure 7.15 shows the frequency response of the actuator for the cases of the MR damper with zero input voltage ($v = V_o$) and with maximum input voltage ($v = V_{max}$). As can be observed, the dynamic response of the actuator is different for both cases. Because the feedforward part of the compensator for actuator dynamics is based on a model of the plant, plant variations must also be considered in controller design.

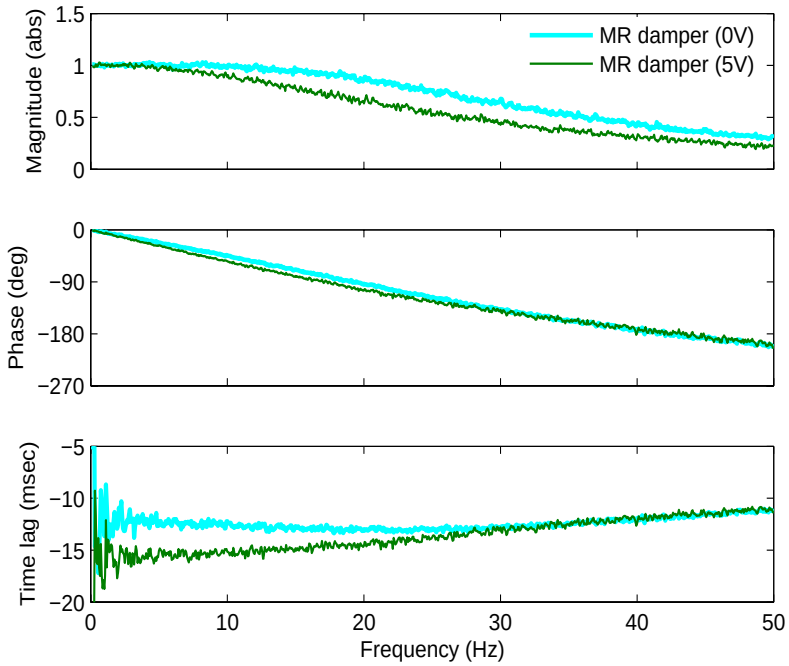

Figure 7.15: Actuator dynamics with MR damper specimen.

Models of actuator dynamics for the cases of zero and maximum input voltage to the MR damper are developed independently. The transfer functions for these two cases (using models with three poles) are given by

$$G_{xu,Vo}(s) = \frac{6118670}{(s+161.5)\ (s^2+222.2s+3.79e4)} \tag{7-21}$$

$$G_{xu,Vmax}(s) = \frac{4056971}{(s+106.1)\ (s^2+221s\ +\ 3.82e4)}. \tag{7-22}$$

For cases in which the input voltage applied to the MR damper switches between V_o and V_{max} during the structural response (e.g., clipped-optimal control algorithm, Dyke, et al., 1996), the compensation algorithm for actuator dynamics developed previously can be modified to take into account the difference in the models for each voltage input. The feedforward part of the controller (which is the one based on the model of the plant) can be selected depending on the voltage command, v, sent to the MR damper, as given by

$$G_{FF}(s) = \begin{cases} G_{FF,Vo}(s) & \text{for} \quad v = V_o \\ G_{FF,Vmax}(s) & \text{for} \quad v = V_{max} \end{cases} \tag{7-23}$$

where the two feedforward controllers, $G_{FF,Vo}$ and $G_{FF,Vmax}$, are designed independently, using the method with modified inverse dynamics presented previously in this chapter.

Although easy to implement, this simple switching compensation algorithm has the disadvantage that produces a discontinuous control signal whenever there is a change

in the voltage command to the MR damper. Therefore, to properly implement the combined compensator, a model that accurately represents the dynamics of the actuator must first be developed when the MR damper specimen is subjected to voltage changes. This model can then be used to develop a feedforward controller that produces smooth control signals.

Model of actuator dynamics with semiactive MR damper specimen

The models of actuator dynamics developed for the two extreme cases of the MR damper voltage can be combined using a smooth transition between the two representative models. In control system theory, this type of smooth transition is called *bumpless transfer* and is typically used when switching between different regulators (Åström & Wittenmark, 1984).

An algorithm was developed in this study to represent the dynamics of the actuator with the MR damper specimen. The algorithm combines individual models of actuator dynamics (i.e., $G_{xu,Vo}$ and $G_{xu,Vmax}$) using a smooth transition. Figure 7.16 shows the block diagram of this model of actuator dynamics.

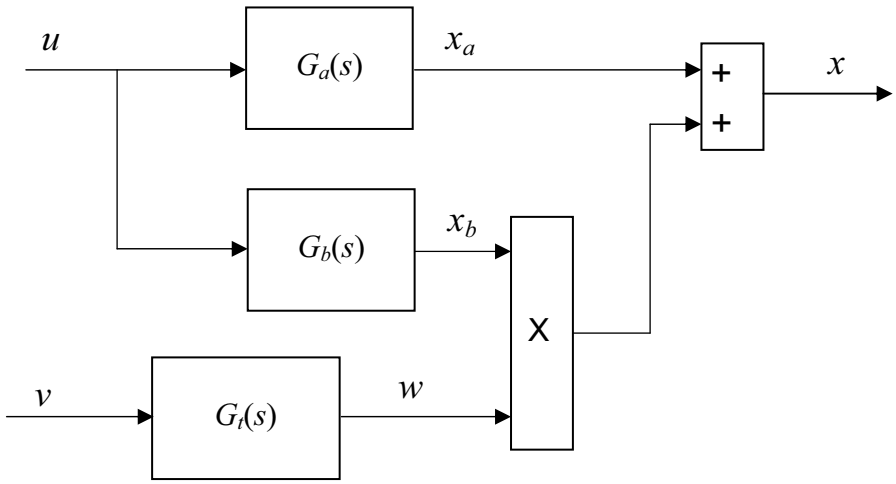

Figure 7.16: Block diagram of algorithm for actuator dynamics with bumpless transfer.

The model is given by the following equations, where capital letters have been used to represent variables in the Laplace domain:

$$X(s) = X_a(s) + X_b(s)W(s) \tag{7-24}$$

where

$$X_a(s) = G_a(s)U(s) \tag{7-25}$$

$$X_b(s) = G_b(s)U(s) \tag{7-26}$$

$$W(s) = G_t(s)V(s) \tag{7-27}$$

and the two transfer functions, $G_a(s)$ and $G_b(s)$, are given by

$$G_a(s) = G_{xu,Vo}(s) \tag{7-28}$$

$$G_b(s) = G_{xu,Vmax}(s) - G_{xu,Vo}(s) \tag{7-29}$$

The transfer function, $G_t(s)$, is used to model the dynamics of the actuator associated with the change in the voltage of the MR damper. This transfer function provides a smooth transition between the two transfer functions, $G_a(s)$ and $G_b(s)$, and is given by

$$G_t(s) = \frac{1/V_{max}}{\tau_t s + 1} \tag{7-30}$$

where τ_t is the time constant of the transfer filter. As the time constant becomes small, the transition becomes faster, approaching a simple switching algorithm, while for large values of the time constant the transition is slower and smoother.

This actuator dynamics algorithm, in addition to providing a smooth transition between the two states, V_o and V_{max}, also provides a representation of the system dynamics for intermediate values of the input voltage, v.

This model was used to represent the dynamics of the actuator with the MR damper considered in this study. The time constant of the transition filter, τ_f, was determined using parameter estimation with measured experimental data. For the experimental data, a random displacement excitation reference signal with a 5 Hz bandwidth was commanded to the actuator, while simultaneously applying a square voltage signal (with 0.5 Hz frequency and changing from 0 to 5 V) to the MR damper. The resulting estimated value of the time constant of the transition filter was $\tau_f = 0.0048$.

Figure 7.17 compares the results obtained from the model and the experimental data. As can be observed, excellent agreement is achieved between the displacement obtained from the model and from the experiment.

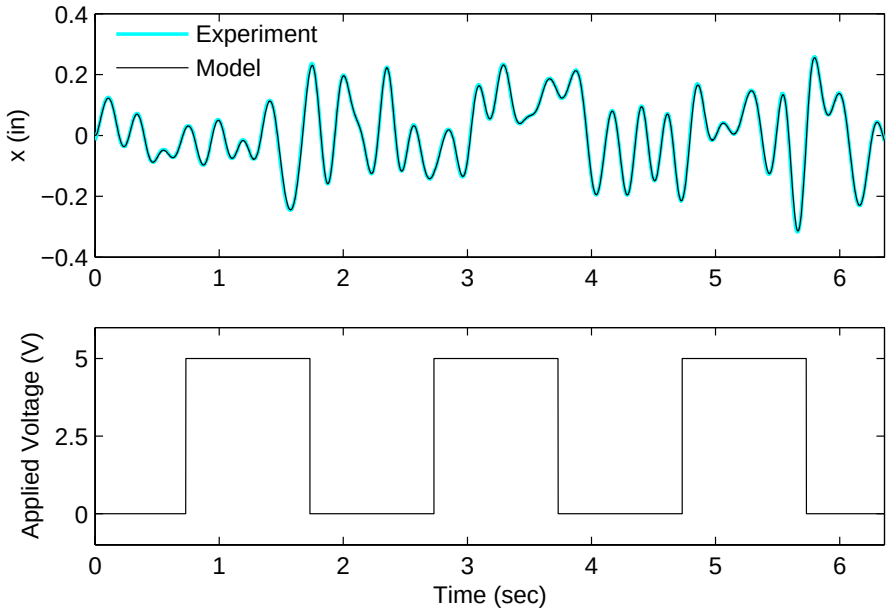

Figure 7.17: Comparison between predicted (model) and experimentally obtained responses of actuator with MR damper specimen under variable input voltage.

7.4.2 Model-based feedforward controller for MR damper with variable input voltage

The actuator dynamics model presented in the previous section is used as a basis to modify the feedforward term of the combined controller to include the effects of changes in plant dynamics. Figure 7.18 shows a schematic block diagram of the modified feedforward term, $G_{FF}(s)$, of the controller that accounts for the variations on actuator dynamics (caused by changes on the applied voltage to the MR damper). As can be observed, the configuration of the controller is similar to the model developed for actuator dynamics with the smooth transition between the two states V_o and V_{max},.

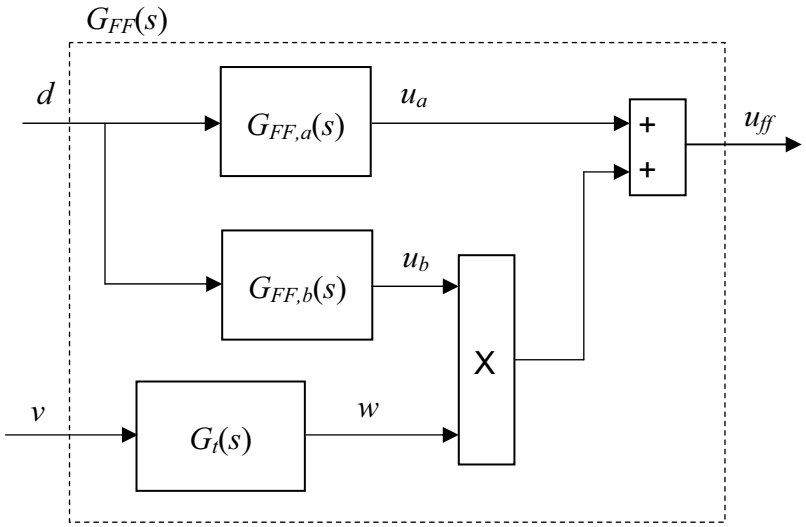

Figure 7.18: Block diagram of feedforward part of combined controller.

The controller is given by the following equations, with capital letters used to represent variables in the Laplace domain:

$$U_{ff}(s) = U_a(s) + U_b(s)W(s) \tag{7-31}$$

where

$$U_a(s) = G_{FF,a}(s)D(s) \tag{7-32}$$

$$U_b(s) = G_{FF,b}(s)D(s) \tag{7-33}$$

$$W(s) = G_t(s)V(s) \tag{7-34}$$

and the transfer functions $G_{FF,a}(s)$, $G_{FF,b}(s)$, and $G_t(s)$ are given by

$$G_{FF,a}(s) = G_{FF,Vo}(s) \tag{7-35}$$

$$G_{FF,b}(s) = G_{FF,Vmax}(s) - G_{FF,Vo}(s) \tag{7-36}$$

$$G_t(s) = \frac{1/V_{max}}{\tau_t s + 1} \tag{7-37}$$

The two individual feedforward terms, $G_{FF,Vo}(s)$ and $G_{FF,Vmax}(s)$, are determined independently using the method of modified inverse dynamics (Section 7.2.2), as given by

$$G_{FF,Vo}(s) = \alpha_{Vo}^{n} \frac{\prod_{i=1}^{n}\left(s - p_{xuVo,i}\right)}{\prod_{i=1}^{n}\left(s - \alpha\, p_{xuVo,i}\right)}, \qquad G_{FF,Vmax}(s) = \alpha_{Vmax}^{n} \frac{\prod_{i=1}^{n}\left(s - p_{xuVmax,i}\right)}{\prod_{i=1}^{n}\left(s - \alpha\, p_{xuVmax,i}\right)} \tag{7-38}$$

where p_{xuVo} and p_{xuVmax} are the poles for the cases of $v = V_o$ and $v = V_{max}$, respectively; n is the number of poles in each model; and α_{Vo} and α_{Vmax} are the values of the parameter α (as defined in the method of modified inverse dynamics, Section 7.2.2) for each of the individual controllers, $G_{FF,Vo}(s)$ and $G_{FF,Vmax}(s)$, respectively.

7.4.3 Experimental verification

The algorithm developed for the feedforward part of the compensator was verified experimentally using the MR damper specimen subjected to changes on the applied voltage. The reference or desired displacement was the same as in the previous cases in this chapter, i.e., a bandlimited white noise with a bandwidth of 5 Hz and an RMS of 0.11 in (2.85 mm). Simultaneously a square voltage signal having 0.5 Hz frequency and changing from 0 to 5 V was applied to the MR damper. Figure 7.19 shows the results from the experiment. As can be observed, the measured displacement matches very well the desired displacement. Figure 7.20 shows a close-up view of the response during a time interval where there is a change in the voltage applied to the damper. The measured displacement tracks the desired displacement very well. The figure also shows the command displacement calculated by the compensator, which does not possess discontinuities at the point of voltage change, i.e., has a smooth or bumpless transition.

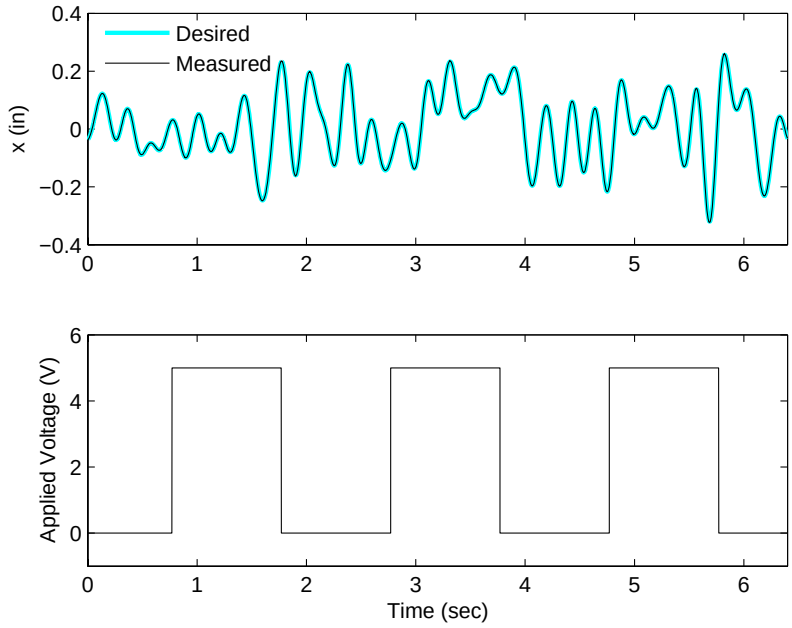

Figure 7.19: Test results of feedforward controller for bandlimited white noise reference signal and variable input voltage to MR damper

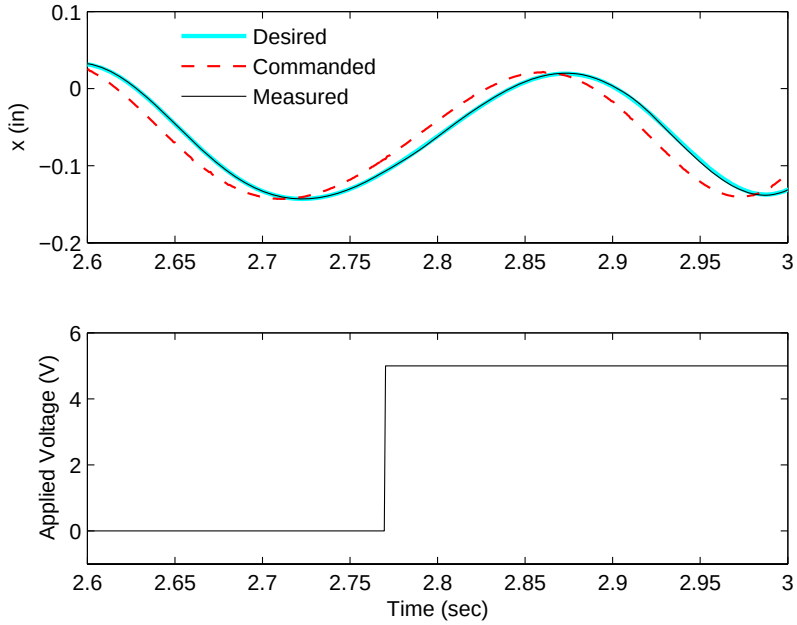

Figure 7.20: Test results of feedforward controller for bandlimited white noise reference signal and variable input voltage to MR damper (close-up view).

Figure 7.21 shows *x*-*y* plots of the response. As can be seen, the plot of measured displacement versus commanded displacement is very close to a straight line, with a slope of one. The error norm for the cases with and without compensation was 2.36% and 23.3%, respectively, demonstrating the good performance of the compensator.

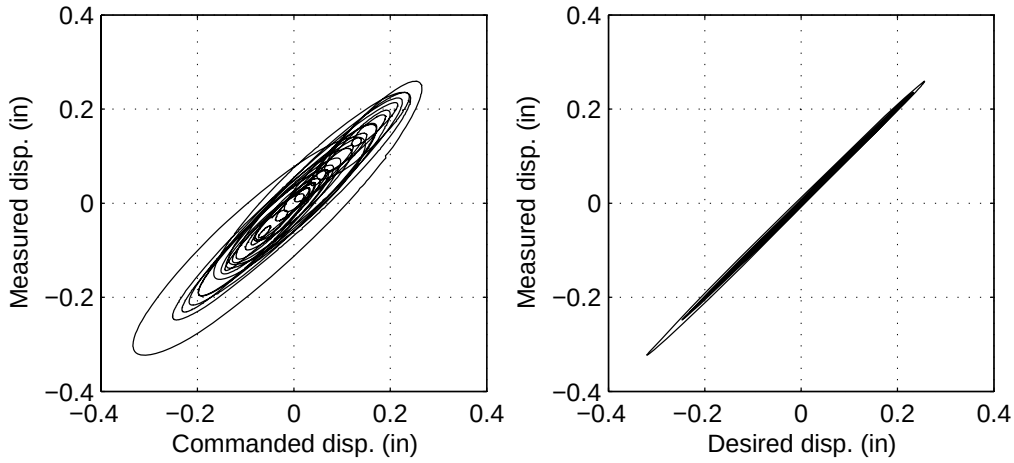

Figure 7.21: Test results of feedforward controller for bandlimited white noise reference signal with variable input voltage to MR damper (*x*-*y* plots).

7.5 Summary

In this chapter, models of actuator dynamics obtained in previous chapters are used to develop model-based strategies to compensate for the effects of actuator dynamics.

First, a feedforward controller is considered. The compensator is based on the inverse of the plant dynamics modified to make the controller realizable. The algorithm provides compensation for both magnitude and phase effects. Experiments conducted demonstrate the good performance of the compensator, which significantly reduces the tracking errors.

A combined feedback-feedforward compensator was then investigated. This compensator combines the good features of both feedforward and feedback strategies. This controller reduces the effect of differences between the estimated model and the actual plant response over the performance of a feedforward-only compensator. This combined feedback-feedforward compensator was verified experimentally; test results demonstrate that this technique produces very good results and improves over the feedforward-only compensator.

A method for modeling and compensating actuator dynamics for cases in which the plant dynamics exhibit significant changes was presented. The algorithm was implemented for the case of an MR damper with variable input voltage. Test results show that the compensator performs very well and is able to provide accurate compensation for actuator dynamics, even when the properties of the MR damper specimen change significantly. As will be shown in the next chapter, this compensation approach facilitates real-time hybrid testing of semi-actively controlled structures employing MR dampers. This approach also provides a framework for compensating actuator dynamics when testing of specimens that exhibit severe changes in material properties (e.g., stiffness and strength degradation).

CHAPTER 8

REAL-TIME HYBRID TESTING OF A SEMIACTIVELY CONTROLLED STRUCTURE

The use of controllable, or semiactive, dampers is increasingly accepted as a means to reduce the response of civil engineering structures due to severe earthquakes and winds. One of the most studied classes of controllable dampers is the magnetorheological (MR) fluid damper. MR dampers offer the reliability of passive devices, yet maintaining the versatility and adaptability of fully active systems (Spencer et al., 1997). MR dampers, as with most semiactive devices, are intrinsically nonlinear; therefore, developing control strategies that can optimally reduce structural responses is challenging (Dyke, 1996). Real-time hybrid testing can be extremely helpful for verifying control strategies for structures that use such devices. This chapter presents an application of the real-time hybrid testing technique to evaluate the response of a semiactively controlled structure that incorporates an MR damper. The purpose of this experiment is to demonstrate how the real-time hybrid testing technique and the model-based compensation approach developed in this study can be used to efficiently and accurately evaluate the response of a structure incorporating a nonlinear rate-dependent semiactive control device. Therefore, no efforts have been placed in this study to develop or improve existing structural control algorithms.

8.1 Structural control

8.1.1 Overview of structural control

In recent years, significant research attention has been devoted to the application and use of structural control devices to reduce the response of civil engineering structures under strong earthquakes and winds. Today, we have many such devices installed in a wide variety of structures (Soong & Spencer, 2002). Passive and active control systems represent the two ends of the spectrum in the use of protective systems for civil structures (Spencer et al., 1997). Passive control systems are limited because they cannot adapt to varying load conditions. Therefore, while passive systems may perform well under the conditions for which they were designed, their efficiency can be limited in other situations (Dyke et al., 1997). Active control systems offer the ability to adapt to changing conditions of both structure and external excitation. However, even though active control systems have been designed and installed in full-scale structures, the engineering community has yet to fully embrace this technology (Yang et al., 2002). This lack of acceptance is in part due to questions regarding cost effectiveness, power requirements, reliability, and the potential that active control systems have to destabilize

the structure (Yang et al., 2002). Semiactive control devices offer an attractive alternative in structural control by providing the adaptability of active control devices while retaining the reliability of passive devices. A semiactive control device is defined as one that cannot increase the mechanical energy of the controlled system (i.e., including both the structure and the control device), but has properties that can be dynamically varied. Because semiactive control devices are inherently stable (in a bounded input – bounded output sense), high authority control strategies may be designed and implemented, which may result in performances that can even surpass that of actively controlled structures (Dyke et al., 1996).

8.1.2 Control algorithm for structure with MR damper

Structural control algorithms based on full-state feedback (i.e., displacements and velocities at every degree-of-freedom) are difficult to implement in practice for full-scale applications. On the other hand, accelerometers have the advantage that they can provide reliable and inexpensive measurements of the absolute acceleration at arbitrary locations of the structure. Dyke et al. (1996) proposed a type of clipped-optimal controller based on acceleration feedback for controlling a structure with an MR damper used as a semiactive control device. This control strategy was verified both numerically (Dyke et al., 1996) and experimentally (Dyke et al., 1997) using a three-story scaled building model equipped with an MR damper and subjected to ground excitation, as shown in Figure 8.1. Results demonstrated that the MR damper and the control strategy were effective in reducing the structural response over a wide range of seismic excitations. Because the semiactive system had the ability to adjust its properties to more effectively control the structure, the proposed clipped-optimal control controller performed better than the two extreme cases of the damper used as a passive device (i.e., no input voltage and constant maximum input voltage to the damper). Furthermore, the semiactive control system was capable of surpassing the performance of a linear active control system, while employing only a small fraction of the power required by the active controller.

Clipped-optimal control based on acceleration feedback

In this section, the clipped-optimal control algorithm based on acceleration feedback that was proposed by Dyke et al. (1996) is reviewed and the design methodology for the controller is provided.

Consider a structure that is subjected to ground excitation and controlled with a single MR damper (see Figure 8.1). The semiactive controller is assumed to be adequate to keep the response of the structure in the linear range, therefore, the equation of motion of the system can be written as

$$\begin{aligned} \dot{\mathbf{z}} &= \mathbf{A}\mathbf{z} + \mathbf{B}f + \mathbf{E}\ddot{x}_g \\ \mathbf{y} &= \mathbf{C}\mathbf{z} + \mathbf{D}f + \mathbf{v} \end{aligned} \tag{8-1}$$

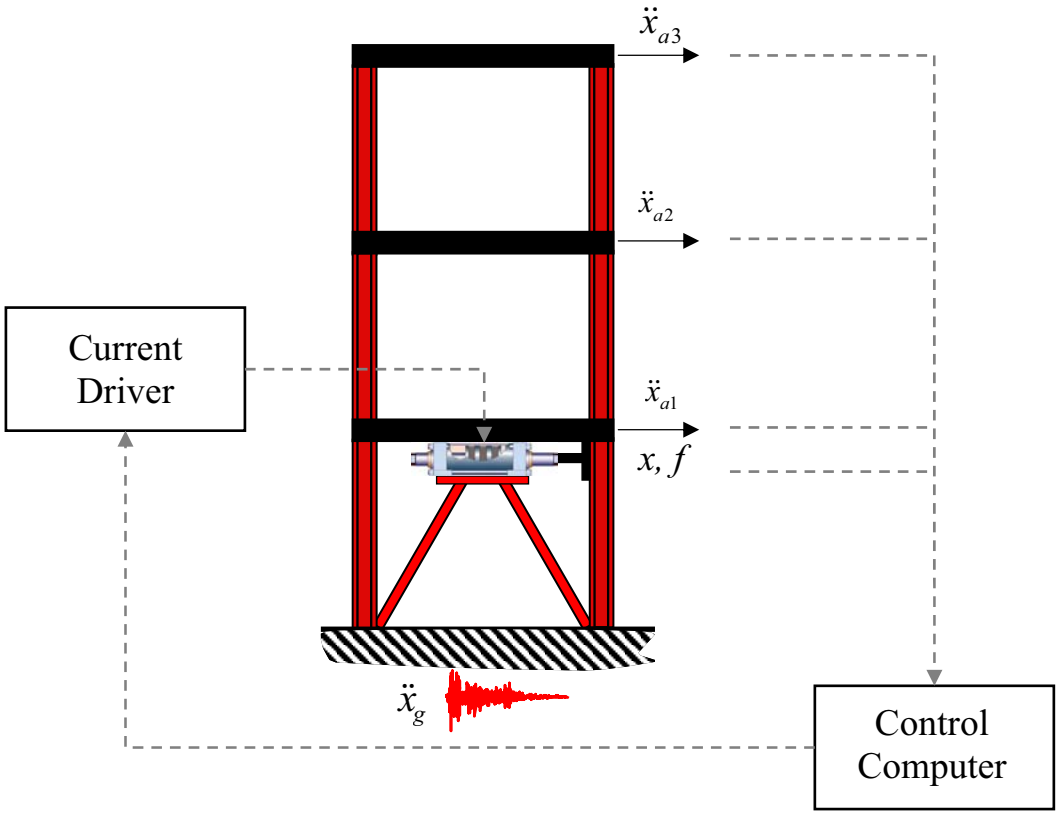

Figure 8.1: Experimental setup of the building model with an MR damper installed (Dyke et al., 1996).

where $\ddot{x}_g$ is the ground acceleration, f is the measured damper force, **z** is the state vector, **y** is the vector of measured outputs, and **v** is the measurement noise vector. The measurements used for feedback are the acceleration at select points on the structure, $\ddot{\mathbf{x}}_\mathbf{a}$, the displacement of the MR damper, x, and the measured control force, f, provided by the MR damper. The vector of output responses from the system is

$$\mathbf{y} = \begin{bmatrix} \ddot{\mathbf{x}}_\mathbf{a} \\ x \end{bmatrix} \tag{8-2}$$

In the clipped-optimal controller, the approach is to append a force feedback loop to induce the MR damper to produce approximately a desired control force, f_c. A linear optimal controller, $\mathbf{K}_c(s)$, is designed using the H_2 / LQG method to determine the desired control force, f_c, based on the measured response vector, **y,** and the measured control force, f, as expressed by

$$f_c = \mathscr{L}^{-1}\left\{-\mathbf{K}_c(s)\mathscr{L}\left(\begin{bmatrix} \mathbf{y} \\ f \end{bmatrix}\right)\right\} \tag{8-3}$$

where $\mathscr{L}\{\cdot\}$ and $\mathscr{L}^{-1}\{\cdot\}$ are the Laplace transform and the inverse Laplace transform, respectively.

The force generated by the MR damper cannot be commanded directly, as it depends on the relative structural displacement and velocity at the point of attachment of the damper (Dyke et al., 1997). However, the voltage, v, and, therefore, the current to the MR damper, can be directly controlled to induce the damper to generate approximately the desired control force. The algorithm for selecting the input voltage to the MR damper is given by the following equation (Dyke et al., 1996)

$$v = V_{\max} H\left\{\left(f_c - f\right) f\right\} \tag{8-4}$$

where $V_{\max}$ is the maximum voltage applied to the current driver, and $H\{\cdot\}$ is the Heaviside step function.

Using the separation principle, the LQG controller can be designed as an LQR (Linear Quadratic Regulator) controller with full-state feedback and a Kalman filter, which provides the estimates of the states based on the measurements. For the H_2 / LQR method, an infinite horizon performance index is selected, which is given by

$$J = \lim_{\tau\to\infty} \frac{1}{\tau} E\left\{ \int_0^{\tau} \left[\left(\mathbf{Cz}\right)^T \mathbf{Q}\left(\mathbf{Cz}\right) + r\, f_c^{\,2} \right] dt \right\} \tag{8-5}$$

where $\mathbf{Q}$ and r are the weights on the output and control, respectively. The Kalman filter equations for the semiactive controlled structure with the MR damper are given by

$$\begin{aligned} \dot{\hat{\mathbf{z}}} &= \mathbf{A}\hat{\mathbf{z}} + \mathbf{B}f + \mathbf{L}(\mathbf{y} - \hat{\mathbf{y}}) \\ \hat{\mathbf{y}} &= \mathbf{C}\hat{\mathbf{z}} + \mathbf{D}f \end{aligned} \tag{8-6}$$

where $\dot{\hat{\mathbf{z}}}$ is the estimated state and $\mathbf{L}$ is the Kalman gain. Assuming the measurement noise to be identically distributed, statistically independent Gaussian white noise processes, the ratio of the spectral densities of measurement noise, ($S_{v_i v_i}$), to process noise ($S_{\ddot{x}_g \ddot{x}_g}$) is defined as

$$\rho = \frac{S_{v_i v_i}}{S_{\ddot{x}_g \ddot{x}_g}} \tag{8-7}$$

Both the LQR gain matrix $\mathbf{K}$ and the Kalman filter gain $\mathbf{L}$ can be determined after solving the corresponding algebraic Ricatti equations. The desired control force determined using the LQG controller is given by

$$f_c = -\mathbf{K}\,\dot{\hat{\mathbf{z}}} \tag{8-8}$$

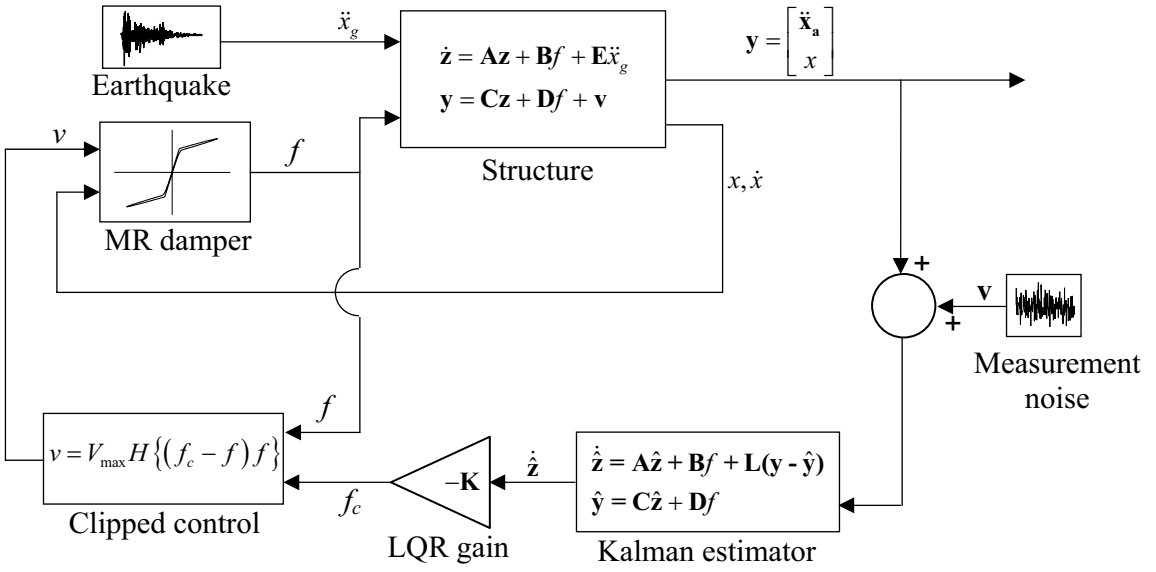

Figure 8.2: Block diagram of semiactive control system.

Figure 8.2 shows a block diagram of the clipped-optimal, semiactive control system. The attractive feature of this control strategy is that the feedback for the controller is based on acceleration measurements, which are readily available, therefore, making the controller implementable for full-scale applications.

8.2 Semi-actively controlled structure

8.2.1 Test structure

The test structure considered in this study is a full-scale version of the structure used by Dyke et al. (1996, 1997). This structure is a three-story steel building which has an MR damper installed between the ground and the first floor (see Figure 8.1). The building is assumed to be equipped with a number of sensors to provide feedback for the control algorithm. These measurements include the absolute acceleration at each of the three floors, the displacement of the damper, and the force applied by the damper to the structure (i.e., control force).

The structure tested by Dyke et al. (1996, 1997) was a scaled model of the prototype building described by Chung et al. (1989). The scaling of the structure was done to conduct the experiments on a small-scale shaking table. However, since the substructure real-time hybrid testing technique is used in this study, there is no need to use a scale model of the entire building. Small-scale physical specimens can be used with the appropriate scaling factors applied only to the physical component. The full-scale properties of the structure were obtained using the parameters of the small-scale model

and scaling factors reported by Dyke (1996). These scaling factors are: length = 7.25, time = 5, mass = 206, force = 60, and acceleration = 0.29.

The dynamic response of the semiactively controlled structure is given by the equation of motion

$$\mathbf{M}_s\ddot{\mathbf{x}} + \mathbf{C}_s\dot{\mathbf{x}} + \mathbf{K}_s\mathbf{x} = G_s f - \mathbf{M}_s L_s \ddot{x}_g \tag{8-9}$$

where the numerical values of the structural parameters are

$$\begin{aligned}
\mathbf{M}_s &= \begin{bmatrix} 115.65 & 0 & 0 \\ 0 & 115.65 & 0 \\ 0 & 0 & 115.65 \end{bmatrix} \text{lb-s}^2/\text{in}, \quad \mathbf{C}_s = \begin{bmatrix} 41.36 & -11.82 & 0 \\ -11.82 & 23.63 & -11.82 \\ 0 & -11.82 & 11.82 \end{bmatrix} \text{lb-s/in} \\
\mathbf{K}_s &= \begin{bmatrix} 56720 & -32330 & 0 \\ -32330 & 64750 & -32330 \\ 0 & -32330 & 32330 \end{bmatrix} \text{lb/in}, \quad G_s = \begin{bmatrix} -1 \\ 0 \\ 0 \end{bmatrix}, \quad L_s = \begin{bmatrix} 1 \\ 1 \\ 1 \end{bmatrix}
\end{aligned} \tag{8-10}$$

The matrices corresponding to the state-space representation of the system are given by

$$\begin{aligned}
\mathbf{A} &= \begin{bmatrix} \mathbf{0} & \mathbf{I} \\ -\mathbf{M}_s^{-1}\mathbf{K}_s & -\mathbf{M}_s^{-1}\mathbf{C}_s \end{bmatrix}, \quad \mathbf{B} = \begin{bmatrix} \mathbf{0} \\ -\mathbf{M}_s^{-1}G_s \end{bmatrix}, \quad \mathbf{E} = \begin{bmatrix} \mathbf{0} \\ -L_s \end{bmatrix} \\
\mathbf{C} &= \begin{bmatrix} -\mathbf{M}_s^{-1}\mathbf{K}_s & -\mathbf{M}_s^{-1}\mathbf{C}_s \\ 1\ 0\ 0 & 0\ 0\ 0 \end{bmatrix}, \quad \mathbf{D} = \begin{bmatrix} -\mathbf{M}_s^{-1}L_s \\ 0 \end{bmatrix}
\end{aligned} \tag{8-11}$$

The natural frequencies of the structure corresponding to the first, second, and third mode are 1.09 Hz, 3.17 Hz, and 4.74 Hz, respectively, with corresponding damping ratios of 0.31%, 0.62%, 0.63%, respectively.

The LQG controller was designed using the same parameters as Dyke et al. (1996) in which the **Q** matrix was selected to weight the absolute acceleration of third floor (i.e., all elements of **Q** equal zero, except for $\mathbf{Q}_{33}$ = 1), $r = 10^{-17}$, and $\rho = S_{v_i v_i} \big/ S_{\ddot{x}_g \ddot{x}_g} = 0.02$. Calculation of the LQR and Kalman gains (i.e., **K** and **L**, respectively) was performed using the control toolbox in MATLAB.

8.2.2 MR Damper

The MR damper specimen used for the experiments is the same one as described previously in this report. Because this is a small-scale damper, a length scale factor, S_L = 7.25, and force scale factor, S_F = 60, are used during the real-time hybrid experiments to relate the response of this component to the rest of the structure.

Model of the MR damper

A model that represents the behavior of the MR damper (including voltage changes) is necessary to predict the behavior of the semiactively controlled structure and allow comparison with the results from the real-time hybrid experiments. The Bingham model (presented in Chapter 5) predicts reasonably well the force-displacement behavior of the MR damper; however, the force-velocity response has considerable errors, especially for velocities near zero (Spencer et al., 1997). When the velocity is small and presents frequent sign changes, the damper force predicted by the model fluctuates significantly (due to the friction element in the model). Therefore, although this model may be adequate for response analysis; it is not adequate for control analysis (Spencer et al., 1997). An alternative model, which is simple to implement and predicts well the behavior of the MR damper, is depicted in Figure 8.3 (Spencer et al., 1997).

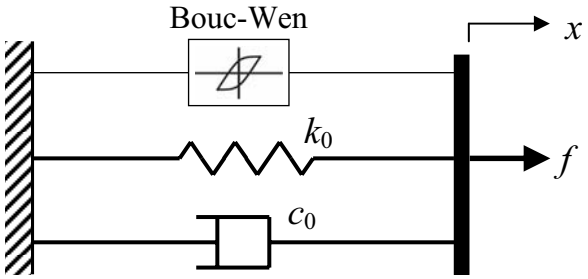

Figure 8.3: Bouc-Wen model of MR damper.

This mechanical idealization is based on the Bouc-Wen model where the damper force is given by

$$f = c_0\dot{x} + k_0\left(x - x_0\right) + \alpha z \tag{8-12}$$

and the evolutionary variable z of the Bouc-Wen model is governed by

$$\dot{z}(t) = -\gamma\left|\dot{x}(t)\right|\left|z(t)\right|^{n-1} z(t) - \beta\dot{x}(t)\left|z(t)\right|^{n} + A\dot{x}(t) \tag{8-13}$$

The parameters γ, β, n, and A control the shape of the hysteretic loop. Similar to the model presented by Spencer et al. (1997), the effect of changes in the voltage applied to the current driver (and, therefore, in the magnetic field in the MR damper) are represented using the following expressions

$$\alpha = \alpha\left(u\right) = \alpha_a + \alpha_b u \tag{8-14}$$

$$k_0 = k_0\left(u\right) = k_{0a} + k_{0b}u \tag{8-15}$$

$$c_0 = c_0\left(u\right) = c_{0a} + c_{0b}u \tag{8-16}$$

where u is the output of a first-order filter introduced to model the dynamics of the MR damper and is given by

$$\dot{u} = -\eta\left(u - v\right) \tag{8-17}$$

The parameters for the Bouc-Wen model were determined using nonlinear, least-squares parameter estimation to fit experimentally measured response of the damper. The experimental data included sinusoidal and bandlimited white noise tests with constant input voltage applied to the damper (0 and 5 V). The tests were similar to the ones described in Section 5.3.2 for the 0 V case, as well as tests in which the input voltage was varied during the experiment (between 0 and 5 V). The resulting parameters of the model are presented on Table 8.1.

Table 8.1: Parameters for MR damper model

Parameter	Value	Unit
α_a	0.190	lb/in
α_b	1.043	lb/in-V
C_{0a}	4.308	lb-s/in
C_{0b}	4.070	lb-s/in-V
K_{0a}	6.496	lb/in
K_{0b}	8.243	lb/in
x_0	0	in
γ	2.716	in^{-2}
β	2.713	in^{-2}
A	10346	-
N	2	-
η	57	s^{-1}

Comparison between the responses obtained from the Bouc-Wen model and the experiment is presented in Figure 8.4 (for a 5 Hz sinusoidal displacement) and in Figure 8.5 (for a 5 Hz bandlimited white noise displacement). The input voltage to the MR damper was set to change from 0 to 5 V at a frequency of 0.5 Hz. As can be observed, the predictions by the model match very well with the experimentally measured response.

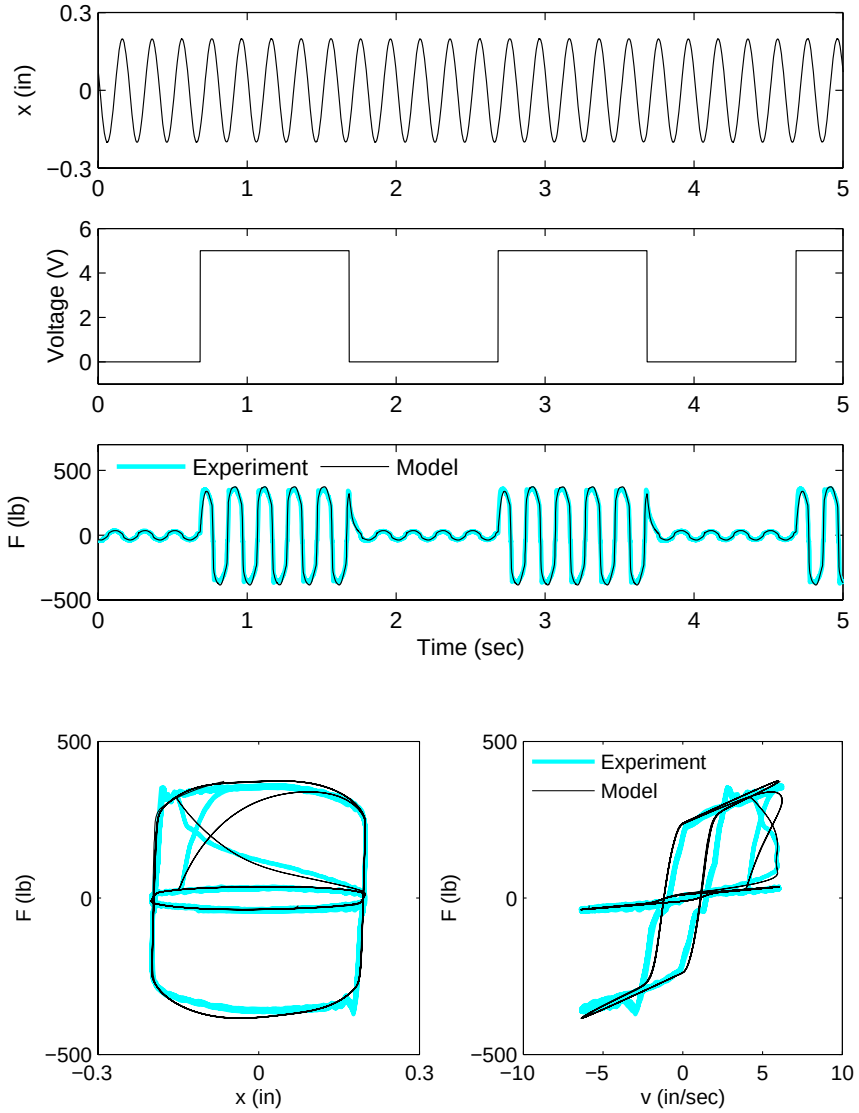

Figure 8.4: Comparison between response from the Bouc-Wen model and experimentally measured data (5 Hz sinusoidal displacement).

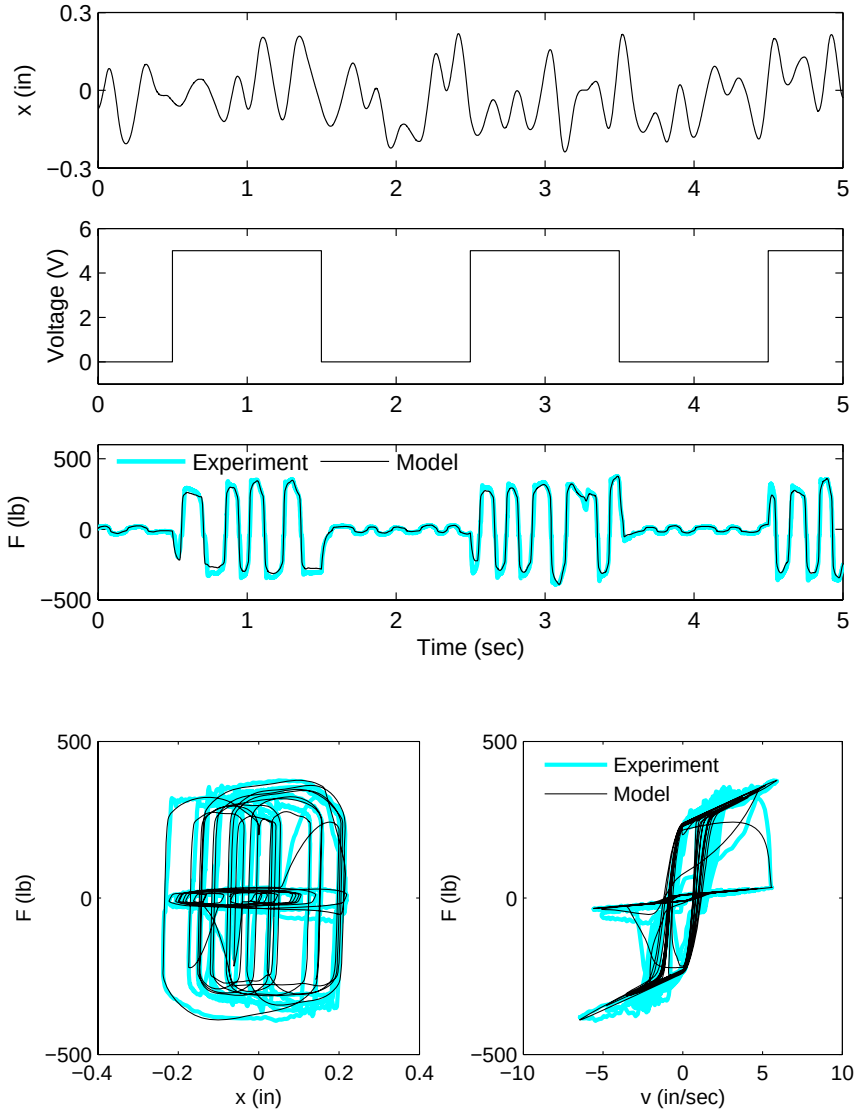

Figure 8.5: Comparison between response from the Bouc-Wen model and experimentally measured data (5 Hz bandlimited white noise displacement).

8.3 Real-time hybrid experiments

Real-time hybrid testing is used to experimentally verify the response of the semiactively controlled building. As shown in Figure 8.6, the structure is divided into two substructures: the MR damper, which is tested experimentally (physical substructure) and the rest of the structure, which is modeled numerically (numerical substructure).

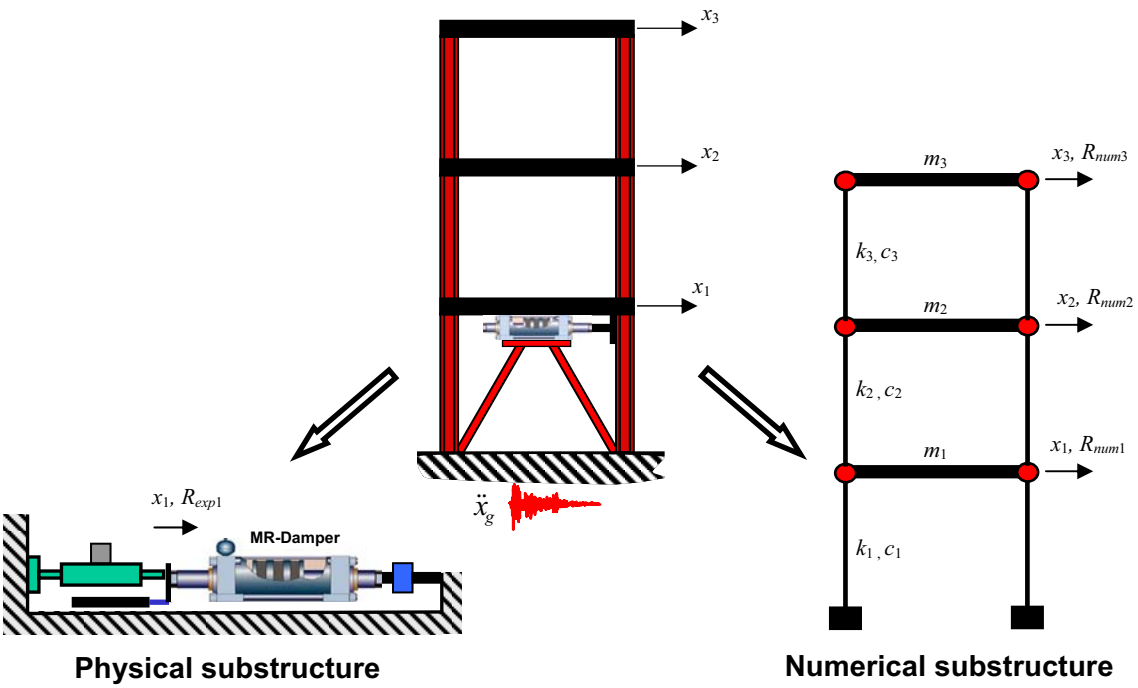

Figure 8.6: Schematic of real-time time hybrid experiment of a semiactively controlled structure.

The structure was subjected to the NS component of the 1940 El Centro earthquake. The ground acceleration record is shown in Figure 8.7. An amplitude scale factor of 0.8 was used. Compensation for actuator dynamics was performed using the model-based approach presented in Chapter 7. The parameters for the feedforward compensator were the same as those used in the previous chapter. The feedback gain of the combined compensator was set to zero, i.e., providing feedforward compensation only. The model of the structure, structural control algorithms, and compensation for actuator dynamics were implemented in SIMULINK using continuous time systems. Numerical integration was performed using the fourth-order Runge-Kutta solver of SIMULINK with a fixed time step of 0.0005 sec (i.e., 2,000 Hz sampling frequency).

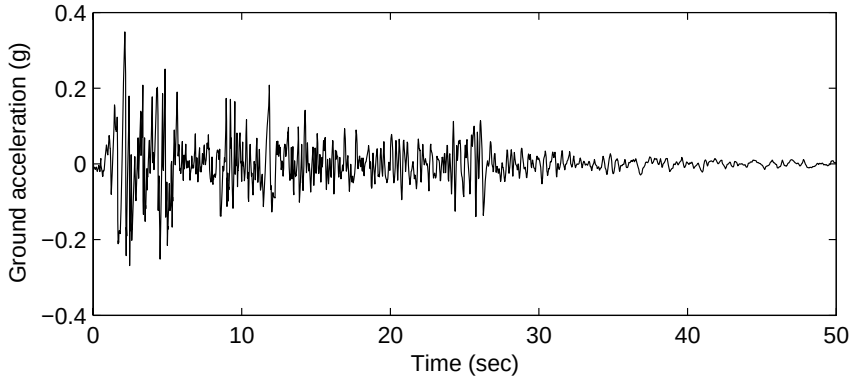

Figure 8.7: Ground acceleration record (NS component of the 1940 El Centro earthquake).

During the real-time hybrid experiments, all of the states (displacements, and velocities at every degree-of-freedom) and accelerations are available for feedback to the LQG controller (because they can be calculated numerically at each time step). However, using all of these parameters as available measurements is not realistic for the full-scale implementation. Therefore, the same measurements that were used by Dyke et al. (1996, 1997) during the shaking-table experiments (i.e., absolute accelerations, damper force, and damper displacement) are used as feedback to the controller during the real-time hybrid experiment. The remaining states of the system required by the controller are estimated using the Kalman filter.

Four different cases of structural control are considered: (a) *uncontrolled structure*: structure without MR damper, (b) *passive-OFF* case: MR damper used as a passive device with zero input voltage, (c) *passive-ON* case: MR damper used as a passive device with constant maximum input voltage (i.e., 5 V), and (d) *controlled* case: voltage to MR damper varies during the experiment as determined by the clipped-optimal control algorithm.

The response of the structure without the MR damper (uncontrolled case), was determined analytically using only numerical simulation. For the other three cases, which use the MR damper (passive-OFF, passive-ON, and clipped-optimal control), the response of the structure was determined from real-time hybrid experiments. Because the significant responses occur during the initial portion of the earthquake, only the first 20 seconds of the response were considered. For each case, the response of the building was also determined numerically using the Bouc-Wen model of the MR damper with the parameters presented previously.

8.3.1 Experimental results

The results from the real-time hybrid experiments as well as the analytically predicted responses are presented in Figures 8.8, 8.9, and 8.10. The hysteretic behavior of the damper for the clipped-optimal control case is shown in Figure 8.11. As can be observed from the time histories and force-displacement/velocity plots, good agreement is found between the experimental and analytical results. Some small discrepancies are assumed to be caused by differences between the model used for the MR damper and the actual specimen.

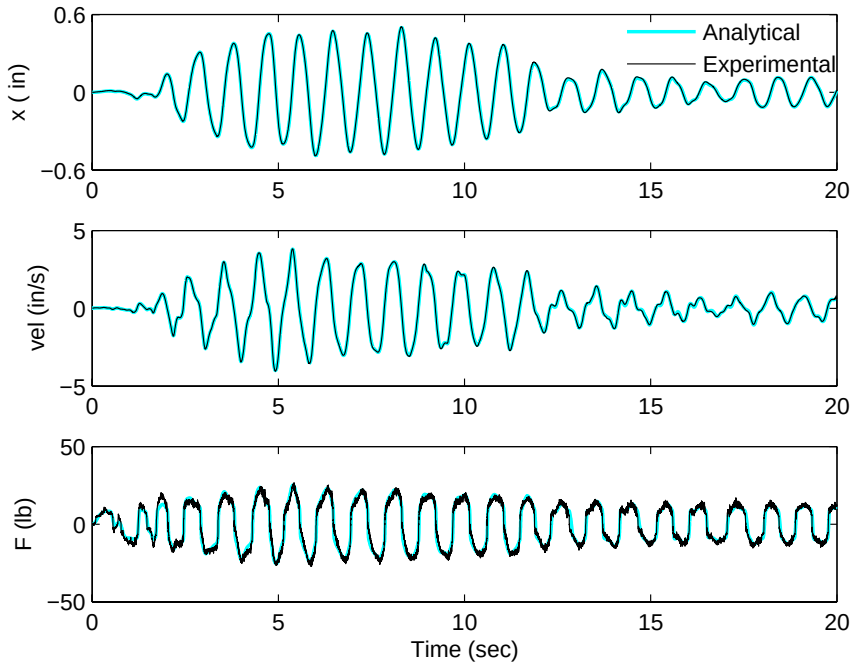

Figure 8.8: Results from real-time hybrid experiment for passive-OFF case.

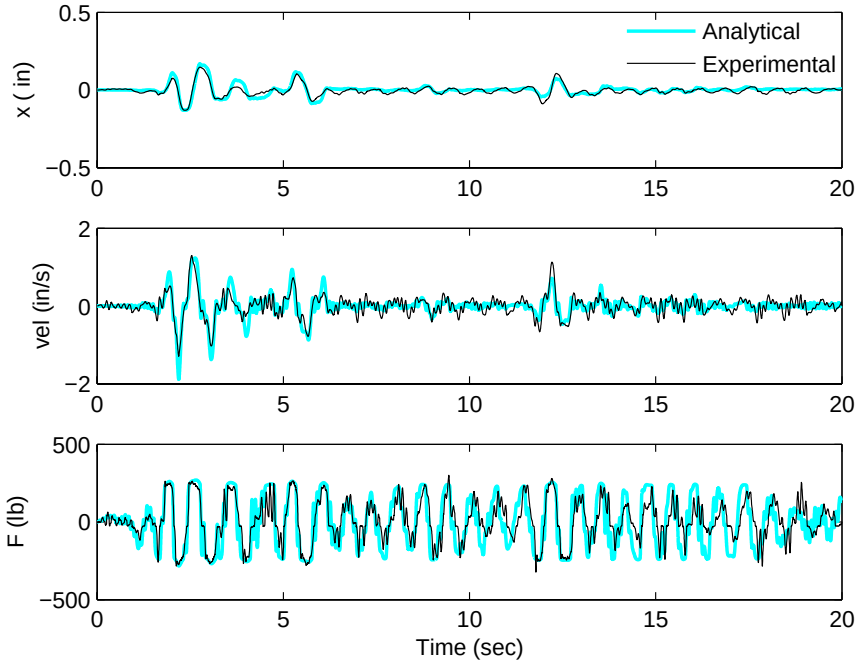

Figure 8.9: Results from real-time hybrid experiment for passive-ON case.

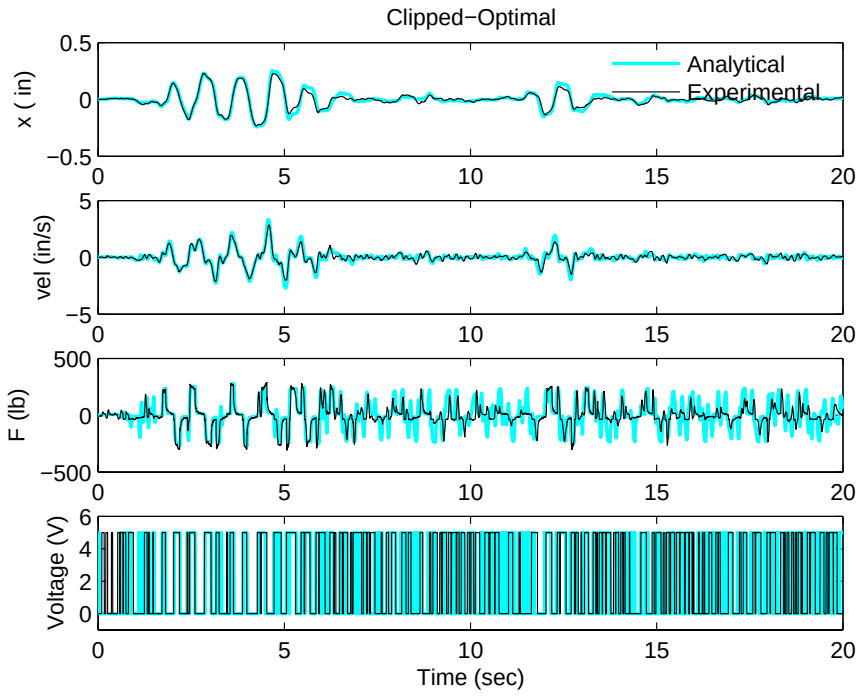

Figure 8.10: Results from real-time hybrid experiment for clipped-optimal case.

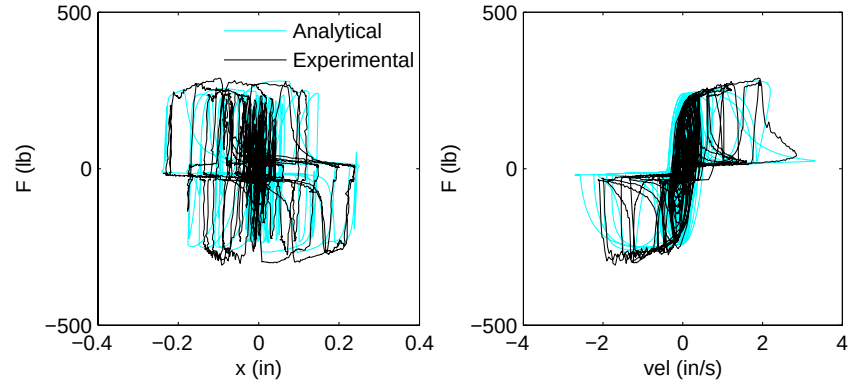

Figure 8.11: Results from real-time hybrid experiment for clipped-optimal case (force-displacement and force-velocity plots).

8.3.2 Performance of model-based actuator dynamics compensation

The model-based compensator for actuator dynamics performed very well during the real-time hybrid experiments for both the case of constant and variable input voltage to the MR damper. Figure 8.12 shows a comparison between the desired or target displacement and the measured displacement for the case of variable voltage to the damper (i.e., clipped-optimal case). As can be observed, except for some small amplitude sensor noise existing on the measured displacement, the two displacements are almost indistinguishable, demonstrating the good performance of the compensator.

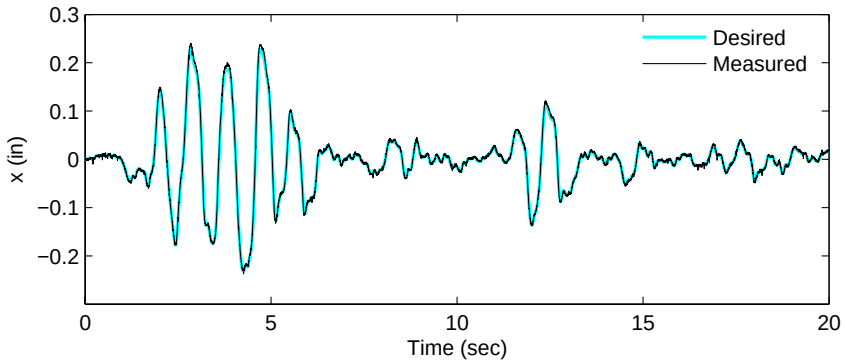

Figure 8.12: Results from model-based compensator during the real-time hybrid test of clipped-optimal case.

The effect of actuator dynamics on real-time hybrid experiments (i.e., the introduction of an equivalent negative damping) is more severe on systems with low structural damping than in systems with high damping. For this reason, some researchers have conducted real-time hybrid testing of systems with damping devices (e.g., MR dampers) without using compensation (see Wu et al., 2006). When the natural frequencies of the test structure are small or the forces generated from the test specimen are small compared to the forces from the numerical substructure, the effect of actuator dynamics is in general also small. Figure 8.13 shows the results of a real-time hybrid test for the passive-OFF case conducted without using compensation for actuator dynamics. Comparison of this figure with the one for the case with-compensation (Figure 8.8) shows that the two results are almost identical, therefore, the effect of actuator dynamics is very small for this case where the damper forces are small. However, when the forces from the test specimen are large, the effects of actuator dynamics become significant even for high damping devices. Figure 8.14 shows the results from the real-time hybrid test for the passive-ON case conducted without using actuator dynamics compensation. As can be seen, the results without compensation are poor (with significant oscillatory behavior) and very different from the ones using the compensation (Figure 8.9). These results demonstrate that accurate actuator dynamics compensation is necessary even when testing systems with high damping.

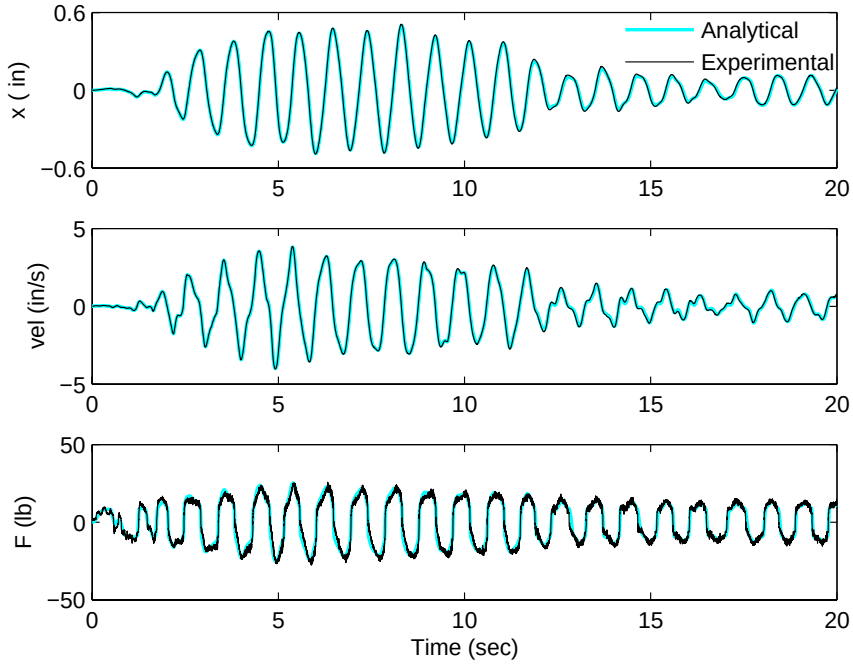

Figure 8.13: Results from real-time hybrid experiment without actuator dynamics compensation for passive-OFF case.

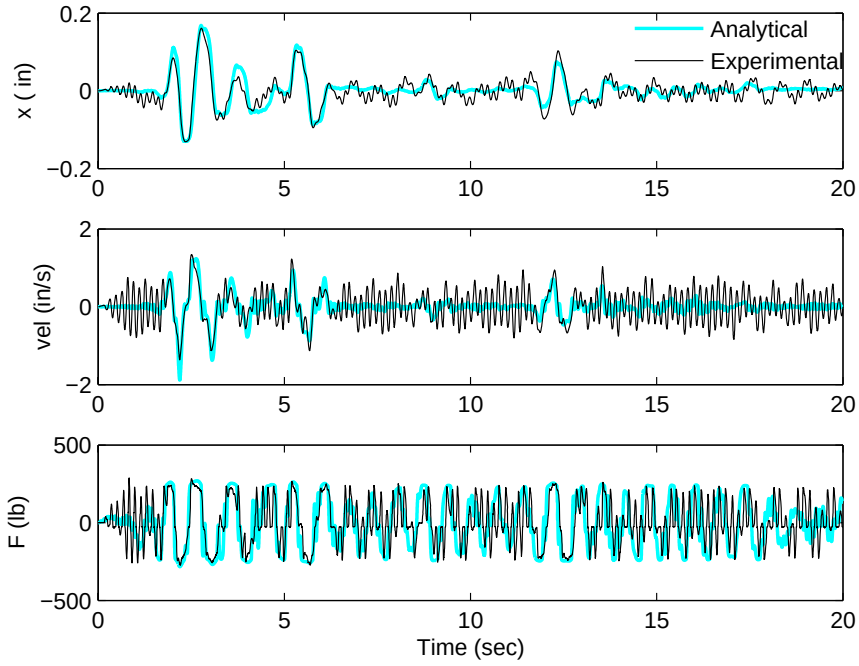

Figure 8.14: Results from real-time hybrid experiment without actuator dynamics compensation for passive-ON case.

8.4 Summary

In this chapter, real-time hybrid testing was used to evaluate the response of a structure equipped with an MR damper. The damper was used for both passive and semiactive control.

Experimental results correlated well with predictions from numerical simulations using a model of the MR damper. Some small differences between the two responses were attributed to differences existing between the estimated model of the MR damper and the actual specimen, highlighting the advantages of the real-time hybrid experiment where the response is obtained directly from the physical specimen.

Soong and Spencer (2002) recognized that in order for innovative vibration control systems to be widely accepted in structural engineering, analytical, and experimental techniques to realistically assess the performance of theses devices and their impact on the structural system are needed. The experiments presented in this chapter demonstrate that real-time hybrid testing provides an efficient and accurate way of testing devices for vibration control including passive and semiactive devices. This testing method allowed evaluation of the response of the device (MR damper), the control strategies, and the performance of the overall structural system. By using the substructuring technique, the overall cost and time of the experiment was greatly reduced. Real-time hybrid testing also allows investigation of the response a structure with an MR damper for cases when the structural system undergoes inelastic deformation. Therefore, this testing technique allows for assessment of the applicability and robustness of controllers designed based on a linear model of the structure, to cases of nonlinear response. Furthermore, since the MR damper does not suffer damage during the experiment, real-time hybrid testing allows parametric studies of the structural system to be conducted.

CHAPTER 9

MODEL-BASED FILTERING IN HYBRID TESTING

In hybrid testing, the experimental restoring forces are measured and fed back in the solution of the equations of motion; thus, errors have a direct and cumulative effect on the computed displacement response. Indeed, these errors can propagate throughout the entire test, adversely affecting the results, and in some cases, even producing damage of the test specimen (Mahin et al., 1989). The hybrid test method is, therefore, more sensitive to experimental errors than are other methods in which a predefined displacement command history is used (i.e., quasi-static and shake-table testing). Techniques to reduce the impact of experimental errors will greatly improve this testing method. This chapter presents background information about the experimental errors encountered in hybrid testing, initial studies of a filtering technique developed for minimizing random errors in hybrid testing (based on a widely used method for linear filtering), and analyses and experiments conducted to verify the method.

9.1 Experimental errors

Common sources of experimental errors encountered in hybrid testing include: inaccurate displacement control of the hydraulic actuators, flexibility in the test setup and reaction frame, calibration errors in the instrumentation, noise generated in the instrumentation and analog to digital converters, precision errors due to limited range of the instrumentation, frictional force in the actuator connections, force relaxation, and strain-rate effects.

The effect of the errors in hybrid testing is, in general, different, depending on whether the errors are systematic or random in nature. Systematic errors are much more severe than random errors. Systematic position control errors in the actuators can be due to overshoot and undershoot. Systematic overshooting numerically dissipates energy in the simulation, resulting in an apparent high-system damping, while systematic undershooting numerically adds energy to the system, resulting in a negative damping, which can even cause system instability (Mahin et al., 1989).

Stiff structures may introduce large force errors at each step, even if the displacements are fairly accurately controlled, as small errors in the displacement produce large force errors. In cases involving stiff multi-degree-of-freedom systems, force fluctuations can occur due to the difficulty in accurately controlling the displacements (Thewalt & Mahin, 1994).

Force relaxation and strain-rate effects also produce systematic errors in the restoring force measurement, especially when yielding occurs. Continuous and real-time hybrid testing have been used to reduce these effects.

Typically the instrumentation used in a test facility has limited precision. If the measured quantity is small compared to the precision of the instruments used, the results will be inaccurate. When the physical substructure involves quantities with different orders of magnitude (e.g., displacement and rotation), assuring that all the quantities are precisely controlled and measured becomes challenging. The MOST experiment (Spencer et al., 2004) and tests conducted by Blakeborough et al. (2001) have demonstrated the difficulty of imposing simultaneously a displacement and a rotation using two coupled actuators. This limitation potentially imposes a severe constraint on the types of tests and scales that can be conducted at a testing facility.

Several techniques have been used to minimize the effect of errors in hybrid testing, e.g., improving displacement control, correcting the measured restoring force for the error between the target and measured displacements using the initial elastic stiffness (so-called *I-modification*), adding numerical damping (especially in the higher modes) to offset the effect of spurious negative damping, and the use of classical lowpass filters to reduce high frequency noise in the measurements. However, some intrinsic noise is unavoidably present on the measurements. Techniques for reducing the effect of these errors will allow increasing the accuracy and types of tests that can be conducted.

9.2 Model-based filtering

Filtering can be viewed as a procedure for noise removal from a measured process to reveal or enhance information about some quantity of interest. All measured data includes some degree of noise from various possible sources. Often, classical filters (e.g., lowpass, bandpass, highpass, or bandreject filters) can be employed to achieve an acceptable result in basic problems. In more complex problems, however, these types of filters fall short of achieving an optimal or best estimate of the desired signal. To achieve an optimum linear filtering solution, model-based filters, such as the Kalman filter, may be used (Zaknich, 2005). Classical filters have the disadvantage of introducing a phase lag on the filtered results, which is undesirable in pseudodynamic and real-time hybrid testing.

9.2.1 The Kalman filter

The Kalman filter was first introduced for discrete-time processes by Kalman (1960), and later extended for the continuous-time case (Kalman & Bucy, 1961). The Kalman filter implements a predictor-corrector type estimator that, under the assumption of the system being linear and the excitation and measurement noise being Gaussian random process, is optimal in the sense that it minimizes the variance of the estimated error covariance in the process (Stengel, 1986). The Kalman filter takes into account system dynamics and inputs, and incorporates measurements and measurement-error statistics into the estimate (Stengel, 1986). The Kalman filter has been used in a broad range of applications and represents the most widely applied result to emerge from the state variable approach of “modern control” theory (Zaknich, 2005). In this study, the Kalman filter is used to filter experimental errors in hybrid testing.

Kalman filter formulation

Consider a linear dynamical system with noise that is represented using the following state-space model

$$\begin{aligned} \dot{\mathbf{z}} &= \mathbf{A}\mathbf{z} + \mathbf{B}\mathbf{u} + \mathbf{G}\mathbf{w} \\ \mathbf{y} &= \mathbf{C}\mathbf{z} + \mathbf{D}\mathbf{u} + \mathbf{v} \end{aligned} \tag{9-1}$$

where **w** and **v** are the process (*input*) and measurement (*output*) noises, respectively, considered white, zero-mean Gaussian random processes and specified by their spectral density matrices, $\mathbf{Q}(t)$ and $\mathbf{R}(t)$, respectively, which are defined as follows

$$E[\mathbf{w}(t)\,\mathbf{w}^{\mathrm{T}}(\tau)] = \mathbf{Q}(t)\,\delta(t-\tau) \tag{9-2}$$

$$E[\mathbf{v}(t)\,\mathbf{v}^{\mathrm{T}}(\tau)] = \mathbf{R}(t)\,\delta(t-\tau) \tag{9-3}$$

The Kalman filter has the general structure of a state estimator, producing an estimate, $\hat{\mathbf{z}}$, of the actual state, **z,** based on the noisy measurements, **y**. The equations of the estimator are formed by including a model of the system dynamics (represented by the **A** and **B** system matrices) and by feeding back the estimation error signal (difference between measured and estimated outputs). The structure of the Kalman filter is given by the block diagram shown in Figure 9.1.

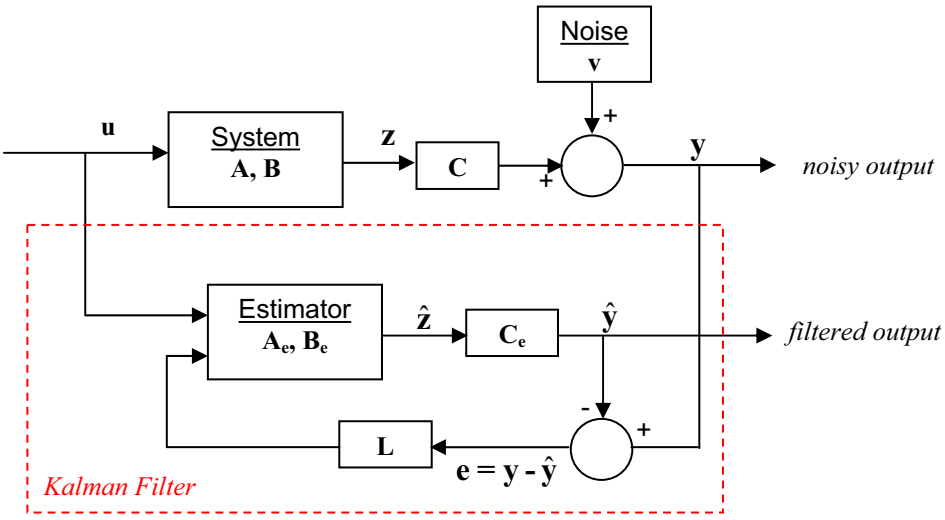

Figure 9.1: Kalman filter block diagram.

Notice that the matrix **D** has been omitted (i.e., **D = 0**), because in the proposed application the input to the system does not have a direct path to the measurements. The equation for the estate estimator is then given by

$$\dot{\hat{\mathbf{z}}} = \mathbf{A}\hat{\mathbf{z}} + \mathbf{B}\mathbf{u} + \mathbf{L}(\mathbf{y} - \hat{\mathbf{y}}) \tag{9-4}$$

where **L** is the estimator gain selected to achieve a satisfactory estimation performance. Analyzing the right-hand side of this equation, the first and second terms give the state estimate (*prediction*), while the last term, called the *corrector* term, represents how much to correct the estimated state based on the measurement. After grouping and rearranging terms, the following estimator equations are obtained:

$$\begin{aligned} \dot{\hat{\mathbf{z}}} &= \mathbf{A}_e\hat{\mathbf{z}} + \mathbf{B}_e\begin{bmatrix}\mathbf{u}\\ \mathbf{y}\end{bmatrix} \\ \hat{\mathbf{y}} &= \mathbf{C}_e\hat{\mathbf{z}} \end{aligned} \tag{9-5}$$

where

$$\mathbf{A}_e = (\mathbf{A} - \mathbf{L}\mathbf{C}_e), \qquad \mathbf{B}_e = [\mathbf{B} \quad \mathbf{L}] \tag{9-6}$$

In the Kalman filter, the matrix gain, **L,** is selected to minimize the error covariance by properly blending prior information and current measurements. Given knowledge of the system, its inputs, and its uncertainties, minimizing this error covariance amounts to minimizing the mean-square estimation error, which is assumed to make $\hat{\mathbf{z}}$ most likely **z** (Stengel, 1986). The Kalman filter is an optimal linear estimator if the stochastic distributions are Gaussian (Zaknich, 2005).

The Kalman filter gain is calculated using the following equation (Stengel, 1986)

$$\mathbf{L}(t) = \mathbf{P}(t)\mathbf{C}^T(t)\mathbf{R}^{-1}(t) \tag{9-7}$$

where the error covariance estimate, $\mathbf{P}(t)$, is defined as

$$\mathbf{P}(t) = E\left[\left(\mathbf{z}(t) - \hat{\mathbf{z}}(t)\right)\left(\mathbf{z}(t) - \hat{\mathbf{z}}(t)\right)^T\right] \tag{9-8}$$

and is calculated from the following Riccati equation

$$\dot{\mathbf{P}}(t) = \mathbf{A}(t)\mathbf{P}(t) + \mathbf{P}(t)\mathbf{A}^T(t) + \mathbf{G}(t)\mathbf{Q}(t)\mathbf{G}(t) - \mathbf{P}(t)\mathbf{C}^T(t)\mathbf{R}^{-1}(t)\mathbf{C}(t)\mathbf{P}(t) \tag{9-9}$$

For the case of time-invariant systems with stationary noises, $\dot{\mathbf{P}}(t) = \mathbf{0}$, and the Kalman filter gain becomes time invariant and can be precomputed based on the noise statistics, **Q** and **R**.

Estimates of the measurement noise covariance may be obtained by examining the response of the sensor devices prior to operation of the filter. The process noise can include input noise and system uncertainties; therefore, the process noise covariances are difficult to obtain by direct measurement, and some tuning is usually required (Juang, 1993). However, the filter gain, **L,** is proportional to the relative magnitude of the process and measurement noises; therefore, the filter performance can be tuned by selecting an appropriate value for their relative magnitudes, even though the individual parameters are not precisely known.

Typically, the Kalman filter is implemented for discrete-time systems in a predictor-corrector way. The equations of the discrete-time system are the following:

$$\begin{aligned} \mathbf{z}_k &= \mathbf{A}\mathbf{z}_{k-1} + \mathbf{B}\mathbf{u}_{k-1} + \mathbf{G}\mathbf{w}_{k-1} \\ \mathbf{y}_k &= \mathbf{C}\mathbf{z}_k + \mathbf{v}_k \end{aligned} \tag{9-10}$$

The predictor-corrector implementation considers a prediction, $\hat{\mathbf{z}}_k^-$ of the state estimation before the measurements $\mathbf{y}$ are considered, and a corrected state estimate $\hat{\mathbf{z}}$ that accounts for the measurements. The implementation of the filter for a time-invariant system is given by the following procedure (Stengel, 1986):

Initialization:

$$\begin{aligned} \hat{\mathbf{z}}_0 &= E\left[\mathbf{z}_0\right] \\ \mathbf{P}_0 &= E\left[(\mathbf{z}_0 - \hat{\mathbf{z}}_0)(\mathbf{z}_0 - \hat{\mathbf{z}}_0)^T\right] \end{aligned} \tag{9-11}$$

For $k = 1, 2, \ldots$

1. State estimate prediction: $\hat{\mathbf{z}}_k^- = \mathbf{A}\hat{\mathbf{z}}_{k-1} + \mathbf{B}\mathbf{u}_{k-1}$ (9-12)

2. Covariance estimate prediction: $\mathbf{P}_k^- = \mathbf{A}\mathbf{P}_{k-1}\mathbf{A}^T + \mathbf{G}\mathbf{Q}_{k-1}\mathbf{G}^T$ (9-13)

3. Filter gain computation: $\mathbf{L}_k = \mathbf{P}_k^-\mathbf{C}^T\left(\mathbf{C}\mathbf{P}_k^-\mathbf{C}^T + \mathbf{R}_k\right)^{-1}$ (9-14)

4. State estimate update: $\hat{\mathbf{z}}_k = \hat{\mathbf{z}}_k^- + \mathbf{L}_k\left(\mathbf{y}_k - \mathbf{C}\hat{\mathbf{z}}_k^-\right)$ (9-15)

5. Covariance estimate update: $\mathbf{P}_k = \left(\mathbf{I} - \mathbf{L}_k\mathbf{C}\right)\mathbf{P}_k^-$ (9-16)

At any step, the estimate of the output is given by $\hat{\mathbf{y}}_k = \mathbf{C}\hat{\mathbf{z}}_k$. Similar to the continuous case, if the noises are stationary, the error covariance and Kalman filter gain do not change with time and can be precomputed.

9.2.2 Model-based filtering in hybrid testing

When standard filters (e.g., lowpass filters) are used to remove random noise on the measured force at discrete time steps, there is an unavoidable time lag in the filtered response resulting from the filter dynamics. This time lag is problematic in hybrid testing, because the algorithm requires the forces at the current time step instead of the forces corresponding to some previous step.

A framework has been developed in this study for filtering noise in the measured restoring forces (and measured displacements) during hybrid experiments using model-based estimation and the Kalman filter. A schematic of the filter implementation is shown

in Figure 9.2. The Kalman filter receives the measured displacements and restoring forces (with noise), $\mathbf{x}^m$ and $\mathbf{R}^m$, respectively, and the input to the system (i.e., ground acceleration, $\ddot{x}_g$) and produces an estimate of the restoring forces, with noise reduced $\hat{\mathbf{R}}$.

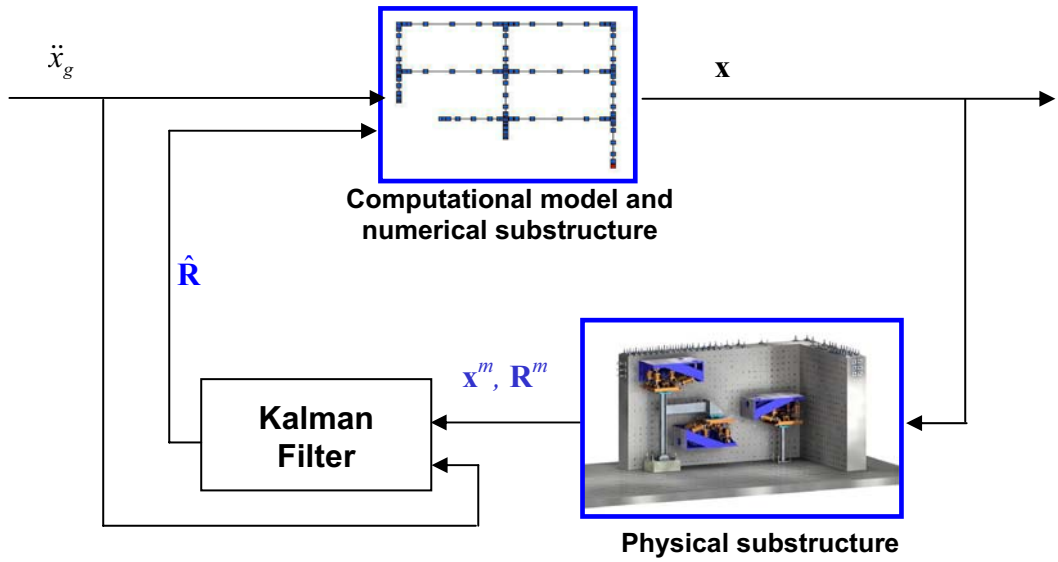

Figure 9.2: Application of Kalman filtering in hybrid testing.

The equations of the Kalman filter for hybrid testing for the case of linear response are given by

$$\begin{aligned} \dot{\hat{\mathbf{z}}} &= \mathbf{A}_e\hat{\mathbf{z}} + \mathbf{B}_e\begin{bmatrix}\ddot{x}_g \\ \mathbf{y}\end{bmatrix} \\ \hat{\mathbf{y}} &= \begin{bmatrix}\hat{\mathbf{x}} \\ \hat{\mathbf{R}}\end{bmatrix} = \mathbf{C}_e\hat{\mathbf{z}} \end{aligned} \tag{9-17}$$

where $\hat{\mathbf{z}} = \begin{bmatrix}\hat{\mathbf{x}}^{\mathrm{T}} & \dot{\hat{\mathbf{x}}}^{\mathrm{T}}\end{bmatrix}^{\mathrm{T}}$ and $\mathbf{y} = \begin{bmatrix}\mathbf{x}^{m\,\mathrm{T}} & \mathbf{R}^{m\,\mathrm{T}}\end{bmatrix}^{\mathrm{T}}$ is the vector with the measured displacements and restoring forces from the physical substructure. The Kalman filter matrices are given by

$$\mathbf{A}_e = (\mathbf{A} - \mathbf{L}\mathbf{C}_e), \qquad \mathbf{B}_e = [\mathbf{B} \quad \mathbf{L}], \qquad \mathbf{C}_e = \begin{bmatrix}\mathbf{I} & \mathbf{0} \\ \mathbf{K}_e^{exp} & \mathbf{0}\end{bmatrix} \tag{9-18}$$

in which $\mathbf{K}_e^{exp}$ is the initial elastic stiffness of the physical substructure.

9.3 Verification experiments

9.3.1 The MOST experiment

The Multi-Site Online Simulation Test (MOST) was a full-scale pseudodynamic experiment conducted in multiple geographical locations on July 30, 2003 (Spencer et al., 2004). The structure used in the experiment (Figure 9.3) represents a two-bay, single-story steel frame, with one pinned beam-column connection at the right and moment connections for the other columns.

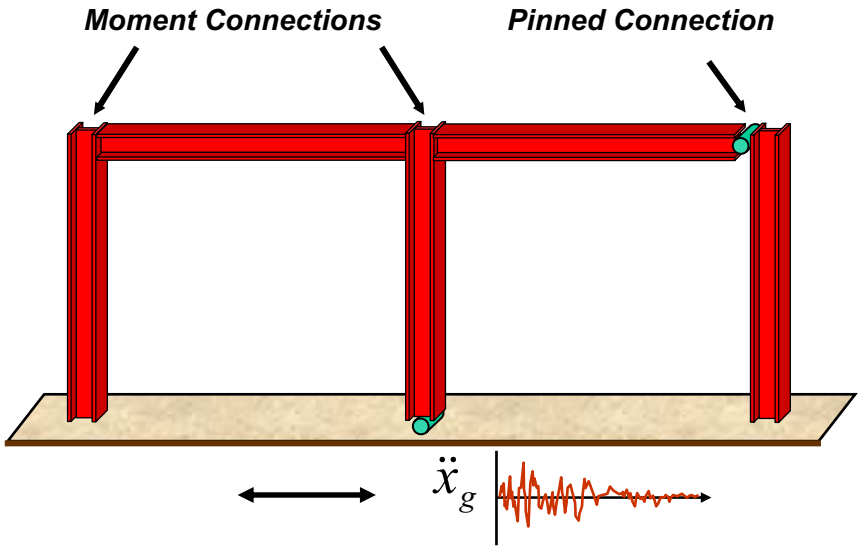

Figure 9.3: Structure tested in the MOST experiment.

The structure was tested using the pseudodynamic substructuring technique. The structure was divided into three substructures, as illustrated in Figure 9.4. The left and right columns were tested at the University of Illinois at Urbana-Champaign (UIUC) and the University of Colorado at Boulder (CU-Boulder), respectively, and the rest of the frame was numerically simulated on a computer at the National Center for Supercomputing Applications (NCSA).

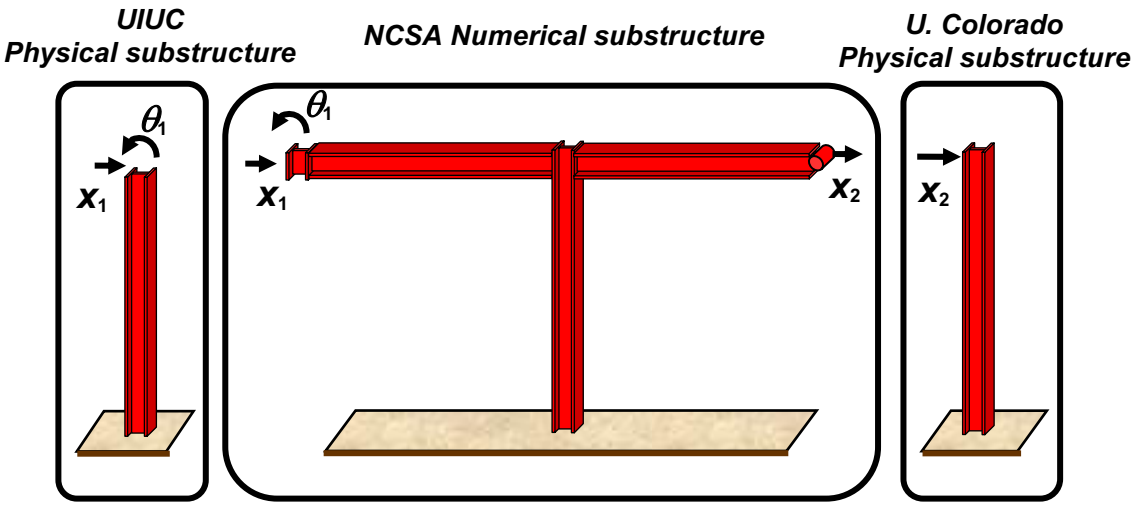

Figure 9.4: Substructures for the MOST experiment.

The Mini-MOST

The Mini-MOST is a small-scale version of the MOST experiment. There are two versions of this system, referred to here as Mini-Most-1 (one degree-of-freedom) and Mini-Most-2 (two degrees-of-freedom). The systems have a single column made of steel plate (which is the test specimen), stepper motors to impose the target displacements, and LVDTs and load-cells to measure the displacements and restoring forces, respectively. The two Mini-MOST systems are shown in Figure 9.5.

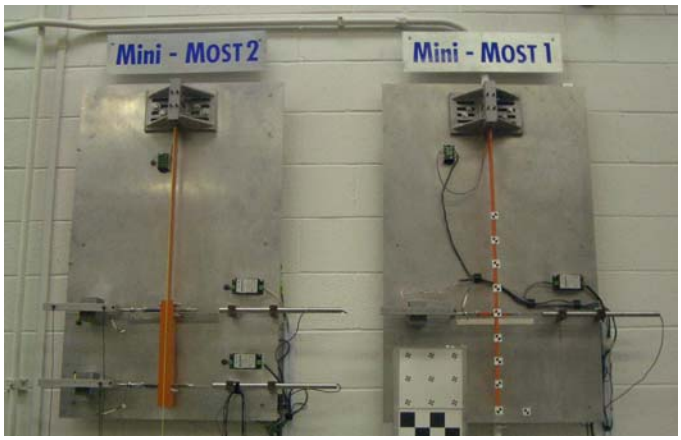

Figure 9.5: Mini-MOST systems.

These two small-scale systems provide complete experimental setups for conducting simple pseudodynamic experiments with linear physical substructures with one and two degrees-of-freedom. Because the left column of the MOST structure is rigidly connected to the beam, the Mini-Most-2 has two degrees-of-freedom, i.e., displacement and rotation at the top of the column. To impose the two degrees-of-

freedom to the Mini-Most-2 substructure, two stepper motors are used, as shown in Figure 9.6.

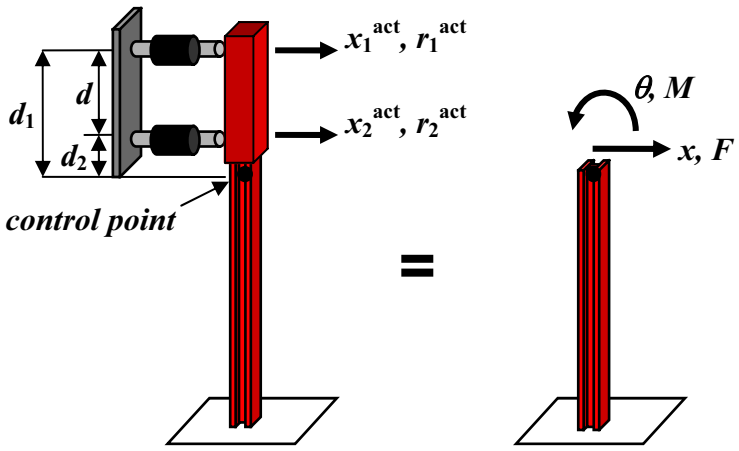

Figure 9.6: Mini-Most-2 physical substructure.

The response of the Mini-Most-2 physical substructure (i.e., displacement, rotation, lateral force, and moment) is calculated with respect to an arbitrary point denoted here as *control point* (see Figure 9.6). Assuming that the rotation, θ, is small and that no deformation is present above the control point, the transformation between the global degrees-of-freedom, $\mathbf{x} = \begin{bmatrix} x & \theta \end{bmatrix}^T$, and the actuator degrees-of-freedom, $\mathbf{x}^{act} = \begin{bmatrix} x_1^{act} & x_2^{act} \end{bmatrix}^T$, is given by

$$\mathbf{x}^{act} = \mathbf{T}\,\mathbf{x} \tag{9-19}$$

where the transformation matrix **T**, is given by

$$\mathbf{T} = \begin{bmatrix} 1 & -d_1 \\ 1 & -d_2 \end{bmatrix} \tag{9-20}$$

During the pseudodynamic experiment, the target displacements, **x,** are transformed to actuator displacements, $\mathbf{x}^{act}$, and applied by the actuators. The measured forces at each actuator, $\mathbf{r}^{act} = \begin{bmatrix} r_1^{act} & r_2^{act} \end{bmatrix}^T$, are then transformed to the restoring forces in global degrees-of-freedom, $\mathbf{r} = \begin{bmatrix} F & M \end{bmatrix}^T$, by

$$\mathbf{r} = \mathbf{T}^T\,\mathbf{r}^{act} \tag{9-21}$$

For the Mini-Most-2 physical substructure, the two stepper motors are located at distances d_1 = 11.5 in (0.292 m) and d_2 = 1.5 in (0.0381 m) from the control point, see Figure 9.6.

9.3.2 Application of the Kalman filter to the Mini-MOST experiment

The Mini-MOST experiment provides a very good test bed for the application of the Kalman filter in hybrid testing. The substructuring technique is used with the Mini-Most-2 (i.e., left column) being the physical substructure, while the rest of the frame (i.e., center frame and right column) is modeled numerically. The Mini-Most-2 is selected as the physical substructure because it possesses two degrees-of-freedom of different magnitude (i.e., displacement and rotation) that are applied using a set of two coupled actuators. Experiments performed using the Mini-Most-2 have shown that unless the properties of the structure are such that the magnitude of both displacement and rotation are adequate in size, the experimental results disagree significantly with the analytical solution, as will be shown later.

9.3.3 Initial experiments

Properties of the Mini-Most-2 (stiffness)

The stiffness of the Mini-Most-2 was evaluated experimentally by first commanding a 12 mm (0.47 in) amplitude triangular signal as the displacement with no rotation, followed by a 0.025-rad (1.43-deg) amplitude triangular signal as the rotation, with no displacement. Figure 9.7 shows the force vs. displacement plots as well as the results from a linear least-squares fit. The response of the specimen is essentially linear, although some nonlinear stiffening effects are observed at large amplitudes, which are produced by the way the stepper motors are attached to the specimen.

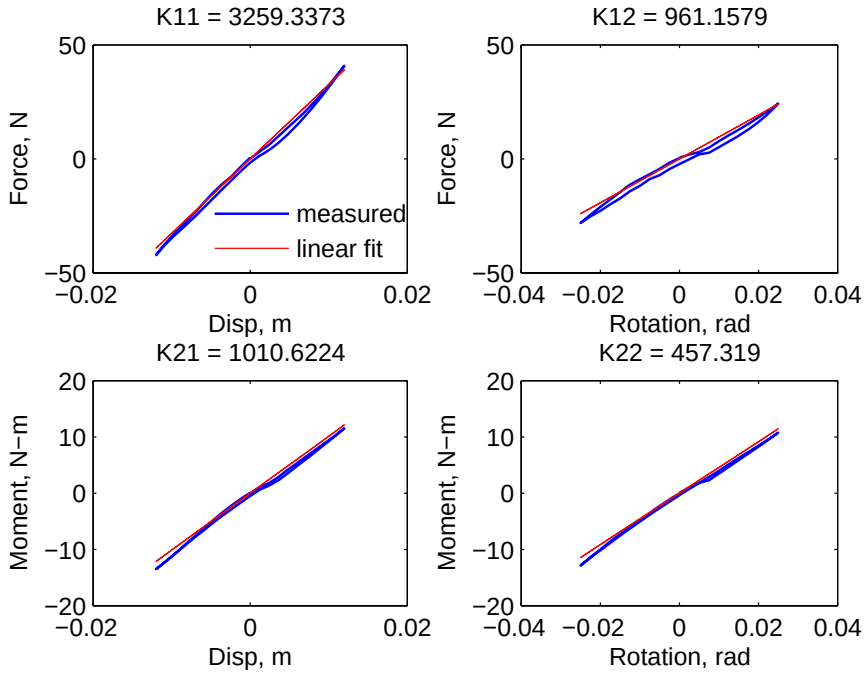

Figure 9.7: Force vs. displacement plots for stiffness evaluation.

The experimentally measured stiffness of the Mini-Most-2 is (using units of *meters* for displacement and *kN* for force):

$$\mathbf{K}_{MM2} = \begin{bmatrix} 3.260 & 0.961 \\ 1.011 & 0.457 \end{bmatrix} \tag{9-22}$$

Experimental results from pseudodynamic testing

To understand the sensitivity of the test results to the magnitude of the displacement and rotation applied to the physical substructure, the stiffness of the beam in the numerical substructure that connects the columns on the MOST structure was varied (by changing the beam's inertia), producing the three cases given on Table 9.1.

Table 9.1: Cases for pseudodynamic simulation.

Case	Beam stiffness	I_{beam} (m^4)	Relative Stiffness	Natural frequency (Hz)
1	Intermediate	1.91E-10	1	3.82
2	Flexible	5.05E-12	1/38	3.09
3	Stiff	7.66e-09	40	4.75

Pseudodynamic tests were conducted for the three cases. The structure was subjected to the artificial earthquake record shown in Figure 5.6 (which was used for the MOST experiment; Spencer et al., 2004) with the amplitude scaled by 60%. The α-OS method was used for integration of the equations of motion with a time step of 0.01 seconds. For this initial set of experiments, only the first 5 seconds of the record was used (i.e., 500 steps). Test results for the three cases considered are shown in Figures 9.8, 9.9, and 9.10.

The experimental results for Case 1 (intermediate) are in very good agreement with the analytical solution. For Case 2 (flexible), the experimental results contain significant noise in the measured moment, which also affects the rotational response. In Case 3 (stiff), the measured rotation has noise and causes the response to deviate from the analytical response.

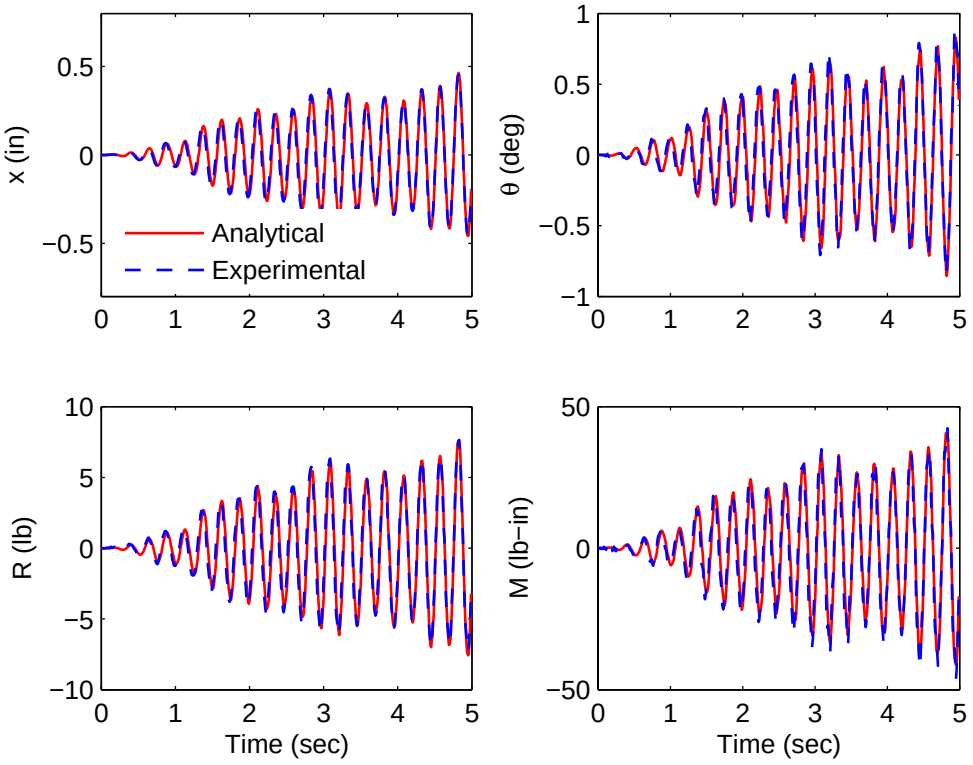

Figure 9.8: Experimental pseudodynamic test results for Case 1 (intermediate).

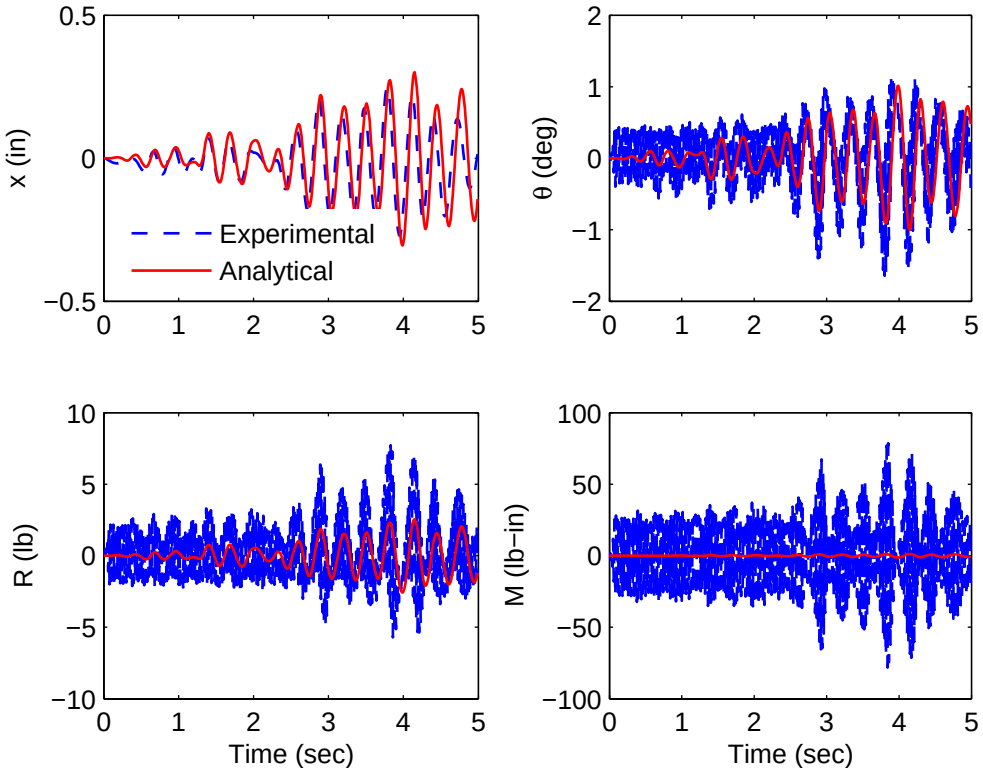

Figure 9.9: Experimental pseudodynamic test results for Case 2 (flexible).

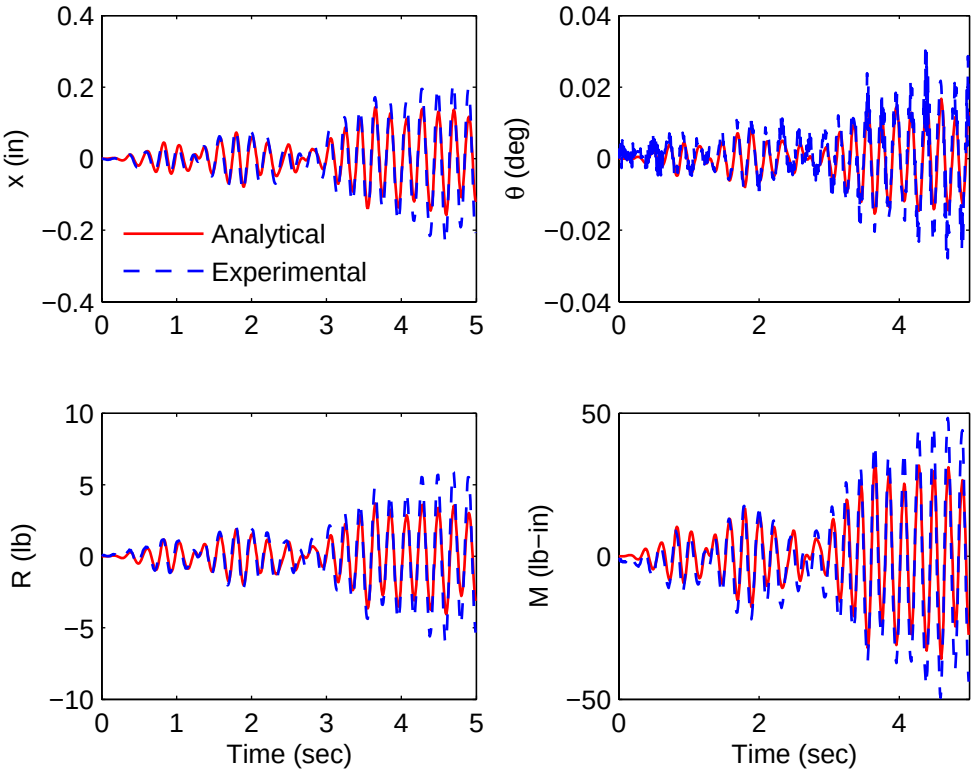

Figure 9.10: Experimental pseudodynamic test results for Case 3 (stiff).

Both extreme cases (Case 2 and Case 3) have proven to be challenging. In Case 2, the beam is so flexible that the column top connection is close to a pinned connection, making the moment very small and, therefore, difficult to control and measure. In Case 3, the beam is so stiff that the frame is close to a shear frame, with the column having very small rotation, which is difficult to control and measure.

Application of the Kalman filter on the Mini-Most-2

The Kalman filter was implemented for the Mini-Most-2 experiment. For the initial tests, the output of the system, **y,** was composed of the measured forces (i.e., lateral force *R* and moment *M*), as given by

$$\mathbf{y} = \begin{bmatrix} R \\ M \end{bmatrix} \tag{9-23}$$

The Kalman filter matrices for the Mini-Most application are the following:

$$\dot{\hat{\mathbf{z}}} = \mathbf{A}_e\hat{\mathbf{z}} + \mathbf{B}_e\begin{bmatrix}\ddot{x}_g \\ \mathbf{y}\end{bmatrix}$$
$$\hat{\mathbf{y}} = \begin{bmatrix}\hat{R} \\ \hat{M}\end{bmatrix} = \begin{bmatrix}\mathbf{K}_{\mathbf{MM2}} & \mathbf{0}_{2x6}\end{bmatrix}\hat{\mathbf{z}} = \mathbf{C}_e\hat{\mathbf{z}} \tag{9-24}$$

where

$$\mathbf{A}_e = (\mathbf{A} - \mathbf{L}\mathbf{C}_e), \qquad \mathbf{B}_e = [\mathbf{B} \quad \mathbf{L}], \qquad \mathbf{C}_e = \begin{bmatrix}\mathbf{K}_{\mathbf{MM2}} & \mathbf{0}_{2x6}\end{bmatrix}. \tag{9-25}$$

Because the noise statistics **Q** and **R** are unknown, the following procedure based on the ratio of the process noise and measurement noise is used to select the parameters for the Kalman filter gain, **L**. First, the noise statistics are expressed in the following form

$$\mathbf{R} = \begin{bmatrix}\sigma_F^2 & 0 \\ 0 & \sigma_M^2\end{bmatrix}, \ \mathbf{Q} = q \tag{9-26}$$

where σ_F^2, σ_M^2, and q are the variances of the force, moment and process noise, respectively. In earthquake analysis with hybrid testing, the input to the dynamic system (i.e., $\ddot{x}_g$) is deterministic, therefore, it contains no random input noise. The process noise covariance is used here as a *fictitious noise* to represent system uncertainties. The relative magnitude between the measurement noise and the process noise can be represented by

$$\mathbf{R}\mathbf{Q}^{-1} = \frac{\begin{bmatrix}\sigma_F^2 & 0 \\ 0 & \sigma_M^2\end{bmatrix}}{q} = \begin{bmatrix}\sigma_F^2/q & 0 \\ 0 & \sigma_M^2/q\end{bmatrix} = \begin{bmatrix}\rho & 0 \\ 0 & \alpha\rho\end{bmatrix} = \rho\begin{bmatrix}1 & 0 \\ 0 & \alpha\end{bmatrix} \tag{9-27}$$

where $\rho = \sigma_F^2/q$ and $\alpha = \sigma_M^2/\sigma_F^2$. By setting q = 1, **R** depends on the parameters, ρ and α, as given by

$$\mathbf{R} = \rho\begin{bmatrix}1 & 0 \\ 0 & \alpha\end{bmatrix} \tag{9-28}$$

The parameter, α, relates the magnitude of the variance in the moment to the variance in the lateral force, whereas ρ defines the relative amount of weight that the filter puts on the measurements and the model. As ρ gets smaller, the estimator believes the measurements more, and as ρ gets larger, the estimator believes the model more.

Pseudodynamic tests were conducted for Case 2 (Flexible) using the Kalman filter. From the force and the moment responses in previous tests and numerical analyses, the parameter, α, was selected as 10^{-2}. Table 9.2 shows the values of ρ used as well as the

resulting error norms (characterized by the distance in the L_2 or Euclidean norm) between the experimental results and analytical solution for each test, given by the following expression:

$$d\_L_2(e) = \sqrt{\frac{\sum_{i=0}^{n}\left[x_i^{\,exact} - \hat{x}_i\right]^2}{\sum_{i=0}^{n}\left[x_i^{\,exact}\right]^2}} \tag{9-29}$$

Table 9.2: Error norm of experimental results using Kalman filter for Case 2.

ρ	Error norm			
	x	θ	R	M
w/o KF[a]	0.687	1.368	2.658	68.227
10^{-9}	0.190	0.200	0.198	1.461
10^{-8}	0.250	0.258	0.273	3.982
10^{-4}	3.172	[b]	[b]	[b]

[a] Test without Kalman filter, [b] Test diverged and had to be stopped.

The tests using the Kalman filter with ρ equal to 10^{-9} and 10^{-8} show a significant improvement over the test without the Kalman filter, especially on the measured moment. For the case of $\rho = 10^{-4}$ the filter gain became very small and the test diverged and had to be stopped.

Figure 9.11 presents the test results for $\rho = 10^{-9}$, showing very good agreement with the analytical solution. By comparing the forces before the filter (*Exp. unfiltered*) and after going through the filter (*Exp. filtered*), the Kalman filter is observed to significantly reduce the noise in the measured forces, improving the overall test results.

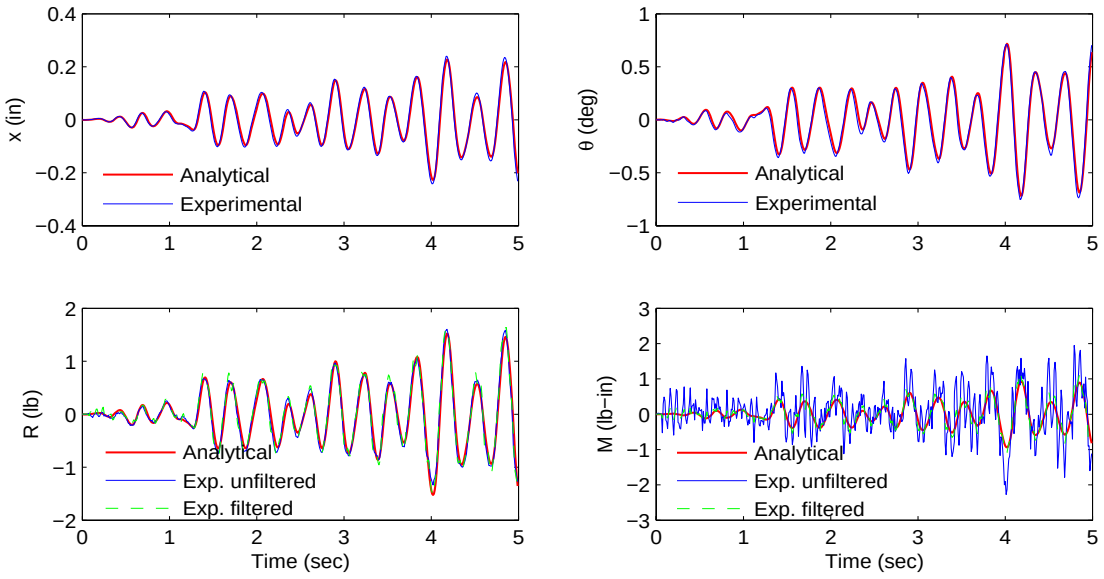

Figure 9.11: Experimental results for Case 2 (Flexible) using Kalman filter ($\rho = 10^{-9}$).

9.3.4 Further experiments

Encouraged by the good results obtained using the Kalman filter for Case 2 (Flexible), a second and more comprehensive set of experiments was conducted. In these experiments the following adjustments were made: improved displacement control and calibration, experimental estimation of noise statistics for Kalman filter, forces and displacements in actuator space used as measurements for the filter, and parametric analyses (numerical simulations and experimental tests) for the three cases considered. These results will be presented in the next section.

Displacement control and calibration

For the experiments presented in the previous section, the calibration data and the Mini-Most-2 controller developed during the NEES-Grid activities were used directly. However, the controller was found to return the target displacements as measured displacements, and the displacement control error was significant. Figure 9.12 shows the target and measured displacements as well as the control error (defined as the difference between *target* and *measured* displacements) for a triangular command displacement profile similar to the one used for the stiffness evaluation. A significant control error is observed, especially for the rotation, where an error as large as 0.32 deg (22% of the target value) is present.

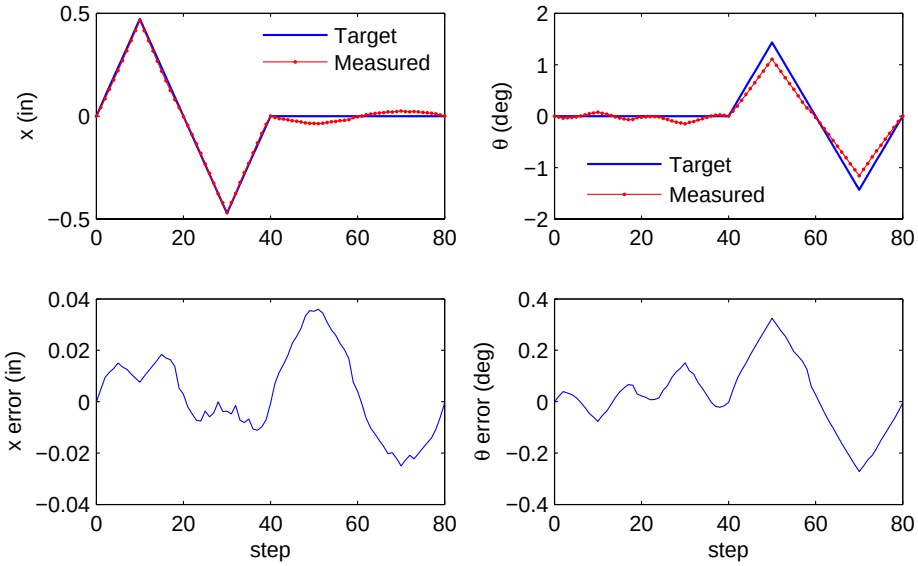

Figure 9.12: Measured displacements and control error.

To solve these problems, the instrumentation (LVDTs and stepper motors) were first recalibrated and a new controller was developed using LabView. The new controller implements a discrete integral control using the measured displacements. This controller then sends back the measured displacements and forces in actuator space (which is more

desirable for the Kalman filter implementation). A schematic diagram of the implementation is shown in Figure 9.13,

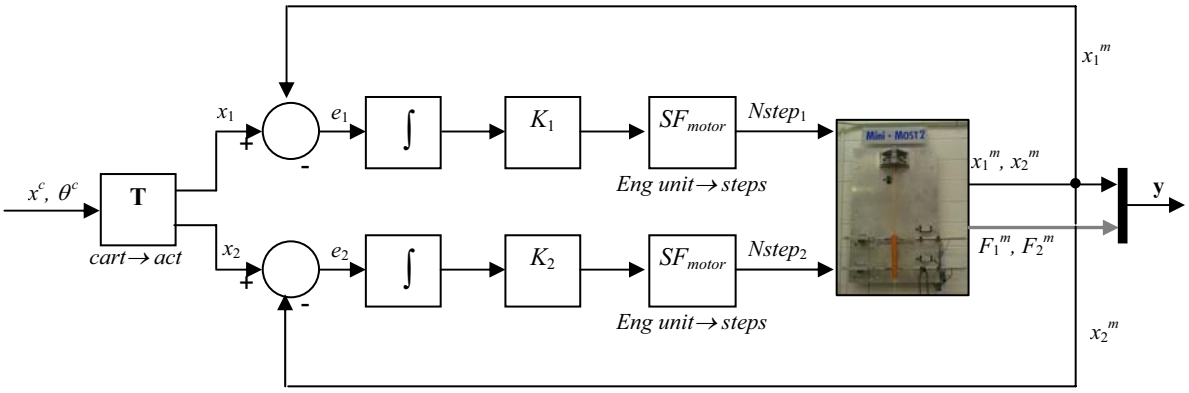

Figure 9.13: New controller for Mini-Most-2 with displacement feedback.

where K_1 and K_2 are the controller gains, and SF_{motor} is a factor to transform from engineering units (e.g, meters) to the number of stepper motor steps (N_{step}). The maximum accuracy that can be achieved is limited by the minimum displacement increment of the motors that corresponds to 1 step, about 0.0005 in (1.25E-5 m); this level of accuracy is considered adequate.

Properties of the Mini-Most-2 (stiffness)

The stiffness of the Mini-Most-2 was reevaluated experimentally using the same triangular displacement wave as for the stiffness evaluation test in the previous section. Figure 9.14 shows the force vs. displacement plots as well as the results from a linear least-squares fit.

The experimentally measured stiffness of the Mini-Most-2 (using units of *meters* for displacement and *kN* for force) is

$$\mathbf{K}_{\text{MM2}} = \begin{bmatrix} 4.088 & 1.264 \\ 1.298 & 0.572 \end{bmatrix} \tag{9-30}$$

which is close to the theoretically calculated stiffness based on the dimensions and properties of the test specimen

$$\mathbf{K}_{\text{MM2}}^{calc} = \begin{bmatrix} 4.552 & 1.416 \\ 1.416 & 0.588 \end{bmatrix} \tag{9-31}$$

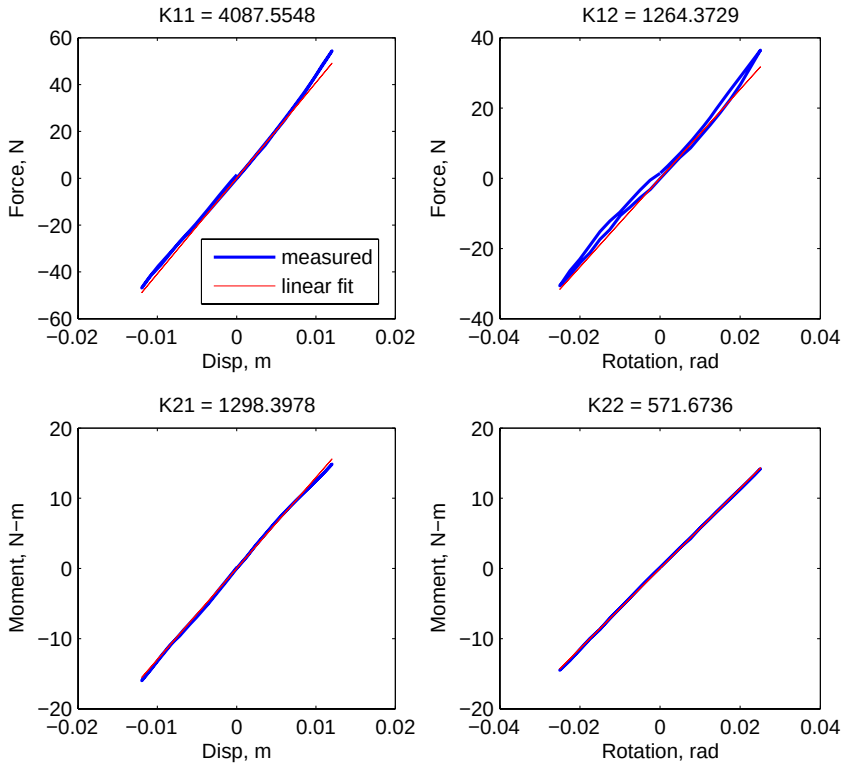

Figure 9.14: Force vs. displacement plots and stiffness evaluation.

Pseudodynamic tests without Kalman filter

Pseudodynamic tests were conducted for the three cases (intermediate, flexible, and stiff) using the new calibration data and improved controller. The test results are shown in Figures 9.15, 9.16, and 9.17 for the three cases, respectively.

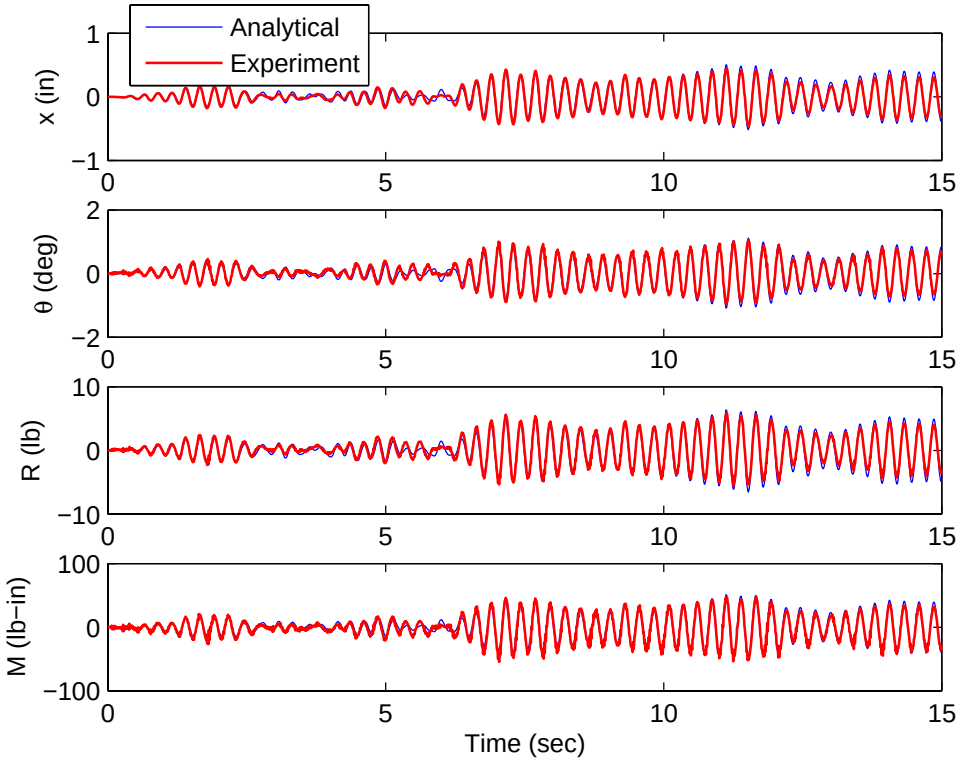

Figure 9.15: Experimental pseudodynamic test results for Case 1 (intermediate).

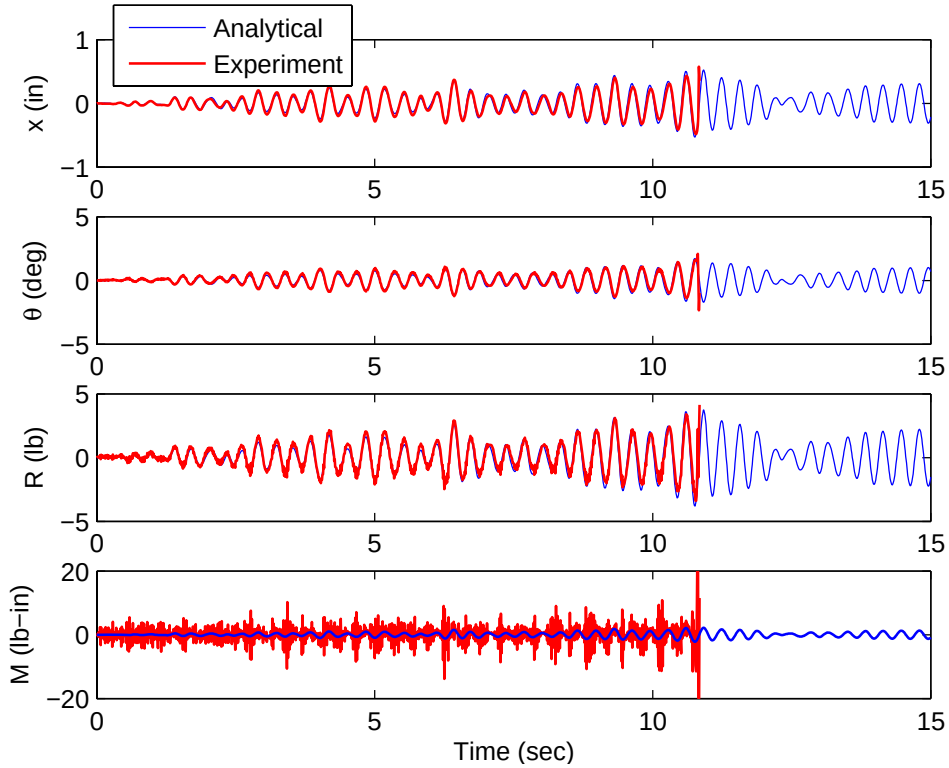

Figure 9.16: Experimental pseudodynamic test results for Case 2 (flexible).

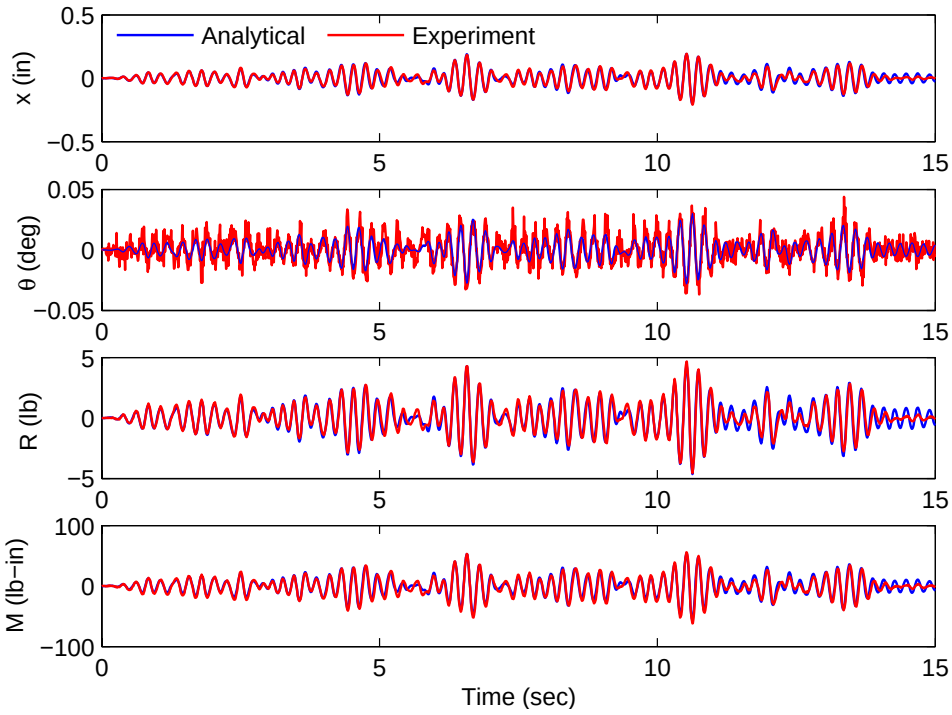

Figure 9.17: Experimental pseudodynamic test results for Case 3 (stiff).

The results from these tests are significantly better than the previous results, showing that accurate calibration and control significantly improve the results from the pseudodynamic tests. However, similar trends for the errors are observed as in the previous cases, but at a much smaller level. The results from Case 1 (intermediate) are in good agreement with the analytical solution. In Case 2 (flexible), the measured moment has significant noise, while in Case 3 (stiff), the rotation has a considerable amount of noise.

The test for Case 2 (Figure 9.16) had to be stopped at about 11 sec because the target displacements started to exceed the maximum limits, which was found to be caused by a saturation limit set on the controller for the target displacements. For this reason, in the following sections only test results up to 10 sec are reported for this case.

Application of the Kalman filter on the Mini-Most-2

The Kalman filter was applied in a similar manner to the previous set of experiments with the difference that for this case, the measured outputs of the system were the measured displacements and forces from the Mini-Most-2 in actuator space, i.e., $\mathbf{y} = \left[x_1^m \quad x_2^m \quad f_1^m \quad f_2^m \right]^{\mathrm{T}}$. The advantage of working directly with the data in actuator space is that the noise statistics can be determined from each sensor and assigned to each parameter independently. The Kalman filter matrices for the Mini-Most application are as follows

$$\dot{\hat{\mathbf{z}}} = \mathbf{A}_e\hat{\mathbf{z}} + \mathbf{B}_e\begin{bmatrix}\ddot{x}_g \\ \mathbf{y}\end{bmatrix}$$
$$\hat{\mathbf{y}} = \begin{bmatrix}\hat{x}_1 \\ \hat{x}_2 \\ \hat{f}_1 \\ \hat{f}_2\end{bmatrix} = \begin{bmatrix}\mathbf{T}_{2x2} & \mathbf{0}_{2x6} \\ [\mathbf{T}^{-T}\mathbf{K}_{\mathbf{MM2}}]_{2x2} & \mathbf{0}_{2x6}\end{bmatrix}\hat{\mathbf{z}} = \mathbf{C}_e\hat{\mathbf{z}} \tag{9-32}$$

with

$$\mathbf{A}_e = (\mathbf{A} - \mathbf{L}\mathbf{C}_e), \qquad \mathbf{B}_e = [\mathbf{B} \quad \mathbf{L}], \qquad \mathbf{C}_e = \begin{bmatrix}\mathbf{T}_{2x2} & \mathbf{0}_{2x6} \\ [\mathbf{T}^{-T}\mathbf{K}_{\mathbf{MM2}}]_{2x2} & \mathbf{0}_{2x6}\end{bmatrix} \tag{9-33}$$

where $\mathbf{T}$ is the transformation matrix between the global degrees-of-freedom $\mathbf{x} = [x \quad \theta]^T$, and the actuator degrees-of-freedom, $\mathbf{x}^{act} = [x_1 \quad x_2]^T$.

Estimation of noise statistics

Because the noise statistics can now be expressed for each sensor independently, estimates of the measurement noise statistics were obtained by examining the response of each sensor device. The error in $x_1{}^m$ and $x_2{}^m$ is determined by analyzing the control error during the previous tests. Figure 9.18 shows the probability distribution of the control error during the test for Case 2 (flexible), which is close to a normal distribution. Similar results are obtained for the other cases (Cases 1 and 3). The noise in $x_1{}^m$ and $x_2{}^m$ is then approximated by a Gaussian process with zero mean and a standard deviation of 7.87e-4 in (2e-5 m).

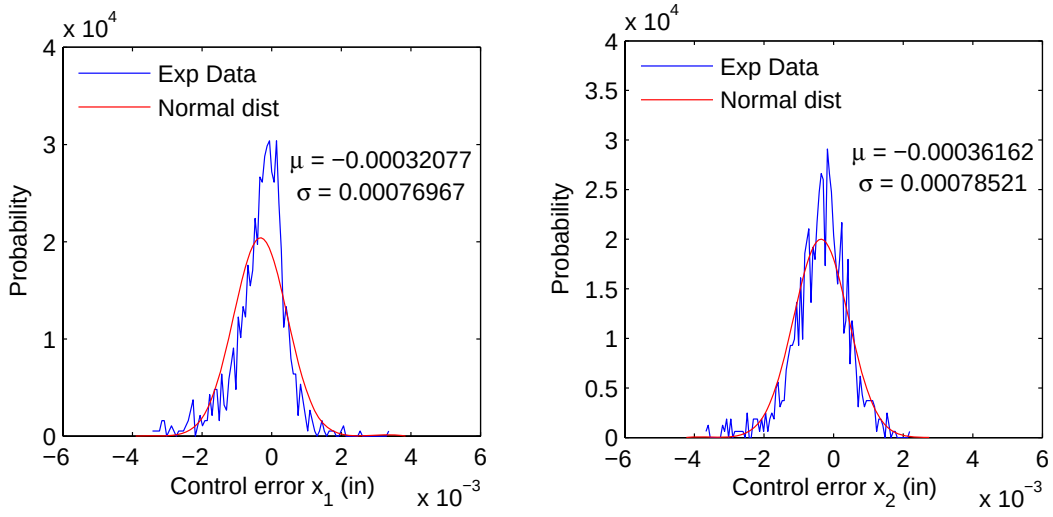

Figure 9.18: Probability distribution of control error for Case 2 (flexible) test.

To determine the noise on the measured forces f_1^m and f_2^m, the two stepper motors were held at a constant position while a large number of discrete load-cell readings were taken (2000 measurements) in the same way as during the pseudodynamic experiments. The probability distribution of the forces is shown in Figure 9.19.

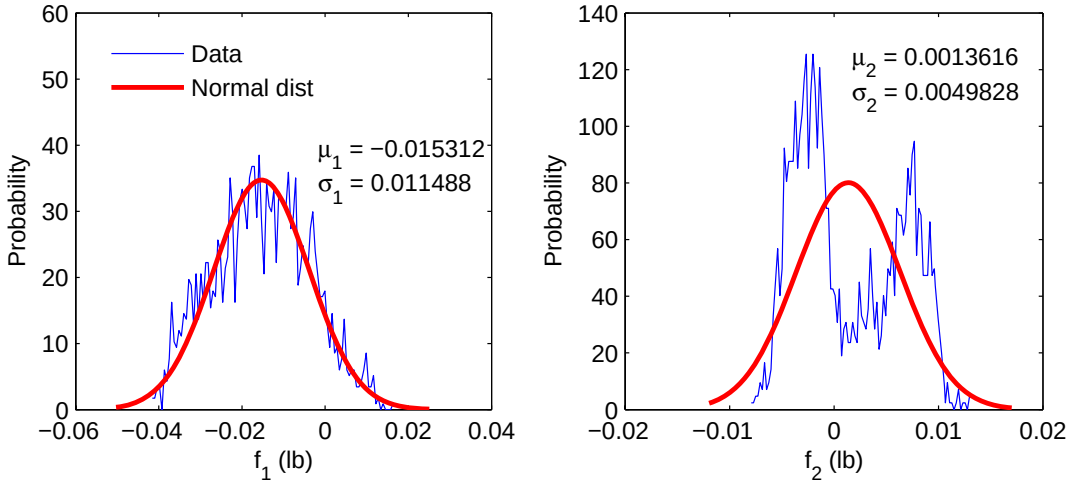

Figure 9.19: Probability distribution of noise in forces.

The noise in the measured forces is approximated by a Gaussian process with zero mean and standard deviations of 0.011 lb (51e-6 KN) and 0.005 lb (22e-6 KN) for f_1^m and f_2^m, respectively.

The process noise is used as a *fictitious noise* to include system uncertainties that are difficult to obtain by direct measurement; therefore, some tuning is still required. The procedure is similar to the one used before, where ρ is used as a weighting parameter between the measurement and process. The relative noise weight, $\mathbf{RQ}^{-1}$ is expressed as

$$\mathbf{RQ}^{-1} = \rho \begin{bmatrix} 1 & & & \\ & 1 & & \\ & & \alpha_{f_1} & \\ & & & \alpha_{f_2} \end{bmatrix} \tag{9-34}$$

where

$$\alpha_{f_1} = \frac{\sigma_{f_1}^2}{\sigma_x^2} = 6.5\ (KN/m)^2, \quad \alpha_{f_2} = \frac{\sigma_{f_2}^2}{\sigma_x^2} = 1.2\ (KN/m)^2 . \tag{9-35}$$

Therefore,

$$\mathbf{RQ}^{-1} = \rho \begin{bmatrix} 1 & & & \\ & 1 & & \\ & & 6.5 & \\ & & & 1.2 \end{bmatrix} \tag{9-36}$$

and by setting $\mathbf{Q} = 1$, $\mathbf{R}$ is given by

$$\mathbf{R} = \rho \begin{bmatrix} 1 & & & \\ & 1 & & \\ & & 6.5 & \\ & & & 1.2 \end{bmatrix} \tag{9-37}$$

Numerical simulation

Before conducting the pseudodynamic experiments using the Kalman filter, a set of numerical simulations was conducted to analyze the effect of the weighting parameter, ρ, on the filter performance. The physical substructure (i.e., Mini-Most-2) was replaced by a numerical model with the same stiffness characteristics. Noise was added to the simulation (control error for x_1^m and x_2^m and measurement noise for f_1^m and f_2^m) based on the noise statistics determined experimentally in the previous section. Simulations were conducted for the three different cases for several values of ρ. The results from the numerical simulations with noise were compared to the analytical solution (without noise); the corresponding error norms are shown in Figures 9.20, 9.21, and 9.22.

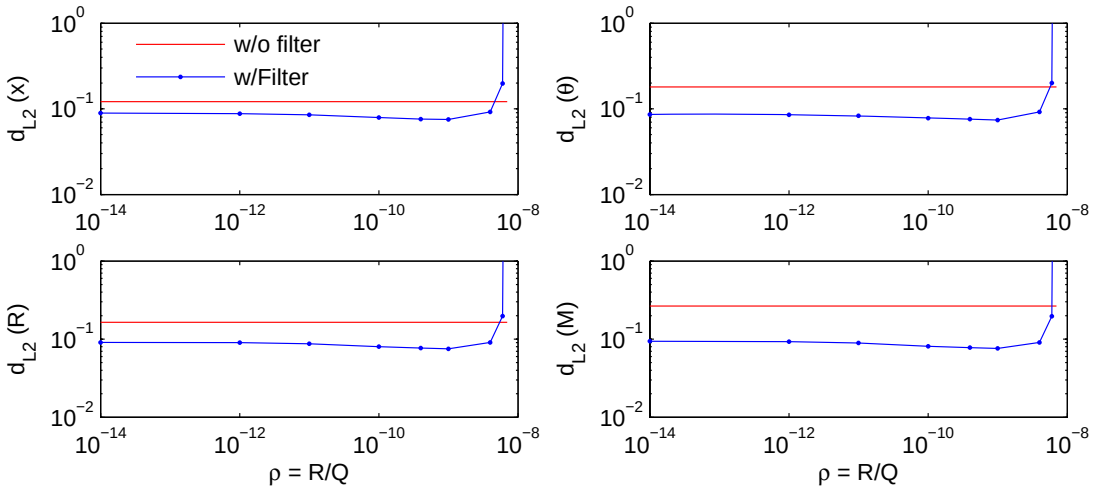

Figure 9.20: Numerical simulation with noise for Case 1 (intermediate).

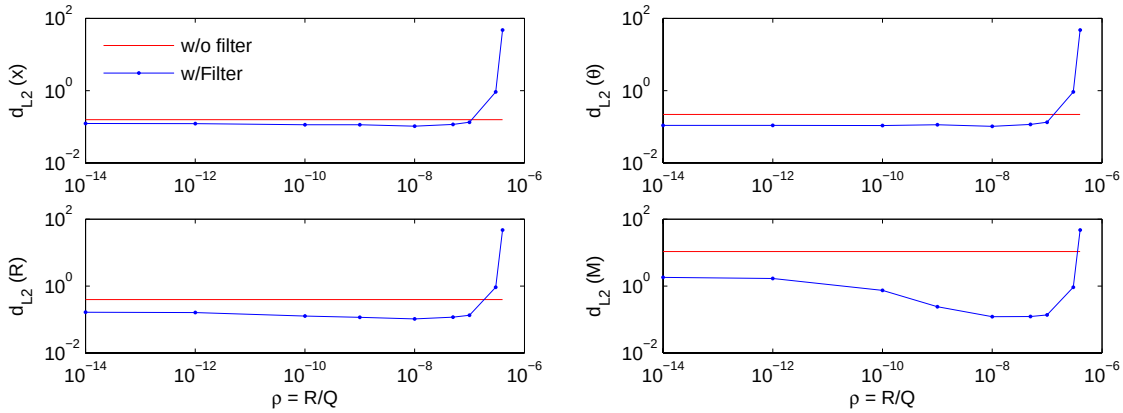

Figure 9.21: Numerical simulation with noise for Case 2 (flexible).

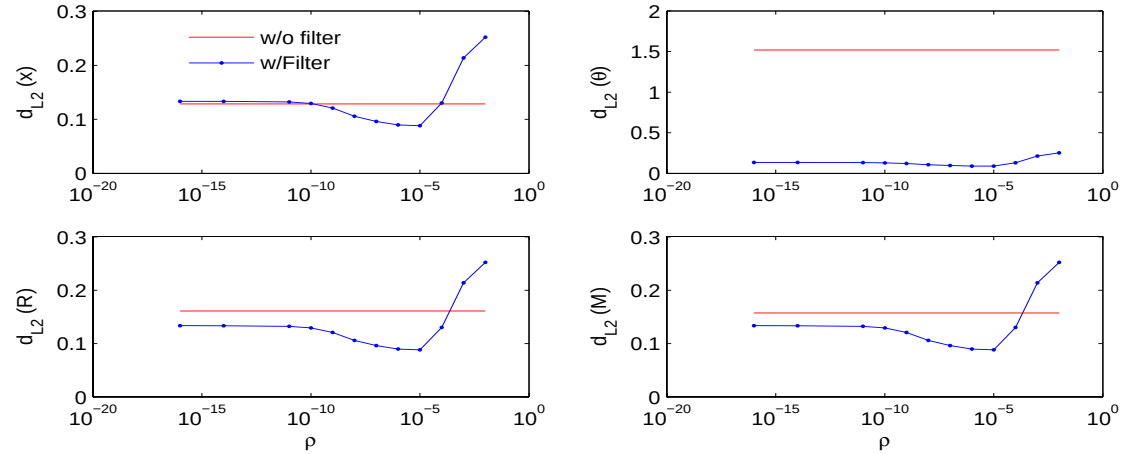

Figure 9.22: Numerical simulation with noise for Case 3 (stiff).

The variation of the error norms is somehow similar for the three cases. There is an optimum value of ρ for which the error norms are minimum (i.e., better filter performance). As ρ gets smaller, the error increases slightly and then reaches a stable value. However, as ρ gets larger than the optimum value, the error norms start to increase rapidly, and if the value gets large enough, the combined system (i.e., experiment and filter) becomes unstable. Divergence occurs when the error covariance matrix, **P,** computed by the filter becomes unreasonably small compared with the actual error in the estimate. When **P** becomes small, it causes the filter gain, **L,** to become too small and new measurements are given too little weight. The model of the system becomes more important in determining the estimates than the measured data. Any error in the model can build up over a period of time and cause a significant degradation in the accuracy of the estimate (Sorenson, 1970). The results from the numerical simulations conducted show that except for large values of ρ, the tests conducted with the filter have a smaller error and, therefore, are more accurate than the tests without the filter.

Experimental results using the Kalman filter

Using the results from the numerical simulations to have a sense of the magnitude of the weighting parameter, ρ, pseudodynamic tests where conducted for a smaller number of values of ρ for the three cases of beam stiffness (intermediate, flexible, and stiff). Results from the pseudodynamic tests for the three cases are shown in Figures 9.23, 9.24, and 9.25.

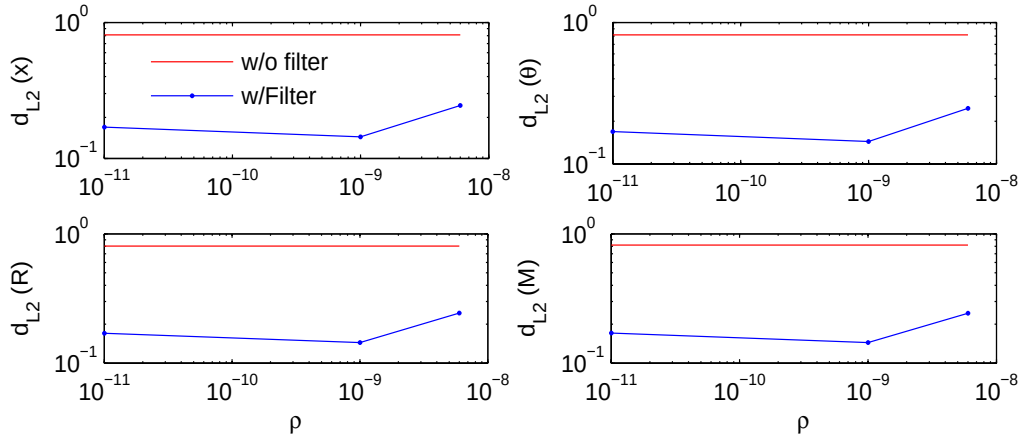

Figure 9.23: Results for pseudodynamic test for Case 1 (intermediate) with Kalman filter.

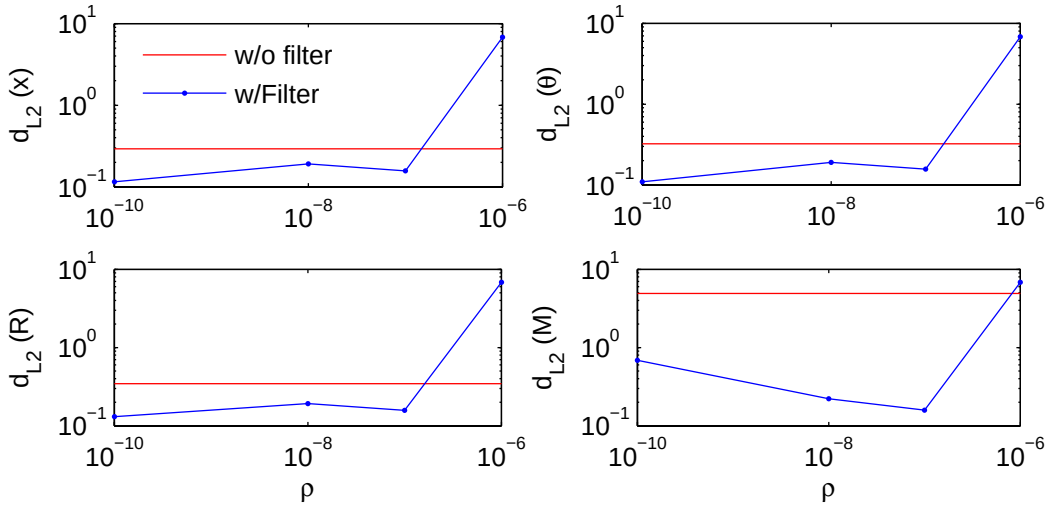

Figure 9.24: Results for pseudodynamic test for Case 2 (flexible) with Kalman filter.

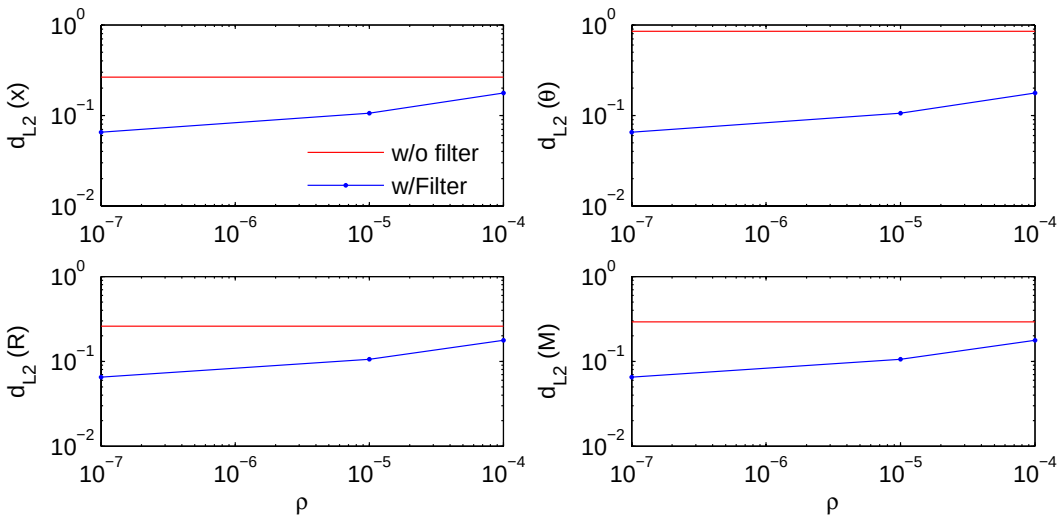

Figure 9.25: Results for pseudodynamic test for Case 3 (stiff) with Kalman filter.

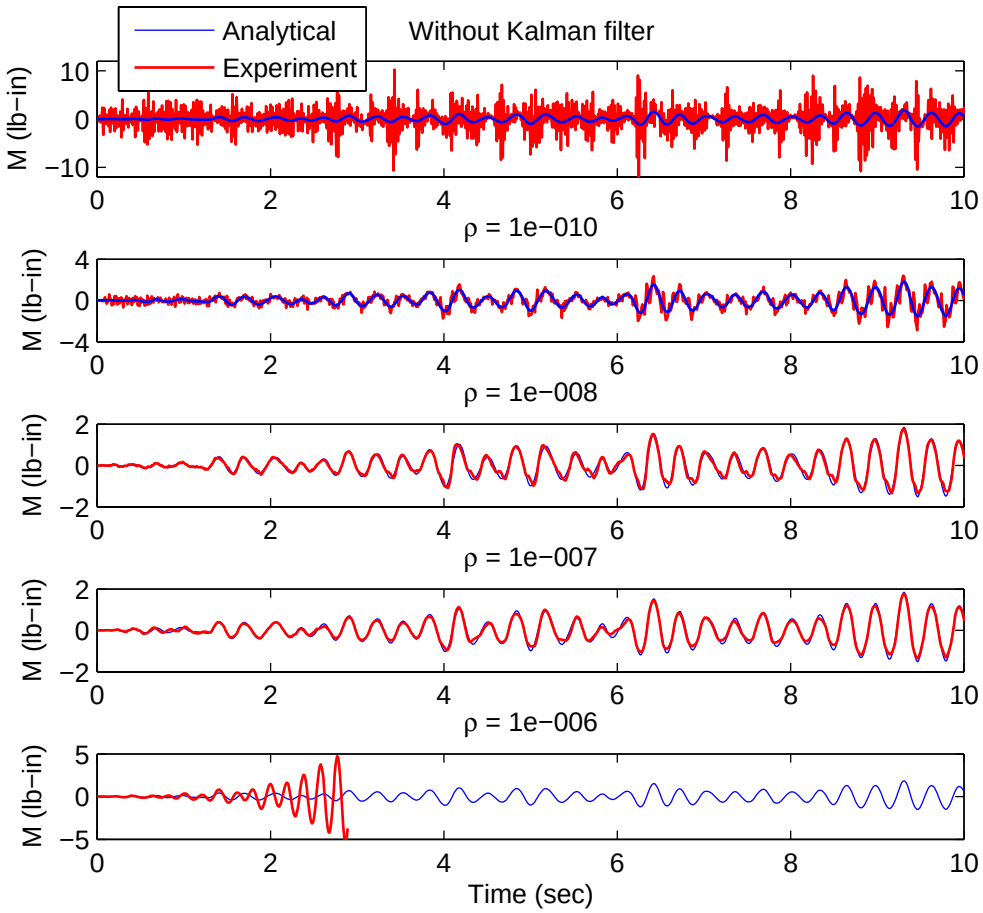

Figure 9.26: Measured moment from pseudodynamic tests for Case 2 (flexible).

By observing the variation of the error norms with respect to the value of ρ for each test, the pseudodynamic tests using the filter are observed to exhibit similar behavior to that of the numerical simulations. Figure 9.26 shows the measured moment in the physical substructure (i.e., Mini-Most-2) for the tests corresponding to Case 2 (flexible) conducted using different values of ρ. Without the filter, a significant amount of noise is present in the measured moment; however, once the filter is included in the experiments, the noise starts to reduce as ρ increases until a point after which divergence occurs (ρ = 1e-6).

Figure 9.27 shows the variation of the error on the measured moment for Case 2 (flexible) using a moving averaging window, where it is easier to observe the reduction of the error and noise as ρ changes. Without the filter, the error is significant, for ρ = 1e-7, the error is minimum, and for for ρ = 1e-6, divergence occurs.

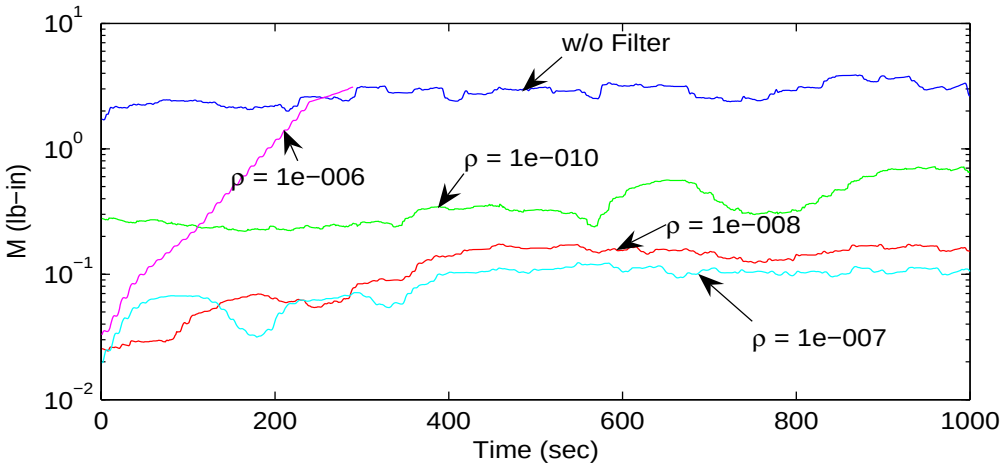

Figure 9.27: Moving error window for Case 2 (flexible).

Figure 9.28 shows the results from the pseudodynamic test for Case 3 (stiff) using the Kalman filter with $\rho = 10^{-7}$. As it can be observed, excellent agreement is achieved between the test results and the analytical solution.

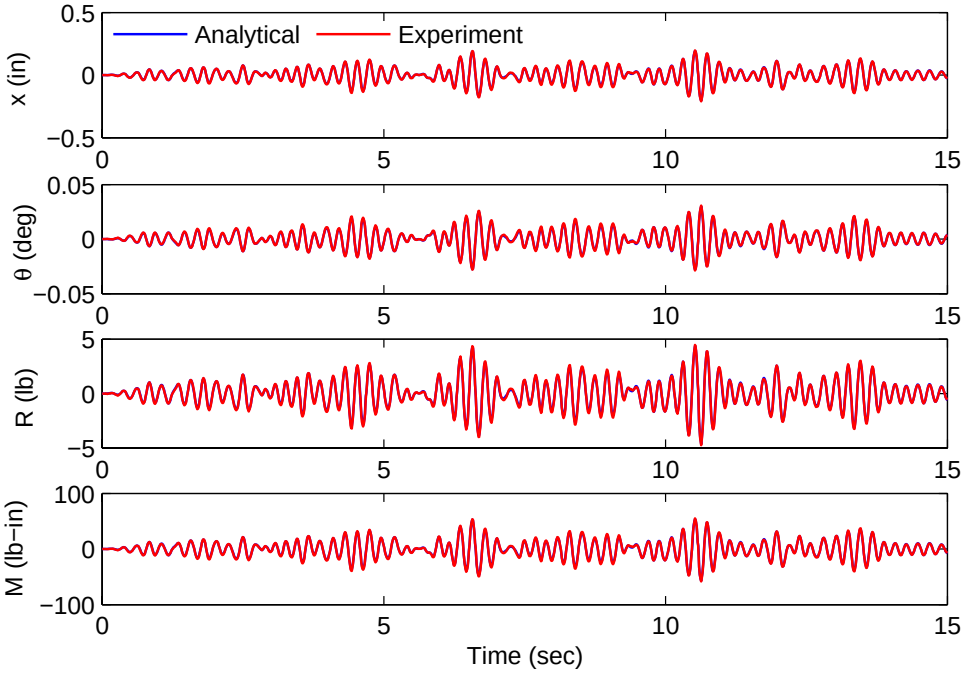

Figure 9.28: Results for pseudodynamic test for Case 3 (stiff) with Kalman filter ($\rho = 10^{-7}$).

Initially, the results from the experiments for Case 3 (stiff) using the Kalman filter were not satisfactory. The error norm actually increased when using the filter. The poor filter performance was caused by a difference in the response obtained from the two time discretization schemes used simultaneously during the experiments with the Kalman filter. Numerical integration of the equation of motion in the pseudodynamic test was performed using the α-OS method, while the Kalman filter matrices were obtain using a first-order-hold approximation. The response obtained from the two methods for Case 3 (stiff) was somewhat different due to a combination of several conditions (e.g., the relatively large natural frequency corresponding to Case 3, a time-step size that was insufficiently small, and the very low damping ratio previously used (0.1%)). The results reported herein for Case 3 (stiff) correspond to experiments using a damping ratio of 2% for all modes (which is a value typically used for steel frames), in which case the two time discretization methods produce similar results. A more definitive solution is to use the same time discretization method for both, equation of motion and Kalman filter.

The results from the pseudodynamic tests conducted show that the Kalman filter significantly improves the response for all three cases (i.e., intermediate, flexible, and stiff), producing a smaller error norm for a wide range of values of the weighting parameter, ρ.

9.4 Effect of stiffness estimate on filter performance

The Kalman filter uses a model of the system to perform the predictions. In general, this model is only an approximation of the real system, and, therefore, may

contain errors with respect to the actual system. This section analyzes the effect of errors in the model and their consequences on the performance of the Kalman filter.

In the proposed application of the Kalman filter for pseudodynamic testing, the model of the system includes the mass of the structure **M**, the damping **C**, and the stiffness **K** (including the contributions from the physical and numerical substructures). In pseudodynamic testing, the properties of the numerical components (i.e., mass, damping, and stiffness of numerical substructure) are known or can be accurately determined; therefore, the only source for errors in the model is the estimate of the initial elastic stiffness of the physical substructure. This stiffness estimate is used in both the system and the output equations of the filter.

The differences between the actual stiffness of the physical substructure $\mathbf{K}^{exp}$ and the stiffness used by the model $\mathbf{K}_m^{exp}$ (e.g., measured initial elastic stiffness) are represented here by the nondimensional parameter, α_k, which is defined by the following equation

$$\mathbf{K}_m^{exp} = \alpha_k \mathbf{K}^{exp} \tag{9-38}$$

Numerical simulation was conducted to analyze the effect of the differences on the model used by the Kalman filter. The test structure was the same as in previous sections (Mini-Most-2), and the flexible beam case was considered (i.e., Case 2), which presents significant noise in the measured moment. A value of $\rho = 10^{-8}$ was used for the filter weighting parameter. Figure 9.29 shows simulation results, including noise, for different values of the parameter, α_k. The results are expressed in terms of the error with respect to the exact solution (i.e., analytical solution for system without noise). Results for the case without the filter are also shown and are used as a reference for the filter performance. As can be observed, the error norms are minimum, and, therefore, the performance of the filter is best when the model used by the filter matches the actual system (i.e., $\alpha_k = 1$). For all the response quantities, the performance of the Kalman filter decreases as the model deviates from the actual system (as represented by the larger error norm). For the measured moment, all of the results using the filter are better than the ones without the filter, despite the errors introduced in the model. However, for the other response quantities (displacement, rotation, and lateral force), the results using the filter are better than the ones without the filter over a very limited range of α_k (close to 1.0). In such cases, the Kalman filter can be used to estimate only the measured moment.

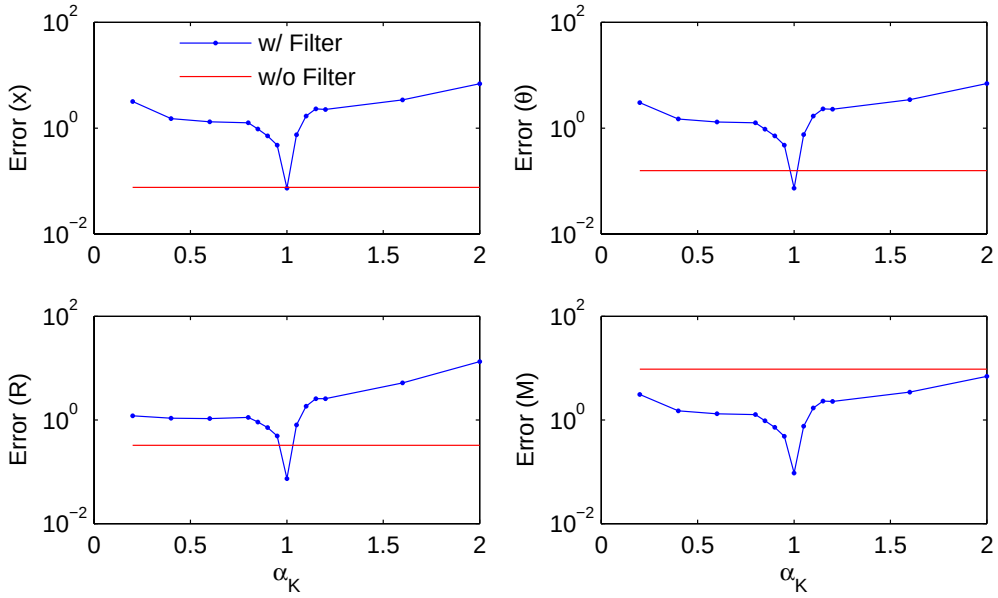

Figure 9.29: Simulation results for Case 2 (flexible) considering errors in model.

The performance of the Kalman filter is also dependent on the filter weighting parameter, ρ. Figure 9.30 shows the error norm for the measured moment for different values of ρ. Two cases of the Kalman filter are presented: (a) with an exact model of the system ($\alpha_k = 1$), and (b) assuming that the stiffness of the physical substructure (used by the filter) is underestimated by 20% ($\alpha_k = 0.8$). As can be observed, for small values of ρ, the difference between the results of the two cases (i.e., $\alpha_k = 0.8$ and 1.0) is small, due to the filter putting significant weight on the measurements and less on the model. As the value of ρ increases, the differences between the two cases are larger, and, therefore, the error due to the underestimation of $\mathbf{K}^{exp}$ is more significant. This result is consistent because as ρ increases, the Kalman filter puts more weight on the estimates from the model and less on the measurements. For the other response quantities, this effect was less evident, because errors in the model had a large impact on the filter performance (see Figure 9.29).

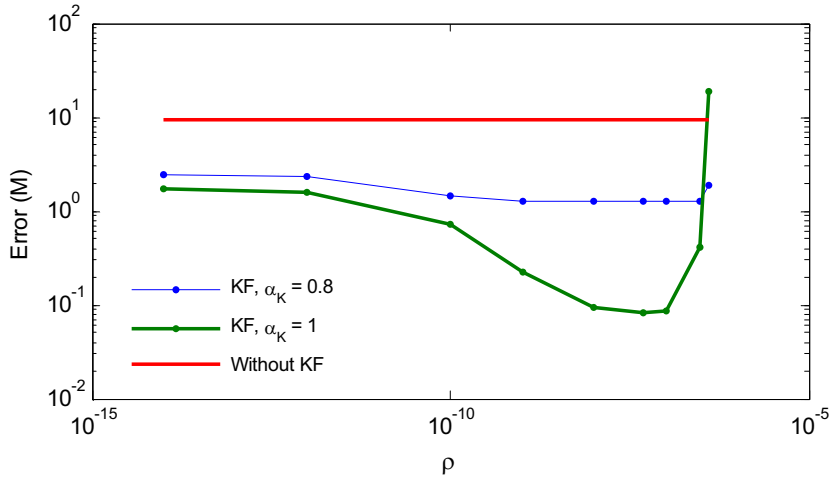

Figure 9.30: Simulation results for Case 2 (flexible) considering errors in model: effect of filter weighting parameter, ρ.

The analysis performed indicates that, in general, the performance of the Kalman filter for hybrid testing is sensitive to differences between the model used by the filter and the actual system.

9.5 Extension to nonlinear structural response

The analyses and experiments presented in the previous sections were limited to cases of linear response. However, hybrid testing is generally used to determine the nonlinear or inelastic response of structures. This section considers extensions of the method for these cases.

9.5.1 Extended Kalman filter

The Kalman filter provides an optimum solution for the state estimation and filtering of linear systems (Stengel, 1986). However, almost all real systems and processes are nonlinear, and in many cases approximating the system with a linear model is not appropriate. This problem led to the development of extensions of the Kalman filter theory to nonlinear systems. The Extended Kalman Filter (EKF) is an approximation that allows the Kalman filter to be adopted for application to nonlinear systems through an appropriate linearization procedure (Zaknich, 2005). The basic idea of the EKF is to linearize the state-space model at each time instant around the most recent state estimate. Once each linear model is determined, the standard Kalman filter equations can be applied (Zaknich, 2005).

Consider a general continuous nonlinear system described by the following dynamic, output, and observation equations (Stengel, 1986)

$$\begin{aligned}\dot{\mathbf{z}}(t) &= \mathbf{f}\left[\mathbf{z}(t), \mathbf{u}(t), \mathbf{w}(t), t\right] \\ \mathbf{y}(t) &= \mathbf{h}\left[\mathbf{z}(t), t\right] \\ \mathbf{y}^m(t) &= \mathbf{h}\left[\mathbf{z}(t), t\right] + \mathbf{v}(t)\end{aligned} \tag{9-39}$$

where **f** and **h** are nonlinear functions, and the remaining parameters are as defined in previous sections. The EKF retains the linear calculation of covariance and gain matrices, and it updates the state estimate using a linear function of a filter residual; however, it uses the original nonlinear equations to propagate the state and define the output vector. The filter equations are given by

$$\begin{aligned}\dot{\hat{\mathbf{z}}}(t) &= \mathbf{f}\left[\hat{\mathbf{z}}(t), \mathbf{u}, t\right] + \mathbf{L}(t)\left[\mathbf{y}^m(t) - \hat{\mathbf{y}}(t)\right], \quad \hat{\mathbf{z}}(0) = \hat{\mathbf{z}}_0 \\ \hat{\mathbf{y}}(t) &= \mathbf{h}\left[\hat{\mathbf{z}}(t), \mathbf{u}, t\right]\end{aligned} \tag{9-40}$$

The Kalman filter gain, $\mathbf{L}(t)$, and error covariance estimate, $\mathbf{P}(t)$, are calculated using the following equations

$$\mathbf{L}(t) = \mathbf{P}(t)\mathbf{C}^T(t)\mathbf{R}^{-1}(t) \tag{9-41}$$

$$\dot{\mathbf{P}}(t) = \mathbf{A}(t)\mathbf{P}(t) + \mathbf{P}(t)\mathbf{A}^T(t) + \mathbf{G}(t)\mathbf{Q}(t)\mathbf{G}(t) - \mathbf{P}(t)\mathbf{C}^T(t)\mathbf{R}^{-1}(t)\mathbf{C}(t)\mathbf{P}(t) \tag{9-42}$$

where

$$\mathbf{A}(t) = \frac{\partial \mathbf{f}}{\partial \mathbf{z}}, \quad \mathbf{B}(t) = \frac{\partial \mathbf{f}}{\partial \mathbf{u}}, \quad \mathbf{G}(t) = \frac{\partial \mathbf{f}}{\partial \mathbf{w}}, \quad \mathbf{C}(t) = \frac{\partial \mathbf{h}}{\partial \mathbf{z}} \tag{9-43}$$

These time-varying Jacobians are functions of the state estimate and the input and, therefore, cannot be precomputed. Consequently, the gain matrix and filter equations must be calculated in real time as the process develops (Stengel, 1986).

In hybrid testing, the system response is analyzed at discrete time steps; therefore, the Kalman filter has to be implemented in discrete form. A nonlinear discrete system can be represented by the following equations

$$\begin{aligned}\mathbf{z}_{k+1} &= \mathbf{f}\left(\mathbf{z}_k\right) + \mathbf{B}\mathbf{u}_k + \mathbf{G}\mathbf{w}_k \\ \mathbf{y}_k &= \mathbf{h}\left(\mathbf{z}_k\right) \\ \mathbf{y}^m{}_k &= \mathbf{h}\left(\mathbf{z}_k\right) + \mathbf{v}_k\end{aligned} \tag{9-44}$$

where **f** and **h** are nonlinear functions of the state vector **z**, and the **B** and **G** matrices are assumed linear and time invariant. The nonlinear functions, **f** and **h,** can be expanded using the Taylor series about the corrected and predicted states, $\hat{\mathbf{z}}_k$ and $\hat{\mathbf{z}}_k^-$, respectively, as given by

$$\begin{aligned}\mathbf{f}(\mathbf{z}_k) &= \mathbf{f}(\hat{\mathbf{z}}_k) + \mathbf{F}(\hat{\mathbf{z}}_k)[\mathbf{z}_k - \hat{\mathbf{z}}_k] + \ldots \\ \mathbf{h}(\mathbf{z}_k) &= \mathbf{h}(\hat{\mathbf{z}}_k^-) + \mathbf{H}(\hat{\mathbf{z}}_k^-)[\mathbf{z}_k - \hat{\mathbf{z}}_k^-] + \ldots\end{aligned} \tag{9-45}$$

where

$$\mathbf{F}(\hat{\mathbf{z}}_k) = \left.\frac{\partial \mathbf{f}}{\partial \mathbf{z}}\right|_{\hat{\mathbf{z}}_k} \quad \text{and} \quad \mathbf{H}(\hat{\mathbf{z}}_k^-) = \left.\frac{\partial \mathbf{h}}{\partial \mathbf{z}}\right|_{\hat{\mathbf{z}}_k^-}. \tag{9-46}$$

The discrete EKF can be implemented using the following procedure (Kamen & Su, 1999):

Initialization:

$$\begin{aligned}\hat{\mathbf{z}}_0 &= E[\mathbf{z}_0] \\ \mathbf{P}_0 &= E[(\mathbf{z}_0 - \hat{\mathbf{z}}_0)(\mathbf{z}_0 - \hat{\mathbf{z}}_0)^T]\end{aligned} \tag{9-47}$$

For $k = 1, 2, \ldots$

- Prediction

$$\hat{\mathbf{z}}_k^- = \mathbf{f}(\hat{\mathbf{z}}_{k-1}) + \mathbf{B}\mathbf{u}_{k-1} \tag{9-48}$$

$$\mathbf{P}_k^- = \mathbf{F}(\hat{\mathbf{z}}_{k-1})\mathbf{P}_{k-1}\mathbf{F}^T(\hat{\mathbf{z}}_{k-1}) + \mathbf{G}\mathbf{Q}_{k-1}\mathbf{G}^T \tag{9-49}$$

- Filter gain computation and update

$$\mathbf{H}(\hat{\mathbf{z}}_k^-) = \left.\frac{\partial \mathbf{h}}{\partial \mathbf{z}}\right|_{\hat{\mathbf{z}}_k^-} \tag{9-50}$$

$$\mathbf{L}_k = \mathbf{P}_k^-\mathbf{H}^T(\hat{\mathbf{z}}_k^-)\left[\mathbf{H}(\hat{\mathbf{z}}_k^-)\mathbf{P}_k^-\mathbf{H}^T(\hat{\mathbf{z}}_k^-) + \mathbf{R}_k\right]^{-1} \tag{9-51}$$

$$\hat{\mathbf{z}}_k = \hat{\mathbf{z}}_k^- + \mathbf{L}_k\left[\mathbf{y}^m{}_k - \mathbf{h}(\hat{\mathbf{z}}_k^-)\right] \tag{9-52}$$

$$\mathbf{P}_k = \left[\mathbf{I} - \mathbf{L}_k\mathbf{H}(\hat{\mathbf{z}}_k^-)\right]\mathbf{P}_k^- \tag{9-53}$$

$$\mathbf{F}(\hat{\mathbf{z}}_k) = \left.\frac{\partial \mathbf{f}}{\partial \mathbf{z}}\right|_{\hat{\mathbf{z}}_k} \tag{9-54}$$

9.5.2 Application of Extended Kalman filter in pseudodynamic testing

In pseudodynamic testing, the discrete form of the nonlinear functions **f** and **h** depends on the algorithm used for numerical integration of the equation of motion. When the Central Difference Method is used, the nonlinear discrete model of the system is given by

$$\begin{aligned} \underbrace{\begin{bmatrix} \mathbf{x}_{k+1} \\ \mathbf{x}_k \end{bmatrix}}_{\mathbf{z}_{k+1}} &= \underbrace{\begin{bmatrix} \mathbf{a_1} & \mathbf{a_2} \\ \mathbf{I} & \mathbf{0} \end{bmatrix}\begin{bmatrix} \mathbf{x}_k \\ \mathbf{x}_{k-1} \end{bmatrix} + \begin{bmatrix} \mathbf{a_3 R}(\mathbf{x}_k) \\ \mathbf{0} \end{bmatrix}}_{\mathbf{f}(\mathbf{z}_k)} + \underbrace{\begin{bmatrix} \mathbf{b_1} \\ \mathbf{0} \end{bmatrix}}_{\mathbf{B}} F_k^{ext} \\ y_k &= \underbrace{\begin{bmatrix} \mathbf{x}_k \\ \mathbf{R}(\mathbf{x}_k) \end{bmatrix}}_{\mathbf{h}(\mathbf{z}_k)} \end{aligned} \tag{9-55}$$

where

$$\begin{aligned} \mathbf{a_1} &= \left[\frac{1}{\Delta t^2}\mathbf{M} + \frac{1}{2\Delta t}\mathbf{C}\right]^{-1}\left[\frac{2}{\Delta t^2}\mathbf{M}\right], \quad \mathbf{a_2} = \left[\frac{1}{\Delta t^2}\mathbf{M} + \frac{1}{2\Delta t}\mathbf{C}\right]^{-1}\left[\frac{1}{\Delta t^2}\mathbf{M} - \frac{1}{2\Delta t}\mathbf{C}\right] \\ \mathbf{a_3} &= -\left[\frac{1}{\Delta t^2}\mathbf{M} + \frac{1}{2\Delta t}\mathbf{C}\right]^{-1}, \qquad \mathbf{b_1} = \left[\frac{1}{\Delta t^2}\mathbf{M} + \frac{1}{2\Delta t}\mathbf{C}\right]^{-1} \end{aligned} \tag{9-56}$$

The only nonlinear parameter is the restoring force, **R**(**x**), which can be expanded using the Taylor series about the displacement estimate, $\hat{\mathbf{x}}_k$ as given by

$$\mathbf{R}\left(\mathbf{x}_k\right) = \mathbf{R}\left(\hat{\mathbf{x}}_k\right) + \mathbf{K}_t\left(\hat{\mathbf{x}}_k\right)\left[\mathbf{x}_k - \hat{\mathbf{x}}_k\right] + \ldots \tag{9-57}$$

where $\mathbf{K}\left(\hat{\mathbf{x}}_k\right)$ is the tangent stiffness matrix given by

$$\mathbf{K}_t\left(\hat{\mathbf{x}}_k\right) = \left.\frac{\partial \mathbf{R}}{\partial \mathbf{x}}\right|_{\hat{\mathbf{x}}_k}. \tag{9-58}$$

In real-time hybrid testing, the restoring force depends also on the velocity; therefore, it is necessary to express both the restoring force and tangent stiffness in terms of the entire state vector $\mathbf{z} = \left[\mathbf{x}^{\mathrm{T}} \quad \dot{\mathbf{x}}^{\mathrm{T}}\right]^{\mathrm{T}}$.

The matrices, **F** and **H**, required by the Extended Kalman Filter, are obtained using the linearized form of the restoring forces, and are given by the following equations

$$\mathbf{F} = \begin{bmatrix} \mathbf{a}_1 + \mathbf{a}_3 \mathbf{K}_t & \mathbf{a}_2 \\ \mathbf{I} & \mathbf{0} \end{bmatrix}$$
$$\mathbf{H} = \begin{bmatrix} \mathbf{I} & \mathbf{0} \\ \mathbf{K}_t^{exp} & \mathbf{0} \end{bmatrix} \tag{9-59}$$

Therefore, to extend the method for filtering errors in hybrid testing to cases of nonlinear response, the tangent stiffness of the physical substructure, $\mathbf{K}_t^{exp}$ and the entire system, $\mathbf{K}_t$, need to be determined. The Broyden formula presented previously in this report (see Equation 5-3) can also be used in this case to obtain estimates of the tangent stiffness. However, when the forces and displacements contain significant noise, estimation of the tangent stiffness may be challenging.

9.5.3 Numerical example

The procedure developed for using the Extended Kalman Filter in pseudodynamic testing is verified using numerical simulation. The test structure considered is the same as in the previous examples presented in this chapter, with the difference that the single-degree-of-freedom column (right column) is used as the physical substructure for this case (i.e., Mini-Most-1 experiment). The force-displacement relationship corresponding to the physical substructure is modeled using a bilinear hysteretic model with a yield displacement of 0.24 in (6.10 mm) and a ratio of post- to preyield stiffness of 0.05. The rest of the frame is assumed to remain in the elastic range. Experimental errors (control error for the displacement and measurement noise for the restoring force) were added to the simulation in a similar way as in the previous experiments (using the values determined experimentally for actuator-1 of the Mini-Most-2). However, for this case (Mini-Most-1), the magnitude of the errors had to be increased significantly (by factors of 5 and 50 for the control error and force noise, respectively) to produce comparable effects on the response as in the previous examples using the Mini-Most-2. This result confirms the fact that the effect of experimental errors is much more severe when the actuators are coupled. The results from the pseudodynamic numerical simulation without using the filter are presented in Figures 9.31 and 9.32. The error norms for the displacement and force are 0.432 and 0.585, respectively.

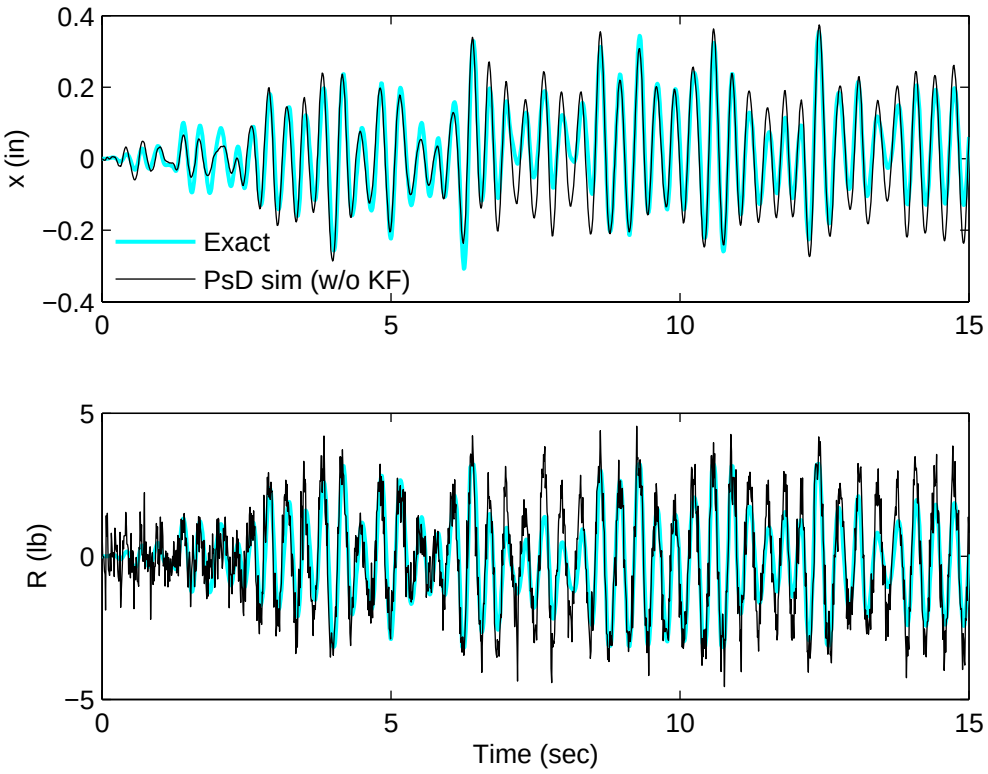

Figure 9.31: Results for nonlinear response without Kalman filter (time histories).

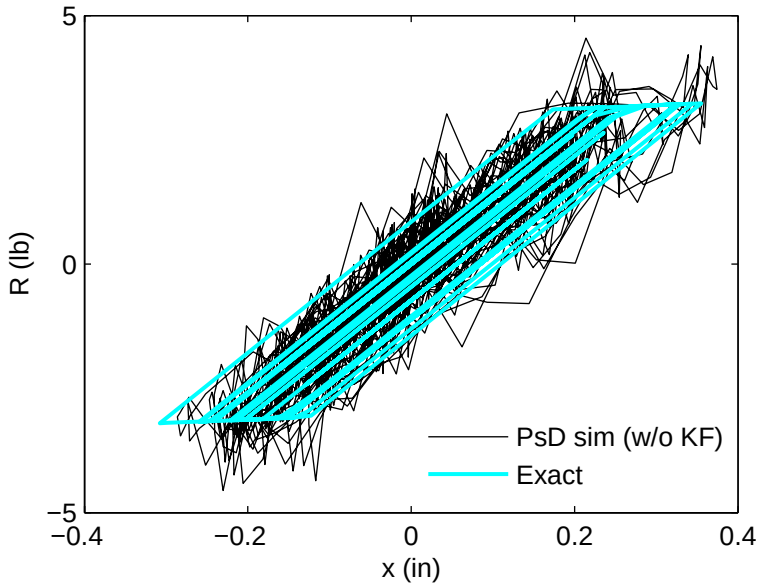

Figure 9.32: Results for nonlinear response without Kalman filter (force-deformation).

Initially, the Kalman filter was applied using the elastic stiffness of the physical substructure for the filter model. Results showed that although the filter effectively reduced the noise, the response of the system was not accurately simulated; the linear model in the filter cause the filtered response to be rather linear, instead of the actual bilinear response. The Extended Kalman Filter was then applied. For the tangent stiffness of the physical substructure, the stiffness value used to calculate the restoring force at each step was used (i.e., elastic stiffness or postyield stiffness). This procedure, although unrealistic, eliminates the uncertainty associated with the determination of the tangent stiffness using noisy measurements. The results of the simulations using the EKF with a filter weighting parameter ρ of 10^3 are presented in Figures 9.33 and 9.34. As can be observed, the filter effectively reduces the noise and captures the nonlinear behavior of the response. The error norms for the displacement and force are 0.112 and 0.089, respectively (which correspond to reductions on the error of 3.8 and 6.5, respectively, as compared to the case without the filter).

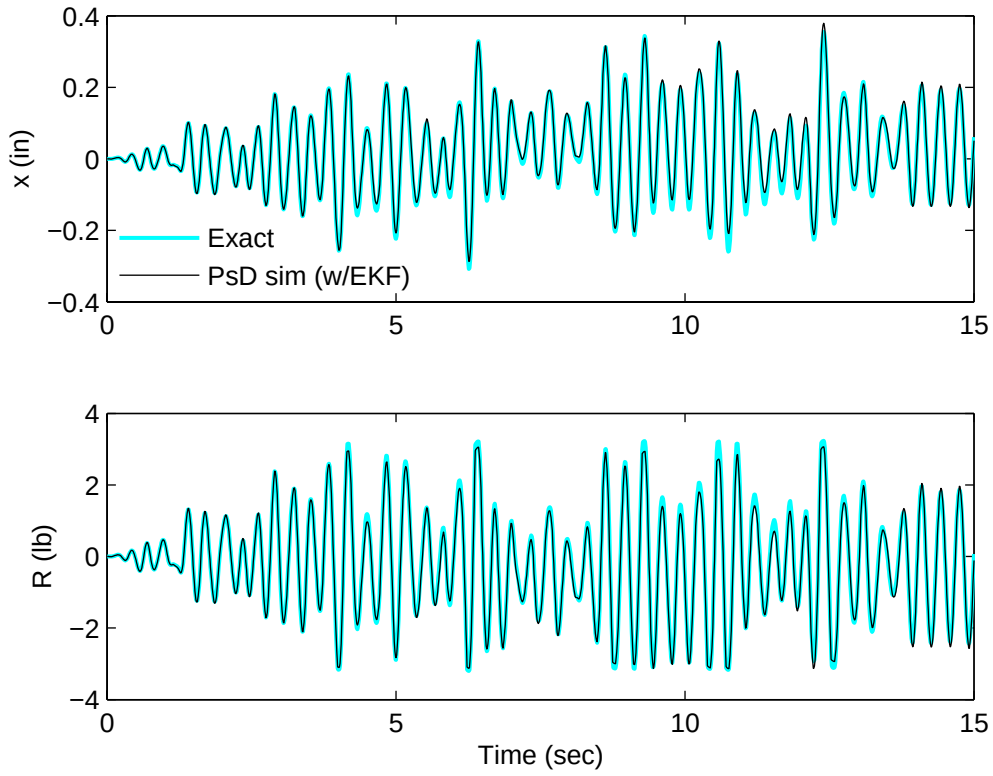

Figure 9.33: Results using Extended Kalman filter (time histories).

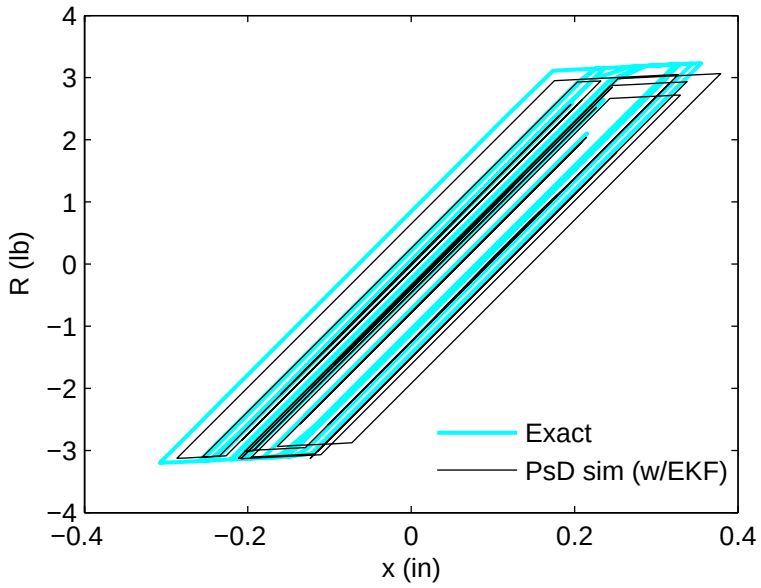

Figure 9.34: Results using Extended Kalman Filter (force-deformation).

The results of simulations conducted using different values of the filter weighting parameter, ρ, are presented in Figure 9.35. The filter performance is characterized by the error norm with respect to the exact solution. As opposed to the cases of linear response in which the variation of the filter performance with ρ was smooth, for the nonlinear responses, significant scatter is found.

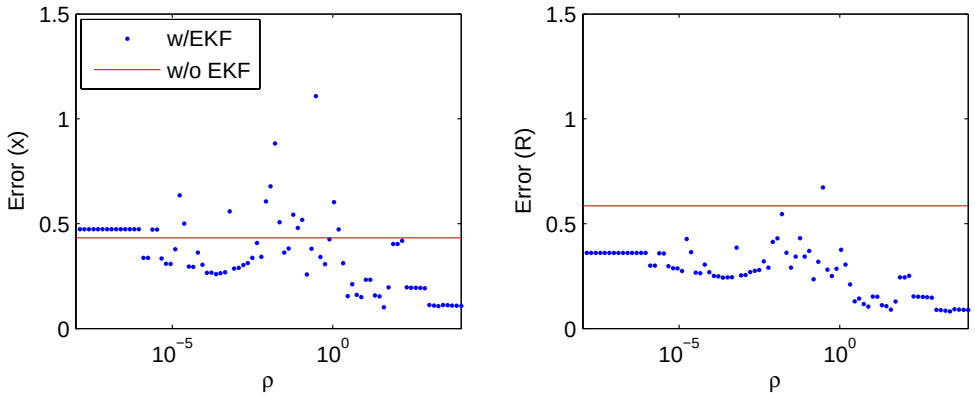

Figure 9.35: Results using Extended Kalman Filter with different values of ρ.

The performance of the filter was also found to be rather sensitive to specific parameters such as the yield displacement. Figures 9.36 and 9.37 show the results of the simulations using the EKF for the case when the value of the yield displacement is reduced to 0.2 in (5.08 mm). As can be observed in Figure 9.36, although the simulation is accurate at the beginning, after about 6 sec, the results start to deviate from the exact response, presenting an offset in both displacement and force values. Figure 9.37 shows the hysteretic filtered response, which also shows significant discrepancies with the exact

behavior. The magnitude possesses a clear offset in the forces, which is more evident in the post-yielding behavior.

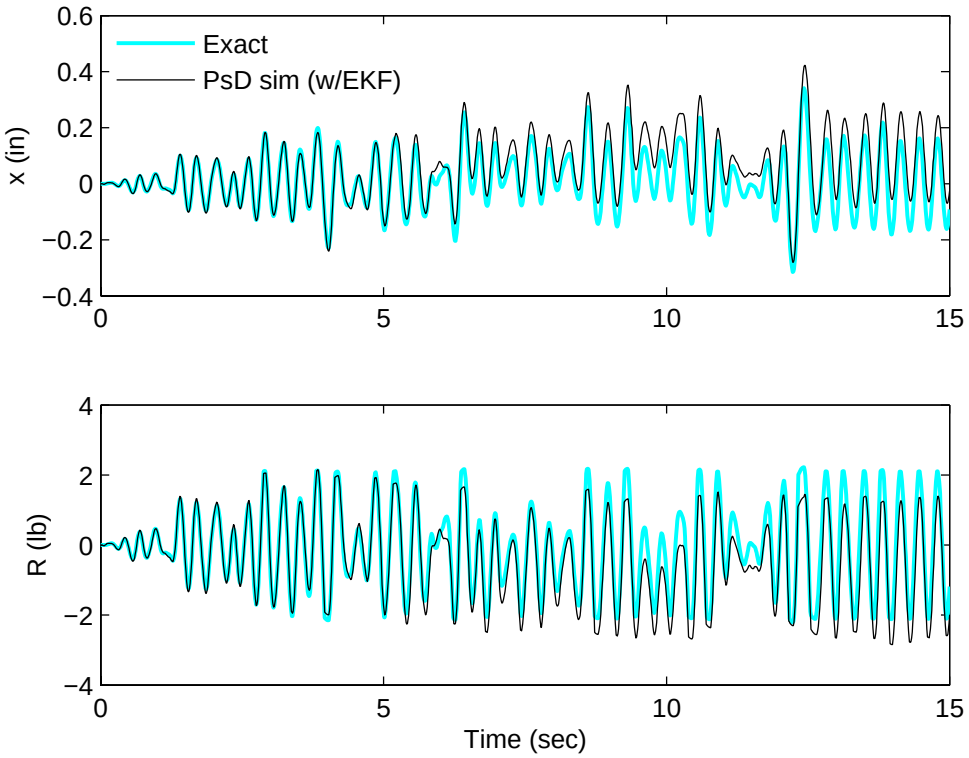

Figure 9.36: Results using Extended Kalman Filter (time histories).

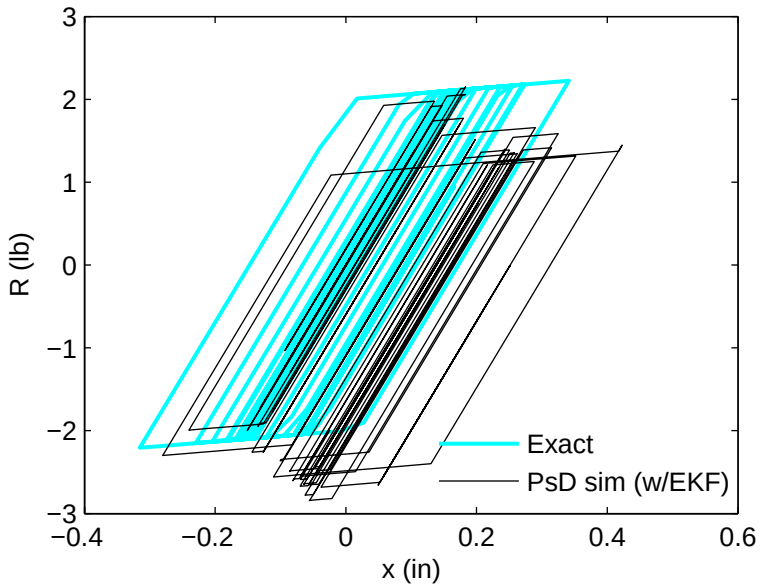

Figure 9.37: Results using Extended Kalman Filter (force-deformation).

Possible causes for this lower filter performance are the fact that in the application for hybrid testing, the model is linearized with respect to the actual measured state, as opposed to the estimated state, while the Extended Kalman Filter is only an approximation. More research is needed to verify both numerically and experimentally the filtering technique for cases of nonlinear inelastic response.

9.6 Summary

Minimizing experimental errors is very important in hybrid testing because errors can accumulate and propagate throughout the entire simulation. A technique for reducing the effect of experimental errors on the measurements from the physical substructures during hybrid experiments was presented. The technique is based on the concept of model-based filtering using the Kalman filter.

Initially, the method was verified numerically and experimentally by conducting pseudodynamic tests on a linear structure (Mini-Most-2). The physical substructure possessed two-degrees-of-freedom (displacement and rotation), which were imposed by two actuators. Pseudodynamic experiments conducted without the filter demonstrated that the accuracy of the test results was very sensitive to experimental errors and to the relative values of the degrees-of-freedom imposed on the specimen. Experiments conducted using the model-based filter demonstrated that the filtering technique significantly reduced the effects of the experimental errors, producing responses with good agreement with the analytical "exact" response.

The Kalman filter uses a model of the system to perform the predictions. Analyses were conducted to determine the effect of differences between the model used by the filter and the actual system on the performance of the Kalman filter. Results showed that in general, the performance of the Kalman filter on hybrid testing is sensitive to differences between the model and the actual system.

The application of the filtering technique for hybrid testing of structures with inelastic response was also considered. An approximation that allows extending the Kalman filter to nonlinear applications (Extended Kalman Filter) was reviewed and implemented for hybrid testing. The method requires linearization of the model at each time step, which in hybrid testing corresponds to the calculation of the tangent stiffness. Numerical simulations were performed assuming that the tangent stiffness was known. Results indicated that the method was able to effectively reduce the noise on the measurements while retaining the inelastic characteristics of the response. However, the method was found to be rather sensitive to some factors like the filter weighting parameter and the amount of inelastic deformation (e.g., yield displacement).

Experiments and analyses conducted show that the application of the Kalman filter to hybrid testing allows reducing the effect of experimental errors and, therefore, providing more accurate results; however, further development is still needed.

CHAPTER 10

CONCLUSIONS AND RECOMMENDATIONS

10.1 Conclusions

In the studies presented in this report, model-based strategies for real-time hybrid testing have been developed and experimentally verified for structures under seismic excitation. These model-based techniques provide accurate compensation for the effects of time delays and actuator dynamics and, therefore, allow expanding the capabilities of the real-time hybrid testing technique to broader types of structural systems. Real-time hybrid experiments were successfully conducted for structures with relatively high natural frequencies and for a structure incorporating a semiactive control device, namely an MR damper. Because it is capability to test rate-dependent components, real-time hybrid testing is a very effective technique to test devices associated with vibration control.

The background for this study was first provided. The hybrid testing technique was reviewed as well as its extensions. Emphasis was placed on real-time hybrid testing; challenges for this testing technique, as well as sources and effects of time delays and lags, were identified. Current methods for real-time hybrid testing were reviewed, and shortcomings of these techniques were identified, demonstrating the need for more rational methods to account for effects of time delays and actuator dynamics.

The experimental setup used for conducting real-time hybrid experiments was presented. The testing system uses equipment developed at the Smart Structures Technology Laboratory and combines fast hardware and software with high-performance hydraulic components. Characterization tests showed that the system is capable of performing high-speed computations and communication, as well as delivering the high loading rates required for fast hybrid testing. Experiments with sampling frequencies as high as 2,000 Hz were conducted. Because time delays and actuator dynamics are critical parameters in real-time hybrid testing, characterizations tests were conducted to quantify these parameters. Test results showed that the time lag associated with the dynamics of the actuator was the dominant factor, while computing time and delays related to communication, converters, and the controller were, in general, relatively small.

Traditional delay compensation approaches, which use only information from the displacements at a few previous time steps, only perform well when the time delays relative to the natural period of the structure are small. In this study, an approach for real-time hybrid testing was developed in which time delay/lag compensation was implemented using model-based response prediction. This method incorporates known information about the system and the excitation, which results in a more accurate

prediction of the response. This approach allows for the handling of larger delays, stability improvements, and testing of structures with higher natural frequencies or with more degrees-of-freedom. The efficacy of the proposed strategy was experimentally verified using both linear-elastic (spring) and rate-dependent (MR damper) test specimens. Results from the experiments demonstrated that the model-based compensation approach allows accurate testing of systems with natural frequencies about twice as large as the traditionally-used polynomial extrapolation method; structures with frequencies as high as 13 Hz for linear response and 15 Hz for inelastic response were successfully tested. Experimental results for the structure with the MR damper verified that the approach and testing system presented are capable of accurately testing rate-dependent devices.

To analyze the effects of actuator dynamics on the accuracy and stability of real-time hybrid testing, a numerical model of the testing system was developed. First, the equations for modeling the different components of the testing system (including servo-hydraulic actuator, controller, and test specimen) were reviewed and subsequently used to develop a model of the entire system. The dynamics of the testing system were represented concisely by the actuator transfer function, from the command displacement to the measured displacement. Two important characteristics of this transfer function are: (1) both magnitude and phase lag (and, therefore, time lag) are not constant but vary with frequency, and (2) the dynamics of the actuator are dependent on the test specimen (actuator-specimen interaction).

Using experimental data, the parameters for the testing system used in this study were identified. Because the dynamics of the actuator depend on the test specimen, different representations of the actuator transfer function were obtained for different test specimens and testing conditions. The model was then used to investigate the effect of the dynamics of the testing system and specimen on the accuracy and stability of real-time hybrid experiments. Methods for predicting the stability of the hybrid experiment were developed based on the actuator dynamics models. Stability analysis conducted in the frequency domain confirmed that the minimum damping of the system required for stability increases as the natural frequency of the test structure and time lag of the actuator increase. The mass of the experimental component (which includes the mass of the test specimen, attachments, and actuator's piston) was found to be important on the stability of the hybrid experiment. For the example considered, when this mass became larger than 2% of the mass of the test structure, the real-time hybrid simulation became unstable. The model of actuator dynamics was shown to be valuable for investigating the stability of the real-time hybrid testing technique as well as the effect of the different parameters.

The models and insight obtained regarding the dynamics of the testing system were used to develop model-based compensation techniques for actuator dynamics that account for both phase and magnitude effects. First, a feedforward compensator was considered. This compensator was based on the inverse of a model of the plant dynamics (i.e., actuator transfer function) with some modifications to make it realizable. The effect of the compensator was to make the compensated system have a magnitude close to one, and a phase that tends to zero. The experimental results demonstrated that the

performance of the compensator was excellent, significantly reducing tracking errors. For a sinusoidal displacement, the error norm was reduced from 7.48% (without compensation) to 0.98% (with compensation).

A combined feedforward-feedback compensator was then proposed. The feedback term was used to reduce the effect of differences between the model used for the feedforward compensator and the actual system. Experimental results produced error norms about half of the ones obtained with feedforward-only compensation. However, because feedback is used, the compensator has the potential to produce unstable responses when the feedback gain is set too high. The compensator was then extended to account for variations on the dynamics of the actuator by modifying the feedforward portion of the compensator. Linearized models of the actuator-specimen system were obtained for different operating points; individual feedforward controllers were designed for each operating point and then combined using a smooth transition. The algorithm was implemented for the case of an MR damper with variable input voltage. Experimental results using predefined displacement signals demonstrated the good performance of the compensator, which provided accurate compensation, even when the properties of the MR damper (and, therefore, actuator dynamics) changed significantly. Furthermore, testing of the MR damper specimen demonstrates the effectiveness of the algorithm to test specimens with complex nonlinear hysteretic response that are often encountered in building structures.

The compensation techniques developed were used to conduct real-time hybrid testing of a semiactively controlled structure under earthquake loading. The structure was equipped with an MR damper, which was tested experimentally. Several cases were considered: uncontrolled (without MR damper), passive control (voltage to the MR damper held constant), and semiactive control (voltage to MR damper varied during the experiment according to the clipped-optimal control algorithm). For all of the cases considered, the results from the experiments were in very good agreement with analytical results. Experimental results demonstrated the effectiveness of the real-time hybrid testing method to efficiently and accurately evaluate the response, not only for rate-dependent energy dissipation devices, but also the performance of the structural control strategy and overall structural system.

The hybrid test method is more sensitive to experimental errors than other methods, such as quasi-static and shaking-table testing in which a predefined displacement command history is used. Following a description of the types of errors typically encountered in hybrid testing, a filtering technique based on the concept of model-based filtering was developed to mitigate the effect of random errors in hybrid testing. The technique is based on the Kalman filter, which is a widely used method for linear filtering. The method was verified experimentally using a linear structure with a two-degree-of-freedom physical substructure (Mini-Most-2 system) that was particularly sensitive to experimental errors. Experiments conducted demonstrated that the filtering technique significantly reduced the effects of the experimental errors, resulting in overall improvements in the test results.

Because the proposed filtering technique is model-based, analyses were conducted to estimate the impact of differences between the model used by the Kalman filter and the actual system. Numerical simulation indicated that, in general, the performance of the filter is sensitive to differences between the model and the actual system.

The filtering technique was extended to nonlinear response cases using the Extended Kalman Filter. Numerical analyses indicated that the method effectively reduced the noise on the measurements while retaining the inelastic character of the response. However, the method was found to be rather sensitive to factors such as the filter weighting parameters and the amount of inelastic deformation (e.g., yield displacement). The experiments and analyses conducted show that the application of the Kalman filter to hybrid testing reduces the effect of experimental errors; however, further development is still needed.

The experiments conducted demonstrate that substructure real-time hybrid testing is an efficient method to experimentally evaluate the response of structural systems in which the conventional slow-speed pseudodynamic testing is not applicable (e.g., structures having rate dependent components). The model-based strategies and compensation techniques developed in this study allow accurate testing of structures with supplementary energy dissipation devices (including passive and semiactive control devices).

10.2 Future Studies

This section provides recommendations for future studies related to this work.

- The experiments conducted in this study used small-scale actuator and test specimens. Efforts should be directed toward verifying the proposed real-time hybrid testing strategies using larger-scale structures.

- When using actuators with larger force capacity and full-scale test specimens, the hydraulic natural frequency (oil-column resonance) is expected to occur at a smaller frequency; therefore, its effect on the hybrid experiments may be more significant and should be assessed.

- The experiments conducted in this study involved one physical substructure with a single actuator. Extension of the methodologies and techniques developed should be investigated for multiple physical substructures and with more than one degree-of-freedom.

- Although the digital signal processor used in this study performed satisfactorily, its technology is more than a decade old. Newer and faster processors should allow real-time hybrid experiments to be conducted for structures with more degrees-of-freedom or with more complex numerical substructures.

- Significant scatter is present in the results available in the literature for the strain-rate effect on conventional structural materials. Reported results indicate that the effect is significantly smaller for cyclic tests than for monotonic tests (therefore, depends on the type of loading). Real-time hybrid testing should be used to verify the strain-rate effect on conventional structural materials under realistic earthquake loading histories.

- Actuator dynamics are dependent on the test specimen. Most specimens respond nonlinearly. In this study, the effect of the nonlinear behavior of the MR damper on the dynamics of the actuator was accounted for using linearized models at two different operating points, and then using a smooth transition between these points. This model was used to develop model-based compensation that accounted for the specimen variations. Although this method produced very good results, nonlinear compensation strategies should be investigated.

- The model-based filtering technique for nonlinear hybrid experiments based on the Extended Kalman Filter was implemented numerically; however, this technique should also be verified experimentally.

- The filtering technique proposed in this study was based on the Kalman filter (which is a model-based filter). The applicability of other filters that do not require a model of the system and do not produce a time lag should be investigated (e.g., acausal filters).

REFERENCES

Åström, K. J., & Wittenmark, B. (1984). *Computer controlled systems: theory and design.* Prentice-Hall, New Jersey.

Baber, T. T., & Wen, Y. K. (1981). "Random vibration of hysteretic degrading systems." *Journal of Engineering Mechanics*, ASCE, 107(6): 1069-1087.

Blakeborough, A., Williams, M. S., Darby, A. P., & Williams, D. M. (2001). "The development of real-time substructure testing." *Philosophical Transaction of the Royal Society: Theme Issue on Dynamic Testing of Structures*, A 359: 1869-1891.

Carrion, J. E., & Spencer, B. F. (2006). "A model-based delay compensation approach for real-time hybrid testing." *Proceedings of the US-Taiwan Workshop on Smart Structural Technology for Seismic Hazard Mitigation*, Taipei, Taiwan.

Chang, K.-C., & Lee, G. C. (1987). "Strain rate effect on structural steel under cyclic loading." *Journal of Engineering Mechanics*, ASCE, 113(9): 1292-1301.

Chang, S.-Y. (1998). "A time integration pseudodynamic algorithm." *11th European Conference on Earthquake Engineering*. A. A. Balkema: Rotterdam.

Chang, Y-Y., Yang, Y-S., Wang, S-J., Lin, M-L., Weng, Y-T ., Wang, K-J., Deng, H-Z ., Lau, D. T., & Tsai, K-C. (2005). "Hybrid testing of a multi-span bridge." *Proceedings of The First International Conference on Advances in Experimental Structural Engineering*, Nagoya, Japan, 307-314.

Chen, C-T. (1993). *Linear system theory and design, 3rd edition*. Oxford University Press, New York.

Chung, L. L., Lin, R. C., Soong, T. T., & Reinhorn, A. M. (1989). "Experiments on active control for MDOF seismic structures." *Journal of Engineering Mechanics*, ASCE, 115(8): 1609–1627.

Clough, R. W., & Penzien, J. (1993). *Dynamics of Structures*, *2nd edition*, McGraw-Hill, New York.

Combescure, D., & Pegon, P. (1997). "α-Operator Splitting time integration technique for pseudodynamic testing error propagation analysis." *Soil Dynamics and Earthquake Engineering*, 16:427-443.

Conte, J. P., & Trombetti, T. L. (2000). "Linear dynamic modeling of a uni-axial shaking table system." *Earthquake Engineering and Structural Dynamics*, 29(9): 1375-1404.

Darby, A. P., Blakeborough, A., & Williams, M. S. (1999). "Real-time substructure tests using hydraulic actuator." *Journal of Engineering Mechanics*, ASCE, 125(10):1133-1139.

Darby, A. P., Williams, M. S., & Blakeborough, A. (1999). "Stability and delay compensation for real-time substructure testing." *Journal of Engineering Mechanics*, ASCE, 128(12): 1276-1284.

Darby, A. P., Blakeborough, A., & Williams, M. S. (2001). "Improved control algorithm for real-time substructure testing." *Earthquake Engineering and Structural Dynamics*, 30(3): 431–448.

Dermitzakis, S. N., & Mahin, S. A. (1985). "Development of substructuring techniques for on-line computer controlled seismic performance testing." *Report UCB/EERC-85/04*, Earthquake Engineering Research Center, University of California, Berkeley.

Dimig, J., Shield, C., French, C., Bailey, F., & Clark, A. (1999). "Effective force testing: A method of seismic simulation for structural testing." *Journal of Structural Engineering*, 125(9): 1028-1037.

Dyke, S. J., Spencer, B. F., Quast, P., & Sain, M. K. (1995). "Role of control-structure interaction in protective system design." *Journal of Engineering Mechanics*, ASCE, 121(2): 322-338.

Dyke, S. J. (1996). "Acceleration feedback control strategies for active and semi-active systems: modeling, algorithm development and experimental verification." Ph.D. Dissertation, University of Notre Dame, IN.

Dyke, S. J., Spencer Jr., B. F., Sain, M. K., & Carlson, J. D. (1996). "Modeling and control of magnetorheological dampers for seismic response reduction." *Smart Materials and Structures*, 5: 565-575.

Dyke, S. J., Spencer, Jr., B. F., Sain, M. K., & Carlson, J. D. (1997). "An Experimental Study of MR Dampers for Seismic Protection." *Smart Materials and Structures*: *Special Issue on Large Civil Structures*.

Ellis, G. (2000). *Control system design guide*. Academic Press, San Diego, CA.

Emmons, A., & Christenson, R. (2006). "Proposed full-scale experimental verification of semiactive control applied to a nonlinear structure." *Proceedings of the 17th Analysis and Computation Conference* (*ASCE*), Paper No. 4.

Franklin, G. F., Powell, J. D., & Emani-Naeini, A. (2002). *Feedback control of dynamic systems*. Prentice-Hall, New Jersey.

Ghaboussi, J., Yun, G.J., & Hashash, Y.M.A. (2006). "A novel predictor–corrector algorithm for sub-structure pseudo-dynamic testing." *Earthquake Engineering and Structural Dynamics*, 35(4): 453-476.

Hakuno, M., Shidawara, M., & Hara, T. (1969). "Dynamic destructive test of a cantilever beam controlled by an analog-computer." *Trans. Jpn Soc. Civ. Engrs*, 171: 1–9. (In Japanese).

Hilber, H. M., Hughes, T.J.R., & Taylor, R. L. (1977). "Improved numerical dissipation for time integration algorithms in structural dynamics." *Earthquake Engineering and Structural Dynamics*, 5(3): 283-292.

Horiuchi, T., Nakagawa, M., Sugano, M., & Konno, T. (1996). "Development of a real-time hybrid experimental system with actuator delay compensation." *In Proc. 11th World Conf. Earthquake Engineering*, Paper No. 660.

Horiuchi, T., Inoue, M., Konno, T., & Namita Y. (1999). "Real-time hybrid experimental system with actuator delay compensation and its application to a piping system with energy absorber." *Earthquake Engineering and Structural Dynamics*, 28(10): 1121-1141.

Hughes, T.J.R., & Liu, W. K. (1978). "Implicit–explicit finite elements in transient analysis: stability theory." *Journal of Applied Mechanics*, 45: 375–378.

Hughes, T.J.R., Pister, K. S., & Taylor R. L. (1979). "Implicit–explicit finite elements in non-linear transient analysis." *Computer Methods in Applied Mechanics and Engineering*, 17(18): 159–182.

Juang, J. N. (1993). *Applied System Identification*. Prentice Hall.

Jung, R-Y., & Shing, P. B. (2006). "Performance evaluation of a real-time pseudodynamic test system." *Earthquake Engineering and Structural Dynamics*, 35(7): 789-810.

Kalman, R. E. (1960). "A new approach to linear filtering and prediction problems". *Transactions of the ASME, Journal of Basic Engineering*, 82: 35-45.

Kalman, R. E., & Bucy, R. S. (1961). "New results in linear filtering and prediction theory." *Transactions of the ASME, Journal of Basic Engineering*, 83: 95-108.

Kamen, E. W., & Su, J. K. (1999). *Introduction to Optimal Estimation*. Springer, London.

Kim, S. B., Spencer, B. F., & Yun, C-B. (2005). "Frequency domain identification of multi-input, multi-output systems considering physical relationships between measured variables." *Journal of Engineering Mechanics*, ASCE, 131(5): 461-472.

Krempl, E. (2001). "Relaxation behavior and modeling." *International Journal of Plasticity*, 17: 1419-1436.

Magonette, G. (2001). "Development and application of large-scale continuous pseudo-dynamic testing techniques." *Philosophical Transaction of the Royal Society: Theme Issue on Dynamic Testing of Structures*, A 359: 1771-1799.

Mahin, S. A., & Bertero, V. V. (1972). "Rate of loading effects on uncracked and repaired reinforced concrete members." *Report No. EERC 72-9,* Earthquake Engineering Research Center, University of California, Berkeley.

Mahin, S. A., & Shing, P. B. (1985). "Pseudodynamic method for seismic testing." *Journal of Structural Engineering*, 111(7): 1482-1503.

Mahin, S. A., et al. (1985). "Extension of pseudodynamic methods for seismic performance evaluation." *Proc., Joint Tech. Meeting*, U.S.-Japan Cooperative Earthquake Res. Program, Maui, Hawaii.

Mahin, S. A., Shing, P. B., Thewalt, C. R., & Hanson, R. D. (1989) "Pseudodynamic test method. Current status and future directions." *Journal of Structural Engineering*, ASCE, 115(8): 2113-2128.

Malvern, L. E. (1951). "The propagation of longitudinal stress waves of plastic deformation in a bar of material exhibiting a strain-rate effect." *Journal of Applied Mechanics*, 18(2): 203-208.

Merritt, H. E. (1967). *Hydraulic control systems*. Wiley, New York.

MOOG. "Electrohydraulic valves a technical look." *Moog Technical Paper*.

Mosqueda, G., Stojadinovic, B., & Mahin, S. (2004). "Geographically distributed continuous hybrid simulation." *Proceedings of the 13th World Conference on Earthquake Engineering*, Vancouver, Canada, Paper No. 0959.

Nakashima, M., Kaminosono, T., Ishida, I., & Ando, K. (1990). "Integration techniques for substructure pseudo dynamic test." *Proceedings*, *Fourth U.S. National Conference on Earthquake Engineering*, Volume 2, EERI, Palm Springs, CA.

Nakashima, M., Kato, H., & Takaoka, E. (1992). "Development of real-time pseudo dynamic testing." *Earthquake Engineering and Structural Dynamics*, 21(1):79-92.

Nakashima, M., & Masaoka, N. (1999). "Real time on-line test for MDOF systems." *Earthquake Engineering and Structural Dynamics*, 28(4):393-420.

Newmark, N. M. (1959). "A method of computation for structural dynamics." *Journal of Engineering Mechanics*, ASCE, 85: 67–94.

Plesha, M. E., & Belytschko, T. (1985). "A constitutive operator splitting method for nonlinear transient analysis." *Computers and Structures*, 20(4): 767-777.

Poley, R. (2005). "DSP control of electro-hydraulic servo actuators", *Texas Instruments Application Report*.

Schenck Pegasus. "Model 132A Servovalve", *Product Datasheet*.

Shield, C, French, C, & Timm, J. (2001). "Development and implementation of the effective force testing method for seismic simulation of large-scale structures." *Philosophical Transaction of the Royal Society: Theme Issue on Dynamic Testing of Structures*, A 359: 1911-1929.

Shing P. B., & Mahin, S. A. (1988). "Rate-of-loading effects on pseudodynamic tests." *Journal of Structural Engineering*, ASCE, 114(11):2403-2420.

Shing P. B., Vannan, M. T., & Cater, E. (1991). "Implicit time integration for pseudodynamic tests." *Earthquake Engineering and Structural Dynamics*, 20(6):551-576.

Shing, P. B., Nakashima, M., & Bursi, O. S. (1996). "Application of pseudodynamic test method to structural research." *Earthquake Spectra*, EERI, 12(1):29-54.

Shing, P. B., Spacone, E., & Stauffer, E. (2002). "Conceptual design of fast hybrid test system at the University of Colorado." *Proceedings, Seventh U.S. National Conference on Earthquake Engineering*, Boston.

Shing, P. B., Wei, Z., Jung, R. Y., Stauffer, E. (2004). "NEES fast hybrid test system at the University of Colorado." *Proceedings of the 13th World Conference on Earthquake Engineering*, Vancouver, Canada, Paper No. 3497.

Soong T. T., & Spencer Jr., B. F. (2002). "Supplemental energy dissipation: state-of-the-art and state-of-the practice." *Engineering Structures*, 24: 243–259.

Sorenson, H. W. (1970). "Least-squares estimation: from Gauss to Kalman", *IEEE Spectrum*, 7: 63-68.

Spencer, B. F., Jr., Dyke, S. J., Sain, M. K., & Carlson, J. D. (1997). "Phenomenological model for magnetorheological dampers." *Journal of Engineering Mechanics*, ASCE, 123(3): 230-238.

Spencer, B. F., Jr., & Nagarajaiah, S. (2003). "State of the art of structural control." *Journal of Structural Engineering*, ASCE, 129(7): 845–856.

Spencer, B. F., Jr., et al. (2004). "The MOST experiment: earthquake engineering on the grid", *Technical Report NEESgrid*-2004-41.

Stengel, R. F. (1986). *Stochastic optimal control: Theory and Application*, John Wiley & Sons, Inc., New York.

Stoten, D. P., & Benchoubane, H. (1990). "Robustness of a minimal controller synthesis algorithm." *Int. J. Control*, 51: 967-983.

Stouffer, D. C., & Dame, L. T. (1996). *Inelastic deformation of metals*, John Wiley & Sons, Inc., New York.

Takanashi, K. et al . (1974). "Seismic failure analysis of structures by computer-pulsator on-line system." *J. Inst. of Industrial Sci.*, Univ. of Tokyo, Tokio, Japan, 26(11):13-25. (In Japanese).

Takanashi, K. et al . (1975). "Nonlinear earthquake response analysis of structures by a computer actuator on-line system. (Part 1: details of the system.)." *Trans. Architectural Inst. of Japan*, Tokio, Japan, 229: 77-83. (In Japanese).

Takanashi, K., Udagawa, K., Seki, M., Okada, T., & Tanaka H. (1975). "Nonlinear earthquake response analysis of structures by a computer-actuator on-line system" *Bulletin of Earthquake Resistant Structure Research Center 8, Institute of Industrial Science*, University of Tokyo, Tokyo, Japan.

Takanashi, K., Udagawa, K., & Tanaka, H. (1978). "Earthquake response analysis of steel frames by computer-actuator on-line system". *Proc., 5th Japan Earthquake Engrg. Symp.*, 1321-1328.

Takanashi, K., & Ohi, K. (1983). "Earthquake response analysis of steel structures by rapid computer-actuator on-line system, (1) a progress report, trial system and dynamic response of steel beams." *Bull. Earthquake Resistant Struct. Research Center* (*ERS*), Inst. of Industrial Sci., Univ. of Tokyo, Tokyo, Japan, 16: 103-109.

Takanashi, K., & Nakashima, M. (1987). "Japanese activities on on-line testing." *Journal of Engineering Mechanics*, ASCE, 113(7): 1014-1032.

Tsai, K.-C., Yeh, C.-C., Yang, Y.-S. Wang, K.-J., Wang, S.-J., & Chen, P.-C. (2003). "Seismic hazard mitigation: internet-based hybrid testing framework and examples." *International Colloquium on Natural Hazard Mitigation: Methods and Applications*, France, May 2003.

Umekita, K., Kametani, M., & Miyake, N. (1995). "Development of super real-time controller which can perform analysis with measurement/control in real time." *Proc. 5th Robot Symp.*, Robotics Society of Japan, 55-58.

Watanabe, E., Kitada, T., Kunitomo, S., & Nagata, K. (2001). "Parallel pseudodynamic seismic loading test on elevated bridge system through the internet." *The Eight East Asia-Pacific Conference on Structural Engineering and Construction*, Singapore, December 2001.

Welch, G., & Bishop, G. (2004). "An introduction to the Kalman filter". http://www.cs.unc.edu/~welch/kalman/kalmanIntro.html.

Wen, Y. K. (1976). "Method for random vibration of hysteretic systems." *Journal of Engineering Mechanics*, ASCE, 102(2): 249-263.

Williams, D. M., Williams, M. S., & Blakeborough, A. (2001). "Numerical modeling of a servo-hydraulic testing system for structures." *Journal of Engineering Mechanics*, ASCE, 127(8), 816-827.

Wu, B., Bao, H., Ou, J., & Tian, S. (2005). "Stability and accuracy analysis of the central difference method for real-time substructure testing." *Earthquake Engineering and Structural Dynamics*, 34: 705–718.

Wu, B., Wang, Q-Y., Shi, P-F., Ou, J-P., & Guan, X-C. (2006). "Real-time substructure test of JZ20-2NW offshore platform with semi-active MR dampers." *Proceedings of the 4th International Conference on Earthquake Engineering*, Taipei, Taiwan, Paper No. 185.

Yang, G., Spencer Jr., B. F., Carlson, J. D., & Sain, M. K. (2002). "Large-scale MR fluid dampers: Modeling and dynamic performance considerations." *Engineering Structures*, 24: 309–323.

Yang, Y. S., Wang, S. J., Wang, K. J., Lin, M. L., Weng, Y. T., Cheng, W. C., Chang, Y. Y., Tsai, K. C., Lau, D. T., Hsieh, S. H., Lin, F. P., & Lin, S. Y. (2006). "Network system for a transnational collaborative pseudodynamic experiment on a DSCFT-pier bridge system." *The 8th National Conference on Earthquake Engineering*, San Francisco, USA, April 2006, Paper No 810.

Yun, C-B., Lee, I-W., Park, D-U., & Watanabe, E. (2000). "Remote parallel testing using the internet on base isolated bridge." *The Thirteen KKNN Symposium on Civil Engineering*, Taiwan, December 2000.

Zaknich, A. (2005). *Principles of adaptive filters and self-learning systems*. Springer, London.

Zhao, J., French, C., Shield, C., & Posbergh, T. (2006). "Comparison of tests of a nonlinear structure using a shake table and the EFT method." *Journal of Structural Engineering*, 132(9): 1473-1481.

List of Recent NSEL Reports

No.	*Authors*	*Title*	*Date*
001	Nagayama, T. and Spencer, B.F.	Structural Health Monitoring Using Smart Sensors	Nov. 2007
002	Sun, S. and Kuchma, D.A.	Shear Behavior and Capacity of Large-Scale Prestressed High-Strength Concrete Bulb-Tee Girders	Nov. 2007
003	Nagle, T.J. and Kuchma, D.A.	Nontraditional Limitations on the Shear Capacity of Prestressed Concrete Girders	Dec. 2007
004	Kwon, O-S. and Elnashai, A.S.	Probabilistic Seismic Assessment of Structure, Foundation, and Soil Interacting Systems	Dec. 2007
005	Nakata, N., Spencer, B.F., and Elnashai, A.S.	Multi-dimensional Mixed-mode Hybrid Simulation: Control and Applications	Dec. 2007
006	Carrion, J. and Spencer, B.F.	Model-based Strategies for Real-time Hybrid Testing	Dec. 2007